Universitat Autònoma de Barcelona

# Point Defects Engineering in Oxides Thin Films for Energy and Information Technologies

**Yunqing Tang**

Universitat Autònoma de Barcelona

Tesis doctoral

# Point Defects Engineering in Oxides Thin Films for Energy and Information Technologies

Autora:

Yunqing Tang

Directores:

Albert Tarancón Rubio, Alejandro Morata García

y Francesco Maria Chiabrera

# Point Defects Engineering in Oxides Thin Films for Energy and Information Technologies

Autora:

Yunqing Tang

Tesis doctoral

Programa de Doctorado en Ciencia de Materiales

Directores:

Albert Tarancón Rubio, Alejandro Morata García,

Francesco Maria Chiabrera

Tutora:

Gemma Garcia Alonso

Universidad Autónoma de Barcelona (UAB)

Institut de Recerca en Energía de Catalunya (IREC)

2021

Universitat Autònoma de Barcelona

Shaping Energy for a Sustainable Future

El Prof. Albert Tarancón Rubio, el Dr. Alejandro Morata García y el Dr. Francesco Maria Chiabrera, investigadores del Instituto de Investigación en Energía de Cataluña (IREC), CERTIFICAN:

Que la memoria titulada **Point Defects Engineering in Oxides Thin Films for Energy and Information Technologies** presentada por Yunqing Tang para optar al grado de Doctor en el Programa de Ciencia de Materiales de la Universitat Autònoma de Barcelona ha sido realizada bajo su dirección en el Institut de Recerca en Energía de Catalunya (IREC).

Barcelona, Diciembre de 2021

Prof. Albert Tarancón Rubio

Dr. Alejandro Morata García

Dr. Francesco Maria Chiabrera

# Acknowledgements

During the past years, I have received support and encouragement from many people, without them this thesis cannot be accomplished. First and foremost, I would like to express my sincere and deep gratitude to my directors Prof. Albert Tarancón, Dr. Francesco Chiabrera and Dr. Alex Morata. Thanks to Albert for giving me the opportunity to do this thesis in Nanoionics and Fuel Cells group, for providing the helpful suggestions at the weekly technical meetings, for the support on the research topics. I would like to say thank you to Francesco for guiding my interest in physics. Thank you for your patience, encouragement and enthusiasm for the research topics, as well as for devoting time to review research findings. I'd want to express my gratitude to Alex for providing me with advice, assistance, and guidance, which has helped me tremendously when I was facing challenges. I would like to acknowledge my tutor Gemma Garcia Alonso for her tutelage.

I'm grateful to the persons listed below for their help with various technologies. Thanks to Dr. Josep Maria for the XRD measurements; thanks to Dr. Andrea and Dr. Ainara for performing the SIMS experiments; Thanks to Dr. Maciej Oskar for the professional PALS experiments.

Many thanks to my colleagues: Alex, Hemesh, Marc Torrell, Marc Núñez, Nerea, Iñigo, Gotzon, Juan Carlos, Lucile, Valerie, Simone, Arianna, Marco, Fjorelo, Juande, José and Philipp, thanks for your thoughtful help and suggestions in my daily work. Working with all of you was a wonderful and memorable experience.

I am grateful to my friends with whom I spent pleasant time during these years, chatting with them did enlighten me and motivate me. I also appreciate the encouragement and care I received from my cousin when I was depressed.

Finally, special thanks to my parents for their unconditional support and precious advices in my life. It is my fortune to be their daughter, I will remember their contributions forever.

# Abstract

In today's society, the increased challenges of energy crisis and environmental pollution urge the development of environmentally friendly and pollution-free energy storage and conversion devices, such as solid oxide fuel cells (SOFC), batteries and so on. In addition, the advancement of industrialization and information technologies requires the emergence of safe, efficient and low energy-consumption electronic devices.

Transition metal oxides are promising materials for energy and information applications because of the flexibility of their functional properties. In these materials, point defects have significant effects on the functional properties, such as electrical conductivity, magnetic properties and catalytic activity etc. Thus, understanding and quantifying the point defects in transition metal oxides is crucial for tailoring their functional properties for energy and information applications. This is even more relevant in oxide thin films, where other phenomena, such as homo and hetero interfaces, are known to severely impact their defect concentration but their limited dimensions hinder the applicability of traditional methods for point defect quantification. This thesis is devoted to the quantification and control of point defects in $La_{1-x}Sr_xFeO_{3-\delta}$ (LSF) thin films, a material widely used as electrode in energy and information technologies. Based on the knowledge of defect chemistry, the application of LSF thin films is extended to synaptic transistors. The work is focused on the following aspects: i) Quantification of the point defects in LSF thin films as a function of oxygen partial pressure at intermediate-to-low temperatures by in-situ ellipsometry; ii) study of the defect chemistry of $La_{0.5}Sr_{0.5}FeO_{3-\delta}$ (LSF50) thin films during the ion intercalation process in liquid alkaline electrolyte at room temperature; iii) development of a synaptic transistor with solid electrolyte.

In the first part of this thesis, a novel ellipsometry method for studying the defect chemistry of LSF thin films is developed. Ellipsometry spectra of LSF thin films were highly sensitive to the variation of hole concentration. Through this novel technique, the optical conductivity of LSF thin films can be univocally related with the hole concentration in the LSF thin films with different Sr content (Sr content= 0.2, 0.4 and 0.5). A novel in-situ spectroscopic ellipsometry approach was developed to study the hole concentration in the LSF thin films as a function of oxygen partial pressure from $10^{10}$ to $10^{-17}$ bar at intermediate-to-low temperatures (350 ºC-540 ºC). The results demonstrate the applicability of ellipsometry to study the defect chemistry of oxides thin films

and show the importance of non-dilute behavior in the layers. In this sense, the in-situ ellipsometry approach is able to push the current limits for the direct measurements of point defects in the LSF thin films to intermediate-to-low temperatures, which represents a crucial step forward in the understanding of LSF thin films for low-temperature applications.

In the second part of this thesis, the in-situ ellipsometry technique is extended to measure the concentration of point defects in LSF50 thin films during the ion intercalation process in alkaline electrolyte. A series of ex-situ techniques show that both oxygen and protons were intercalated into LSF50 perovskite structure at moderate electrochemical potentials, giving rise to the variation of hole concentration in the LSF50 thin films as a charge compensation mechanism. In-situ ellipsometry measurements of the optical conductivity during the ion intercalation allowed to develop a defect chemistry model to describe the ionic intercalation in LSF thin films in liquid alkaline electrolytes. Overall, in-situ ellipsometry shows possibility of revealing the defect chemistry of LSF50 thin films during ion intercalation in liquid electrolyte, which is a crucial progress for understanding and tailoring the LSF50 thin films' functional properties for energy and information applications.

In the third part of this thesis, the proof of concept of the LSF50/$Bi_4V_{1.8}Cu_{0.2}O_{10.7}$ (BICUVOX) synaptic transistor is proved. BICUVOX thin film was found to be suitable as an electrolyte in the synaptic transistor due to its high in-plane ionic conductivity at low temperatures. LSF50 films were employed as gate and channel due to the tunable electronic structure through modifying the concentration of point defects, such as oxygen vacancies. Writing voltages applied to the gate were found to be able to drive oxide ions from the gate (channel) to the channel (gate) through the BICUVOX electrolyte at low temperatures. Oxide ions incorporated into the channel can vary the oxygen content and modify the electrical conductance of the LSF50 thin film channel. The performance of the LSF50/BICUVOX synaptic transistor at temperature as low as 150 ºC is demonstrated.

In appendix, optical impedance spectroscopy is proposed for LSF thin films. Sinusoidal optical signals as the response of the oscillatory electrical voltages were collected by in-situ/in-operando ellipsometry, a formalism was developed to describe the optical behaviour of the LSF thin films. The electrochemical parameters determined from the optical impedance spectra for the solid-electrolyte electrochemical cell were in good agreement with those derived from the electrochemical impedance spectra, demonstrating the reliability and

applicability of optical impedance spectroscopy for LSF/CGO/YSZ electrochemical cells at intermediate temperatures.

In summary, this thesis deals with the study of the point defects of LSF thin films and its application in synaptic transistors, the novel in-situ ellipsometry approach gets insight into the defect chemistry of LSF thin films. The synaptic transistor with the solid electrolyte BICUVOX based on the defect chemistry of the LSF thin films can be operated at temperatures as low as 150 ºC.

# Resumen

En la sociedad actual, los crecientes desafíos de la crisis de energía y la contaminación ambiental instan al desarrollo de dispositivos de conversión y almacenamiento de energía respetuosos con el medio ambiente y libres de contaminación, como las pilas de combustible de óxido sólido (SOFC), baterías, etc. Además, el avance de la industrialización y de las tecnologías de información requiere la aparición de dispositivos electrónicos seguros, eficientes y de bajo consumo energético.

Los óxidos de metales de transición son materiales prometedores para aplicaciones de energía e información debido a la flexibilidad de sus propiedades funcionales. En estos materiales, los defectos puntuales tienen efectos significativos en las propiedades funcionales, como la conductividad eléctrica, las propiedades magnéticas y la actividad catalítica, etc. Por lo tanto, comprender y cuantificar los defectos puntuales en los óxidos de metales de transición es crucial para adaptar sus propiedades funcionales a las aplicaciones de energía e información. . Esto es incluso más relevante en películas delgadas de óxidos, donde se sabe que otros fenómenos, como las interfaces homogéneas y heterogéneas, impactan severamente su concentración de defectos, pero sus dimensiones limitadas dificultan la aplicabilidad de los métodos tradicionales para la cuantificación de defectos puntuales. Esta tesis está dedicada a la cuantificación y el control de defectos puntuales en películas delgadas de $La_{1-x}Sr_xFeO_{3-\delta}$ (LSF), un material muy utilizado como electrodo en tecnologías de energía e información. Basado en el conocimiento de la química de defectos, la aplicación de películas delgadas de LSF se extiende a transistores sinápticos. El trabajo se centra en los siguientes aspectos: i) Cuantificación de los defectos puntuales en películas delgadas de LSF en función de la presión parcial de oxígeno a temperaturas intermedias a bajas mediante elipsometría in-situ; ii) estudio de la química de defectos de las películas delgadas de $La_{0.5}Sr_{0.5}FeO_{3-\delta}$ (LSF50) durante el proceso de la intercalación de iones en electrolito alcalino líquido a temperatura ambiente; iii) desarrollo de un transistor sináptico con electrolito sólido.

En la primera parte de la tesis, se desarrolla un nuevo método de elipsometría para estudiar la química de defectos de películas delgadas de LSF. Los espectros de elipsometría de las películas delgadas de LSF fueron muy sensibles a la variación de la concentración de huecos. A través de esta nueva técnica, la conductividad óptica de las películas delgadas de LSF se

puede relacionar unívocamente con la concentración de huecos en las películas delgadas de LSF con diferente contenido de Sr (contenido de Sr = 0,2, 0,4 y 0,5). Se desarrolló un nuevo enfoque de elipsometría espectroscópica in-situ para estudiar la concentración de huecos en las películas delgadas de LSF en función de la presión parcial de oxígeno de $10^{10}$ a $10^{-17}$ bar a temperaturas intermedias a bajas (350 ºC-540 ºC). Los resultados demuestran la aplicabilidad de la elipsometría para estudiar la química de defectos de películas delgadas de óxidos y muestran la importancia del comportamiento no diluido en las capas. De esta manera, el método de elipsometría in-situ puede empujar los límites actuales para las mediciones directas de la química de defectos de las películas delgadas de LSF a temperaturas intermedias a bajas, lo que representa un paso crucial adelante en la comprensión de las películas delgadas de LSF para aplicaciones de bajas temperaturas.

En la segunda parte de esta tesis, se amplía la técnica de elipsometría in-situ para medir la concentración de defectos puntuales en películas delgadas LSF50 durante el proceso de intercalación iónica en electrolitos alcalinos. Una serie de técnicas ex-situ muestran que tanto el oxígeno como los protones se intercalaron en la estructura de perovskita de LSF50 a potenciales electroquímicos moderados, dando lugar a la variación de la concentración de huecos en las películas delgadas de LSF50 como mecanismo de compensación de carga. Las mediciones de elipsometría in-situ de la conductividad óptica durante la intercalación de iones permitieron desarrollar un modelo de químico de defectos para describir la intercalación iónica en películas delgadas de LSF en electrolitos alcalinos líquidos. En general, la elipsometría in-situ muestra la posibilidad de revelar la química de defectos de las películas delgadas de LSF50 durante la intercalación de iones en el electrolito líquido, que es un progreso crucial para comprender y adaptar las propiedades funcionales de las películas delgadas de LSF50 para aplicaciones de energía e información.

En la tercera parte de esta tesis se demuestra la prueba de concepto del transistor sináptico LSF50/$Bi_4V_{1.8}Cu_{0.2}O_{10.7}$ (BICUVOX). Se descubrió que la película delgada de BICUVOX era adecuada como electrolito en el transistor sináptico debido a su alta conductividad iónica en el plano a bajas temperaturas. Las capas de LSF50 se emplearon como compuerta y canal debido a la estructura electrónica sintonizable mediante la modificación de la concentración de defectos puntuales, como los vacantes de oxígeno. Se descubrió que los voltajes de escritura aplicados a la compuerta pueden conducir iones de óxido desde la compuerta (canal) al canal (compuerta) a través del electrolito BICUVOX a bajas temperaturas. Los iones de

óxido incorporados en el canal pueden variar el contenido de oxígeno y modificar la conductancia eléctrica del canal de la película delgada de LSF50. Se demuestra el rendimiento del transistor sináptico LSF50 / BICUVOX a la temperatura tan baja como 150 ºC.

En el apéndice, se propone la espectroscopia de impedancia óptica para películas delgadas de LSF. Las señales ópticas sinusoidales como respuesta de los voltajes eléctricos oscilatorios se recogieron mediante elipsometría in-situ/in-operando, se desarrolló un formalismo para describir el comportamiento óptico de las películas delgadas de LSF. Los parámetros electroquímicos determinados a partir de los espectros de impedancia óptica para la celda electroquímica de electrolito sólido estaban en buen acuerdo con los derivados de los espectros de impedancia electroquímica, lo que demuestra la confiabilidad y aplicabilidad de la espectroscopía de impedancia óptica para las celdas electroquímicas LSF/CGO/YSZ a temperaturas intermedias.

En resumen, esta tesis trata del estudio de los defectos puntuales en las películas delgadas de LSF y su aplicación en transistores sinápticos, el novedoso enfoque de elipsometría in-situ da una idea de la química de defectos de las películas delgadas de LSF. El transistor sináptico con el electrolito sólido BICUVOX basado en la química de defectos de las películas delgadas de LSF puede funcionar a las temperaturas tan bajas como 150 ºC.

# Index

# List of Acronyms

| | |
|---|---|
| AFM | Atomic Force Microscopy |
| BICUVOX | $Bi_4V_{1.8}Cu_{0.2}O_{10.7}$ |
| CA | Chronoamperometry |
| CB | Conduction Band |
| CE | Counter Electrode |
| CGO | Gadolinium-doped Ceria |
| CMOS | Complementary Metal-Oxide-Semiconductors |
| CV | Cyclic Voltammetry |
| CVD | Chemical Vapor Deposition |
| DFT | Density Functional Theory |
| ECT | Electrochemical Transistor |
| EDS | Energy-Dispersive X-Ray Spectroscopy |
| EDL | Electrical Double Layers |
| EDLC | Electric Double Layered Capacitor |
| EGT | Electrolyte-Gated Transistors |
| EG-FET | Electrolyte-Gated Field-Effect Transistor |
| EIS | Electrochemical Impedance Spectroscopy |
| FEM | Finite Element Modelling |
| FTIR | Fourier-Transform Infrared Spectroscopy |
| GBs | Grain Boundaries |
| GDC | Gd-doped Ceria |
| HER | Hydrogen Evolution Reaction |

| | |
|---|---|
| HR-XRD | High-Resolution X-ray Diffraction |
| LA-PLD | Large-Area Pulsed Laser Deposition |
| LASV | Large Amplitude Sinusoidal Voltammetry |
| LSC | $La_{1-x}Sr_xCoO_{3-\delta}$ |
| LSCF | $La_{1-x}Sr_xCo_{1-y}Fe_yO_3$ |
| LSF | $La_{1-x}Sr_xFeO_{3-\delta}$ |
| LFO | $LaFeO_3$ |
| LSAT | $(LaAlO_3)_{0.3}$-$(Sr_2AlTaO_6)_{0.7}$ |
| LSF20 | $La_{0.8}Sr_{0.2}FeO_{3-\delta}$ |
| LSF40 | $La_{0.6}Sr_{0.4}FeO_{3-\delta}$ |
| LSF50 | $La_{0.5}Sr_{0.5}FeO_{3-\delta}$ |
| LSM | $La_{1-x}Sr_xMnO_{3-\delta}$ |
| LSM20 | $La_{0.8}Sr_{0.2}MnO_{3-\delta}$ |
| MBE | Molecular Beam Epitaxy |
| MIEC | Mixed Ionic and Electronic Conductor |
| Nb:STO | Niobium Doped $SrTiO_3$ |
| OER | Oxygen Evolution Reaction |
| o-ps | Ortho-positronium |
| ORR | Oxygen Reduction Reaction |
| PALS | Positron Annihilation Lifetime Spectroscopy |
| PDEs | Partial Differential Equations |
| PEIS | Potentio-Electrochemical Impedance Spectroscopy |
| PES | Photoemission Spectroscopy |
| PLD | Pulsed Laser Deposition |

| | |
|---|---|
| p-ps | Para-positronium |
| PVD | Physical Vapor Deposition |
| RE | Reference Electrode |
| rms | Root mean square roughness |
| RT | Room Temperature |
| SC | Supercapacitor |
| SEM | Scanning Electron Microscopy |
| SOEC | Solid Oxide Electrolysis Cell |
| SOFC | Solid Oxide Fuel Cell |
| SPEIS | Staircase Potentio-Electrochemical Impedance Spectroscopy |
| STF | $SrFe_{1-x}Ti_xO_{3-\delta}$ |
| ToF-SIMS | Time-of-Flight Secondary Ion Mass Spectrometry |
| TPB | Triple Phase Boundaries |
| UV | Ultraviolet |
| VB | Valence Band |
| VE-PALS | Variable Energy Positron Annihilation Lifetime Spectroscopy |
| WE | Working Electrode |
| XAS | X-ray Absorption Spectroscopy |
| XRD | X-Ray Diffraction |
| XPS | X-ray Photoemission Spectroscopy |
| YSZ | Yttria-Stabilized Zirconia |

# 1. Introduction

## 1.1 Motivation

Energy crisis and environmental pollution are the main challenges in today's society as a result of the development and progress of industry. For a long time in the past, the combustion of fossil fuels has greatly increased global carbon emissions that cause global warming, sea level rise and other urgent issues. As a solution of these issues, environmentally friendly energy technologies, such as Solid Oxide Fuel Cells (SOFC) and electrochemical capacitors, are desperately needed to convert and store green, pollution-free and sustainable energy. In addition, the emergence of artificial intelligence and the upgrading of electronic devices have greatly increased the demand for information technologies with low energy consumption, high efficiency, high reliability and safety.

Among the available materials, perovskite oxides are promising candidates for energy and information applications, due to the tremendous flexibility in functional properties that can be tuned not only by the wide variety of compositional elements but also by the point defect configurations in the structure.[1,2] Strontium doped lanthanum ferrite $La_{1-x}Sr_xFeO_{3-\delta}$ (LSF) is a representative paradigm, in which the substitution of $Sr^{2+}$ for $La^{3+}$ allows the generation of point defects in order to maintain electroneutrality. The electrical conductivity, ionic transport behaviour and electrochemical properties of LSF can be optimized by the generated point defects for use in energy and information devices.[3–6] Furthermore, the thin films technologies, which reduce the dimensions of oxides materials to nanoscale, allow for the optimization of the oxides' functional properties by engineering the strain and interface between the thin film and the substrate.[7–10]

This chapter is devoted to the introduction of the defect chemistry and applications of LSF perovskite thin films. The applications of Mixed Ionic and Electronic Conductors (MIEC) in energy and information devices are reviewed in **Section 1.2**; the structure and defect chemistry of LSF, as well as the effects of point defects on LSF thin films' properties are described in **Section 1.3**; the characteristics and advantages of thin films respect to bulk materials are revealed in **Section 1.4**; the peer techniques dedicated to the study of defect chemistry of oxides are described in **Section 1.5**; finally, the scope of this thesis is explained in **Section 1.6**.

## 1.2 Role of MIECs in energy and information applications

### 1.2.1 Energy applications

#### 1.2.1.1 Solid Oxide Fuel Cells (SOFC)/Solid Oxide Electrolysis Cells (SOEC)

The industrialization process and society progress lead to the increasing energy demand as depicted in **Figure 1.1a**.[11] On the one hand, the exhaustion of limited fossil fuels requires the development of sustainable energy sources; on the other hand, as illustrated in **Figure 1,1b**,[12] a significant portion of air pollution is caused by the combustion of fossil fuels, so generation of green and pollution-free energy is required in today's society. A Solid Oxide Fuel Cell (SOFC) as an electrochemical energy conversion device produces electrical energy via redox reactions. It is composed of an anode, a cathode and an electrolyte. In SOFC operation, oxygen gas from surrounding environment is supplied to the cathode, where $O_2$ is reduced to oxygen ions $O^{2-}$, the generated $O^{2-}$ ions pass through the electrolyte and are transported to the anode. Hydrogen is supplied as fuel at the anode and oxidized to $H_2O$, concomitant the liberation of electrons. The released electrons move from the anode to the cathode via an external circuit, generating electricity.[13–15] Opposite to SOFC, a Solid Oxide Electrolysis Cell (SOEC) is a device that converts $H_2O$ and/or $CO_2$ into $H_2$ and/or CO with consumption of electrical energy.[16,17] As well known, hydrogen is a clean fuel, and syngas, which is a mixture of CO and $H_2$, can be used to produce synthetic natural gas and synthetic petrol.[16]

SOFCs and SOECs are highlighted by their flexibility, security and high efficiency in power generation, reducing the emission of toxic and greenhouse gases.[11,13,17] However, the main drawback of SOFCs and SOECs is the high operation temperature above 600 ºC,[13,17] which reduces the cells' lifetime and raises its cost.[11,18] The cells' performance at lower temperature is mainly limited by the electrochemical polarization of electrode materials.[19] Therefore, in the last decades researchers intensively investigated new electrode materials for solid oxide cells. MIECs, which are able to transport both electrons and ions, extend the Oxygen Reduction Reaction (ORR) from Triple Phase Boundaries (TPB) to the electrode bulk, largely increasing the active sites for electrochemical reactions and enhancing the solid oxide cells' performance.[14,20] For instance, $La_{1-x}Sr_xCo_{1-y}Fe_yO_3$ (LSCF) with perovskite structure is found to have high mixed ionic and electronic conductivity, as well as cathodic performance at intermediate temperatures;[21,22] $La_{1-x}Sr_xFeO_3$ (LSF) exhibits good stability and compatibility with Yttrium-Stabilized Zirconia (YSZ) electrolyte, as well as small area-

specific polarization resistance in the temperature range of 650 ºC to 800 ºC;[23] $SrFe_{1-x}Ti_xO_{3-\delta}$ (STF) poses low polarization resistance and high oxygen diffusion rate at low temperatures, making it a good candidate for SOFC cathode materials.[24] In brief, the perovskite materials are of fundamental importance for solid oxide cells.

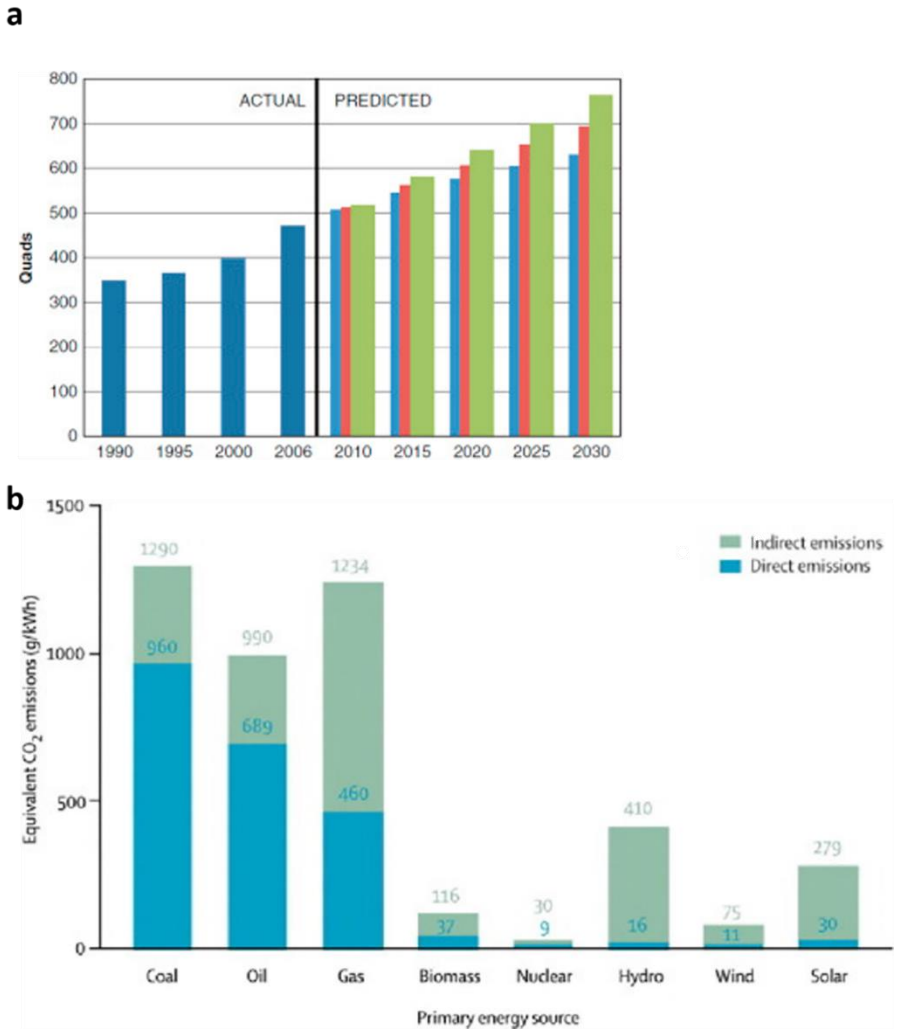


**Figure 1.1 a.** Evolution of the global energy demand. The triple bars represent the prediction of maximum, minimum and average energy demand. Reprinted from Renewable and Sustainable Energy Reviews, 82, Abdallaa, A. M., Hossaina, S., Azad, A. T., Petra, P. M. I., Begum F., Eriksson, S. G., Azad, A. K.. *Nanomaterials for solid oxide fuel cells: A review*. 353-368,[11] Copyright (2017), with permission from Elsevier. **b.** Sources of the emission of CO. Reprinted from Dey *et al.*,[12] with permission from Elsevier.

#### 1.2.1.2 Supercapacitors (SC)

A supercapacitor (SC) is an alternative energy conversion and storage device that consists of a negative electrode and a positive electrode separated by a liquid electrolyte. It is characterized by high power density, stability, fast charge and discharge process, non-

toxicity and low cost.[25–27] Differing from the batteries that convert chemical energy into electricity via chemical reactions, according to the charge storage mechanism, SCs can be classified into two categories: Electrical Double Layered Capacitor (EDLC) and pseudocapacitor. As the mechanisms depicted in **Figure 1.2**,[28] in EDLC electronic charges are accumulated and stored on the electrode surface, the electrodes are therefore based on the materials with high specific surface area, such as graphene, activated carbon, porous carbon and carbon nanotubes etc.;[27,29] in pseudocapacitor charges are stored through the Faradaic reactions occurred at the electrolyte/electrode interface. Pseudocapacitors can be divided into three types according to the reaction mechanism: underpotential deposition, redox pseudocapacitor and intercalation pseudocapacitor.[25,28] The underpotential deposition is based on the deposition of one metal on the surface of another metal under the effects of Nernstian voltages; the charge storage in redox pseudocapacitor is based on the Faradaic-characteristic redox reactions that occur on the electrode surface; and the charge storage in intercalation pseudocapacitor consists in the insertion or intercalation of cations into the electrode bulk (see **Figure 1.2b-d**).[25,28]

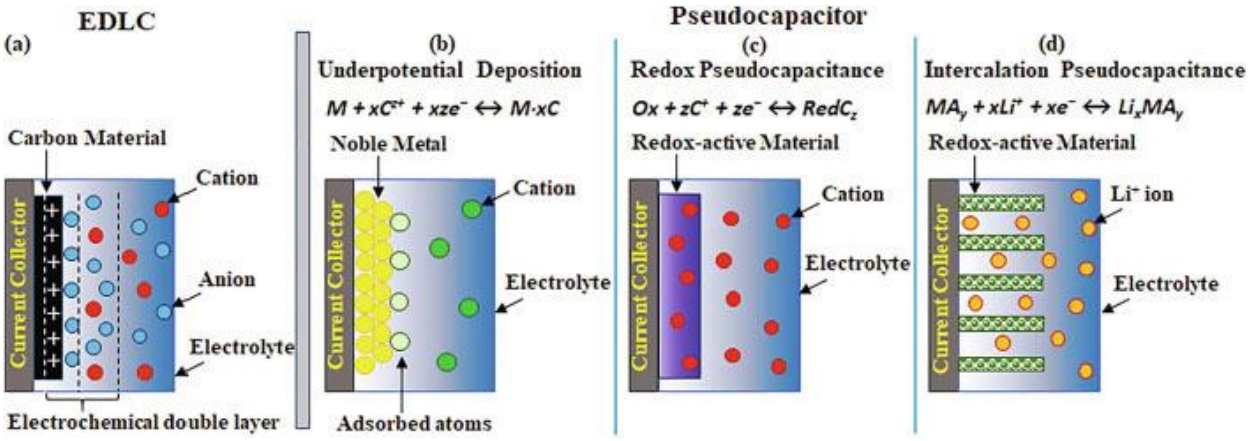


**Figure 1.2** Mechanisms of charge storage for **a.** EDLC, **b.** Underpotential deposition, **c.** Redox pseudocapacitor and **d.** Intercalation pseudocapacitor. Reprinted from Coordination Chemistry Reviews, 431, Tomar, A. K., Joshi, A., Singh, G., Sharma, R. K., *Perovskite oxides as supercapacitive electrode: Properties, design and recent advances*, 213680,[28] Copyright (2021), with permission from Elsevier.

The improvement of the supercapacitors' performance is primarily focused on the electrode materials in order to amplify the potential window, increase the active surface area, miniaturize the device, and increase the energy density, cycling stability and electrochemical capacitance etc. In recent years, there has been a surge of interest in perovskite materials as electrodes in pseudocapacitors. It was reported that the perovskite $BiFeO_3$ shows good

stability, high specific capacitance of 81 F $g^{-1}$ and specific energy density of 6.6832 J $g^{-1}$ in aqueous NaOH electrolyte.[30] The redox reactions which change the oxidation state of Mn in $La_{1-x}Sr_xMnO_3$ (LSM) lead to high specific capacitance, energy and power density in KOH electrolyte, and good stability even after thousands of charging and discharging cycles;[31,32] Wang *et al*. found that Sr doping in $LaFeO_3$ (LFO) enhanced the electrochemical performance of the material in $Na_2SO_4$ electrolyte.[33] Therefore, understanding the mechanisms of perovskite electrode materials is critical for enhancing the performance of oxides materials in supercapacitors.

#### 1.2.1.3 Water splitting

The increase of $CO_2$ in the atmosphere forces the quest for a carbon-free energy vehicle. Among the different possibilities investigated in the past, hydrogen stands as the most clean, sustainable and pollution-free energy for vehicle. Thus, hydrogen production have become the focus of many works. One of the most interesting and clean methods for hydrogen production is water splitting. It is based on the decomposition of water into $H_2$ and $O_2$ under the application of an electrical overpotential. Water splitting can be separated in two parts: Oxygen Evolution Reaction (OER) that oxidizes water into $O_2$ takes place at anode and Hydrogen Evolution Reaction (HER) that reduces water into $H_2$ takes place at cathode. Water is employed as the reactive material for water splitting and its abundance significantly lowers the cost; Additionally, the pollution-free water splitting process gives rise to high purity of $H_2$.[34] Nevertheless, the efficiency of water splitting is limited by the sluggish HER and OER.[35] Several electrocatalysts based on Ir and Pt metals have been reported to pose excellent electrocatalytic performance,[36] but their high price hinders their widespread application. Perovskite materials have been widely studied as the electrocatalyst materials for water splitting due to their low cost and high flexibility in functional properties. For instance, Matsumoto *et al*. revealed the excellent electrocatalytic performance of LSM in alkaline media;[37] Liu *et al*. reported that the cation deficiency in $Sr_{1-x}Nb_{0.1}Co_{0.7}Fe_{0.2}O_{3-\delta}$ was able to boost the OER activity by increasing the surface oxygen vacancies and the active sites;[38] Wang *et al*. discovered that a simple Fe-doping in $SrCoO_{3-\delta}$ would improve the OER activity and durability of the electrocatalyst.[39]

## 1.2.2 Information applications

### 1.2.2.1 Electrolyte-Gated Transistors (EGT)

An Electrolyte-Gated Transistor (EGT), which enables the simulation of artificial synapses with low energy consumption and low voltage, is a promising device for neuromorphic applications.[40] In comparison with two-terminal EGTs, three-terminal EGTs show outstanding time efficiency because the signal transmission and self-learning processes can be performed simultaneously.[41,42]

As the schematic representation of EGT shown in **Figure 1.3a**,[43] a three-terminal EGT is composed of a drain, a source and a gate. The drain and source are situated at the two opposite ends of a semiconductor channel, which is separated from the gate by an electronic insulating electrolyte.[44] Channel's conductance, which simulates synaptic weight, can be modulated by the voltage applied between the gate and the source.[45] Based on the mechanism of operation, EGTs can be classified into two groups: Electrolyte-Gated Field-Effect Transistor (EG-FET) and Electrochemical Transistor (ECT). In EG-FET with impermeable semiconductor, the voltage applied between the gate and the drain causes the charge carriers (holes and electrons) to move and accumulate at the electrolyte/channel and gate/electrolyte interfaces forming Electrical Double Layers (EDL);[43,44,46] in ECT the applied gate voltage causes reversible incorporation or release of ions into the channel, with $O^{2-}$ and $H^{+}$ ions being the most prevalent.[40,43,44,46] Depending on the polarity of the gate voltage, EGT can be operated in both carrier accumulation and depletion modes, as shown in **Figure 1.3b** and **c**. In recent years, synaptic EGTs based on $SrMO_{3-\delta}$ (M=Fe or Co etc.) have been investigated,[40,41,45,47,48] the electrolyte-gated oxygen incorporation process controls the electrical properties of $SrMO_{3-\delta}$, resulting in synaptic transistors with non-volatility, long-term plasticity, good stability and reversibility.[40,41,45,47,48]

A large number of researches have been focused on the synaptic transistors based on ionic liquid electrolytes,[40–42,44] but the difficulty in integration hinders the fabrication of the devices. In turn, the solid electrolytes (for instance, Yttria-Stabilized Zirconia (YSZ) and Gd-doped Ceria (GDC)) enable the integration with other components of the devices and facilitate the fabrication.[49–51] In solid-electrolyte synaptic transistors, gate voltage is able to pump oxide ions into (or out of) the channel through the electrolyte with ionic conductivity, changing the conductance state of the channel.[49,51] The main drawback of the conventional solid-state electrolytes is its low ionic conductivity at room temperature. Besides, synaptic

transistors based on extraction and injection of lithium ions ($Li^+$) have attracted a lot of interest. However, integration with other components and miniaturization in dimensions are problematic for some of the solid-state electrolytes based on $Li^+$ ions.[52]

Thus, the investigation of synaptic transistors with good performance becomes more and more important.

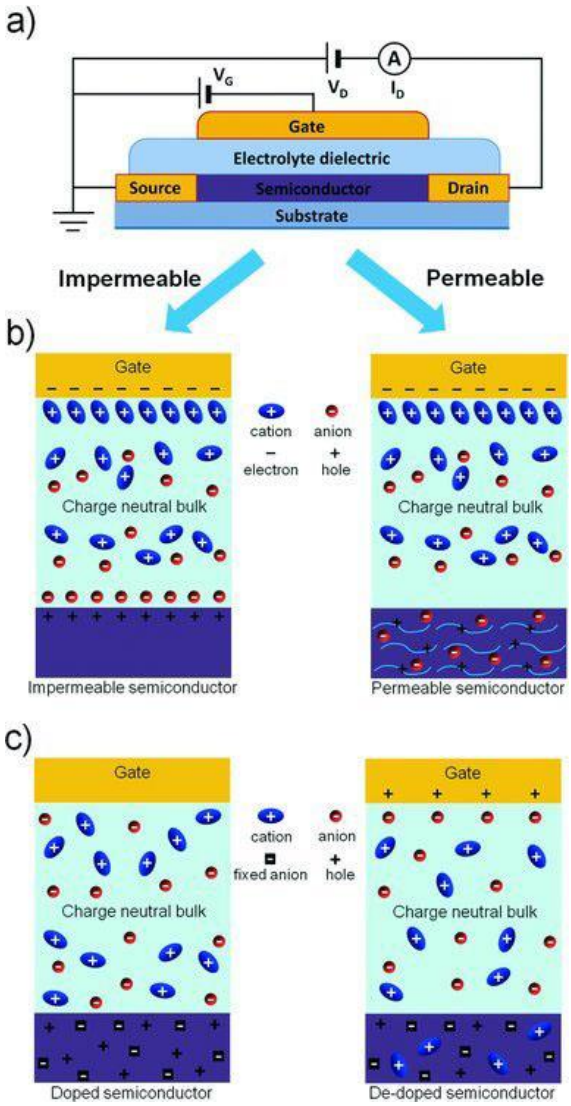


**Figure 1.3 a.** Schematic representation of the cross section of a representative EGT. **b.** Carrier accumulation mode and **c.** Carrier depletion mode of the EGT with impermeable (left) and permeable (right) semiconductor channel. Reprinted from Advanced Materials, 25, Kim, S. H.; Hong, K.; Xie, W.; Lee, K. H.; Zhang, S.; Lodge, T. P.; Frisbie, C. D., *Electrolyte-Gated Transistors for Organic and Printed Electronics*, 1822-1846,[43] Copyright © 2013 WILEY-VCH Verlag GmbH & Co.

## 1.3 $La_{1-x}Sr_xFeO_{3-\delta}$ (LSF): a paradigm of MIEC perovskite oxide

$La_{1-x}Sr_xFeO_{3-\delta}$ (LSF) has been widely investigated as cathode for SOFCs and SOECs,[53–55] electrode for supercapacitors,[56] catalyst for electrochemical water splitting,[6,57] and channel for memristors and synaptic transistors.[41,47] LSF with perovskite structure is highlighted by their electrical and electrochemical performance.[58,59] Furthermore, the abundance of Fe significantly reduces the costs, making LSF suitable for fundamental studies. As a paradigmatic MIEC perovskite oxide, the concentration of point defects in LSF strongly impacts the LSF's functional properties.[60–62] In this section, the perovskite structure and point defects in LSF will be discussed.

### 1.3.1 Crystal structure of $La_{1-x}Sr_xFeO_{3-\delta}$

LSF is a perovskite oxide material. Perovskite structure can be written as $ABX_3$, the A-site is usually occupied by cations of rare earth lanthanide metals or alkali earth metals, such as La, Pr, Sr and Ca etc., the B-site is usually occupied by cations of transition metals, such as Fe, Mn, Cr, Co and so on, and the X-site is occupied by oxygen anions. As illustrated in **Figure 1.4**,[63] depending on the coordinator system, perovskite structure can be represented in two forms: in one of them, the B-site cations are located in the center of the unit cell, the A-site cations are located at the corners of the cell and the oxygen anions are located in the center of the faces of the cubic cell. In the alternative representation, the A-site cations are located in the center of the cubic cell, the B-site cations are located at the corners of the structure and the oxygen anions are located at the edges. Each A-site cation is coordinated by 12 oxygen anions, while each B-site cation is in the $BO_6$ octahedra with a six-anion coordination.

Depending on the radius of the A-site and B-site cations, the perovskite structure is usually found to be distorted with the Goldschmidt tolerance factor ($t$):[1,9,62]

$$t = \frac{r_A + r_O}{\sqrt{2}(r_B + r_O)} \qquad \text{(Equation 1.1)}$$

Where $r_A$, $r_B$ and $r_O$ denote the radius of the A-site, B-site cations and oxygen anions, respectively. The perovskite structure is considered to be stable if $0.77 \leq t \leq 1$.[64]

LSF bulk materials with perovskite structure have been commonly synthesized by a variety of chemical methods, such as solid state reaction or wet routes like sol-gel.[62,65–67]

Orthorhombic structure is found for LSF with low Sr content, while with increasing the Sr amount, the perovskite structure becomes distorted and the symmetry turns to be rhombohedral.[65,66]

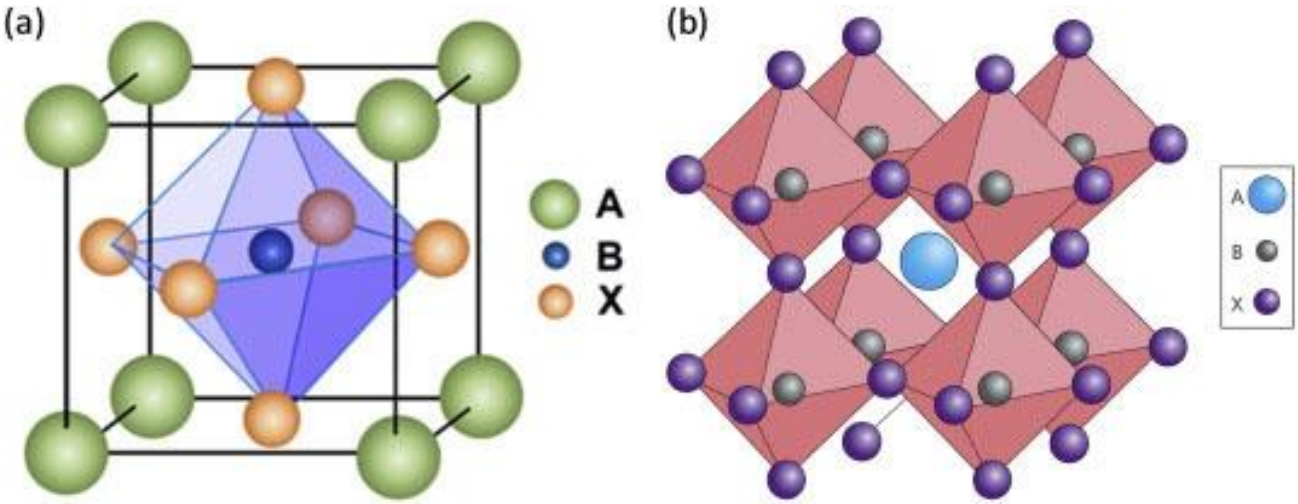


**Figure 1.4** Schematic representations of perovskite structure. Reprinted from Materials Today Energy, 7, Moniruddin, M.,Ilyassov, B., Zhao, X., Smith, E., Serikov, T., Ibrayev, N., Asmatulu, R., Nuraje, N. *Recent Progress on Perovskite Materials in Photovoltaic and Water Splitting Applications*, 246-259,[63] Copyright (2017), with permission from Elsevier.

### 1.3.2 Defect chemistry of $La_{1-x}Sr_xFeO_{3-\delta}$[i]

Defects are defined by the deviations or imperfections from the ideal structure that result from the deficit of atoms or excess of interstitial atoms in the structure.[68] The vacancies and extra interstitial atoms are defined as point defects. The two main types of intrinsic structural defects are: Schottky defects and Frenkel defects. If ions escape from their proper sites and leave vacancies in the structure, Schottky defects are formed. On the other side, when ions in the structure move to occupy the interstitial sites, Frenkel defects are formed. The Schottky defects predominate over the Frenkel defects in the LSF family of materials due to the packed structure that impedes the formation of interstitial defects.[68]

In LSF, the substitution of $La^{3+}$ by $Sr^{2+}$ results in the creation of oxygen vacancies or electron holes for charge compensation. The produced electronic defects (holes or electrons) are trapped by the metal atoms, giving rise to the defects such as $Fe^{4+}$ holes and $Fe^{2+}$ electrons. The global electroneutrality can be expressed as:

[i] In this thesis, the point defects are expressed using Kröger-Vink notation. The symbol $M_N^x$ represent the occupation of ion *M* on *N* site and $V_O^{\cdot\cdot}$ represents oxygen vacancies. The symbol's subscript x can be $'$, × or ● that means the negative, neutral or positive effective charge.

$$La^{3+}Fe^{3+}O_3 \xrightarrow{+Sr} La_{1-x}{}^{3+}Sr_x{}^{2+}Fe_{1-y}^{3+}Fe_y^{4+}O_{3-\delta} + \frac{\delta}{2}O_2 \quad \text{(Equation 1.2)}$$

According to the models proposed in various published works,[3,69] point defects on the A site can be $La_{La}^{\times}$, $Sr_{La}'$ and $V_{La}'''$, point defects on the B site can be $Fe_{Fe}'$, $Fe_{Fe}^{\times}$, $Fe_{Fe}^{\cdot}$, $V_{Fe}'''$, and point defects on oxygen are $O_O^{\times}$ and $V_O^{\cdot\cdot}$. In terms of electroneutrality, the sum of the positive charges must equal the sum of the negative charges as:

$$[Sr_{La}'] + [Fe_{Fe}'] + 3[V_{La}'''] + 3[V_{Fe}'''] = [Fe_{Fe}^{\cdot}] + 2[V_O^{\cdot\cdot}] \quad \text{(Equation 1.3)}$$

The concentration of point defects in LSF can be tuned by the equilibrium of the material with the gas atmosphere as described by **Equations 1.4** and **1.5**:[3,60,70–74]

$$\frac{1}{2}O_2 + 2Fe_{Fe}^{\times} + V_O^{\cdot\cdot} \leftrightarrow O_O^{\times} + 2Fe_{Fe}^{\cdot} \quad \text{(Equation 1.4)}$$

$$\frac{1}{2}O_2 + 2Fe_{Fe}' + V_O^{\cdot\cdot} \leftrightarrow O_O^{\times} + 2Fe_{Fe}^{\times} \quad \text{(Equation 1.5)}$$

The disproportionation reaction of $Fe_{Fe}^{\times}$ can be expressed as:[3,60,70–74]

$$2Fe_{Fe}^{\times} \leftrightarrow Fe_{Fe}^{\cdot} + Fe_{Fe}' \quad \text{(Equation 1.6)}$$

The equilibrium constant $K_i$ for charge disproportionation is:

$$K_i = \frac{[Fe_{Fe}^{\cdot}][Fe_{Fe}']}{[Fe_{Fe}^{\times}]^2} \quad \text{(Equation 1.7)}$$

In addition, the Schottky reaction also should be taken into account:[3,69,75]

$$3[V_O^{\cdot\cdot}] + [V_{La}'''] + [V_{Fe}'''] \leftrightarrow nil \quad \text{(Equation 1.8)}$$

Since this thesis is focused on LSF with a large Sr amount (20%~50% in mol), the effect of the Schottky reaction is negligible and the point defects in the materials are denominated by the doping.[3,75] $[V_{Fe}''']$ is therefore assumed to be negligible. Furthermore, the vacancies at La site ($V_{La}'''$) which are caused by the non-stoichiometric La/Fe ratio are also believed to be negligible under the optimal Pulsed Laser Deposition (PLD) conditions.[60,74]

Thus, the main point defects in LSF are $La_{La}^{\times}$, $Sr_{La}'$, $Fe_{Fe}'$, $Fe_{Fe}^{\times}$, $Fe_{Fe}^{\cdot}$ and $V_{Fe}'''$, and the A-site, B-site and oxygen stoichiometry can be written as:

$$[La_{La}^{\times}] + [Sr_{La}'] = 1 \quad \text{(Equation 1.9)}$$

$$[Fe_{Fe}^{\times}] + [Fe_{Fe}^{\cdot}] + [Fe_{Fe}'] = 1 \quad \text{(Equation 1.10)}$$

$$[O_O^{\times}] + [V_O^{\cdot\cdot}] = 3 \qquad \text{(Equation 1.11)}$$

According to the model developed by Mizusaki *et al.*,[74] as depicted in **Figure 1.5**, the evolution of the concentration of point defects in LSF materials with oxygen partial pressure ($pO_2$) can be divided into three regions: In oxidizing conditions, charges are compensated by iron holes $Fe_{Fe}^{\cdot}$ and oxygen vacancies $V_O^{\cdot\cdot}$ (Region I); when $pO_2$ decreases, the concentration of iron holes decreases and the concentration of oxygen vacancies increases following **Equation 1.4**; In reducing atmosphere (Region II), iron holes are totally depleted and the point defects in LSF are dominated by oxygen vacancies, a plateau is reached with an oxygen vacancy concentration of $0.5[Sr_{La}']$; Under extremely reducing $pO_2$, iron electrons $Fe_{Fe}'$ begin to form and oxygen vacancies increase again following **Equation 1.5**.

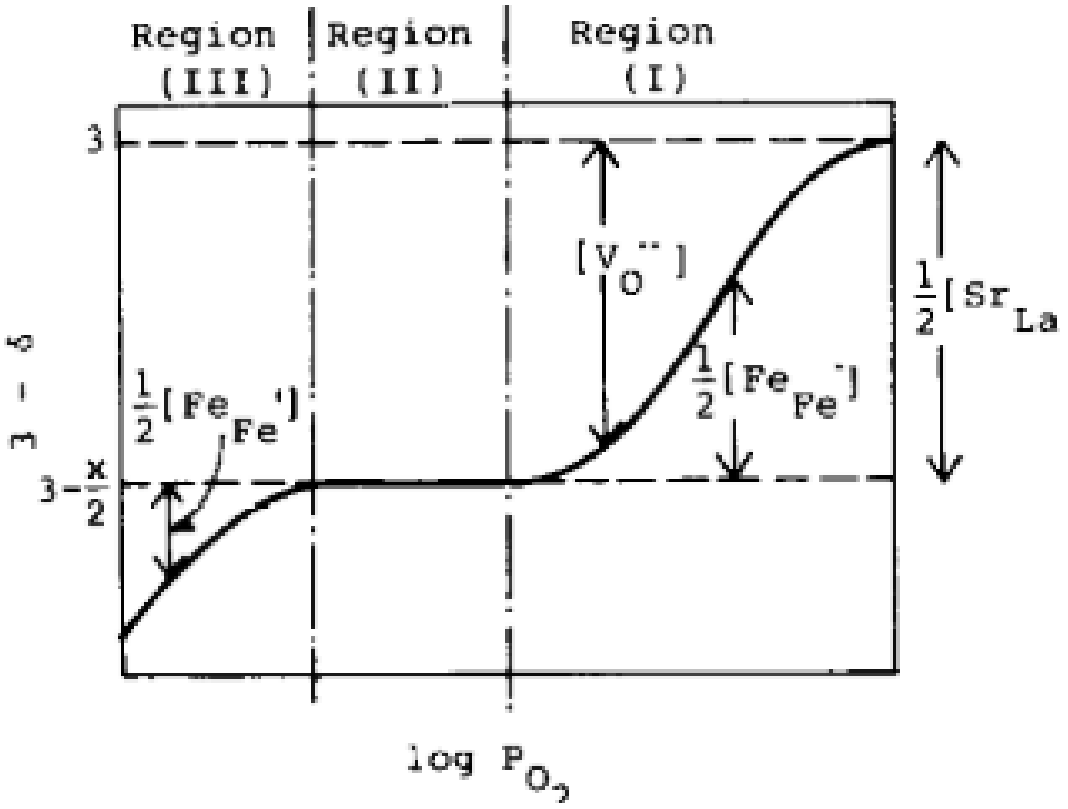


**Figure 1.5** Representation of the evolution of the oxygen nonstoichiometry as a function of oxygen partial pressure. Reprinted from Journal of Solid State Chemistry, 58, Mizusaki, J., Yoshihiro, M., Yamauchi, S., Fueki, K., *Nonstoichiometry and defect structure of the perovskite-type oxides $La_{1-x}Sr_xFeO_{3-\delta}$*, 257-266,[74] Copyright (1985), with permission from Elsevier.

Taking into account the temperature and oxygen partial pressure range studied in this thesis, the concentration of $Fe_{Fe}'$ is negligible. Thus, the oxygen incorporation reaction in LSF is

dominated by **Equation 1.4** and the equilibrium constant ($K_{ox}$) can be obtained considering a dilute representation of the chemical potential:[3,60,70–74]

$$K_{ox} = \frac{[Fe_{Fe}^{\cdot}]^2[O_O^{\times}]}{[V_O^{\cdot\cdot}][Fe_{Fe}^{\times}]^2 pO_2^{\frac{1}{2}}} = \frac{[Fe_{Fe}^{\cdot}]^2(3-\delta)}{\delta(1-[Fe_{Fe}^{\cdot}])^2 pO_2^{\frac{1}{2}}} = \exp(-\frac{\Delta H_{ox}^{\circ}}{RT} + \frac{\Delta S_{ox}^{\circ}}{T}) \quad \text{(Equation 1.12)}$$

Where $\Delta H_{ox}^{\circ}$ and $\Delta S_{ox}^{\circ}$ denote the standard enthalpy and entropy for the oxygen incorporation reaction, $R$ is gas constant and $T$ is temperature.

## 1.3.3 Effects of the point defects on the LSF thin films' properties

### 1.3.3.1 Defect chemistry-tailored electronic structure

Several studies were dedicated to the investigation of the electronic structure of LSF using different functional characterization techniques, such as Photoemission Spectroscopy (PES),[76] X-ray Photoemission Spectroscopy (XPS),[77] X-ray Absorption Spectroscopy (XAS),[76,77] and Fourier-Transform Infrared Spectroscopy (FTIR).[78] The electronic structure and the density of states of LFO and LSF derived from the Density Functional Theory (DFT) simulations are schematically illustrated in **Figure 1.6**. The Valence Band (VB) of LFO and LSF consists of the occupied $t_{2g}$ and $e_g$ orbitals of the hybridized Fe 3d and O 2p states, while the Conduction Band (CB) consists of the unoccupied minority $t_2g$ and $e_{2g}$ orbitals. The creation of $Fe^{4+}$ holes as a result of the charge compensation in LSF induces an acceptor state within the band gap between VB and CB.[77,79] The hybridized Fe 3d/O 2p orbitals shift toward the Fermi level as the Sr amount increases, lowering the bandgap and favoring electrical conduction and OER.[61] Furthermore, as the Sr content in LSF increases, the degree of hybridization of the Fe 3d and O 2p orbitals becomes stronger.[61,76,80]

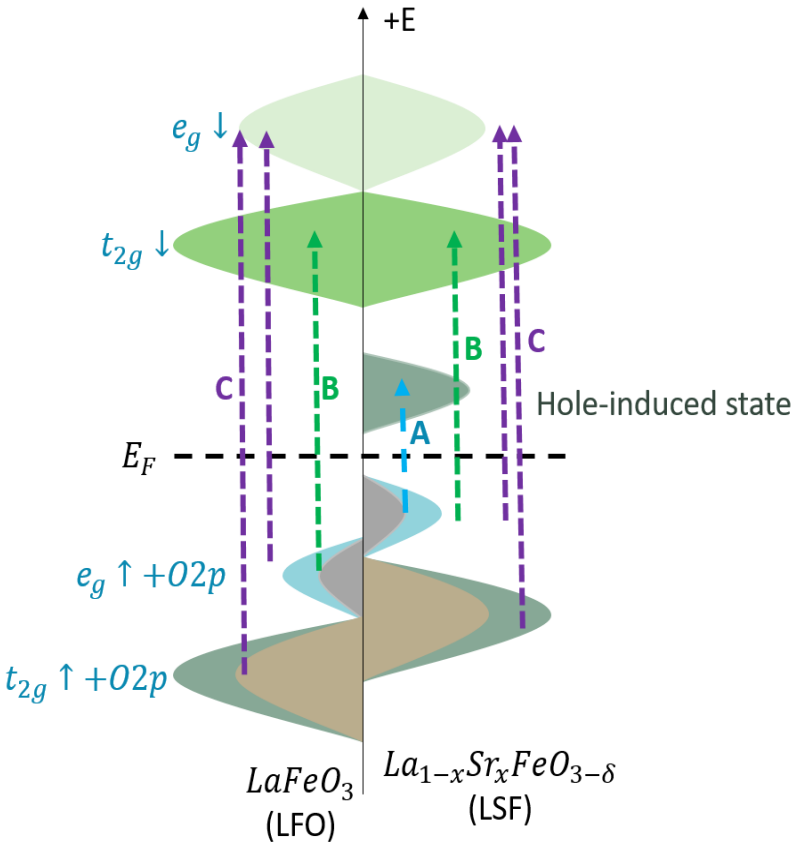


**Figure 1.6** Schematic representation of the electronic structure for LFO and LSF, the letters "A" "B" and "C" denote the electronic transitions.[77–82]

### 1.3.3.2 Defect-dependent optical properties

Several previous studies have informed the effects of electron holes on the optical properties of LSF thin films,[77,79,83] the optical absorption spectra of LSF epitaxial thin films reported by Scafetta *et al*. are illustrated in **Figure 1.7**.[83] The optical properties of LSF thin films are substantially influenced by the Sr content. An increase in the Sr amount increases the intensity of the optical features "A" and "B" while weakening the feature "C". Considering that oxygen vacancies in the LSF thin films were previously reduced by annealing in oxygen gas, the variation of the optical absorption with Sr content is primarily attributed to the concentration of $Fe^{4+}$ holes that emerge for charge compensation. As the optical features "A" "B" and "C" are directly related to the electronic excitations highlighted in **Figure 1.6**, the optical feature "A" at low energy is associated with the electron transfer from the top of VB to the $Fe^{4+}$ hole-induced state; the feature "B" is attributed to the electron promotion from the hybridized Fe 3d/O 2p orbitals in the VB toward the unoccupied $t_{2g}$ orbitals in the CB;

and the feature "C" corresponds to the electron excitation from the deeper majority electronic state to the empty minority spin Fe $e_g$ orbitals.[77,79,83] With increased Sr amount, the intensification of spectral weight of the optical features "A" and "B" implies an increase in the density of states; additionally, the decrease in the onset energy for the transition "B" with increasing Sr content reveals a narrowing of the bandgap between VB and CB, corroborating the electronic structure extracted from the XAS and XPS results.[76,77,79,83]

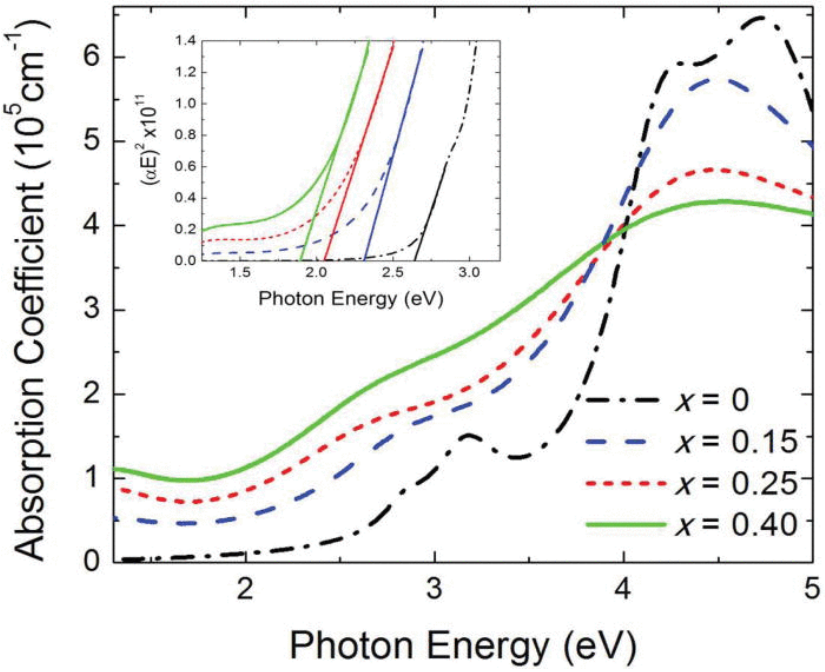


**Figure 1.7** Optical absorption spectra for epitaxial LSF thin films, the inset shows the Tauc plot of the onset energy of the transition. Reprinted from Scafetta, M. D., Xie, Y. J., Torres, M., Spanier, J. E., May, S. J., *Optical Absorption in Epitaxial $La_{1-x}Sr_xFeO_3$ Thin Films*. Appl. Phys. Lett. 2013, 102 (8), 0–5,[83] with the permission of AIP Publishing.

#### 1.3.3.3 Defect-dependent electrical and mass transport performance

The electrical conductivity of LSF can be written as a sum of the ionic and electronic conductivities:

$$\sigma = \sigma_{ion} + \sigma_p + \sigma_n \qquad \text{(Equation 1.13)}$$

Where $\sigma_{ion}$ is the ionic conductivity which is independent of oxygen partial pressure, $\sigma_p$ and $\sigma_n$ represent the conductivity associated with the holes and electrons, respectively.

As the oxygen partial pressure-dependent electrical conductivity depicted in **Figure 1.8a**,[59] the examplified measurements for LSF at 900ºC show that the electrical conductivity of LSF decreases with increasing $pO_2$ in the low $pO_2$ regime, but it increases with increasing $pO_2$ in

the high $pO_2$ regime. Under oxidizing atmospheres, the charges in LSF are mainly compensated by the generation of $Fe^{4+}$ holes, the electrical conductivity of LSF is denominated by polaron hopping, which denominates p-type conduction.[59,71,84,85] Thus, the electrical conductivity is proportional to $pO_2^{1/4}$ as:[84]

$$\sigma_p = e\mu_p(\frac{K_{ox}[V_O^{\cdot\cdot}]}{[O_O^{\times}]})^{\frac{1}{2}}[Fe_{Fe}^{\times}](pO_2)^{\frac{1}{4}} \qquad \text{(Equation 1.14)}$$

Where $e$ is the electron charge; $\mu_p$ is the hole mobility which also shows a dependence on $pO_2$ due to the large variation of band structure related to the electron holes and oxygen vacancies.[86]

Under reducing atmospheres, the predominant charge carriers in LSF are $Fe^{2+}$ electrons and the electrical conductivity is defined by n-type conduction, which has a $pO_2^{-1/4}$ dependence according to:[59,71,84,85]

$$\sigma_n = e\mu_n(\frac{K_{ox}'[V_O^{\cdot\cdot}]}{[O_O^{\times}]})^{\frac{1}{2}}[Fe_{Fe}'](pO_2)^{\frac{1}{4}} \qquad \text{(Equation 1.15)}$$

Where $\mu_n$ is the electron mobility and $K_{ox}'$ is the equilibrium constant for oxygen incorporation reaction at extremely reducing conditions.

Bongio *et al*. described the impact of Sr content on the LSF's electrical behaviour.[87] As shown in **Figure 1.8b**, the maximum electrical conductivity at 900 ° C was found in $La_{0.5}Sr_{0.5}FeO_{3-\delta}$, in which the maximum $[Fe^{4+}]/[Fe^{3+}]$ ratio is present.[87] The electrical conductivy increases with the Sr content in the regime of $x$<0.5, where electron holes predominate over oxygen vacancies and increase with the Sr amount;[85] While the electrical conductity decreases with increasing Sr content in the regime of $x$>0.5, where oxygen vacancies are more favorable than electron holes and the concentration of electron holes decreases with increasing Sr amount.[87]

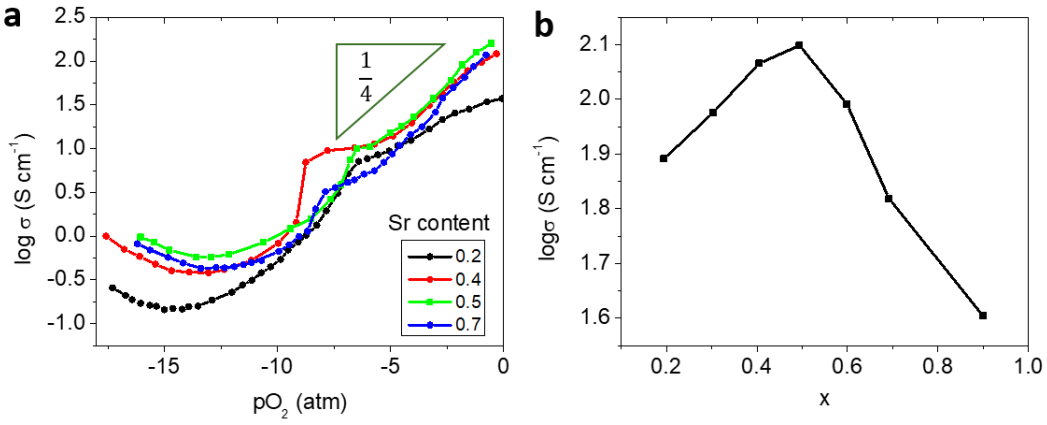


**Figure 1.8 a.** Oxygen partial pressure dependence of the electrical conductivity of LSF at 900 ºC. Data taken from the research published by Patrakeev *et al.*[59] **b.** Sr content (*x*) dependence of the electrical conductivity of LSF at 900 ºC in air. Data extracted from the research published by Bongio *et al.*[87]

The oxygen mass transport properties of LSF have been investigated in various works.[3,71,88–92] Both the surface exchange coefficient $k_{ox}$ and the diffusion coefficient of oxygen ions $D_O$ are found to be highly related to oxygen vacancies in LSF. Ritzmann *et al.*[93] suggest that the formation of oxygen vacancies is favored in LSF with large Sr amount due to a decrease in the enthalpy of oxygen vacancy formation, resulting in more active sites for oxygen incorporation. Moreover, due to the equivalence between the conductivity of oxide ions and conductivity of oxygen vacancies:[90,92]

$$C_V D_V = C_O D_O \qquad \text{(Equation 1.16)}$$

Where $C_V$ and $C_O$ are the concentrations of oxygen vacancies and oxygen ions, respectively. $D_V$ and $D_O$ are the diffusion coefficients of oxygen vacancies and oxygen ions, respectively.

Thus, the diffusion coefficient of oxygen ions is directly proportional to the concentration of oxygen vacancies as:

$$D_O = \frac{C_V D_V}{C_O} \qquad \text{(Equation 1.17)}$$

Therefore, as the data shown in **Figure 1.9**,[90–92] both $k_{ox}$ and $D_O$ increase with the Sr amount, in other words, with the concentration of oxygen vacancies.

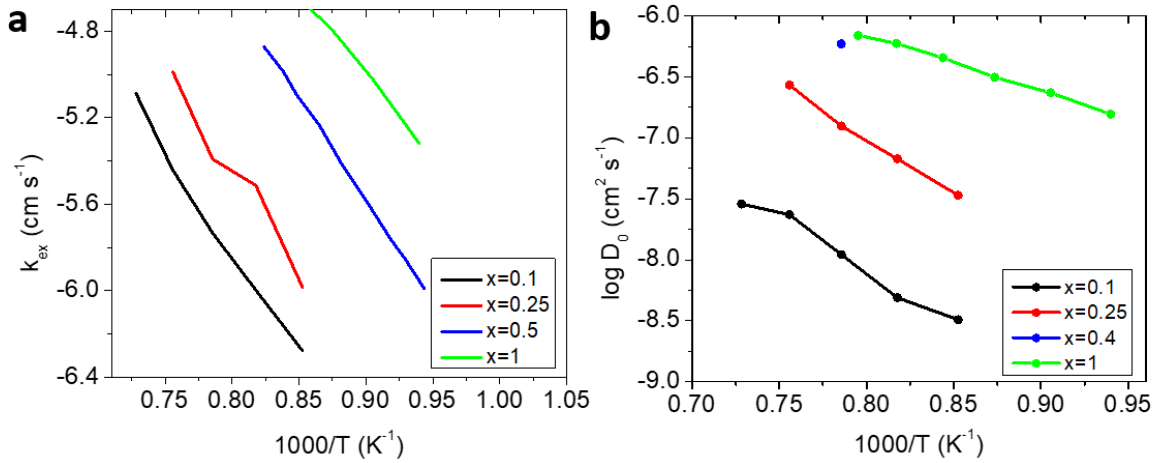


**Figure 1.9 a.** Surface exchange coefficient and **b.** Oxygen ion diffusion coefficient of LSF at different temperatures in oxygen partial pressure between 0.05 and 0.07 atm. Data extracted from the references.[90–92]

### 1.3.3.4 Effects of point defects on electrochemical properties

In terms of electrochemical properties, Shen *et al.*[61] discussed the enhancement of OER activity of LSF with Sr doping, revealing that the current density and Tafel slope increase with the Sr content. This enhancement is associated with the change in the LSF's electronic structure as a result of the presence of $Fe^{4+}$ holes. On the one hand, as the Sr content increases, the VB shifts closer to the Fermi level ($E_F$), improving the band alignment with water, and increasing the reaction rate and efficiency;[61,94] On the other hand, the Sr substitution in LSF leads to a new electronic state situated between the CB and VB, reducing the bandgap and boosting the electron transfer;[77,79] moreover, the increased concentration of $Fe^{4+}$ holes related to the Sr doping improves the degree of hybridization of the Fe 3d and O 2p orbitals, concomitant a shortening of the Fe-O bond length,[57,61,80] optimizing the electron transfer between the Fe ions and oxygen species, and resulting in higher OER current.[57,61,94] Aside from $Fe^{4+}$, Shen *et al.*[57] revealed that the oxygen vacancies on the surface can boost the OER activity by providing more accessible sites for oxygen species adsorption and oxygen ion diffusion.

Not only the OER performance, but also the electrochemical capacitance of LSF is strongly influenced by oxygen vacancies and $Fe^{4+}$ holes. In the work published by Alexander *et al.*,[56] $Fe^{4+}$ holes were revealed to be able to modulate the redox reaction potential, while oxygen

vacancies in the LSF structure were uncovered to provide more available sites for the $OH^-$ incorporation, improving the charge capacity.

In brief, understanding and quantifying the defect chemistry of LSF is important for optimizing the materials' properties.

## 1.4 Thin film processing for enhancing functional materials in the field of energy and information

Ion conduction in electrolyte of the electrochemical devices is achieved by ion transport in the electrolyte materials which pose high ionic conductivity. The cationic substitution in oxide materials may lead to the creation of oxygen vacancies, favoring the migration of oxygen.[95] The well-known solid-state electrolytes, such as YSZ and GDC, show good ionic conductivity at high temperatures.[96,97] The main shortcoming of these solid-state electrolytes is their poor ionic conductivity at low temperature, which prevents their use in low-temperature applications. As a solution of this issue, thin films with nanometric thickness are able to improve the oxide ions migration at low temperatures by reducing the ion diffusion length and introducing grain boundaries.[98,99]

Oxides with mixed ionic and electronic conductivity extend the ORR from the TPB to the electrode bulk, enhancing the electronic and ionic transport performance for the aforementioned energy and information applications. Thin film technologies reduce the materials' dimensions and alter the MIECs' functional properties compared to bulk materials. The large surface area/thickness ratio defined by the geometry of thin films increases the active sites for ions incorporation and reduces the diffusion length for the ions transport, boosting the kinetics of ORR and enhancing the materials' electrochemical properties, such as capacity, lifetime and so on.[10,100–102] Furthermore, oxygen vacancies accumulated at the grain boundaries and interfaces in thin films facilitate the oxygen incorporation and diffusion, hence defining the conduction mechanism.[99,103,104]

Unlike bulk materials, the thin films' properties can be engineered by the thickness, orientation, grain boundary configuration, and the strain induced by the mismatch of lattice parameters between the film and the substrate.[7–9] Saranya *et al.*[105] reported the ability to change the nature of LSM thin films' conductivity with the fast oxygen surface exchange and oxygen diffusivity at grain boundaries. The decrease in the films' thickness causes strain, affecting the materials' structural, electrical and optical properties.[106–108] For instance, Biswas and Jeong[109] reported a metal-insulator transition in $SrIrO_3$ thin films, which was explained by the disorder arising from the increased grain boundaries with the decrement of films' thickness. The strain originated from the difference in the lattice parameters between the thin film and the substrate has the potential to distort the perovskite structure and change the defect concentration in the thin film, particularly oxygen vacancies.[7,8,110] The strain was

found to be capable of increasing the metal-insulator transition temperature in ferrite thin films,[111] enhancing the surface oxygen exchange,[112] and reducing the Curie temperature,[113] thereby engineering the electrocatalytic,[9] electrochemical,[112] ferroelectric[9] and electrical properties.[111,113] Finally, the thin film technologies enable the control of the thin films' orientation in order to acquire the optimum functional properties for the anisotropic features.[114,115]

Furthermore, on the one hand, nanometric-thick thin films offer the possibility of scaling down the energy and information devices, allowing for their use in portable devices;[116,117] on the other hand, thin films promote circuit integration with microfabrication technologies and demonstrate flexibility of substrate for film deposition, allowing transistors to be used in wearable applications.[118]-

Given the benefits provided by the well-defined geometry of thin films, understanding the defect chemistry and engineering the point defects in thin films are essential for controlling their functional properties and enhancing their applications in energy and information domains.

## 1.5 Currently available techniques for defect chemistry study in thin films

Because direct quantification of point defects in transition metal oxides is challenging, numerous approaches have been devised to explore defect chemistry indirectly. For instance, thermogravimetry and coulometric titration,[72,74,119–122] which are widely employed for studying the nonstoichiometry of bulk materials, are based on measuring the change in the materials' mass at high temperatures under different $pO_2$. However, the reduced mass and small thickness of thin films limit their application in nanometric-thick films.[123] By measuring the defect-tailored chemical expansion, X-ray Diffraction (XRD) was employed to explore the oxygen non-stoichiometry in oxides,[124] but the application of bulk atomic lattice refinement models and the strain associated with the mismatch between film and substrate may cause inaccuracy in the concentration of point defects for thin films. Because the electrical capacitance of the electrode is directly proportional to the concentration of the species involved in the oxygen incorporation reaction, Schmid *et al.*[125,126] proposed an alternative electrochemical approach involving Electrochemical Impedance Spectroscopy (EIS) to extract the point defect concentration from the chemical capacitance of the electrode (**Figure 1.10a**). The main advantage of the method is the possibility of modelling the defect chemistry in situ and under real electrochemical conditions (*i.e.* under electrochemical bias), which can be used to get mechanistic information about the relation between bulk point defects and oxygen incorporation and evolution reactions.[127] However, the large polarization resistance of the electrode at low temperatures shifts the impedance to extremely low frequencies beyond the measurable range, making the low-temperature measurements difficult. Furthermore, as shown in **Figure 1.10b** electrical conductivity of the thin film as a function of $pO_2$ is considered to be able to describe the concentration of the majority charge carrier in the thin film, which can be used to obtain the equilibrium constant by fitting with a defect chemistry model.[128,129] This approach is highlighted by the facile implementation, however, the carrier mobility is also a function of $pO_2$, which is difficult to separate from the carrier concentration. The UV-Vis optical technologies,[130,131] as promising approaches for quantifying the point defects in oxides, measure the variation of the optical properties under different electrochemical conditions by in-situ setup, providing possibility to get insight into the defect chemistry of thin films in a non-destructive way. For instance, optical transmission was developed to track the defect chemistry and get insight into the kinetics of

oxidation and reduction reactions for Pr doped ceria (**Figure 1.10c**) and La doped $Sr(TiFe)O_{3-\delta}$ thin films.[131] It must note that for optical transmission the substrates of the thin films should be transparent, which hinders its application for some photon energy windows. Recently, in-situ Raman spectroscopy opens a new way for studying the oxygen vacancies in $SrTi_{1-x}Fe_xO_{3-\delta}$ thin films by correlating the Raman shift with the oxygen nonstoichiometry (**Figure 1.10d**).[132]

Furthermore, while all of the aforementioned methods were developed for oxygen incorporation/release reactions in oxide thin films with solid electrolytes, the defect chemistry of oxide thin films during oxidation/reduction processes in liquid electrolytes is yet unknown and poorly understood.

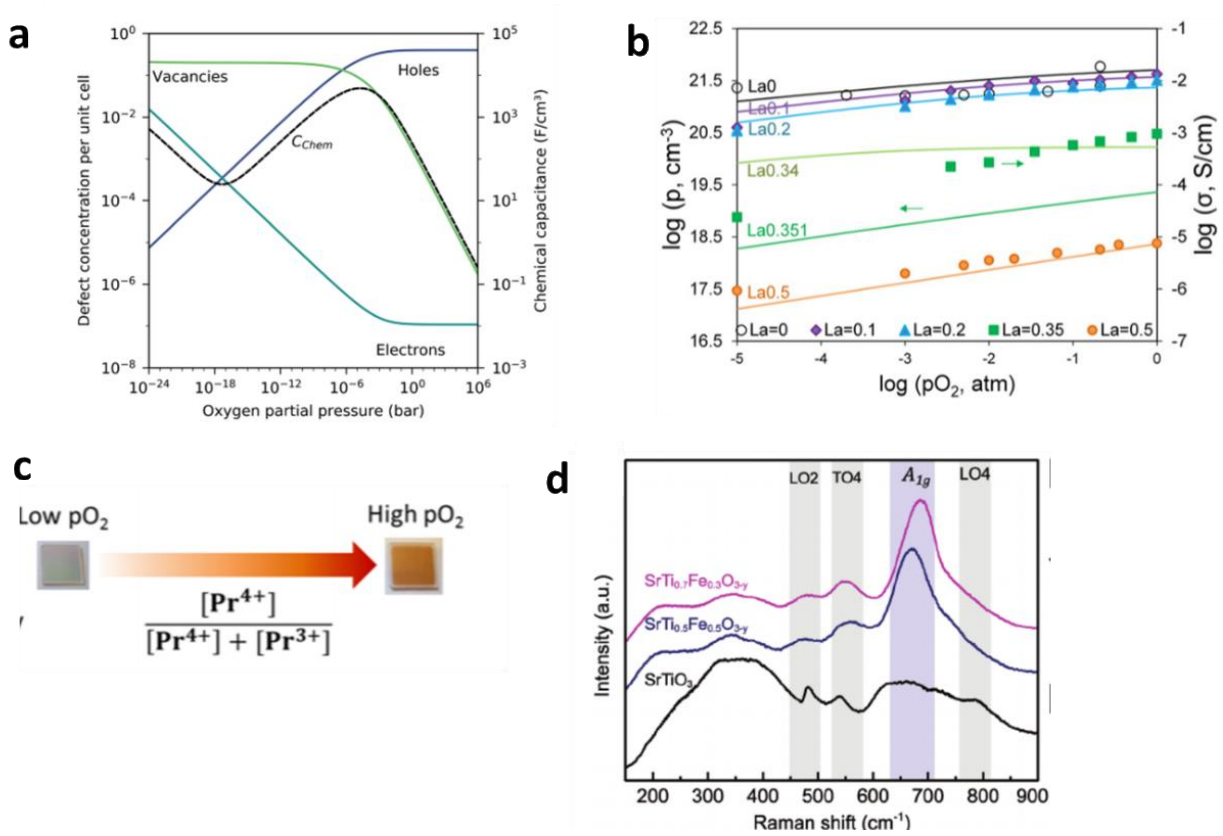


**Figure 1.10** Studies of the defect chemistry in thin films by **a.** Chemical capacitance. Reproduced from Ref. 126 with permission from the PCCP Owner Societies. **b.** Electrical conductivity. Reprinted from Solid State Ionics, 273, Perry, N. H., Pergolesi, D., Bishop, S. R., Tuller, H. L. *Defect Chemistry and Surface Oxygen Exchange Kinetics of La-Doped Sr(Ti,Fe)O3 - α in Oxygen-Rich Atmospheres*. 18-24.[128] Copyright (2015), with permission from Elsevier. **c.** UV-Vis transmission. Reprinted with permission from *Defect Chemistry of Pr Doped Ceria Thin Films Investigated by in Situ Optical and Impedance Measurements.* Chem. Mater. 2017, 29 (5), 1999–2007.[131] Copyright 2017 American Chemical **d.** Raman spectroscopy. Reproduced from Sediva, E., Defferriere, T., Perry, N. H., Tuller, H. L., Rupp, J. L. M. *In Situ Method Correlating Raman Vibrational Characteristics to Chemical Expansion via Oxygen Nonstoichiometry of Perovskite Thin Films*. Adv. Mater. 2019, 31 (33), 1–9.[132] Copyright © 2019 WILEY-VCH Verlag GmbH & Co. KGaA, Weinheim

## 1.6 Scope of this thesis

This thesis is devoted to the engineering of the point defects in the non-stoichiometric LSF thin films for energy and information devices. The ability to tune the functional properties of LSF thin films in energy and information applications (SOFCs, electrochemical capacitors, transistors etc.) requires a thorough understanding of the point defects in the films. Inspired by the previous researches, in this thesis, a novel in-situ ellipsometry spectroscopy method will be proposed to get insight into the defect chemistry of LSF thin films. The concentration of point defects in LSF thin films are indirectly quantified under the real electrochemical conditions (electrochemical bias) through a direct correlation with the optical conductivity.

Based on the knowledge of defect chemistry, the ferrite thin films have been explored for their application in three-terminal electrolyte-gated transistors, in which the modulation of the thin films' electrical properties linked to the point defect concentration acts as the response to the stimulus.

This thesis is organized by the chapters:

**Chapter 2** deals with the experimental techniques employed for the thin film deposition and characterization, with the details of the in-situ ellipsometry technique for the measurements in gas atmosphere and liquid electrolyte, as well as the electrochemical techniques.

**Chapter 3** describes the implementation of the in-situ ellipsometry technique to track the concentration of electron holes in the LSF thin films at intermediate-to-low temperatures and under various equivalent oxygen partial pressures, including a non-dilute defect chemistry model which satisfactorily describes the point defects in the ferrite thin films.

**Chapter 4** is dedicated to determine the mechanism of ion intercalation in $La_{0.5}Sr_{0.5}FeO_{3-\delta}$ (LSF50) thin films in alkaline electrolyte. The defect chemistry of LSF50 thin films during ion intercalation is studied using in-situ ellipsometry. The point defects in the films are indirectly quantified by correlating the optical conductivity at low photon energy to the hole concentration. Finally, a dilute model that enables the description of defect chemistry of LSF50 thin films in liquid electrolyte is involved.

**Chapter 5** presents the design concept of a solid-electrolyte synaptic transistor in which the ionic conductor $Bi_4V_{1.8}Cu_{0.2}O_{10.7}$ (BICUVOX) film is employed as electrolyte and the MIEC LSF50 films are employed as gate and channel materials. The modulation of the electrical

properties of the channel material with the electrochemical bias applied at the gate is described in detail, as well as the performance of the transistor at low temperatures.

Finally, in **Appendix** an "optical impedance spectroscopy" based on the frequency-dependent optical response of LSF thin films to the imposed AC electrical voltages is proposed, the performance of this technique for the solid-electrolyte and liquid-electrolyte LSF electrochemical cells is discussed.

# References


1. Tomar, A. K., Joshi, A., Singh, G. & Sharma, R. K. Perovskite oxides as supercapacitive electrode: Properties, design and recent advances. *Coord. Chem. Rev.* **431**, 213680 (2021).

2. Chen, D. *et al.* Compositional engineering of perovskite oxides for highly efficient oxygen reduction reactions. *ACS Appl. Mater. Interfaces* **7**, 8562–8571 (2015).

3. Søgaard, M., Vang Hendriksen, P. & Mogensen, M. Oxygen nonstoichiometry and transport properties of strontium substituted lanthanum ferrite. *J. Solid State Chem.* **180**, 1489–1503 (2007).

4. Lohne, Ø. F. *et al.* Oxygen Non-Stoichiometry and Electrical Conductivity of $La_{0.2}Sr_{0.8}Fe_{0.8}B_{0.2}O_{3-\delta}$, B = Fe, Ti, Ta. *J. Electrochem. Soc.* **161**, F176–F184 (2014).

5. Kharton, V. V. *et al.* Oxygen Permeability and Ionic Conductivity of Perovskite-Related $La_{0.3}Sr_{0.7}Fe(Ga)O_{3-\delta}$. *J. Electrochem. Soc.* **149**, E125 (2002).

6. Khan, R. *et al.* Role of perovskites as a bi-functional catalyst for electrochemical water splitting: A review. *Int. J. Energy Res.* **44**, 9714–9747 (2020).

7. Rondinelli, J. M. & Spaldin, N. A. Structure and properties of functional oxide thin films: Insights from electronic-structure calculations. *Adv. Mater.* **23**, 3363–3381 (2011).

8. Schlom, D. G., Chen, L. Q., Pan, X., Schmehl, A. & Zurbuchen, M. A. A thin film approach to engineering functionality into oxides. *J. Am. Ceram. Soc.* **91**, 2429–2454 (2008).

9. Hwang, J. *et al.* Tuning perovskite oxides by strain: Electronic structure, properties, and functions in (electro)catalysis and ferroelectricity. *Mater. Today* **31**, 100–118 (2019).

10. Chiabrera, F., Garbayo, I. & Tarancón, A. Nanoionics and Interfaces for Energy and Information Technologies. in *Metal Oxide-Based Thin Film Structures* 409–439 (2018). doi:10.1016/B978-0-12-811166-6.00017-0.

11. Abdalla, A. M. *et al.* Nanomaterials for solid oxide fuel cells: A review. *Renew. Sustain. Energy Rev.* **82**, 353–368 (2018).

12. Dey, S. & Dhal, G. C. Materials progress in the control of CO and $CO_2$ emission at ambient conditions: An overview. *Mater. Sci. Energy Technol.* **2**, 607–623 (2019).

13. Stambouli, A. B. & Traversa, E. Solid oxide fuel cells (SOFCs): A review of an environmentally clean and efficient source of energy. *Renew. Sustain. Energy Rev.* **6**, 433–455 (2002).

14. Marinha, D., Dessemond, L. & Djurado, E. Comprehensive Review of Current Developments in IT-SOFCs. *Curr. Inorg. Chem.* **3**, 2–22 (2013).

15. Alaswad, A., Baroutaji, A., Rezk, A., Ramadan, M. & Olabi, A. G. *Advances in Solid Oxide Fuel Cell Materials*. *Reference Module in Materials Science and Materials Engineering* (Elsevier Ltd., 2020). doi:10.1016/b978-0-12-803581-8.11743-6.

16. Mogensen, M. & Jensen, S. Performance of reversible solid oxide cells: a review. in *Proceedings of the 7th …* 1–11 (2006).

17. Hauch, A. *et al.* Recent advances in solid oxide cell technology for electrolysis. *Science (80-. ).* **370**, (2020).

18. Brandon, N. P. & Parkes, M. A. Fuel Cells: Materials. *Encycl. Mater. Met. Allloys* 377–382 (2016) doi:10.1016/b978-0-12-803581-8.01726-4.

19. Jun, A., Kim, J., Shin, J. & Kim, G. Perovskite as a Cathode Material: A Review of its Role in Solid-Oxide Fuel Cell Technology. *ChemElectroChem* **3**, 511–530 (2016).

20. Weber, A. & Ivers-Tiffée, E. Materials and concepts for solid oxide fuel cells (SOFCs) in stationary and mobile applications. *J. Power Sources* **127**, 273–283 (2004).

21. Maguire, E., Gharbage, B., Marques, F. M. B. & Labrincha, J. A. Cathode materials for intermediate temperature SOFCs. *Solid State Ionics* **127**, 329–335 (2000).

22. Jiang, S. P. Development of lanthanum strontium cobalt ferrite perovskite electrodes of solid oxide fuel cells – A review. *Int. J. Hydrogen Energy* **44**, 7448–7493 (2019).

23. Ralph, J. M., Rossignol, C. & Kumar, R. Cathode Materials for Reduced-Temperature SOFCs. *J. Electrochem. Soc.* **150**, A1518 (2003).

24. Mushtaq, N. *et al.* Perovskite $SrFe_{1-x}Ti_xO_{3-\delta}$ ($x <= 0.1$) cathode for low temperature solid oxide fuel cell. *Ceram. Int.* **44**, 10266–10272 (2018).

25. Afif, A. *et al.* Advanced materials and technologies for hybrid supercapacitors for energy storage – A review. *J. Energy Storage* **25**, 100852 (2019).

26. Nan, H. shan, Hu, X. ying & Tian, H. wei. Recent advances in perovskite oxides for anion-intercalation supercapacitor: A review. *Mater. Sci. Semicond. Process.* **94**, 35–50 (2019).

27. Wang, F. *et al.* Latest advances in supercapacitors: From new electrode materials to novel device designs. *Chem. Soc. Rev.* **46**, 6816–6854 (2017).

28. Tomar, A. K., Joshi, A., Singh, G. & Sharma, R. K. Perovskite oxides as supercapacitive electrode : Properties , design and recent advances. *Coord. Chem. Rev.* **431**, 213680 (2020).

29. Harikrishnan, M. P., Mary, A. J. C. & Bose, A. C. Electrochemical performance of $ANiO_3$ (A= La, Ce) perovskite oxide material and its device performance for supercapattery application. *Electrochim. Acta* **362**, 137095 (2020).

30. Lokhande, C. D., Gujar, T. P., Shinde, V. R., Mane, R. S. & Han, S. H. Electrochemical supercapacitor application of pervoskite thin films. *Electrochem. commun.* **9**, 1805–1809 (2007).

31. Lang, X., Mo, H., Hu, X. & Tian, H. Supercapacitor performance of perovskite $La_{1-x}Sr_xMnO_3$. *Dalt. Trans.* **46**, 13720–13730 (2017).

32. Ma, P. P. *et al.* Effect of A-site substitution by Ca or Sr on the structure and electrochemical performance of $LaMnO_3$ perovskite. *Electrochim. Acta* **332**, 135489 (2020).

33. Wang, W. *et al.* Synthesis, morphology and electrochemical performances of perovskite-type oxide $La_xSr_{1-x}FeO_3$ nanofibers prepared by electrospinning. *J. Phys. Chem. Solids* **124**, 144–150 (2019).

34. Wang, W., Xu, M., Xu, X., Zhou, W. & Shao, Z. Perovskite Oxide Based Electrodes for High-Performance Photoelectrochemical Water Splitting. *Angew. Chemie - Int. Ed.* **59**, 136–152 (2020).

35. Wang, J., Choi, S., Kim, J., Cha, S. W. & Lim, J. Recent advances of first d-block metal-based perovskite oxide electrocatalysts for alkaline water splitting. *Catalysts*

**10**, 770 (2020).

36. Li, Y. *et al.* Recent Advances on Water-Splitting Electrocatalysis Mediated by Noble-Metal-Based Nanostructured Materials. *Adv. Energy Mater.* **10**, 1903120 (2020).

37. Matsumoto, Y. & Sato, E. Oxygen evolution on $La_{1-x}Sr_xMnO_3$ in alkaline. *Electrochim. Acta* **24**, 421–423 (1979).

38. Liu, H. *et al.* Cation deficiency design: A simple and efficient strategy for promoting oxygen evolution reaction activity of perovskite electrocatalyst. *Electrochim. Acta* **259**, 1004–1010 (2018).

39. Wang, W. *et al.* An excellent OER electrocatalyst of cubic $SrCoO_{3-\delta}$ prepared by a simple F-doping strategy. *J. Mater. Chem. A* **7**, 12538–12546 (2019).

40. Huang, H. Y. *et al.* Electrolyte-Gated Synaptic Transistor with Oxygen Ions. *Adv. Funct. Mater.* **29**, 1902702 (2019).

41. Ge, C. *et al.* A Ferrite Synaptic Transistor with Topotactic Transformation. *Adv. Mater.* **31**, 1900379 (2019).

42. Shi, J., Ha, S. D., Zhou, Y., Schoofs, F. & Ramanathan, S. A correlated nickelate synaptic transistor. *Nat. Commun.* **4**, 2676 (2013).

43. Kim, S. H. *et al.* Electrolyte-gated transistors for organic and printed electronics. *Adv. Mater.* **25**, 1822–1846 (2013).

44. Ling, H. *et al.* Electrolyte-gated transistors for synaptic electronics, neuromorphic computing, and adaptable biointerfacing. *Appl. Phys. Rev.* **7**, 011307 (2020).

45. Shi, P. *et al.* Solid-state electrolyte gated synaptic transistor based on $SrFeO_{2.5}$ film channel. *Mater. Des.* **210**, 110022 (2021).

46. Liu, N., Chen, R. & Wan, Q. Recent Advances in Electric-Double-Layer Transistors for Bio-Chemical Sensing Applications. *Sensors* **19**, 3425 (2019).

47. Rao, J. *et al.* An electroforming-free, analog interface-type memristor based on a $SrFeO_x$ epitaxial heterojunction for neuromorphic computing. *Mater. Today Phys.* **18**, 100392 (2021).

48. Zhang, S. & Galli, G. Understanding the metal-to-insulator transition in

$La_{1-x}Sr_xCoO_{3-\delta}$ and its applications for neuromorphic computing. *npj Comput. Mater.* **6**, 170 (2020).

49. Nikam, R. D., Kwak, M. & Hwang, H. All-Solid-State Oxygen Ion Electrochemical Random-Access Memory for Neuromorphic Computing. *Adv. Electron. Mater.* **7**, 2100142 (2021).

50. Tsuchiya, T., Ochi, M., Higuchi, T., Terabe, K. & Aono, M. Effect of Ionic Conductivity on Response Speed of SrTiO3-Based All-Solid-State Electric-Double-Layer Transistor. *ACS Appl. Mater. Interfaces* **7**, 12254–12260 (2015).

51. Krick, A. L. & May, S. J. Evidence for oxygen vacancy manipulation in $La_{1/3}Sr_{2/3}FeO_{3-\delta}$ thin films via voltage controlled solid-state ionic gating. *APL Mater.* **5**, 042504 (2017).

52. Nikam, R. D. *et al.* Near ideal synaptic functionalities in Li ion synaptic transistor using $Li_3PO_xSe_x$ electrolyte with high ionic conductivity. *Sci. Rep.* **9**, 18883 (2019).

53. Holtappels, P., Vogt, U. & Graule, T. Ceramic materials for advanced solid oxide fuel cells. *Adv. Eng. Mater.* **7**, 292–302 (2005).

54. Kammer Hansen, K. & Mogensen, M. Evaluation of LSF based SOFC Cathodes using Cone-shaped Electrodes. *ECS Trans.* **13**, 153–160 (2019).

55. Walch, G., Opitz, A. K., Kogler, S. & Fleig, J. Correlation between hydrogen production rate, current, and electrode overpotential in a solid oxide electrolysis cell with $La_{0.6}Sr_{0.4}FeO_{3-\delta}$ thin-film cathode. *Monatshefte fur Chemie* **145**, 1055–1061 (2014).

56. Alexander, C. T. *et al.* Anion-Based Pseudocapacitance of the Perovskite Library $La_{1-x}Sr_xBO_{3-\delta}$ (B = Fe, Mn, Co). *ACS Appl. Mater. Interfaces* **11**, 5084–5094 (2019).

57. She, S. *et al.* Systematic Study of Oxygen Evolution Activity and Stability on $La_{1-x}Sr_xFeO_{3-\delta}$ Perovskite Electrocatalysts in Alkaline Media. *ACS Appl. Mater. Interfaces* **10**, 11715–11721 (2018).

58. Suresh, K., Panchapagesan, T. S. & Patil, K. C. Synthesis and properties of $La_{1-x}Sr_xFeO_3$. *Solid State Ionics* **126**, 299–305 (1999).

59. Patrakeev, M. V. *et al.* Electron/hole and ion transport in $La_{1-x}Sr_xFeO_{3-\delta}$. *J. Solid State*

*Chem.* **172**, 219–231 (2003).

60. Mizusaki, J., Yoshihiro, M., Yamauchi, S. & Fueki, K. Thermodynamic quantities and defect equilibrium in the perovskite-type oxide solid solution $La_{1-x}Sr_xFeO_{3-\delta}$. *J. Solid State Chem.* **67**, 1–8 (1987).

61. Shen, Z. *et al.* Increased activity in the oxygen evolution reaction by Fe4+-induced hole states in perovskite $La_{1-x}Sr_xFeO_3$. *J. Mater. Chem. A* **8**, 4407–4415 (2020).

62. Kafa, C. A., Triyono, D. & Laysandra, H. Effect of Sr substitution on the room temperature electrical properties of $La_{1-x}Sr_xFeO_3$ nano-crystalline materials. in *AIP Conference Proceedings* vol. 1862 030042 (2017).

63. Moniruddin, M. *et al.* Recent progress on perovskite materials in photovoltaic and water splitting applications. *Mater. Today Energy* **7**, 246–259 (2018).

64. Gupta, S., Mahapatra, M. K. & Singh, P. Lanthanum chromite based perovskites for oxygen transport membrane. *Mater. Sci. Eng. R Reports* **90**, 1–36 (2015).

65. da Silva, R. B. *et al.* Local iron ion distribution and magnetic properties of the perovskites $La_{1-x}Sr_xFeO_{3-\gamma}$. *J. Magn. Magn. Mater.* **466**, 306–310 (2018).

66. Cui, X., Li, S. & Zhu, X. Microstructure and electrical properties of $La_{1-x}Sr_xFeO_3$(x=0-0.6) film by a screen-printing method. *Mater. Lett.* **130**, 267–270 (2014).

67. Nadeev, A. N. *et al.* High-temperature studies of $La_{1-x}Sr_xFeO_{3-\delta}$ solid solutions using synchrotron radiation. *J. Struct. Chem.* **48**, 1105–1109 (2007).

68. Kofstad, P. & Norby, T. *Defects and transport in crystalline solids*. *University of Oslo* vol. 9120 (2007).

69. Poulsen, F. W. Defect chemistry modelling of oxygen-stoichiometry, vacancy concentrations, and conductivity of $(La_{1-x}Sr_x)_yMnO_{3\pm\delta}$. *Solid State Ionics* **129**, 145–162 (2000).

70. Cheng, J., Navrotsky, A., Zhou, X. D. & Anderson, H. U. Thermochemistry of $La_{1-x}Sr_xFeO_{3-\delta}$ solid solutions ($0.0\leq x\leq 1.0$, $0.0\leq\delta\leq 0.5$). *Chem. Mater.* **17**, 2197–2207 (2005).

71. Bae, H. *et al.* Investigations on defect equilibrium, thermodynamic quantities, and

transport properties of $La_{0.5}Sr_{0.5}FeO_{3-\delta}$. *J. Electrochem. Soc.* **166**, F180–F189 (2019).

72. Kuhn, M., Hashimoto, S., Sato, K., Yashiro, K. & Mizusaki, J. Oxygen nonstoichiometry, thermo-chemical stability and lattice expansion of $La_{0.6}Sr_{0.4}FeO_{3-\delta}$. *Solid State Ionics* **195**, 7–15 (2011).

73. Chen, X. & Grande, T. Anisotropic and Nonlinear Thermal and Chemical Expansion of $La_{1-x}Sr_xFeO_{3-\delta}$ (x = 0.3, 0.4, 0.5) Perovskite Materials. *Chem. Mater.* **25**, 3296–3306 (2013).

74. Mizusaki, J., Yoshihiro, M., Yamauchi, S. & Fueki, K. Nonstoichiometry and defect structure of the perovskite-type oxides $La_{1-x}Sr_xFeO_{3-\delta}$. *J. Solid State Chem.* **58**, 257–266 (1985).

75. Yoon, K. J., Zink, P. A., Gopalan, S., Pal, U. B. & Pederson, L. R. Defect Chemistry and Electrical Properties of $(La_{0.8}Ca_{0.2})_{0.95}FeO_{3-\delta}$. *J. Electrochem. Soc.* **156**, B795 (2009).

76. Wadati, H. *et al.* Hole-doping-induced changes in the electronic structure of $La_{1-x}Sr_xFeO_3$: Soft x-ray photoemission and absorption study of epitaxial thin films. *Phys. Rev. B - Condens. Matter Mater. Phys.* **71**, 035108 (2005).

77. Wang, L. *et al.* Hole-induced electronic and optical transitions in $La_{1-x}Sr_xFeO_3$ epitaxial thin films. *Phys. Rev. Mater.* **3**, 025401 (2019).

78. Tajima, S. *et al.* Infrared reflectivity and electronic states in perovskite-type oxides $La_{1-x}Sr_xFeO_3$ and $La_{1-x}Sr_xCoO_3$. *J. Phys. C Solid State Phys.* **20**, 3469–3484 (1987).

79. Smolin, S. Y. *et al.* Static and Dynamic Optical Properties of $La_{1-x}Sr_xFeO_{3-\delta}$: The Effects of A-Site and Oxygen Stoichiometry. *Chem. Mater.* **28**, 97–105 (2016).

80. Scafetta, M. D., Cordi, A. M., Rondinelli, J. M. & May, S. J. Band structure and optical transitions in $LaFeO_3$: Theory and experiment. *J. Phys. Condens. Matter* **26**, 505502 (2014).

81. Wadati, H. *et al.* Hole-doping-induced changes in the electronic structure of $La_{1-x}Sr_xFeO_3$: Soft x-ray photoemission and absorption study of epitaxial thin films. *Phys. Rev. B - Condens. Matter Mater. Phys.* **71**, 035108 (2005).

82. Wadati, H. *et al.* Strong localization of doped holes in $La_{1-x}Sr_xFeO_3$ from angle-

resolved photoemission spectra. *Phys. Rev. B* **74**, 115114 (2006).

83. Scafetta, M. D., Xie, Y. J., Torres, M., Spanier, J. E. & May, S. J. Optical absorption in epitaxial $La_{1-x}Sr_xFeO_3$ thin films. *Appl. Phys. Lett.* **102**, 081904 (2013).

84. Tsipis, E. V. *et al.* Transport properties and thermal expansion of Ti-substituted $La_{1-x}Sr_xFeO_{3-\delta}$ (x = 0.5-0.7). *Solid State Sci.* **7**, 355–365 (2005).

85. Kim, M. C., Park, S., Haneda, H., Tanaka, J. & Shirasaki, S. High temperature electrical conductivity of $La_{1-x}Sr_xFeO_{3-\delta}$ (x>0.5). *Solid State Ionics* **40**–**41**, 239–243 (1990).

86. Patrakeev, M. V., Leonidov, I. A., Kozhevnikov, V. L. & Poeppelmeier, K. R. p-type electron transport in $La_{1-x}Sr_xFeO_{3-\delta}$ at high temperatures. *J. Solid State Chem.* **178**, 921–927 (2005).

87. Bongio, E. V. *et al.* Microstructural and high-temperature electrical characterization of $La_{1-x}Sr_xFeO_{3-\delta}$. *J. Electroceramics* **14**, 193–198 (2005).

88. Preis, W., Bucher, E. & Sitte, W. Oxygen exchange kinetics of $La_{0.4}Sr_{0.6}FeO_{3-\delta}$ by simultaneous application of conductivity relaxation and carrier gas coulometry. *Solid State Ionics* **175**, 393–397 (2004).

89. Yang, Q. & Nicholas, J. D. Porous Thick Film Lanthanum Strontium Ferrite Stress and Oxygen Surface Exchange Bilayer Curvature Relaxation Measurements. *J. Electrochem. Soc.* **161**, F3025–F3031 (2014).

90. Yoo, J., Verma, A., Wang, S. & Jacobson, A. J. Oxygen Transport Kinetics in $SrFeO_{3-\delta}$, $La_{0.5}Sr_{0.5}FeO_{3-\delta}$, and $La_{0.2}Sr_{0.8}Cr_{0.2}Fe_{0.8}O_{3-\delta}$ Measured by Electrical Conductivity Relaxation. *J. Electrochem. Soc.* **152**, A497 (2005).

91. Yoo, J. & Jacobson, A. J. A study of the oxygen transport kinetics in $SrFeO_{3-x}$. *Mater. Res. Soc. Symp. - Proc.* **756**, 105–110 (2003).

92. Ishigaki, T., Yamauchi, S., Kishio, K., Mizusaki, J. & Fueki, K. Diffusion of oxide ion vacancies in perovskite-type oxides. *J. Solid State Chem.* **73**, 179–187 (1988).

93. Ritzmann, A. M., Muñoz-Garcia, A. B., Pavone, M., Keith, J. a & Carter, E. a. Ab Initio DFT+U Analysis of Oxygen Vacancy Formation and Migration in $La_{1-x}Sr_xFeO_{3-\delta}$ (x=0, 0.25,0.5). *Chem. Mater.* **25**, 3011–3019 (2013).

94. Sun, Y. *et al.* Insight into the enhanced photoelectrocatalytic activity in reduced $LaFeO_3$ films. *Chem. Commun.* **53**, 2499–2502 (2017).

95. Nikonov, A. V., Kuterbekov, K. A., Bekmyrza, K. Z. & Pavzderin, N. B. A brief review of conductivity and thermal expansion of perovskite-related oxides for SOFC cathode. *Eurasian J. Phys. Funct. Mater.* **2**, 274–292 (2018).

96. Hui, S. (Rob) *et al.* A brief review of the ionic conductivity enhancement for selected oxide electrolytes. *J. Power Sources* **172**, 493–502 (2007).

97. Omar, S., Wachsman, E. D. & Nino, J. C. Higher ionic conductive ceria-based electrolytes for solid oxide fuel cells. *Appl. Phys. Lett.* **91**, 2005–2008 (2007).

98. Chiabrera, F. *et al.* Engineering Transport in Manganites by Tuning Local Nonstoichiometry in Grain Boundaries. *Adv. Mater.* **31**, 1805360 (2019).

99. Saranya, A. M. *et al.* Unveiling the Outstanding Oxygen Mass Transport Properties of Mn-Rich Perovskites in Grain Boundary-Dominated $La_{0.8}Sr_{0.2}(Mn_{1-x}Co_x)_{0.85}O_{3\pm\delta}$ Nanostructures. *Chem. Mater.* **30**, 5621–5629 (2018).

100. Lu, Q. & Yildiz, B. Voltage-Controlled Topotactic Phase Transition in Thin-Film $SrCoO_x$ Monitored by in Situ X-ray Diffraction. *Nano Lett.* **16**, 1186–1193 (2016).

101. Lesel, B. K., Ko, J. S., Dunn, B. & Tolbert, S. H. Mesoporous $Li_xMn_2O_4$ Thin Film Cathodes for Lithium-Ion Pseudocapacitors. *ACS Nano* **10**, 7572–7581 (2016).

102. Graetz, J., Ahn, C. C., Yazami, R. & Fultz, B. Nanocrystalline and Thin Film Germanium Electrodes with High Lithium Capacity and High Rate Capabilities. *J. Electrochem. Soc.* **151**, A698 (2004).

103. Chiabrera, F. *et al.* Unraveling bulk and grain boundary electrical properties in $La_{0.8}Sr_{0.2}Mn_{1-y}O_{3\pm\delta}$ thin films. *APL Mater.* **7**, 013205 (2019).

104. Chiabrera, F., Morata, A., Pacios, M. & Tarancón, A. Insights into the enhancement of oxygen mass transport properties of strontium-doped lanthanum manganite interface-dominated thin films. *Solid State Ionics* **299**, 70–77 (2017).

105. Saranya, A. M. *et al.* Engineering mixed ionic electronic conduction in $La_{0.8}Sr_{0.2}MnO_{3+\delta}$ nanostructures through fast grain boundary oxygen diffusivity. *Adv. Energy Mater.* **5**, 1500377 (2015).

106. Kim, H. *et al.* Effect of film thickness on the properties of indium tin oxide thin films. *J. Appl. Phys.* **88**, 6021–6025 (2000).

107. Salim, M. A. Effect of thickness on the optical properties of ZnO thin films prepared by pulsed laser deposition technique (PLD). *Iraqi J. Phys.* **15**, 114–121 (2019).

108. Singh, A., Khan, Z. R., Vilarinho, P. M., Gupta, V. & Katiyar, R. S. Influence of thickness on optical and structural properties of $BiFeO_3$ thin films: PLD grown. *Mater. Res. Bull.* **49**, 531–536 (2014).

109. Biswas, A. & Jeong, Y. H. Growth and engineering of perovskite $SrIrO_3$ thin films. *Curr. Appl. Phys.* **17**, 605–614 (2017).

110. Yamamoto, T. *et al.* Strain-induced creation and switching of anion vacancy layers in perovskite oxynitrides. *Nat. Commun.* **11**, 5923 (2020).

111. Hirai, K. *et al.* Strain-induced significant increase in metal-insulator transition temperature in oxygen-deficient Fe oxide epitaxial thin films. *Sci. Rep.* **5**, 7894 (2015).

112. Koo, B. *et al.* Enhanced oxygen exchange of perovskite oxide surfaces through strain-driven chemical stabilization. *Energy Environ. Sci.* **11**, 71–77 (2018).

113. Gan, Q., Rao, R. A., Eom, C. B., Garrett, J. L. & Lee, M. Direct measurement of strain effects on magnetic and electrical properties of epitaxial $SrRuO_3$ thin films. *Appl. Phys. Lett.* **72**, 978–980 (1998).

114. Zhu, Y. *et al.* Tuning proton-coupled electron transfer by crystal orientation for efficient water oxidization on double perovskite oxides. *Nat. Commun.* **11**, 4299 (2020).

115. Inoue, S. *et al.* Anisotropic oxygen diffusion at low temperature in perovskite-structure iron oxides. *Nat. Chem.* **2**, 213–217 (2010).

116. Yu, M. & Feng, X. Thin-Film Electrode-Based Supercapacitors. *Joule* **3**, 338–360 (2019).

117. Traversa, E. Toward the miniaturization of solid oxide fuel cells. *Electrochem. Soc. Interface* **18**, 49–52 (2009).

118. Myny, K. The development of flexible integrated circuits based on thin-film

transistors. *Nat. Electron.* **1**, 30–39 (2018).

119. Kuhn, M., Hashimoto, S., Sato, K., Yashiro, K. & Mizusaki, J. Oxygen nonstoichiometry and thermo-chemical stability of $La_{0.6}Sr_{0.4}CoO_{3-\delta}$. *J. Solid State Chem.* **197**, 38–45 (2013).

120. Onuma, S. *et al.* Oxygen nonstoichiometry of the perovskite-type oxide $La_{1-x}Ca_xCrO_{3-\delta}$ (x=0.1, 0.2, 0.3). *Solid State Ionics* **174**, 287–293 (2004).

121. Kuhn, M., Kim, J. J., Bishop, S. R. & Tuller, H. L. Oxygen nonstoichiometry and defect chemistry of perovskite-structured $Ba_xSr_{1-x}Ti_{1-y}Fe_yO_{3-y/2+\delta}$ solid solutions. *Chem. Mater.* **25**, 2970–2975 (2013).

122. Mizusaki, J., Mima, Y., Yamauchi, S. & Fueki, K. Nonstoichiometry of the perovskite-type oxides $La_{1-x}Sr_xCoO_{3-\delta}$. *J. Solid State Chem.* **80**, 102–111 (1989).

123. Seh, H., Fritze, H. & Tuller, H. L. Defect chemistry of langasite III: Predictions of electrical and gravimetric properties and application to operation of high temperature crystal microbalance. *J. Electroceramics* **18**, 139–147 (2007).

124. Marrocchelli, D., Perry, N. H. & Bishop, S. R. Understanding chemical expansion in perovskite-structured oxides. *Phys. Chem. Chem. Phys.* **17**, 10028–10039 (2015).

125. Schmid, A., Rupp, G. M. & Fleig, J. Voltage and partial pressure dependent defect chemistry in $(La,Sr)FeO_{3-\delta}$ thin films investigated by chemical capacitance measurements. *Phys. Chem. Chem. Phys.* **20**, 12016–12026 (2018).

126. Chen, D., Bishop, S. R. & Tuller, H. L. Non-stoichiometry in oxide thin films: A chemical capacitance study of the praseodymium-cerium oxide system. *Adv. Funct. Mater.* **23**, 2168–2174 (2013).

127. Schmid, A., Rupp, G. M. & Fleig, J. How to Get Mechanistic Information from Partial Pressure-Dependent Current-Voltage Measurements of Oxygen Exchange on Mixed Conducting Electrodes. *Chem. Mater.* **30**, 4242–4252 (2018).

128. Perry, N. H., Pergolesi, D., Bishop, S. R. & Tuller, H. L. Defect chemistry and surface oxygen exchange kinetics of La-doped $Sr(Ti,Fe)O_{3-\alpha}$ in oxygen-rich atmospheres. *Solid State Ionics* **273**, 18–24 (2015).

129. Moffitt, S. L. *et al.* Confirmation of the Dominant Defect Mechanism in Amorphous

In-Zn-O Through the Application of in Situ Brouwer Analysis. *J. Am. Ceram. Soc.* **98**, 2099–2103 (2015).

130. Gunkel, F., Christensen, D. V., Chen, Y. Z. & Pryds, N. Oxygen vacancies: The (in)visible friend of oxide electronics. *Appl. Phys. Lett.* **116**, 120505 (2020).

131. Kim, J. J., Bishop, S. R., Chen, D. & Tuller, H. L. Defect Chemistry of Pr Doped Ceria Thin Films Investigated by in Situ Optical and Impedance Measurements. *Chem. Mater.* **29**, 1999–2007 (2017).

132. Sediva, E., Defferriere, T., Perry, N. H., Tuller, H. L. & Rupp, J. L. M. In Situ Method Correlating Raman Vibrational Characteristics to Chemical Expansion via Oxygen Nonstoichiometry of Perovskite Thin Films. *Adv. Mater.* **31**, 1902493 (2019).

# 2. Experimental methods

## 2.1 Introduction

The objective of this chapter is to provide an overview of the methodologies and techniques used in this thesis. In **Section 2.2,** the Pulsed Laser Deposition (PLD) technique used for fabricating samples in thin film is introduced and its mechanisms are discussed. Furthermore, the Large-Area PLD (LA-PLD) employed in this thesis for growing thin films and the solid-state synthesis used for fabricating the PLD targets are presented. In **Section 2.3,** the techniques used for structural and compositional characterization in this thesis are discussed. **Section 2.4** details the principles of ellipsometry technique and its applications for in-situ measurements, as well as the data analysis. A series of electrical configurations and electrochemical techniques employed in this thesis are covered in **Section 2.5**. In **Section 2.6,** the Time-of-Flight Secondary Ion Mass Spectrometry (ToF-SIMS) used for characterizing the depth profiles of reactive particles in thin films is described. The Positron Annihilation Lifetime Spectroscopy (PALS) employed for characterizing open-volume and negatively charged defects in the structure is introduced in **Section 2.7**. Finally, **Section 2.8** is devoted to describe the Finite Element Modelling method employed for simulating the distribution of electrochemical potential in the thin films.

## 2.2 Thin film deposition

### 2.2.1 Pulsed Laser Deposition (PLD)

Physical Vapor Deposition (PVD) as a powerful technology for thin film deposition is based on converting atoms or molecules of a liquid or solid material into a vapor under vacuum conditions. The vapor is then carried towards the substrate, where it condenses on the surface to form a thin film. Depending on the existence of collisions in the deposition process, the PVD process can be divided into evaporation and sputtering. Among the PVD techniques, Pulsed Laser Deposition (PLD) technique has been developed prosperously in the fields of oxides[1–4], graphene[5], amorphous thin films[6,7] for semiconductors, sensors, superconductors, electronic, optical and optoelectronic devices etc. PLD involves removing the material species (atoms, ions or molecules etc.) from a solid target with an energetic laser, vaporizing the species into a plasma plume, and forming a thin film on the substrate surface. As a form of PVD technology it is distinguished from other traditional techniques such as Chemical Vapor Deposition (CVD), Molecular Beam Epitaxy (MBE), and magnetron sputtering by the stoichiometric transfer of materials, high versatility and flexibility.[8–10]

As illustrated in **Figure 2.1,** an energetic laser beam is emitted and focused on the target material after the transmission through a series of optical components (lens, mirrors etc.), the energetic laser ablates the target material, resulting in the formation of a luminous plasma plume composed of the energetic species that are ejected away from the target and deposited on the substrate. A PLD system consists of a laser excimer, a series of optical components, a vacuum chamber equipped with pumps to regulate the atmosphere inside the chamber, a substrate holder and a collection of target holders, ultraviolet (UV) lamps for heating the substrate, and motors for moving and rotating the substrate and target.

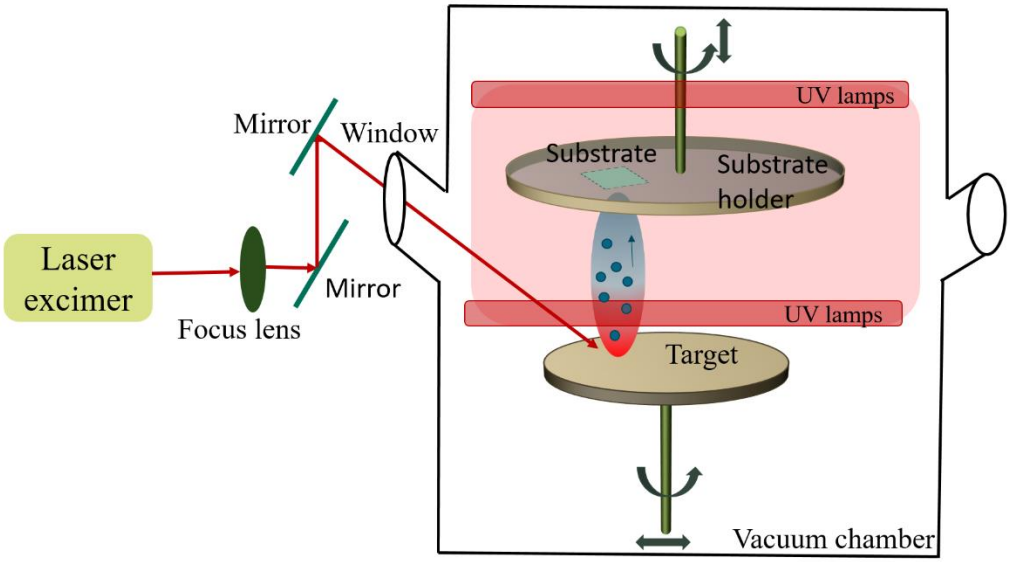


**Figure 2.1** Schematic representation of the PLD system.

Despite the mechanism of PLD is relatively complex, the deposition process can be divided into three stages:

i) Laser-target interaction: In this stage, the energetic laser is radiated and focused on the target surface at an angle of incidence of 45º,[11] the transfer of the energy of the laser pulses to the target material induces local heat of the target. Once reached the critical temperature, the target material is ablated and evaporated away from the target forming a luminous plasma. Relating to the excitation mechanism the ablation can be classified in electronic, thermal, exfoliation and hydrodynamics ablation.[12]

ii) Plasma plume expansion: A plasma comprised of the energetic species is formed above the target surface and expands to the substrate that is in parallel to the target. As a function of the background gas pressure, the plume expansion can be divided into three regimes: Vacuum, transition and diffusion regimes. Since there is no background gas in the vacuum regime, the scattering of the ablated particles is negligible and the stoichiometry of the film grown in this regime is most probably close to that of the target material.[13] The increased background gas pressure found in the transition regime causes the interactions of the ablated species with the background gas to be significant, resulting in a plume splitting into fast zone and slow zone, the resulting film is deficient in heavy element.[14–17] In the diffusion regime, the highest gas pressure confines the plasma plume, the plume is more homogeneous in

elemental composition and the deposition rate is determined by the diffusion coefficient of the species in the background gas.[18]

iii) Film growth on substrate: Once the sputtered species adsorbed on the substrate surface, the adsorbed species react with each other, diffuse on the surface and then nucleate, this process directly determines the morphology and the crystallinity of the grown film. In PLD, there are three distinctive growth modes:[12,19,20] a) Volmer-Weber mode, which gives rise to the formation of clusters or islands on the surface, results in a polycrystalline film with notable roughness; b) Frank-Van der Merwe mode, which consists in a layer by layer growth, leads to an epitaxial thin film with smooth surface and c) Stranski- Krastanov mode, which is considered as a combination of the two aforementioned modes, consists in the nucleation of clusters or islands after the formation of the first monolayers, leading to the formation of polycrystalline thin films with rough surface.

In general, the following deposition factors have a direct impact on the morphology, microstructure, and crystallinity of the grown thin film:

- *Substrate temperature and nature*: On the one hand, the heating of the substrates improves the mobility of the species adsorbed on the surface, benefiting the crystallization of the thin film;[21,22] on the other hand, the substrate's characteristics heavily influence the film growth mode.[23] The significant mismatch between the lattice parameters of the substrate and the deposited film leads to a polycrystalline-characteristic film. In opposite, the good match between the thin film and the substrate results in an epitaxial film.
- *Laser frequency*: A few studies[24,25] have revealed the impact of laser frequency on the microstructure of the grown thin films, elucidating that high laser frequency increases the density of the adsorbed species with smaller sizes on the substrate surface but leads to an inhomogeneous microstructure and smaller film roughness. In contrary, low laser frequency gives rise to a homogenous microstructure of the films but reduces the smoothness of the final films.
- *Target-to-substrate distance*: The target-to-substrate distance substantially influences the kinetic energy of the arriving species on the substrate surface. Shorter target-to-distance increases the kinetic energy of the target species, resulting in a dense and thick film with strong adhesion to the substrate.[14,26] Nevertheless, the short distance may cause the rebound of adsorbed species on the surface, damaging the

quality of the final film.[14,15,27] Large target-to-distance decreases the kinetic energy of the species close to the substrate and reduces the film thickness.[28] Moreover, the longer distance is expected to increase the number of scattering events between the material species and the background gas, resulting in a more oxidized plume.[14,29,30]

- *Background gas*: $O_2$ and Ar are the most common gases used in PLD. The inert gas Ar causes elastic and kinetic interactions between the plasma plume and the background gas, whilst the reactive gas $O_2$ causes oxygen to be incorporated into films influencing the oxygen stoichiometry.[14,15,31] Several reported studies investigated the dependence of the stoichiometry of $SrTiO_3$ thin film on the oxygen pressure during the deposition and found that the oxidation of the species in the plasma plume controls the stoichiometry of the grown film.[32,33]

Therefore, selecting proper deposition parameters is critical for producing a final film with optimal characteristics. **In this thesis,** the $La_{1-x}Sr_xFeO_{3-\delta}$ (LSF) and $La_{1-x}Sr_xMnO_{3-\delta}$ (LSM) thin films were deposited by PLD with a laser fluence of 0.54 J $cm^{-1}$ (spot size: 30 $mm^2$) at laser frequency of 10 Hz in an oxygen partial pressure of $6.7 \cdot 10^{-3}$ mbar with an oxygen gas flow of 5 sccm, the target-to-substrate distance was set to 90 mm and the substrate temperature was kept at 700 ºC, with the exception of the LSF50 films in the LSF/BICUVOX/LSAT and LSF/FTO samples, which was kept at 600 ºC and 500 ºC, respectively. (**Chapter 5** and **Appendix**). $Bi_4V_{1.8}Cu_{0.2}O_{10.7}$ (BICUVOX) thin films were deposited with a laser fluence of 0.45 J $cm^{-1}$ at a laser frequency of 10 Hz under the partial oxygen pressure of 0.267 mbar, the target-to-substrate distance was set to 110 mm and the substrate temperature was kept at 600 ºC.[34]

### 2.2.2 Large-Area Pulsed Laser Deposition (LA-PLD)

The main disadvantage of PLD is that the small angular distribution of the plasma plume causes small-area film deposition (≈ 1 $cm^2$) and inhomogeneity for large-area film, restricting the technology's industrialization.[10,35] Nevertheless, the innovation of Large-Area PLD (LA-PLD) breaks this limitation and amplifies the applicable substrate size up to 6 inches.[36] LA-PLD uses a focused laser to raster the rotating target linearly with a controlled mirror, resulting in a broad angular expansion of the plasma plume that is able to uniformly cover the large-size substrate. The deposition mechanism and parameter effects are identical to those of a conventional PLD. However, to achieve homogeneity in thickness and

microstructure of the final films, the target-to-substrate distance should be increased. **Figure 2.2** shows the LA-PLD system used in this thesis for thin films deposition.


**Figure 2.2** LA-PLD machine of PLD-5000 model from PVD Products® used for thin film deposition at IREC with the major components indicated: (1) laser excimer, (2) lens and mirrors, (3) vacuum chamber, (4) load lock chamber and (5) substrate motor, respectively.

### 2.2.3 PLD targets fabrication

As well as commercial targets, home-made $La_{0.6}Sr_{0.4}FeO_{3-\delta}$ and $La_{0.5}Sr_{0.5}FeO_{3-\delta}$ (LSF40 and LSF50) targets were employed for thin films deposition in this thesis. The target materials were synthesized by conventional solid-state reaction. The dehydrated oxides reactants $La_2O_3$, $SrCO_3$ and $Fe_2O_3$ in powder were stoichiometrically mixed according to the reaction in **Equation 2.1** and milled together in an agate mortar.

$$\frac{1-x}{2}La_2O_3 + \frac{x}{2}Fe_2O_3 + xSrCO_3 \rightarrow La_{1-x}Sr_xFeO_{3\pm\delta} + CO_2 \uparrow \qquad \text{(Equation 2.1)}$$

The mixture was then heated up to 1250 ºC in air at a rate of 5 ºC $min^{-1}$ for 12 hours. Once the materials were synthesized, the powder was uniaxially die-pressed into a one-inch or two-inch pellet, followed by sintering at 1300 ºC in air for 12 h.

## 2.3 Microstructural and compositional characterization

### 2.3.1 X-Ray Diffraction (XRD)

Monochromatic X-rays are produced by the collisions of accelerated electrons with a metal anode under an electric field, the X-rays are radiated to a material and coherently scattered by the atoms of the material due to the interactions between the photons of the electromagnetic X-rays and the electrons of the atoms (**Figure 2.3**), this process is known as X-Ray Diffraction (XRD). Constructive interferences between the dispersed beams reinforce the beams intensity, giving rise to diffraction peaks.

The constructive interferences take place when the path difference equals to a multiple of the wavelength following Bragg´s law:

$$n\lambda = 2d \sin\theta \qquad \text{(Equation 2.2)}$$

Where $n$ is an integer (1, 2, 3…), $\lambda$ is the X-rays wavelength, $d$ is the distance between the diffraction planes and $\theta$ is the angle of incidence.

XRD provides microstructural and compositional information of crystalline materials, such as the crystallographic structure, phase, lattice parameters and grain size etc, because the wavelength of X-rays is of the same order of magnitude as the spacing of the atoms in the structure.

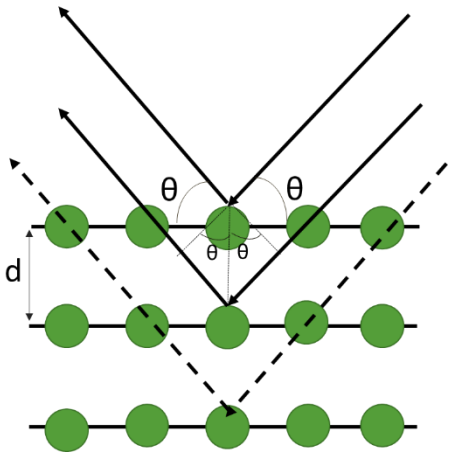


**Figure 2.3** Sketch of the Bragg's law and X-rays path in XRD

**In this thesis,** the XRD measurements were carried out for characterizing the quality of the deposited thin films in a coupled θ-2θ Bragg-Brentano configuration. A Bruker D8 Advance

diffractometer at IREC and a PANAlytical X'Pert PRO MRD diffractometer at Scientific and Technological Centers at University of Barcelona (CCiTUB) with a Cu $K_\alpha$ radiation source ($\lambda$=1.54187 Å) were employed. High-Resolution XRD (HR-XRD) measurements were performed at CCiTUB to identify the epitaxial LSF thin films in the LSF/LSM/Nb:STO samples (see **Chapter 4**) using a PANAlytical X'Pert-PRO MRD diffractometer with a Cu $K_\alpha$ radiation source and a combination of a parabolic mirror and a Germanium monochromator with two reflections. The obtained diffractograms were analyzed using X'Pert HighScore Plus software.

### 2.3.2 Scanning Electron Microscopy (SEM)

SEM is a powerful tool for characterizing morphology and topography of materials in a wide variety from powders to thin films. An electron beam composed of accelerated and energetic electrons is focused on and scanned over the surface of a material, exciting secondary electrons, back-scattered electrons, characteristic X-rays and fluorescent X-rays along the materials' profile. The excited secondary electrons are commonly used for studying the materials' morphology; Back-scattered electrons, which are more energetic and related to the atomic number of the composition than the secondary electrons, are usually employed to study the compositional distribution by visualizing the image contrast as a result of the different atomic weight.

**In this thesis,** the cross-section of the thin films fabricated by PLD (see **Chapter 3**) and the morphology of the LSF films (see **Chapter 4**) were obtained in secondary electrons mode using a Zeiss Auriga scanning electron microscope at IREC.

### 2.3.3 Energy-Dispersive X-Ray Spectroscopy (EDS)

An energetic electron beam excites electrons from the inner orbitals of an atom's electronic structure, leaving electron holes. X-rays are produced when electrons from the outer orbitals fall into the inner orbitals, filling the gaps. The emitted X-rays are characteristic of the energy difference between the two orbitals and the nature of the atoms. A microanalysis system collects and analyzes the produced X-rays, providing qualitative and quantitative information on the chemical components contained in the materials.

**In this thesis,** a Zeiss Auriga SEM-coupled energy-dispersive X-ray spectroscope at IREC was employed to reveal the cationic stoichiometry in the deposited LSF thin films.

### 2.3.4 Atomic Force Microscopy (AFM)

AFM is a technique based on the interaction between the surface and the probe that consists of a sharp tip mounted on a cantilever, governed by the scanning of the probe along the surface. It is able to visualize the tri-dimensional topography of a surface with high resolution on nanometric scale. The two main operational modes for topography measurements are:[37]

- *Contact mode*: In this mode, the tip maintains a constant touch with the surface and scans over the surface. There are two methods to measure topography: i) maintaining the force constant: the movement of the tip in the direction z is recorded to generate the topographical images while the deflection of the cantilever is kept constant. ii) Maintaining the height constant: in this case, the topography is visualized using the feedback signals from the cantilever deflection, which is detected by a laser beam reflected at the cantilever surface.
- *Tapping mode*: When a sharp tip approaches the surface and scans over it, the cantilever oscillates at the resonant frequency, the variation of the amplitude of the oscillations as a function of the interaction force between the tip and the surface is collected as feedback signals to generate the topographic images.

**In this thesis,** the topography of the polycrystalline LSF thin films was characterized in tapping mode using an atomic force microscope of XE 100 model from Park System Corp. located at IREC. The obtained AFM images were processed using XEI software. The topography images of LSF thin films are shown in **Chapter 3**.

## 2.4 Optical properties characterization

### 2.4.1 Ellipsometry

Ellipsometry is a non-destructive and contactless technique for characterizing structural (e.g. thin film thickness and dielectric constants) and optical (e.g. optical absorption coefficient) properties of a material. It is based on the measurements of the variation of the polarization state of a light beam after it is reflected from the surface of a sample. As in the sketch of ellipsometry illustrated in **Figure 2.4**., a Xenon lamp employed as light source emits a spectrum of light beams oriented in random directions, which are then linearly polarized by a rotating polarizer and obliquely incident on a sample. The linearly polarized light can be decomposed into two perpendicular *p*- and *s*- components: the propagation of the *p*-polarized light is perpendicular to the incidence plane and that of the *s*-polarized light is parallel to the incidence plane. After being reflected due to the interactions between the polarized light and the material, the linearly polarized light transforms into an elliptically polarized beam with a change in phase and amplitude of the electric field along both the *s*- and *p*- propagation directions. The elliptically polarized light subsequently passes through a modulator and an analyzer, where it is again transformed into a linearly polarized light. The detector collects the light beam and transforms it into an optical spectrum.

The *s*- and *p*- components of the complex Fresnel reflection coefficient ($r_s$ and $r_p$) of the sample can be written as:

$$r_s = \frac{E_{r,s}}{E_{i,s}} \quad , \quad r_p = \frac{E_{r,p}}{E_{i,s}} \qquad \text{(Equation 2.3)}$$

Where $E_{in,s}$ and $E_{in,p}$ are the electric field for the incident *s*- and *p*- polarized light, respectively. $E_{r,s}$ and $E_{r,p}$ are the electric field for the reflected *s*- and *p*- light, respectively.

The incidence angle is set to 70 ° which is close to the Brewster angle of the material in order to maximize the difference between $r_p$ and $r_s$.[38]

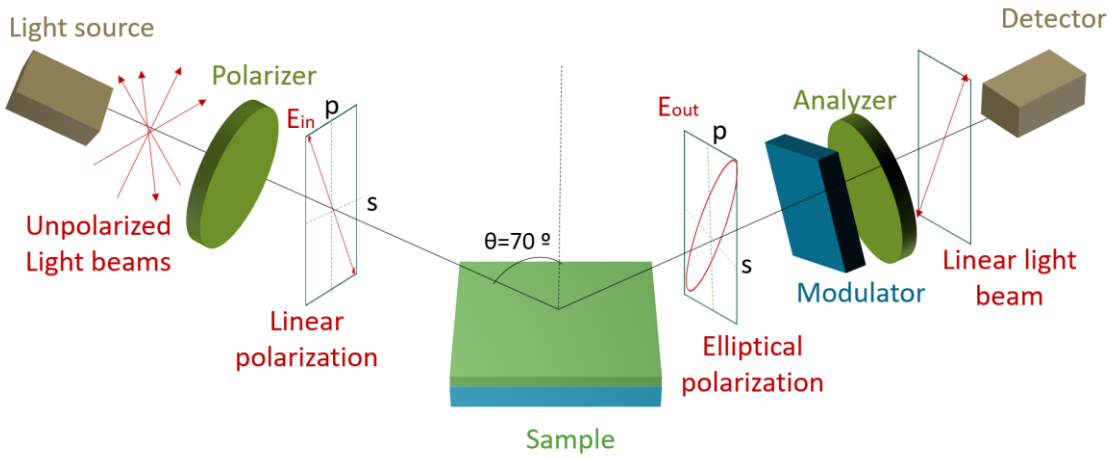


**Figure 2.4** Sketch of the components and the light path in ellipsometry experiments

Ellipsometry measures the variation of the polarization state of the light beam through the difference in phase shift (Δ) and the ratio of amplitude change (Ψ) that are shown in **Figure 2.5**. The complex reflectance ratio ($\rho$) is defined by the ratio between the $r_p$ and $r_s$ of the material and it can be calculated using the measured ellipsometric parameters Δ and Ψ as:

$$\rho = \frac{r_p}{r_s} = \tan(\Psi) \cdot e^{i\Delta} \qquad \text{(Equation 2.4)}$$

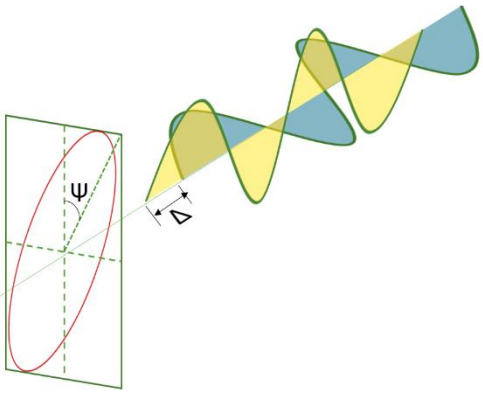


**Figure 2.5** Elliptical polarization of the light beam in s- and p- components with the ellipsometric parameters Δ and Ψ indicated.

Ellipsometry presents the main benefits of its high precision and reproducibility due to the measurements of the difference or ratio between two values, which are insensitive to fluctuations.[39] Since the reflection coefficient is strongly related to the optical properties, electronic structure and thickness of the material, the material's complex dielectric constant

($\tilde{\varepsilon}$) and complex refractive index ($\tilde{n}$) can be obtained from the measured reflection coefficient using an appropriate mathematical model. For instance, in the case of a semi-infinite material, the dielectric coefficients can be expressed as:[40]

$$\tilde{\varepsilon} = \varepsilon_1 + i\varepsilon_2 = \tilde{n}^2 = n + ik = sin^2(\theta)\left[1 + tan^2(\theta)(\frac{1-\rho}{1+\rho})^2\right] \quad \text{(Equation 2.5)}$$

Where $\varepsilon_1$ and $\varepsilon_2$ are the real part and imaginary part of the complex dielectric constant, respectively. Herein, the dielectric constant of air is assumed to be unity. *n* and *k* are denoted as the refractive index and the extinction coefficient of the material, respectively.

Therefore, the optical absorption coefficient ($\alpha$) which is related to the extinction coefficient can be expressed as:

$$\alpha = \frac{4\pi k}{\lambda} \quad \text{(Equation 2.6)}$$

Where $\lambda$ is the wavelength.

**In this thesis,** the thickness and optical properties of several thin films were measured employing an ellipsometer UVISEL from Horiba Scientific. As shown in **Figure 2.6** the ellipsometer consists of an UV Xenon lamp of 75 W that provides a broad spectral range from 0.6 eV to 5.3 eV, a linear polarizer, a modulator oriented at 0º, an analyzer oriented at 45 º, a monochromator iHR320 (Horiba) that selects the desirable wavelength, a sincerity CCD detector (Horiba) composed of photomultipliers for wavelengths in the UV-visible range and a InGaAs photodiode for wavelengths in the near infrared range. The monochromator and multiwavelength setups enable the acquisition of the elllipsometric spectra that are adapted to the needs. The monochromator allows real-time ellipsometric measurements at a single wavelength with high resolution in a broad spectra range of 0.6 eV to 5.3 eV, whereas the multiwavelength setup allows real-time measurements at various wavelengths at the same time but in a narrower spectral range of 1.5 eV to 4.9 eV. The acquired ellipsometry data were processed and analyzed in DeltaPsi 2 software.

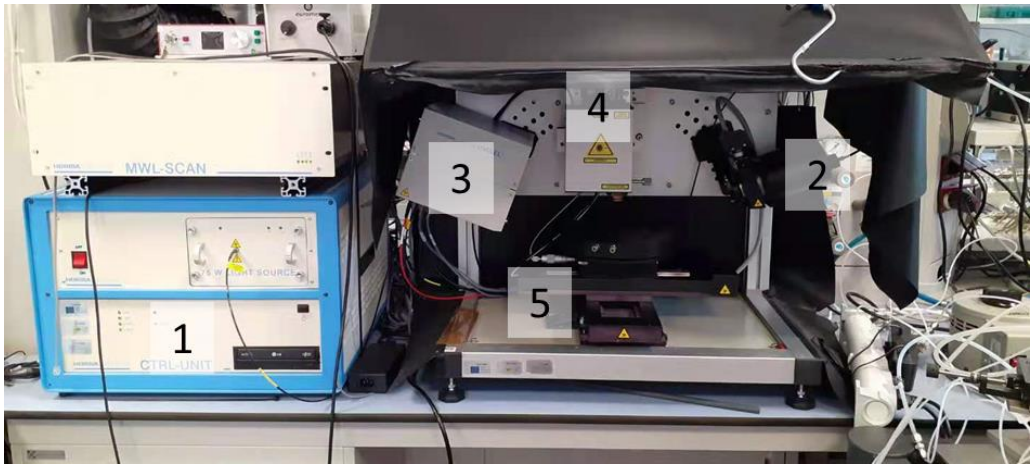


**Figure 2.6** Ellipsometer UVISEL from Horiba Scientific at IREC with the components indicated: (1) Light source, (2) linear polarizer, (3) modulator and analyzer, (4) Raman superhead and (5) sample stage.

## 2.4.2 In-situ/operando ellipsometry characterization

### 2.4.2.1 Characterization of electrochemical cells with solid-state electrolyte

An experimental setup for in-situ ellipsometry measurements, illustrated in **Figure 2.7**, includes a Linkam stage (THMS600) that enables the temperature control and electrical connections, as well as a cover made by aluminum film which allows the light beam to pass through while reducing heat dissipation. A polarized light beam enters into the stage at an angle of incidence of 70º and is focused on the sample with a spot size of 2 $mm^2$. After the interactions with the sample, the light beam is reflected and detected by the detector and the optical spectra are obtained in a photon energy range from 0.6 eV to 5.0 eV with a step of 0.05 eV using the monochromatic ellipsometry. The measurements can be performed at different temperatures ranging from 50 ºC to 600 ºC and at various applied voltages, in other words, at various equivalent oxygen pressures in a range of $10^{10}$ bar to $10^{-17}$ bar (see below).

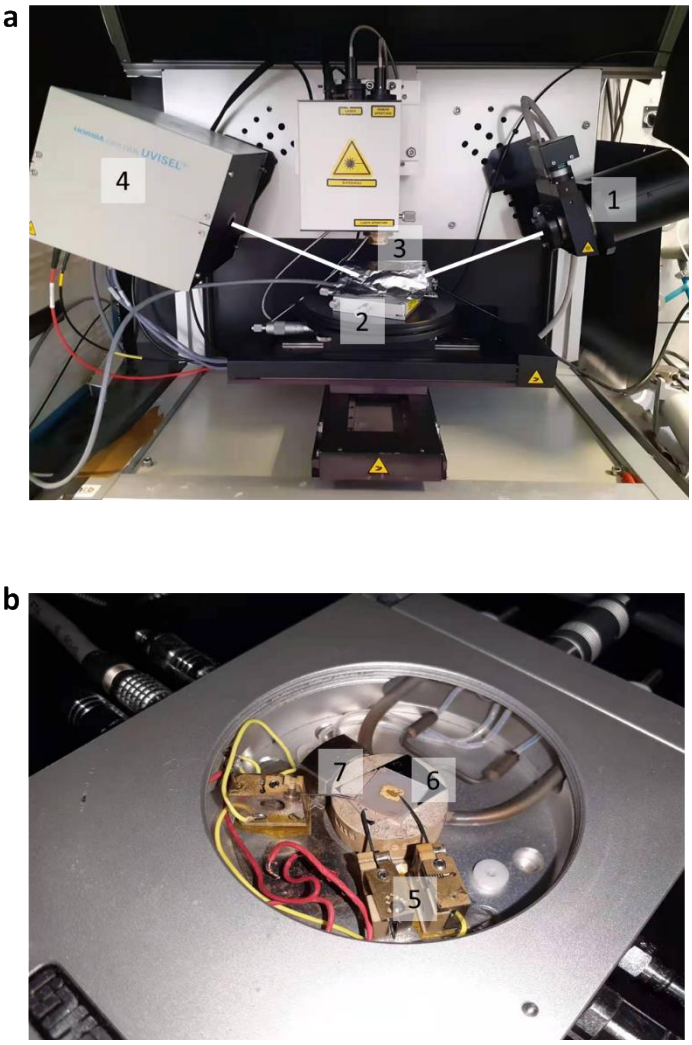


**Figure 2.7** Experimental setup at IREC for in-situ ellipsometry characterization of electrochemical cells with solid-state electrolyte under real electrochemical conditions. **a.** Global sight of the setup with the components indicated: (1) Polarizer, (2) Linkam stage, (3) Cover made by aluminum film and (4) Modulator and analyzer. **b.** Configuration of the sample with electrical connections in the setup. (5) Electrical contact probes, (6) Sample and (7) Thermal stage.

**In this thesis**, in-situ/operando ellipsometry measurements for solid-electrolyte electrochemical cells were performed on LSF/CGO/YSZ samples in air at intermediate temperatures under real electrochemical conditions. The results are presented in **Chapter 3**. As the schematic representation of the measurements shown in **Figure 2.8**, silver paste was used on the backside of the YSZ substrate as counter electrode. For increasing the current collection, gold paste was painted on the 2 mm x 3 mm sides of the LSF thin films which act as working electrode. On one corner of the YSZ electrolyte, a silver reference electrode was painted, which was used to check the potential applied across the YSZ electrolyte. DC voltage bias ($\Delta V$) was applied between the LSF layer (working electrode) and the silver

counter electrode both in anodic and cathodic modes using a potentiostat of the model of SP-150 from Biologic in order to tailor the equivalent oxygen partial pressure in the LSF thin films ($p_{O_2}^{LSF}$) according to the Nernst potential:

$$p_{O_2}^{LSF} = p_{O_2}^{RE} \cdot \exp(\frac{4e\Delta V}{k_b T}) \qquad \text{(Equation 2.7)}$$

Where $p_{O2}^{RE}$ is the oxygen partial pressure of the environment, $k_b$ is the Boltzmann constant, $e$ is the electron charge, $T$ is temperature of the sample and $\Delta V$ is the overpotential losses in the LSF thin film, which is calculated by subtracting the YSZ electrolyte and back electrode resistive contributions from the applied electrochemical bias.

Once the voltage-induced current in the LSF thin film was stabilized, the ellipsometry measurements were carried out.

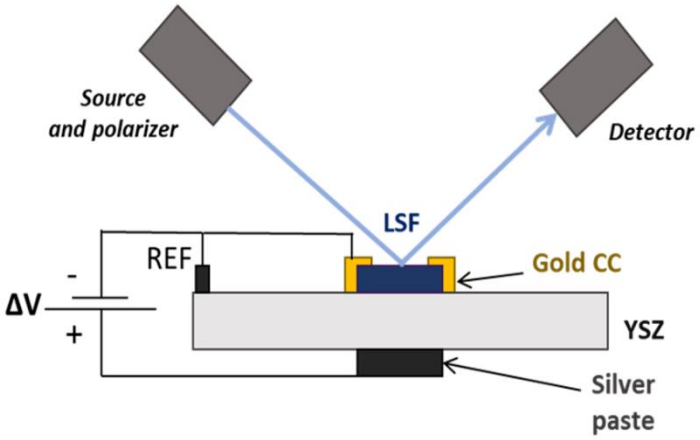


**Figure 2.8** Schematic representation of in-situ ellipsometry measurements for solid-electrolyte cells.

#### 2.4.2.2 Characterization of electrochemical cells with liquid electrolyte

As shown in **Figure 2.9**, a home-made chamber fabricated by 3D printing using a Prusa i3 style 3D printer and Acrilonitril Butadiene Styrene was employed for the characterization of liquid-electrolyte electrochemical cells. The chamber is equipped with two transparent optical windows which are perpendicularly tilted to the incident light beam in order to ensure full optical transmission of the light beam. Besides, the chamber architecture is adapted to the introduction of the reference electrode. In-situ/operando measurements can be carried out in this setup using a three-electrode configuration, in which a counter electrode (activated

carbon), a reference electrode (silver wire) and a liquid electrolyte are introduced into the chamber.

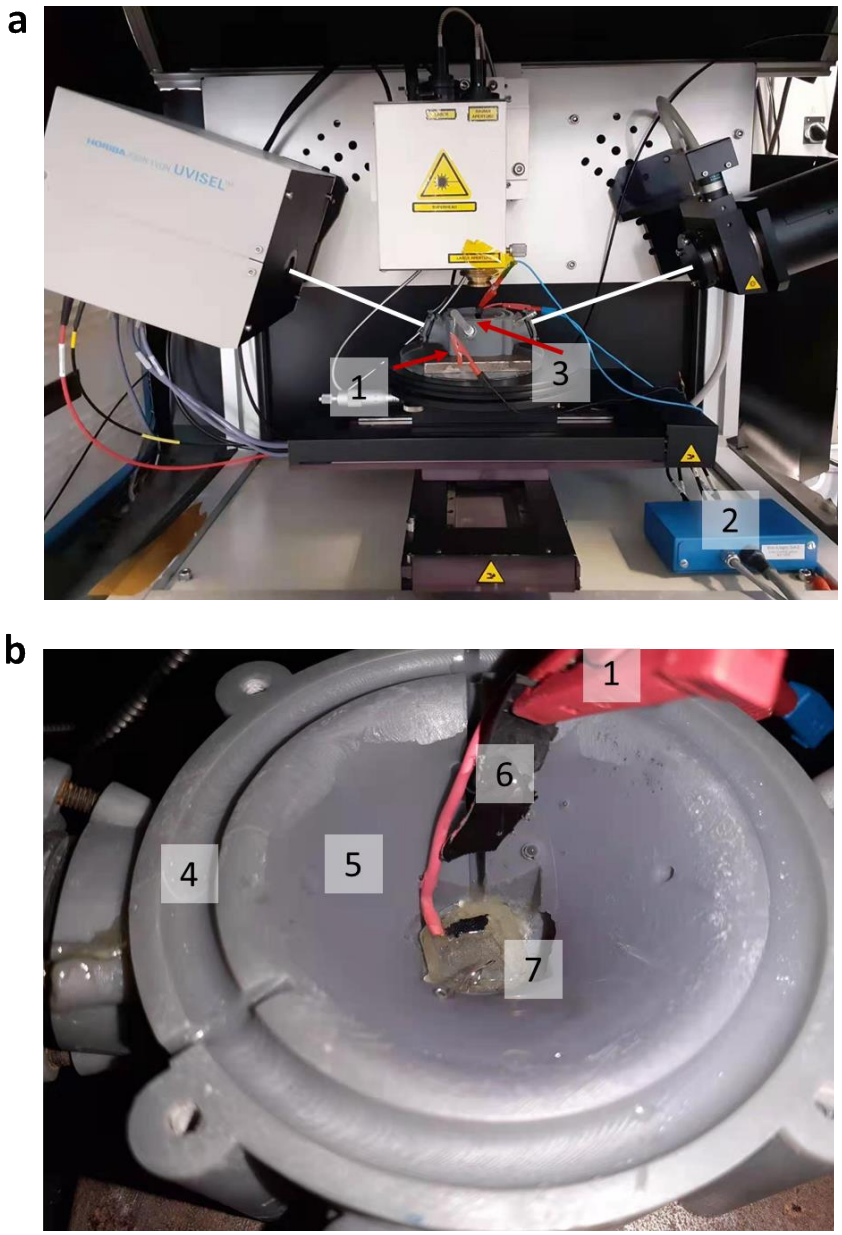


**Figure 2.9** Experimental setup for in-situ ellipsometry characterization of electrochemical cells with liquid electrolyte. **a.** Global picture of the setup with the elements indicated: (1) Electrical connections, (2) Terminal of the potentiostat and (3) Reference electrode **b.** Electrical configuration of the sample inside the chamber with the components indicated (4) Home-made chamber, (5) 0.1 M KOH electrolyte, (6) Counter electrode and (7) Sample.

**In this thesis,** this in-situ ellipsometry setup was employed for tracking the optical properties of thin film electrodes during the ions intercalation reaction in an alkaline electrolyte (0.1 M KOH solution). For the measurements in liquid electrolyte, the electrical contact of the LSF

and LSM thin films (working electrodes) was extended using a copper wire attached to the sample surface. In order to avoid undesirable reactions, the samples were encapsulated using a robust epoxy resin while an active area of the material of interest was left to be exposed to the electrolyte and to the light beam focus of the ellipsometer. LSF50 film was polarized with a DC voltage bias, and the ellipsometry measurements were taken in static mode (see **Chapter 4**) and in kinetic mode (see **Appendix**) to detect the change in the optical properties with the oxidation state of the material.

In the static ellipsometry measurements, the polarization potentials ranging from 0.5 V to -0.4 V were applied to the LSF thin films using chronoamperometry (see **Section 2.5.4**) and the optical spectra were acquired in a photon energy range of 1.5 eV to 4.85 eV with a step of 0.05 eV at each applied potential, the results are discussed in **Chapter 4**. For the real-time ellipsometry characterization, an AC potential with amplitude of 0.05 V was applied to the LSF thin film using Large Amplitude Sinusoidal Voltammetry (LASV) (see **Section 2.5.5**), the ellipsometry was devoted to track the change in optical properties of the sample over time. Ellipsometry spectra were collected at different frequencies using the multi-wavelength ellipsometry in a photon energy range of 1.5 eV to 4.9 eV and the results are shown in **Appendix**.

### 2.4.3 Ellipsometry data analysis

Collected ellipsometry raw data were modeled and fitted in DeltaPsi2 Software (Horiba) using an appropriate physical and mathematical model to extract the optical and structural properties of thin films. Due to the finite thickness of the thin films, **Equation 2.5** cannot be applied and a mathematical model that takes into account the thickness of the layers needs to be considered. Herein, the LSF40/CGO/YSZ sample measured at 400 ºC in air atmosphere, is being taken as an example to demonstrate the methodologies for ellipsometric data analysis. The ellipsometry raw data $\Delta$ and $\Psi$ shown in **Figure 2.10a** were modeled using a four-layer model as illustrated in the inset of **Figure 2.10a**: from the bottom to the top, the bottom layer represents the substrate, the second layer represents the interlayer, the third one is the film of interest and the top layer is composed by 50% vol. of the LSF thin film and 50% vol. of Void (in case of LSF films in liquid media, this layer is composed by 50% vol. of the LSF thin film and 50% vol. of the liquid media), considered to be roughness of the sample (typically<4 nm).

After that, the raw data were fitted employing a series of Lorentzian oscillators,[41] of which the dielectric constant can be written as:[42]

$$\varepsilon = \varepsilon_0 + \sum_{j=1}^{n} \frac{f_j \omega_{0,j}^2}{\omega_{0,j}^2 - \omega^2 + i\gamma_{j\omega}} \qquad \text{(Equation 2.8)}$$

Where $\varepsilon_0$ denotes the high frequency dielectric constant, $\omega$ denotes the angular frequency of the light beam, $\omega_{0,j}, f_j$ and $\gamma_j$ are the resonance frequency, intensity and broadness of the corresponding oscillator, respectively.

To extract the optical properties of LSF from the raw data, the previously fitted optical spectra of the interlayer and the substrate were employed. In addition, the roughness and thickness of LSF thin films are kept free. The ellipsometry data fitting gives sensitivity to all of the parameters, both those of the oscillators and the films thickness. Thereby, the sensitivity of the parameters of the corresponding oscillator, which was provided by the DeltaPsi2 program during the data fitting procedure, was used to determine the optical parameter errors. The optical conductivity of the thin films can be computed from the extracted parameters as follows:

$$\sigma_{optical} = \frac{4\pi nk}{\lambda Z} \qquad \text{(Equation 2.9)}$$

Where $n$ is the refractive index, $k$ is the extinction coefficient, $\lambda$ is the wavelength and $Z$ is a physical constant referring to the impedance of free space.

A high-quality fitting of ellipsometry data of the exemplified LSF sample with a negligible error $\chi^2$=0.04 is shown in **Figure 2.10a**, the extracted optical conductivity of the LSF thin film as well as the Lorentzian oscillators used for the modelling are plotted in **Figure 2.10b.** In general, the model and the method used for the data fitting are suitable for the LSF films studied in this thesis.

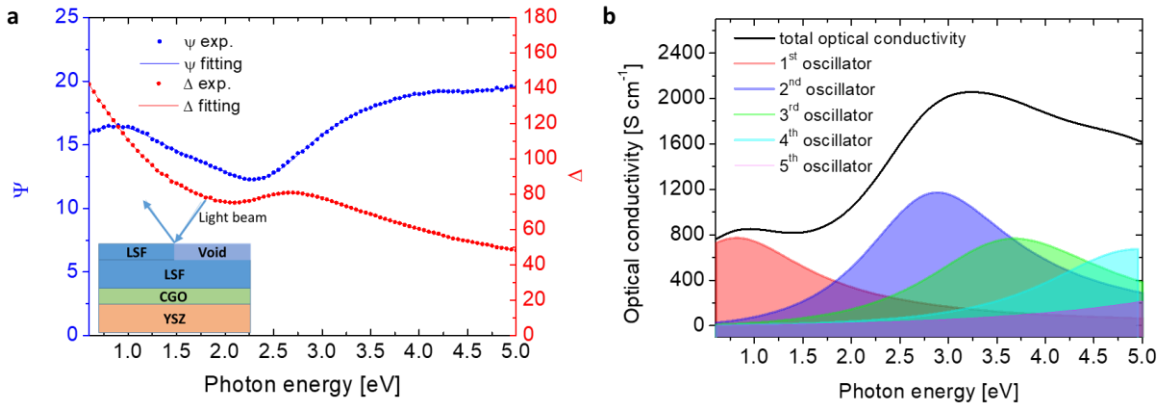


**Figure 2.10 a.** Modelling and fitting (solid lines) of ellipsometry raw data Δ and $\Psi$ (symbols) for the exemplified LSF40/CGO/YSZ sample measured at 400 ºC in air atmosphere, the inset illustrates the model employed in the procedure. **b.** Extracted optical conductivity for the LSF thin film and deconvolution of the Lorentzian oscillators used for the data fitting.

## 2.5 Electrical and electrochemical measurements

### 2.5.1 Two-probe method

The two-probe approach consists in applying a voltage bias (or electric current) between two points of the material and measuring the induced electric current intensity (or voltage) between these two points as illustrated in **Figure 2.11**. The electrical conductivity ($\sigma$) can be expressed as inverse of the resistivity ($\rho$) according to the equation:

$$\sigma = \rho^{-1} = \frac{d}{RLt_f} \qquad \text{(Equation 2.10)}$$

Where $R$ denotes the resistance of the material; $d$ denotes the distance between the two electrodes; $L$ denotes length of the electrodes and $t_f$ denotes the film thickness. The two-probe method is preferred here since it is better suited for measuring electrical properties of materials with high resistivity than a conventional four-probe method (due to some factors, such as surface leakage, which can cause relevant inaccuracies).[43]

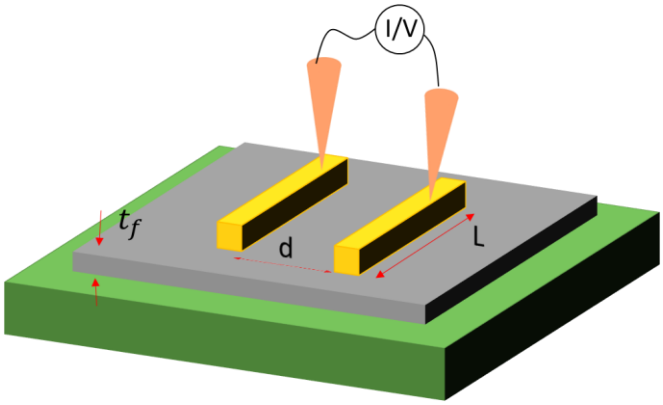


**Figure 2.11** Schematic representation of the two-probe method for the electrical characterization of layers.

**In this thesis,** electrical properties of the LSF50 thin film channel in LSF50/BICUVOX synaptic transistors were measured in air using the two-probe approach with a sourcemeter (Kethley 2400) (**Figure 2.12a**). The temperature of the sample was controlled between room temperature and 300 ºC by a Linkam stage (TMS600) as shown in **Figure 2.12b**. The resulting electrical properties are discussed in **Chapter 5**.

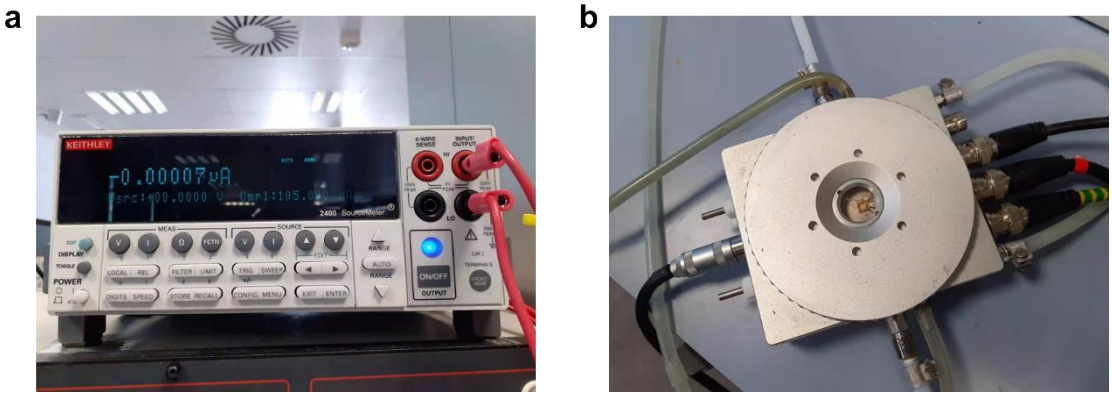


**Figure 2.12** Equipment used for the electrical characterization of layers **a.** Sourcemeter (Kethley 2400) **b.** Linkam stage (TMS600) with controlled temperature, atmosphere and two- and four-probe electrical access.

### 2.5.2 Electrochemical Impedance Spectroscopy (EIS)

EIS is a powerful technique for determining the complex electrical impedance of the components in an electrochemical cell across a wide frequency range. Its high sensitivity to phenomena taking place at the surface and interface allows measurements of electrochemical features as well as redox reactions occurring in the electrode in the electrochemical cell. EIS as a sensitive and non-destructive electrochemical technique has been widely used to investigate the corrosion of coatings,[44] degradation of membranes,[45] and performance of SOFCs.[46]

EIS technique extends the Ohm's law to AC current for frequency-dependent resistors, for which a sinusoidal-form potential $V$ with small amplitude $V_0$ and angular frequency $\omega$ gives rise to an AC current response in sinusoidal shape at the same frequency with amplitude $I_0$ and a phase shift $\varphi$ respect to the input potential.

The input potential ($V(t)$) can be expressed as a function of time as:

$$V(t) = V_0 \sin(\omega t) \qquad \text{(Equation 2.11)}$$

Where $\omega$ is defined by the frequency in Hertz ($f$) as: $\omega = 2\pi f$

The induced current ($I(t)$) can be written as:

$$I(t) = I_0 \sin(\omega t + \varphi) \qquad \text{(Equation 2.12)}$$

Analogous to the Ohm's law, the complex impedance ($Z$) is calculated as:

$$Z(\omega) = \frac{V}{I} = \frac{V_0 \sin(\omega t)}{I_0 \sin(\omega t + \varphi)} = Z_0 \frac{\sin(\omega t)}{\sin(\omega t + \varphi)} \qquad \text{(Equation 2.13)}$$

The expression of impedance can be related to Euler's formula and rewritten in a complex number as:

$$Z(\omega) = Z_0 \exp(-i\varphi) = Z_0 \cos\varphi - iZ_0 \sin\varphi = Z'(\omega) - iZ''(\omega) \qquad \text{Equation (2.14)}$$

Where *Z'* and *Z''* represent the real and imaginary parts of the complex impedance, respectively.

The impedance data are commonly plotted in a Nyquist plot in accordance with **Equation 2.14**, in which the real part (*Z'*) is plotted along the abscissa axis and the imaginary part in negative values (*–Z''*) is plotted along the ordinate axis. The Nyquist plot of a typical Randles circuit is exemplified in **Figure 2.13**. The Randles circuit is composed by a resistance of electrolyte ($R_s$), a Faradaic polarization resistance *($R_p$)* and a double-layer capacitance ($C_{dl}$). The $R_s$ is found to be in series with the parallel connection of $R_p$ and $C_{dl}$. The Nyquist plot is characterized in a semicircle-shape arc, the electric parameters of the circuit components can be derived by fitting with the appropriate model. In this example, the value of $R_s$ is given by the intercept of the arc with the abscissa axis at high frequency, as well as the sum of $R_s$ and $R_p$ is given by the intercept at lower frequency. Each point on the arc represents the impedance at the corresponding frequency, the imaginary part of impedance achieves the maximum value at the center of the semicircular arc following the relationship:

$$\omega_M = \frac{1}{R_p C_{dl}} = \frac{2\pi}{\tau_M} \qquad \text{(Equation 2.15)}$$

Where $\omega_M$ denotes the frequency at which the –Z'' has the maximum absolute value and $\tau_M$ represents the characteristic time for the electrochemical reaction.

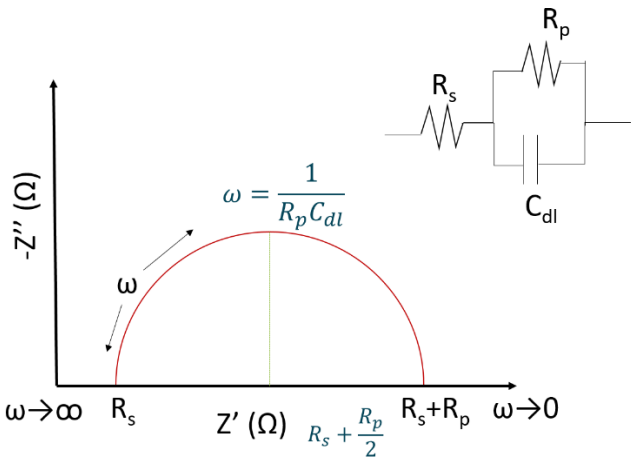


**Figure 2.13** Nyquist plot of a representative Randles circuit. The inset shows the equivalent circuit of the Randles circuit.

**In this thesis,** EIS spectra were recorded in the frequency range of 1 MHz to 0.1Hz with an amplitude of 0.05 V. EIS and equivalent circuit modelling were employed for LSF/CGO/YSZ samples in order to subtract the chemical capacitive contribution of the YSZ electrolyte and determine the chemical potential for the LSF thin films, the resulting EIS spectra are presented in **Chapter 3**. The measurements were conducted with a three-electrode configuration using Staircase Potentio-Electrochemical Impedance Spectroscopy (SPEIS) and Potentio-Electrochemical Impedance Spectroscopy (PEIS) provided by a SP-150 Biologic potentiostat (**Figure 2.14a**). Furthermore, EIS was employed for characterizing the ionic conductivity of the BICUVOX thin film electrolyte in the synaptic transistors at various temperatures using the two-probe method described in **Section 2.5.1** with a Linkam stage (**Figure 2.12b**) to control the temperature and an impedance analyzer (**Figure 2.14b**) to record the EIS spectra. The results are detailed in **Chapter 5.**

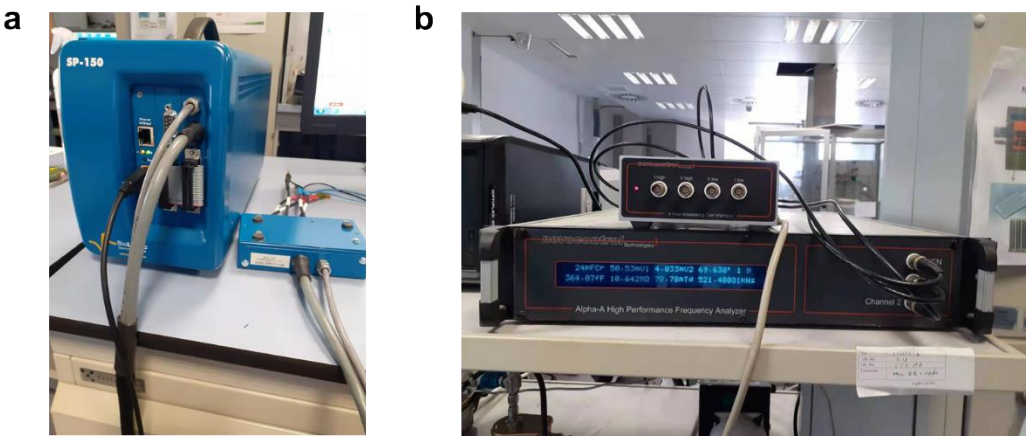


**Figure 2.14 a.** Potentiostat SP-150 from Biologic. **b.** Alpha-A Novocontrol impedance analyzer with ZG4 electrochemical interface located at IREC

### 2.5.3 Cyclic Voltammetry (CV)

CV is a versatile and sensitive electrochemical technique that is widely used for evaluating the redox reactions occurred in the materials of interest for fuel cells,[47] Lithium ions batteries,[48] and other applications.[49] It is based on the electrical current measurements that sweep the potential in both forward and backward directions over a range of values. The redox reaction is an electron transfer process that can be written as:

$$M^{n+} + ne^- \leftrightarrow M \qquad \text{(Equation 2.16)}$$

The concentration of the reduced species ($[M]$) and the oxidized species ($[M^{n+}]$) on the electrode surface is controlled by the electrochemical potential ($E$) agreeing with the Nernst equation:

$$E = E_0 + \frac{RT}{nF} ln \frac{[M]}{[M^{n+}]} \qquad \text{(Equation 2.17)}$$

Where $E_0$ denotes the standard potential of the species, $R$ denotes the gas constant which equals to 8.314 J $K^{-1}$ $mol^{-1}$, $n$ denotes the number of transferred electrons in mol and $F$ denotes the Faraday constant.

A representative cyclic voltammogram is shown in **Figure 2.15**, the potential sweeps from a positive starting potential $E_1$ towards a negative switching potential $E_2$ giving rise to a reduction reaction $M^{n+} + ne^- \rightarrow M$ at the electrode and resulting in a cathodic peak at the potential $E_{p,c}$ with the peak current $I_{p,c}$. Once reached the switching potential $E_2$, the potential sweeps backward to the positive potential $E_1$, leading to an oxidation reaction $M + ne^- \rightarrow$

$M^{n+}$ at the surface of the electrode, an anodic peak at the potential $E_{p,a}$ with the current $I_{p,a}$ arises. The separation between the cathodic and anodic peaks ($\Delta E_p$) is associated with the diffusion of the species.[50]

At the potential $E_{p,a}$ (or $E_{p,c}$), the Nernst potential gives rise to a gradient of species concentration between the bulk electrode and the surface. Beyond the potential $E_{p,a}$ (or $E_{p,c}$), the decrease of current with potential is governed by the diffusion of the species from the surface (or the bulk) to the bulk (or the surface) following the Fick's law, the peak current ($I_p$) for the electrochemically reversible reactions is given by the Randles-Sevcik equation as:

$$I_p = \pm 2.69 * 10^5 n^{3/2} A C D^{1/2} v^{1/2} \qquad \text{(Equation 2.18)}$$

Where $A$ is the active area exposed to the electrolyte in $cm^2$, $C$ is the bulk concentration of the species in mol $cm^{-3}$, $D$ is the species' diffusion coefficient in $cm^2\ s^{-1}$ and $v$ is the scan rate in mV $s^{-1}$.

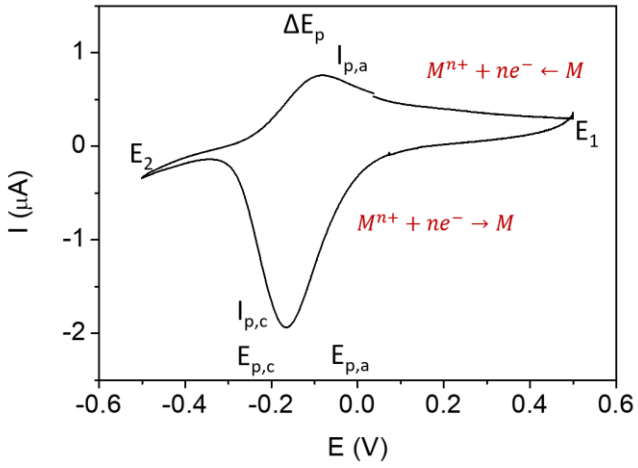


**Figure 2.15** A representative cyclic voltammogram

**In this thesis,** CV was employed to identify redox reactions taking place in LSF50 thin films given by the ions intercalation in the alkaline electrolyte. The CV measurements were performed in a range of potential from 0.5 V to -0.5 V vs Ag/AgCl at a scan rate of 0.5 m $V^{-1}$ using the setup shown in **Figure 2.9b** and the SP-150 Biologic potentiostat shown in **Figure 2.14a**. The resulting voltammograms are illustrated in **Chapter 4**.

### 2.5.4 Chronoamperometry (CA)

CA is a well-known electrochemical technique that involves applying a DC voltage to the electrode and monitoring the evolution of the current over time (see **Figure 2.16**). Several functional parameters of the material of interest, such as diffusion coefficient, capacity, amount of the transferred electrons, active area and so on can be extracted from the current. The area under the I-t curve represents the transferred charge ($Q$) induced by the potential which can be calculated through an integral formula:

$$Q = \int_{t_1}^{t_2} I(t)d(t) \qquad \text{(Equation 2.19)}$$

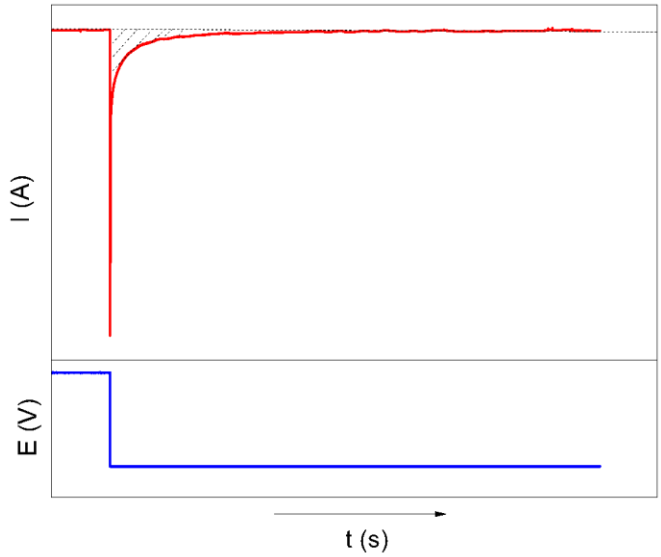


**Figure 2.16** Single-step potential waveform (blue) and current response waveform (red) for CA, the shadow represents the area integrated under the current curve.

**In this thesis**, CA technique provided by the potentiostat SP-150 from Biologic (**Figure 2.14a**) was employed for applying potentials to LSF working electrodes for varying the oxidation state of LSF thin films according to the Nernst equation. This method was used in the in-situ and ex-situ ellipsometry measurements for LSF thin films detailed in **Chapter 3** and **Chapter 4**.

### 2.5.5 Large Amplitude Sinusoidal Voltammetry (LASV)

LASV entails applying a sinusoidal AC potential ($V$) with the amplitude ($V_0$) and the frequency ($f$) (**Equation 2.11**) to the electrode and monitoring the current response, which is governed by the reversible charge transfer process (**Equation 2.16**) on the electrode surface.

**In this thesis,** LASV was used in the in-situ ellipsometry measurements for evaluating the real-time ellipsometry response of LSF thin films to the input sinusoidal potential at various frequencies. The potential was applied to LSF40/CGO/YSZ samples with an amplitude of 0.05 V and frequencies ranging from 0.01 Hz to 1 Hz using the SP-150 potentiostat from Biologic (**Figure 2.14a**). Obtained results are discussed in **Appendix**.

## 2.6 Time-of-Flight Secondary Ion Mass Spectrometry (ToF-SIMS)

ToF-SIMS is an analytical technique that aims at investigating composition for thin films or for surface of bulk materials. In comparison with conventional SIMS, ToF-SIMS is highlighted by the very broad detectable mass range, the high sensitivity and the excellent mass and spatial resolution.[51] The principle is based on a short-time primary ion beam that bombards the surface of the sample, the ion beam is typically composed by energetic ions such as $He^+$, $Xe^+$, $Ar^+$, $Ne^+$, $Ga^+$ or $Cs^+$ . The primary ion beam has a higher energy than the bond energy of the ions on surface, which causes secondary ions (atoms, molecules, ions, or molecular fragments) to sputter away from the surface. The time of flight ($t$) of the sputtered secondary ions from the surface to the detector is proportional to its mass ($m$) as:

$$t = L\sqrt{\frac{m}{2zE_k}} \qquad \text{(Equation 2.20)}$$

Where $L$ is the travel length of the ions, $z$ is the charge and $E_k$ is the kinetic energy of the sputtered secondary ions.

As a consequence, the ions are distinguished by their specific mass and the generated mass spectra can be used to determine the composition of the sample.

**In this thesis,** ToF-SIMS was used for determining the nature of ions involved in LSF50 thin films during ion intercalation in alkaline electrolyte. The ToF-SIMS measurements were performed using an ION-ToF instrument located at Imperial College London in United Kingdom. The results are presented in **Chapter 4**.

## 2.7 Positron-Annihilation Lifetime Spectroscopy (PALS)

PALS is based on the annihilation of positrons accompanied by analysis of the subsequent emission of gamma rays. PALS is well known as a non-destructive characterization technique for qualification and quantification of open-volume and negatively charged defects in materials.[52–54] Positrons from a radioactive beam penetrate into a material, thermalize and interact with the surrounding electrons forming a "positronium". The positronium can be found in two states: para-positronium (*p-ps*) and ortho-positronium (*o-ps*) with anti-parallel and parallel spins of positrons and electrons, respectively. Positrons lifetime is defined as the duration time from the emission of positrons to the detection of the gamma rays, the *p-ps* and *o-ps* are characterized by the lifetime of 125 ps and 142 ns, respectively.[55] The parameters of the *o-ps* are of interest to characterize the defects as the intensity and lifetime of *o-ps* directly provides information of the size and amount of the open-volume defects.[55,56] As the lifetime of positrons is sensitive to the interaction of positrons with electrons in the lattice, PALS can be used to detect and quantify negatively charged defects in solids.[57] In Variable Energy Positron Annihilation Lifetime Spectroscopy (VEPALS), positrons are implanted with variable beam energies, which allows to control the penetration depth of positrons and is useful for studying thin films.[58]

**In this thesis,** VEPALS measurements were performed on four post-treated LSF50/LSM/Nb:STO samples in order to determine the nature of defects in the LSF50 thin films . Two of the samples were respectively annealed in 100% dry $O_2$ atmosphere and 100% dry $N_2$ atmosphere, the another two samples were fully oxidized and reduced in 0.1 M KOH solution by CA, respectively. The VEPALS measurements were conducted at Mono-energetic Positron Source (MePS) beamline. The measurements were carried out in collaboration with the Helmholtz-Zentrum Dresden-Rossendorf (HZDR) in Germany and were conducted by Dr. Maciej Oskar Liedke. PALS results are shown in **Chapter 4**.

## 2.8 Finite Element Modelling (FEM)

FEM is a mathematical method for solving complex systems through the discretization of the complex domain into numerous smaller parts called "elements" that are interconnected by nodes or boundaries. The original solution of the phenomena taking place in the complex system under study is usually based on Partial Differential Equations (PDEs) which cannot be solved using analytical methods. However, PDEs can be numerically solved by discretizing them into finite elements, which can be a series of algebraic equations or ordinary differential equations.[59] The solutions of the original system are obtained by the reassembling of the finite element solutions through a spatial transformation.[60]

**In this thesis**, FEM was used to determine the distribution of equipotential regions in thin film electrodes such as LSF layers deposited on YSZ (100) substrates. These systems were modelled using COMSOL Multiphysics Modelling software. The geometry of the model, as shown in **Figure 2.17a**, consists of an electrolyte YSZ layer and an electrode LSF thin film on top. It is possible to distinguish two type of currents: i) the electronic current ($i_e$) along the film length and ii) the ionic current ($i_i$), flowing from the YSZ electrolyte, perpendicular to the LSF film. The electronic current in the LSF thin film was simulated with the electrical current, which assumes negligible ohmic losses perpendicular to the layer (dependent variable: electronic potential $\Delta\Phi_e$). A fixed potential was applied on the borders of the electrodes, simulating the negligible ohmic resistance of the gold current collector (**Figure 2.17b** and **c**). The ionic current in the YSZ electrolyte was simulated by the electric current module (dependent variable: ionic potential $\Delta\Phi_i$). The two modules were connected by imposing the same normal current density entering/exiting the electrode surface $i_{orr} = (\Delta\Phi_e - \Delta\Phi_i)/\tilde{R}_{pol}$, where $\tilde{R}_{pol}$ is the polarization resistance of the LSF electrode. In the model, LSF was considered surface limited (infinite oxygen diffusion in the thin film) and the ionic conductivity of YSZ was fixed at $10^{-4}$ S cm$^{-1}$.

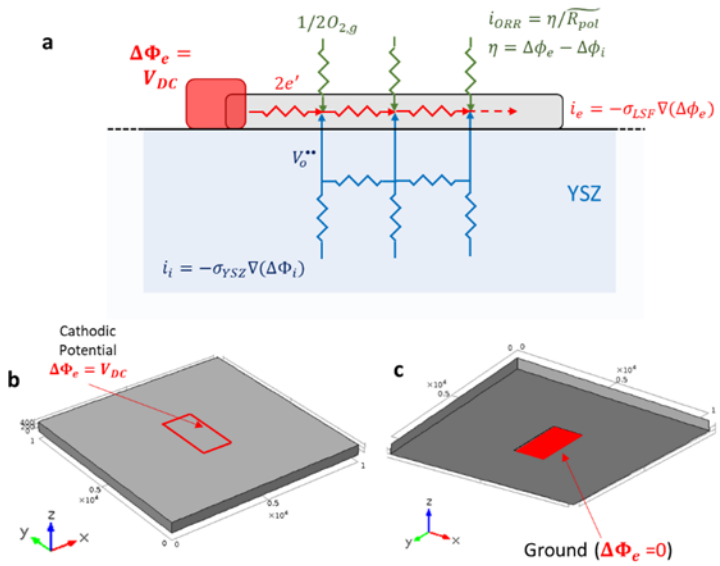


**Figure 2.17 a.** Schematic representation of the geometry of the model for FEM. Boundary conditions for **b.** LSF electrode and **c.** back-side silver counter electrode

# References


1. Zhao, J. L., Li, X. M., Bian, J. M., Yu, W. D. & Gao, X. D. Structural, optical and electrical properties of ZnO films grown by pulsed laser deposition (PLD). *J. Cryst. Growth* **276**, 507–512 (2005).

2. Salim, E. T., Al-Douri, Y., Al Wazny, M. S. & Fakhri, M. A. Optical properties of Cauliflower-like $Bi_2O_3$ nanostructures by reactive pulsed laser deposition (PLD) technique. *Sol. Energy* **107**, 523–529 (2014).

3. Suresh, A., Gollakota, P., Wellenius, P., Dhawan, A. & Muth, J. F. Transparent, high mobility InGaZnO thin films deposited by PLD. *Thin Solid Films* **516**, 1326–1329 (2008).

4. Villanueva, Y. Y., Liu, D. R. & Cheng, P. T. Pulsed laser deposition of zinc oxide. *Thin Solid Films* **501**, 366–369 (2006).

5. Bleu, Y. *et al.* Review of graphene growth from a solid carbon source by pulsed laser deposition (PLD). *Front. Chem.* **6**, 572 (2018).

6. Gutwirth, J., Wágner, T., Němec, P., Kasap, S. O. & Frumar, M. Thermal and optical properties of $AgSbS_2$ thin films prepared by pulsed laser deposition (PLD). *J. Non. Cryst. Solids* **354**, 497–502 (2008).

7. Dohmen, R., Becker, H.-W., Meißner, E., Etzel, T. & Chakraborty, S. Production of silicate thin films using pulsed laser deposition (PLD) and applications to studies in mineral kinetics. *Eur. J. Mineral.* **14**, 1155–1168 (2002).

8. Krebs, H.-U. *et al.* Pulsed Laser Deposition (PLD) -- A Versatile Thin Film Technique. in *Advances in Solid State Physics* (ed. Kramer, B.) 505–518 (Springer Berlin Heidelberg, 2003). doi:10.1007/978-3-540-44838-9_36.

9. Ogugua, S. N., Ntwaeaborwa, O. M. & Swart, H. C. Latest development on pulsed laser deposited thin films for advanced luminescence applications. *Coatings* **10**,1078 (2020).

10. Bao, Q., Chen, C., Wang, D., Ji, Q. & Lei, T. Pulsed laser deposition and its current research status in preparing hydroxyapatite thin films. *Appl. Surf. Sci.* **252**, 1538–1544 (2005).

11. Mihailescu, I. N. & György, E. Pulsed Laser Deposition: An Overview. in *International Trends in Optics and Photonics* (ed. Asakura, T.) 201–214 (Springer, Berlin, Heidelberg, 1999). doi:10.1007/978-3-540-48886-6_13.

12. Krebs, H. U. Pulsed Laser Deposition of Metals. in *Pulsed Laser Deposition of Thin Films: Applications-Led Growth of Functional Materials* (ed. Eason, R.) 363–382 (Wiley-Interscience, 2006). doi:10.1002/9780470052129.ch16.

13. Amoruso, S. Plume characterization in pulsed laser deposition of metal oxide thin films. in *Metal Oxide-Based Thin Film Structures* (eds. Pryds, N. & Esposito, V.) 133–160 (Elsevier, 2018). doi:10.1016/B978-0-12-811166-6.00006-6.

14. Ojeda-G-P, A., Döbeli, M. & Lippert, T. Influence of Plume Properties on Thin Film Composition in Pulsed Laser Deposition. *Adv. Mater. Interfaces* **5**, 1701062 (2018).

15. Indrizzi, L., Ohannessian, N., Pergolesi, D., Lippert, T. & Gilardi, E. Pulsed Laser Deposition as a Tool for the Development of All Solid-State Microbatteries. *Helv. Chim. Acta* **104**, e2000203 (2021).

16. Gonzalo, J., Gómez San Román, R., Perrière, J., Afonso, C. N. & Pérez Casero, R. Pressure effects during pulsed-laser deposition of barium titanate thin films. *Appl. Phys. A Mater. Sci. Process.* **66**, 487–491 (1998).

17. Ojeda-G-P, A., Schneider, C. W., Döbeli, M., Lippert, T. & Wokaun, A. The importance of pressure and mass ratios when depositing multi-element oxide thin films by pulsed laser deposition. *Appl. Surf. Sci.* **389**, 126–134 (2016).

18. Pereira, A. *et al.* Pulsed laser deposition and characterization of textured Pd-doped-$SnO_2$ thin films for gas sensing applications. *Thin Solid Films* **497**, 142–148 (2006).

19. Ashfold, M. N. R., Claeyssens, F., Fuge, G. M. & Henley, S. J. Pulsed laser ablation and deposition of thin films. *Chem. Soc. Rev* **33**, 23–31 (2004).

20. Fornari, C. I., Fornari, G., Rappl, P. H. de O., Abramof, E. & Travelho, J. dos S. Monte Carlo Simulation of Epitaxial Growth. in *Epitaxy* 113–129 (2018). doi:10.5772/intechopen.70220.

21. Yahya, K. z., Haider, A. J., Tarek, H. S. & Al-Haddad, R. M. Effect of Substrate Temperature on Nanostructure Titanium Dioxide Thin Films Prepared by PLD. *Eng.*

*&Tech.Journal* **32**, 434–443 (2014).

22. De Moure-Flores, F. *et al.* CdTe thin films grown by pulsed laser deposition using powder as target: Effect of substrate temperature. *J. Cryst. Growth* **386**, 27–31 (2014).

23. Mukherjee, D. *et al.* Challenges in the stoichiometric growth of polycrystalline and epitaxial $PbZr_{0.52}Ti_{0.48}O_3/La_{0.7}Sr_{0.3}MnO_3$ multiferroic heterostructures using pulsed laser deposition. *J. Appl. Phys.* **112**, 064101 (2012).

24. Plonczak, P. *et al.* Tailoring of $La_xSr_{1-x}Co_yFe_{1-y}O_{3-\delta}$ nanostructure by pulsed laser deposition. *Adv. Funct. Mater.* **21**, 2764–2775 (2011).

25. Guan, L., Zhang, D. M., Li, X. & Li, Z. H. Role of pulse repetition rate in film growth of pulsed laser deposition. *Nucl. Instruments Methods Phys. Res. Sect. B Beam Interact. with Mater. Atoms* **266**, 57–62 (2008).

26. Mostako;, A. T. T. & Khare, A. Effect of target–substrate distance onto the nanostructured rhodium thin films via PLD technique. *Appl. Nanosci.* **2**, 189–193 (2012).

27. Kim, H. S. & Kwok, H. S. Correlation between target-substrate distance and oxygen pressure in pulsed laser deposition of $YBa_2Cu_3O_7$. *Appl. Phys. Lett.* **61**, 2234–2236 (1992).

28. Paek, J. Y., Chang, I., Lee, M. H., Ji, S. & Cha, S. W. Influence of target to substrate distance on properties of Y-doped $BaZrO_3$Thin films grown by pulsed laser deposition. *Int. J. Precis. Eng. Manuf.* **14**, 839–843 (2013).

29. Budai, J. *et al.* Reactive pulsed laser deposition of hydrogenated carbon thin films: The effect of hydrogen pressure. *J. Appl. Phys.* **100**, 043501 (2006).

30. Galca, A. C. *et al.* Substrate-target distance dependence of structural and optical properties in case of $Pb(Zr,Ti)O_3$ films obtained by pulsed laser deposition. *Appl. Surf. Sci.* **257**, 5938–5943 (2011).

31. Chen, X. Y., Xiong, S. B., Sha, Z. S. & Liu, Z. G. The interaction of ambient background gas with a plume formed in pulsed laser deposition. *Appl. Surf. Sci.* **115**, 279–284 (1997).

32. Groenen, R. *et al.* Research Update: Stoichiometry controlled oxide thin film growth

by pulsed laser deposition. *APL Mater.* **3**, 070701 (2015).

33. Orsel, K. *et al.* Influence of the oxidation state of $SrTiO_3$ plasmas for stoichiometric growth of pulsed laser deposition films identified by laser induced fluorescence. *APL Mater.* **3**, 106103 (2015).

34. Garbayo, I. *et al.* Thin film oxide-ion conducting electrolyte for near room temperature applications. *J. Mater. Chem. A* **7**, 25772–25778 (2019).

35. Morintale, E., Constantinescu, C. & Dinescu, M. Thin films development by pulsed laser-assisted deposition. *Phys. AUC* **20**, 43–56 (2010).

36. Greer, J. A. & Tabat, M. D. Large-area pulsed laser deposition: Techniques and applications. *J. Vac. Sci. Technol. A Vacuum, Surfaces, Film.* **13**, 1175–1181 (1995).

37. BLANCHARD, C. R. Atomic Force Microscopy. *Chem. Educ.* **1**, 1–8 (1996).

38. Butt, H.-J., Graf, K. & Michael Kappl. Thin Films on Surfaces of Liquids. in *Physics and Chemistry of Interfaces* 280–298 (Wiley-VCH, 2003). doi:https://doi.org/10.1002/3527602313.ch13.

39. Losurdo, M. *et al.* Spectroscopic ellipsometry and polarimetry for materials and systems analysis at the nanometer scale: state-of-the-art, potential, and perspectives. *J. Nanoparticle Res.* **11**, 1521–1554 (2009).

40. Woollam, J. A. *et al.* Overview of variable-angle spectroscopic ellipsometry (VASE): I. Basic theory and typical applications. *Opt. Metrol. A Crit. Rev.* **10294**, 1029402 (1999).

41. Maulana, L. Z. *et al.* Inexpensive Home-Made Single Wavelength Ellipsometer ($\lambda$ = 633 nm) for Measuring the Optical Constant of Nanostructured Materials. *IOP Conf. Ser. Mater. Sci. Eng.* **202**, 012031 (2017).

42. Willett-Gies, T., Delong, E. & Zollner, S. Vibrational properties of bulk $LaAlO_3$ from Fourier-transform infrared ellipsometry. *Thin Solid Films* **571**, 620–624 (2014).

43. Swartzendruber, L. J. *Calculations for Comparing Two-Point and Four-Point Probe Resistivity Measurements on Rectangular Bar-Shaped Semiconductor Samples*. *National Bureau of Standards* (U.S. Department of Commerce, National Bureau of Standards, 1964).

44. Conde, A. & De Damborenea, J. J. Electrochemical impedance spectroscopy for studying the degradation of enamel coatings. *Corros. Sci.* **44**, 1555–1567 (2002).

45. Blommaert, M. A., Vermaas, D. A., Izelaar, B., In'T Veen, B. & Smith, W. A. Electrochemical impedance spectroscopy as a performance indicator of water dissociation in bipolar membranes. *J. Mater. Chem. A* **7**, 19060–19069 (2019).

46. Jiang, S., Zhou, W., Sunarso, J., Ran, R. & Shao, Z. A cobalt-free layered oxide as an oxygen reduction catalyst for intermediate-temperature solid oxide fuel cells. *Int. J. Hydrogen Energy* **40**, 15578–15584 (2015).

47. Fricke, K., Harnisch, F. & Schröder, U. On the use of cyclic voltammetry for the study of anodic electron transfer in microbial fuel cells. *Energy Environ. Sci.* **1**, 144–147 (2008).

48. Kim, T. *et al.* Applications of voltammetry in lithium ion battery research. *J. Electrochem. Sci. Technol.* **11**, 14–25 (2020).

49. Wang, H.-W. *et al.* Cyclic Voltammetry in Biological Samples: A Systematic Review of Methods and Techniques Applicable to Clinical Settings. *Signals* **2**, 138–158 (2021).

50. Elgrishi, N. *et al.* A Practical Beginner's Guide to Cyclic Voltammetry. *J. Chem. Educ.* **95**, 197–206 (2018).

51. Sodhi, R. N. S. Time-of-flight secondary ion mass spectrometry (TOF-SIMS):—versatility in chemical and imaging surface analysis. *Analyst* **129**, 483–487 (2004).

52. Keeble, D. J. *et al.* Identification of A- and B-site cation vacancy defects in perovskite oxide thin films. *Phys. Rev. Lett.* **105**, 226102 (2010).

53. Qin, M. *et al.* Point defect structure of La-doped $SrTiO_3$ ceramics with colossal permittivity. *Acta Mater.* **164**, 76–89 (2019).

54. Sundar, C. S. & Viswanathan, B. Positron annihilation spectroscopy. in *Metals Materials and Processes* vol. 8 1–23 (1996).

55. Sharma, S. K. & Pujari, P. K. Role of free volume characteristics of polymer matrix in bulk physical properties of polymer nanocomposites: A review of positron annihilation lifetime studies. *Prog. Polym. Sci.* **75**, 31–47 (2017).

56. Bigg, D. M. A review of positron annihilation lifetime spectroscopy as applied to the physical aging of polymers. *Polym. Eng. Sci.* **36**, 737–743 (1996).

57. Gubicza, J. Chapter 2 - Characterization Methods of Lattice Defects. in *Defect Structure and Properties of Nanomaterials (Second and Extended Edition)* (ed. Gubicza, J.) 27–57 (Woodhead Publishing, 2017). doi:https://doi.org/10.1016/B978-0-08-101917-7.00002-5.

58. Kršjak, V. *et al.* A new approach to near-surface positron annihilation analysis of ion irradiated ferritic alloys. *Nanoscale Adv.* **3**, 6596–6607 (2021).

59. Henrotte, F., Meys, B., Hedia, H., Dular, P. & Legros, W. Finite element modelling with transformation techniques. *IEEE Trans. Magn.* **35**, 1434–1437 (1999).

60. Zienkiewicz, O. ., Taylor, R. . & Zhu, J. . *The Finite Element Method: Its Basis and Fundamentals*. (Butterworth-Heinemann, 2005).

# 3. Quantification of point defects in $La_{1-x}Sr_xFeO_{3-\delta}$ thin films by in-situ ellipsometry

## 3.1 Introduction

Point defects, imperfections and higher dimensional extended defects are known to severely impact the overall functional properties of transition metal oxides (see **Chapter 1**).[1,2] The knowledge and quantification of the chemical reactions that dominate the defect concentration in oxide thin films (*i.e.* defect chemistry) is essential for understanding the material's behaviour and for engineering their properties. This is especially relevant at intermediate-to-low temperatures (below 500 ºC), where a high electrochemical activity and the nanometric dimensions of the thin films allow the point defect equilibrium with the environment,[3] hampering the use of the high temperature defect chemistry model from the bulk counterpart.

Although many different techniques are available for the measurement of the defect concentration in bulk oxides such as thermogravimetry or coulometric titration, the reduced mass and thickness of thin films pose severe challenges in their applicability to nanometric-thick layers.[4] Overall, there is a lack of available experimental techniques able to estimate the defect chemistry in such oxides thin films at intermediate-to-low temperatures.

This chapter is devoted to the growth and characterization of thin films of the relevant material $La_{1-x}Sr_xFeO_{3-\delta}$ (LSF) and the study of its defect chemistry in the low-to-intermediate temperature range using a novel in-situ spectroscopic ellipsometry approach. It can be divided into the following sections:

- In **Section 3.2**, high-quality films with target formulation $La_{0.8}Sr_{0.2}FeO_{3-\delta}$ (LSF20), $La_{0.6}Sr_{0.4}FeO_{3-\delta}$ (LSF40) and $La_{0.5}Sr_{0.5}FeO_{3-\delta}$ (LSF50) were deposited by Pulsed Laser Deposition (PLD).
- In **Section 3.3**, a relation between the low-energy transition and holes concentration found by ex-situ ellipsometry measurements confirms the viability of ellipsometry for studying the defect chemistry of LSF thin films. Furthermore, the impact of temperature and grain boundaries on the optical properties is discussed.
- In **Section 3.4,** the point defects concentration in LSF20, LSF40 and LSF50 thin films was unveiled as a function of oxygen pressure ($pO_2$) for the intermediate-to-low temperature range by in-situ ellipsometry, the equilibrium constants for oxygen incorporation reaction were extracted from the defect chemistry modelling using a non-dilute model.

## 3.2 Development of $La_{1-x}Sr_xFeO_{3-\delta}$ thin films

LSF20 LSF40 and LSF50 thin films were deposited by Large-Area Pulsed Laser Deposition (LA-PLD) on Gadolinium-doped Ceria (CGO)-coated Yttria Stabilized Zirconia (YSZ) (001) substrates. The CGO layer (~10 nm) was deposited on YSZ substrates as a diffusion barrier to prevent the formation of secondary phases at the LSF/YSZ interface.[5,6] The LSF films were grown with an energy fluency of 0.54 J $cm^{-2}$ at a frequency of 10 Hz. The substrate was kept at 700 °C, in an oxygen partial pressure of 0.0067 mbar during the deposition and the substrate-to-target distance was set to 90 mm. The CGO barrier layer was deposited under the same conditions but at a temperature of 750 °C. As shown in **Figure 3.1a**, all the LSF thin films were deposited using a microfabricated Si mask that allowed the deposition of 2 mm x 3 mm rectangular layers at the center of the 10 mm x 10 mm YSZ (001) substrates. The cross-section image of the exemplified LSF50 film shown in **Figure 3.1b** confirms the high density of the thin films deposited by PLD.

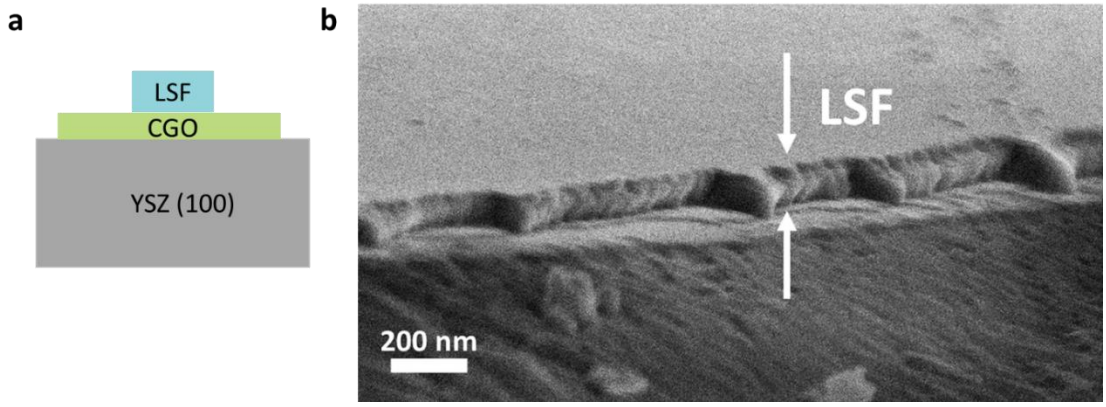


**Figure 3.1 a.** Schematic representation of LSF thin films deposited on YSZ (100) substrates with the CGO barrier layer. **b.** Cross-section morphology of the LSF50 thin film characterized by SEM.

As-deposited LSF thin films were characterized by X-Ray Diffraction (XRD), as depicted in **Figure 3.2**. LSF20 thin film shows a pseudo-cubic polycrystalline structure with two main orientations along the (h00) and (hk0) directions, while LSF40 and LSF50 films present a single (h00) preferential orientation. The increase of the Sr content in the LSF layers gives rise to a shrinkage of the out-of-plane lattice parameter, as shown by the progressive shift towards higher angles of the (100) diffraction peaks in **Figure 3.2b**. This contraction of the unit cell with the Sr content is associated with a subsequent partial oxidation of the Fe ions, being the ionic radius of the $Fe^{4+}$ smaller than the one of the $Fe^{3+}$.[7–9]

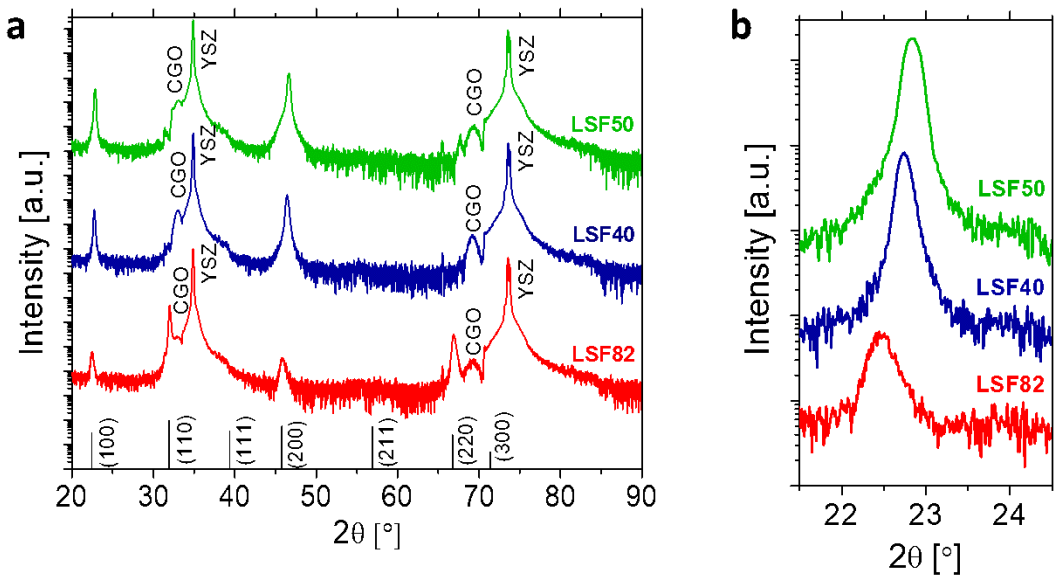


**Figure 3.2 a.** XRD patterns of the as-deposited LSF20, LSF40 and LSF50 thin films on the (100)-oriented YSZ substrate with the CGO interlayer. The CGO and YSZ phases are labelled while the LSF phase is identified by indicating the reflection peaks. **b.** Detail of the (100) diffraction peak showing the shift towards higher 2θ angles while increasing the Sr content.

$LaFeO_3$ (LFO) thin film was also deposited on top of a Sapphire (0001) substrate to better understand the effect of Sr-doping on the perovskite crystal structure, see **Figure 3.3a**. The LFO thin film shows a pure phase with a pseudo-cubic polycrystalline structure. As plotted in **Figure 3.3b**, the out-of-plane lattice parameter obtained from XRD confirms the contraction of the pseudo-cubic LSF structure with the increased Sr content, and this contraction of the unit cell with Sr content is consistent with literature data.[7–11] Here, the lattice parameter is plotted as a function of the real Sr content in the thin films. The latter was measured by Energy-Dispersive X-Ray Spectroscopy (EDS), revealing a Sr content of 0.17±0.01, 0.34±0.01 and 0.44±0.01 for the LSF20, LSF40 and LSF50 thin films, respectively. The good matching of the lattice parameter with bulk references shown in **Figure 3.3b** confirms that the textured LSF40 and LSF50 layers are not expected to be subjected to misfit elastic strain imposed by the substrate. As discussed above, the difference in the radius between $Fe^{3+}$ and $Fe^{4+}$ is principally responsible for the variation of the out-of-plane lattice parameter of the LSF thin films. Nevertheless, as the LSF thin films were not fully oxidized during the PLD process, a portion of Fe atoms exist as $Fe^{3+}$, which explains the discrepancy of the obtained lattice parameter from a linear approximation.

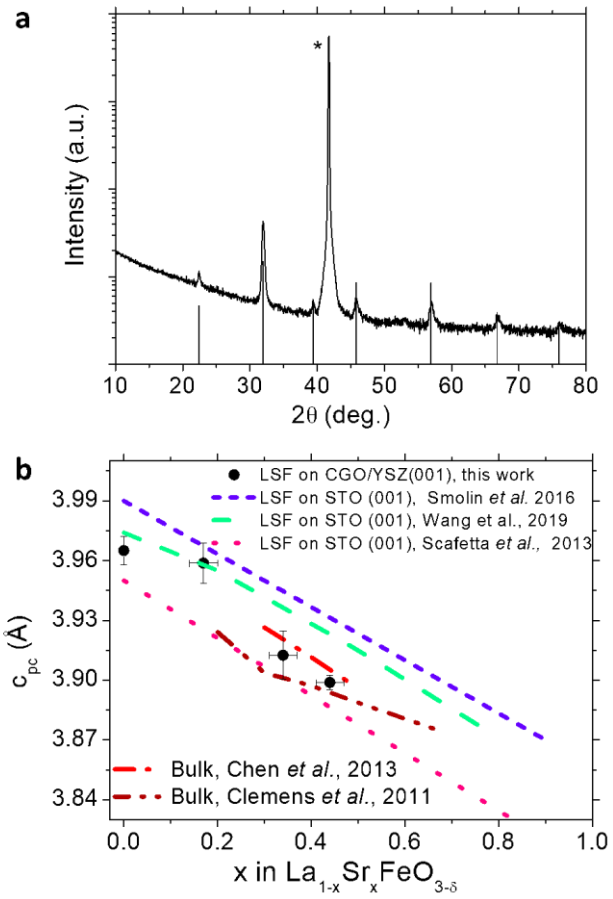


**Figure 3.3 a.** XRD pattern of the $LaFeO_3$ (LFO) thin film deposited on the (0001)-oriented Sapphire substrate. The LFO phase was identified and the asterisk represents the diffraction peak of the substrate. **b.** Comparison of the of out-of-plane lattice parameter of LSF thin films as a function of Sr content with literature. [7–11]

Structural differences among the samples are also confirmed by surface topography measured using Atomic Force Microscopy (AFM), see **Figure 3.4a-c**. Here, a nanocrystalline structure is clearly observed for the LSF20 with a root mean square roughness (rms) of 0.9 nm, while a smoother surface was measured for the LSF40 and LSF50 layers with a rms of 0.3 nm. The increase of structural order in the samples with higher Sr content is due to the decrease of the lattice parameter observed rising the Sr concentration, progressively approaching the half diagonal of the in-plane lattice constant of the CGO (3.85 Å) and allowing a textured growth.[12,13] It must be noted here that the presence of high-angle grain boundaries in the LSF20 thin film may locally modify the point defect concentration, as was previously found in other MIEC materials (see the discussion in **Section 3.3.2**).[14]

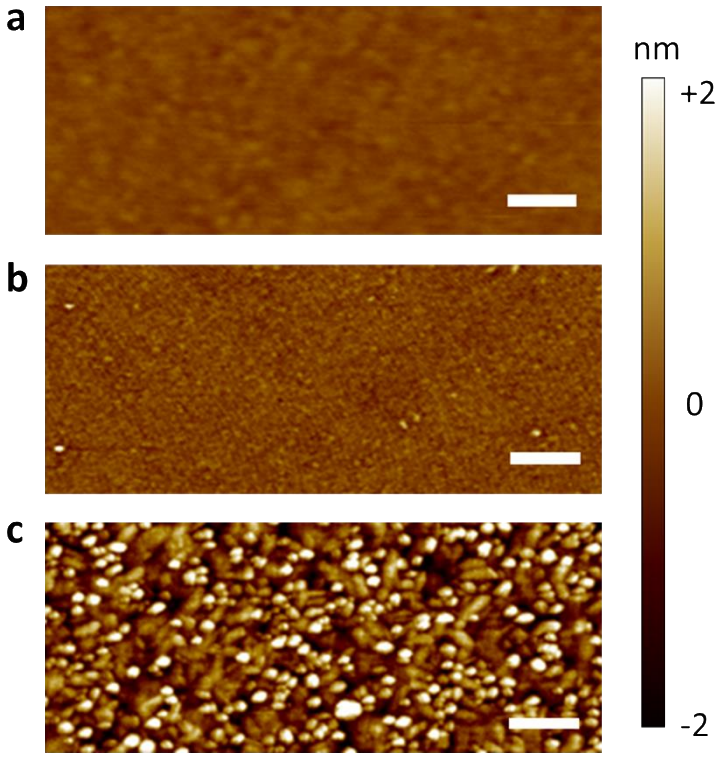


**Figure 3.4** AFM images of the as-deposited **a.** LSF50 **b.** LSF40 and **c.** LSF20 thin films. The scale bar in the images is equal to 250 nm.

Spectroscopic ellipsometry was used to determine the thickness of the LSF thin films, yielding the thickness of 94±1 nm, 98±1 nm and 112±1 nm for the LSF50, LSF40 and LSF20 thin films, respectively. Overall, it is possible to conclude that the deposited LSF layers provide a representative set of samples for the study of the defect chemistry in LSF thin films.

## 3.3 Effects of chemical and structural defects on the optical conductivity of $La_{1-x}Sr_xFeO_{3-\delta}$

### 3.3.1 Electronic holes concentration as a function of the Sr content

Electronic holes strongly modify the optical absorption and the bandgap of the LSF family.[10,11,15] Although this effect is well documented in literature, to the best knowledge of the author, a direct relation between hole concentration and optical features is still lacking. For this reason, as a first step, here we study the optical properties of LSF thin films at room temperature by spectroscopic ellipsometry. In order to remove all the oxygen vacancies and observe the true effect of electronic holes on the optical absorption, the samples were fully oxidized by electrochemical method at 400 ºC (see experimental details in **Section 3.4.1** and **Chapter 2**).

Under these conditions, the concentration of holes in the films is entirely determined by the Sr content and the electronic equilibrium can be written as:

$$[Sr_{La}{}'] = [Fe_{Fe}^{\bullet}] = x \qquad \text{(Equation 3.1)}$$

Where $[Sr_{La}{}']$ and $[Fe_{Fe}^{\bullet}]$ are the concentration of Sr and localized electronic holes represented according to the Kröger-Vink notation, respectively.

Moreover, LFO thin films with null hole concentration (x = 0) were also measured for comparison.

The ellipsometry data were processed using the five-Lorentzian oscillator model detailed in **Chapter 2** (see **Section 2.4.3**) and the resulted optical conductivity spectra are shown in **Figure 3.5a**. Observing the optical conductivity, one can clearly note that increasing the hole doping leads to strong modifications of the optical properties of the material, consisting in an increase of spectral weight of the low energy transitions around 1 eV and 3 eV (named "A" and "B", respectively) and a decrease of the high energy features around 4.5 eV (labelled "C"). These results are in good agreement with previously reported works, which deeply analyzed the origin of optical transitions in the LSF system by means of different spectroscopy techniques.[8,11,16,17] According to these studies, the parent $LaFeO_3$ presents a semiconductor structure in which the valence band is mainly composed by hybridized O 2p-Fe $e_g$ orbitals and the conduction band by empty minority spin Fe $t_{2g}$ states, while changing

the Fe oxidation state in LSF through Sr doping introduces new intra-bandgap states, as depicted in **Figure 3.5b**. The exchange of electrons between all these bands have been directly correlated to the "A", "B" and "C" features observed in the optical conductivity spectra (see **Figure 3.5b**). More specifically, transition "A" corresponds to the electron promotion from the valence band to the intra-bandgap states induced by hole doping while transitions "B" and "C" are assigned to the transfer of electrons from O 2p-Fe $e_g$ orbitals to Fe $t_{2g}$ states and from deeper electronic states towards the empty minority spin Fe $e_g$ orbitals, respectively.[18] In the energy range considered, Sr doping mainly affects optical transitions indirectly by modifying the concentration of holes in the system, which induces new Fe intra-bandgap electronic states as illustrated in **Figure 3.5b**, and not directly since available Sr electronic states are far from the Fermi level.[10,11,15]

For the purpose of investigating the defect chemistry of LSF, transition "A" was analyzed in more detail since this feature is correlated with the concentration of holes in the doped system.[1917] For this analysis, the contribution of the transition "A" to the total spectra was deconvoluted (see **Section 2.4.3**, **Chapter 2** ) showing a linear relationship between the associated maximum of the optical conductivity and the concentration of holes in the system, see **Figure 3.5c.** Moreover, as illustrated in **Figure 3.5a**, the fully reduced LSF50 sample ($[Fe_{Fe}^{\bullet}]\sim 0$) shows an optical spectra similar to the LFO layer and no low energy transition "A", confirming that electronic holes are at the origin of the changes observed in the optical properties. The strong experimental and theoretical relation between transition "A" and the electron holes in LSF suggests that ellipsometry may be used to track the defect chemistry of LSF thin films.

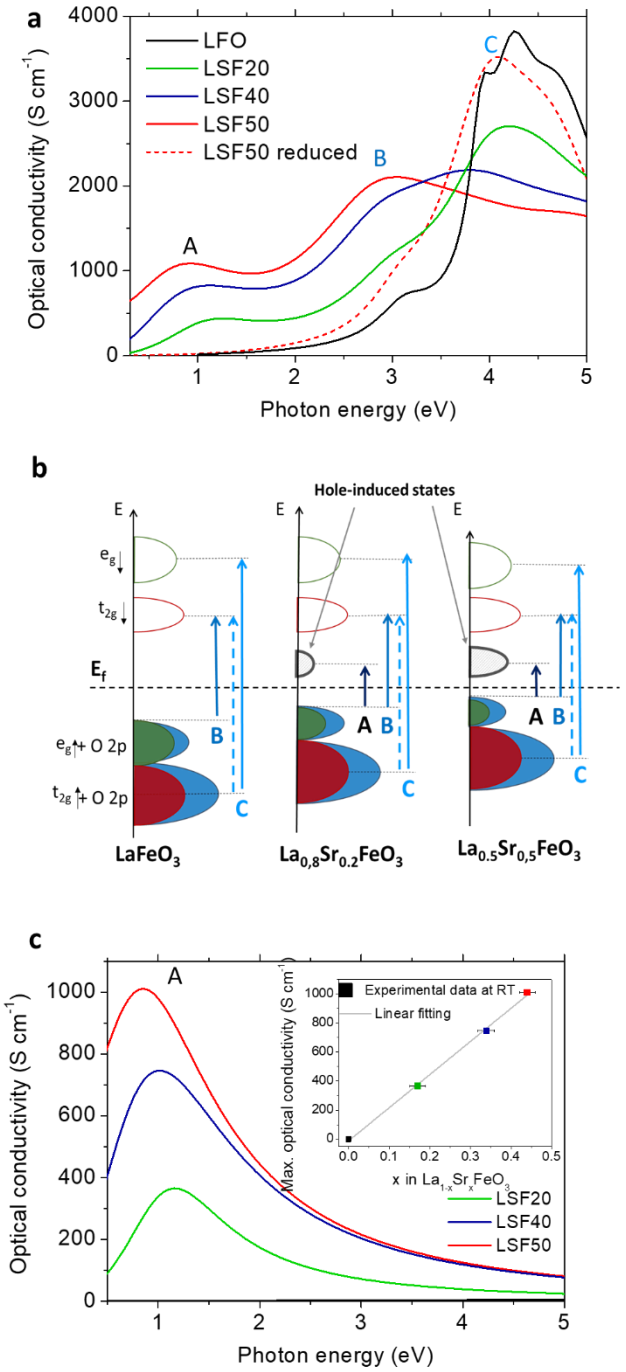


**Figure 3.5 a.** Optical conductivity spectra of the fully oxidized LFO, LSF20, LSF40 and LSF50 thin films measured by spectroscopic ellipsometry at room temperature. **b.** Sketch of the LSF electronic band structure and main optical transitions.[8,10,15,17,18,20]. **c.** The deconvoluted optical conductivity of the low energy transition "A". The inset shows the linear relation between the maximum optical conductivity and the hole concentration in the LSF system at room temperature.

### 3.3.2 Impact of (micro)structural features on the optical conductivity

In this section, the possible uncertainties coming from the presence of structural defects will be discussed. For example, if LSF films present misfit strain, structural defects or other phenomena able to modify both the electronic band structure and the energetics of oxygen incorporation in layers, the linear relation found in the previous section may not hold anymore. Moreover, grain boundaries or dislocations could introduce local modification of the concentration of electron holes, introducing uncertainties in the quantification of the optical conductivity.

As previously stated (see **Figure 3.1b)**, PLD deposition conditions for the fabrication of dense thin films layer were selected, which reduces the effects of some structural defects such as pores. Nevertheless, it is well known that Grain Boundaries (GBs) or dislocations may be present holding different composition than the grain bulk,[14,21] which could lead to changes in the overall optical properties measured by ellipsometry. Generally speaking, grain boundaries in oxides are expected to present an accumulation of oxygen vacancies in the grain core along with a depletion of positive defects concentration in the grain boundaries´ surroundings for maintaining charge neutrality.[22] Due to the high Sr concentration of our LSF thin films, the extension of the space charge will probably be very small (small Debye length), and mainly composed by hole depletion (most numerous positive defect). Therefore, the effect of GBs could be simulated by an effective medium composed by 95% of bulk LSF and 5% of fully reduced GBs, considering an average grain size of 40 nm and a GB width of 1 nm. We performed a set of simulation of the $\Delta$ and $\Psi$ ellipsometry angles expected in our system, where the GB optical properties are set equal to the fully reduced LSF50 layer and the optical properties of the bulk are varied from fully oxidized to fully reduced (see **Figure 3.6**). From the simulations, it is possible to observe that small differences are detected in $\Psi$ angle in the fully oxidized samples but these tends to reduce while reducing the thin films. As commented in the previous section, these differences may produce small uncertainties in the exact quantification of the transition "A" in the fully oxidized thin films at room temperature, which may vary its linearity depending on the film´s structure. Nevertheless, the effect of GBs is expected to be of minor importance in the in-situ electrochemical analysis of LSF thin films, since a minor variation is observed between the homogeneous and heterogeneous model while reducing the sample. For this reason, the quantification of the defect chemistry based on the Brower analysis in LSF thin

films still holds its validity.

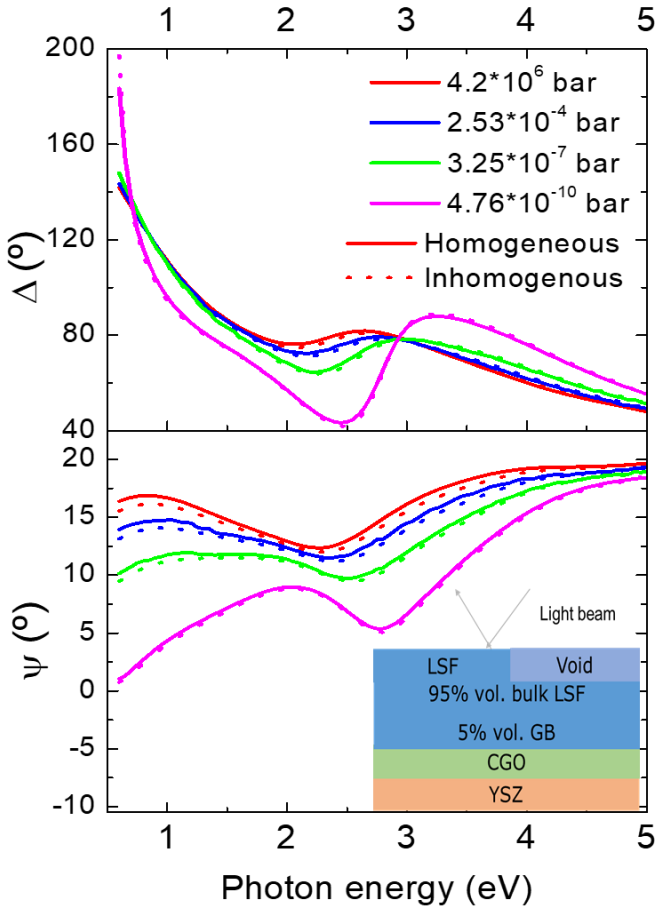


**Figure 3.6** Simulation of optical parameters for the homogeneous and inhomogeneous LSF50 sample at 400 ºC, the inset shows the model used for simulating the inhomogeneous sample.

### 3.3.3 Temperature dependence of the optical conductivity in LSF

In order to explore the effect of temperature on the optical properties of LSF, the LSF50 sample was electrochemically oxidized (see experimental details in **Section 3.4**) at 540ºC with a subsequent cooling step to room temperature maintaining the anodic voltage therefore ensuring a fully oxidized state. The optical conductivity of the sample was then characterized by ellipsometry at each temperature.

The extracted optical conductivity spectra of the LSF50 thin film recorded at different temperatures are exemplified in **Figure 3.7a**. As expected, the spectral weight of the transition "A" gradually strengthens with sample cooling. Moreover, the transition "B" can be assigned to a direct transition due to the temperature independent optical conductivity

edge. The plotting of the maximum of optical conductivity of transition “A” is shown in **Figure 3.7b,** confirming the visual observation. A similar behaviour documented in literature associates the temperature effect to the increased phonon absorption and the modified electronic structure.[18] Nevertheless, the linear relation found at room temperature (**Figure 3.5**) still holds also at high temperature, although a different slope is observed due to the effect of temperature on the electronic band structure,[18] see **Figure 3.7c**. In summary, although the temperature is a factor that affects the electronic band structure of the semiconductor-like materials, the low energy optical transition can be used to track the concentration of holes in LSF at any temperature.

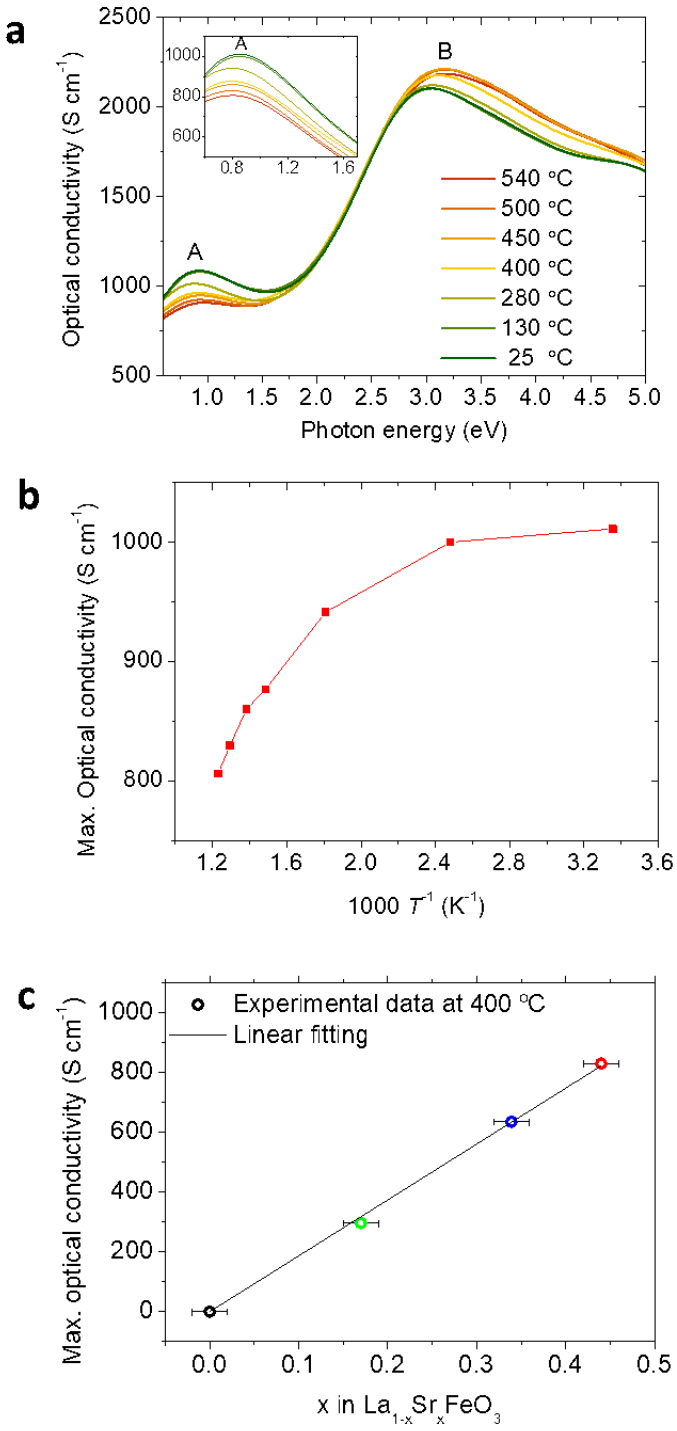


**Figure 3.7 a.** Optical conductivity spectra of the fully oxidized LSF50 thin film measured at different temperatures, the inset shows the extracted oscillator at transition "A". **b.** Evolution of the maximum of the optical conductivity at transition "A" as a function of temperature. **c.** Linear relation between the maximum optical conductivity at transition "A" and the hole concentration in LSF system at 400 ºC.

## 3.4 Quantification of points defects in $La_{1-x}Sr_xFeO_{3-\delta}$ thin films

### 3.4.1 In-situ ellipsometry analysis under voltage bias

#### 3.4.1.1 Control of the equivalent oxygen partial pressure in LSF

We investigate here the variation of optical conductivity in LSF thin films under real operation conditions. In particular, it is possible to measure the material under test as an electrode of an electrochemical cell. If this cell is employed as an oxygen pump against the material, i.e. pumping oxygen in and out the electrode, a wide range of equivalent oxygen partial pressures can be covered by simply applying a voltage bias.[23,2425]

In this chapter, Ag/YSZ/LSF electrochemical cells were fabricated and afterwards measured in a dedicated setup with electrical probes and a heating stage designed for in-situ/operando spectroscopic ellipsometry analysis (see details in **Section 2.4.2.1, Chapter 2**). As the sketch depicted in **Figure 3.8**, DC voltage bias ($\Delta V$) was applied between the LSF layer and the silver counter electrode both in anodic ($\Delta V>0$) and cathodic ($\Delta V<0$) modes varying the chemical potential in the LSF thin films. The variation of the optical properties is tracked by ellipsometry. Under cathodic bias, the voltage forces the gaseous oxygen to be reduced and incorporated into the LSF, while under anodic polarization, the cell operates in reverse way extracting oxygen through the film surface. This electrochemical bias modifies the oxygen chemical potential of the LSF layer, varying the equivalent oxygen partial pressure experienced by the material ($p_{O_2}^{LSF}$) according to the Nernst potential: [23–25]

$$p_{O_2}^{LSF} = p_{O_2}^{RE} \cdot \exp\left(\frac{4e\Delta E}{k_b T}\right) \qquad \text{(Equation 3.2)}$$

Where $p_{O_2}^{RE}$ is the oxygen partial pressure of the environment, $k_b$ is the Boltzmann constant and $e$ is the electron charge. The overpotential $\Delta E$ at LSF electrodes can be calculated by subtracting the resistive contributions of the YSZ substrates ($R_{YSZ}$) and the silver counter electrode ($R_{Ag}$) to the applied electrochemical bias (the inset of **Figure 3.8**), as:

$$\Delta E = V_{DC} - R_{YSZ} \cdot I_{DC} - R_{Ag} \cdot I_{DC} \qquad \text{(Equation 3.3)}$$

Where $V_{DC}$ is the applied DC voltage bias and $I_{DC}$ is the induced current flowing in the sample.

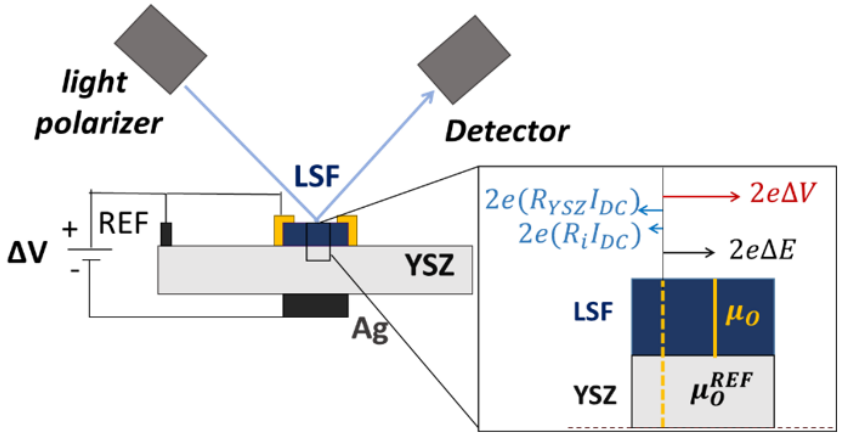


**Figure 3.8** Schematic representation of the in-situ ellipsometry measurements. The inset illustrates the oxygen chemical capacitance and the resistive contributions in the samples.

An anodic Nernstian voltage induces an electrical current from the LSF electrode to the counter electrode (and opposed, in the case of a cathodic voltage), passing through the YSZ substrate. Considering the similarity of the electrochemical behaviour of the studied materials, the LSF50 sample measured at 400 ºC is taken as a representative example; **Figure 3.9a** shows the measured electrical current as a function of the Nernstian voltage. Impedance spectroscopy measurements were carried out at each potential to measure the resistive contributions in series to the LSF electrode (see **Figure 3.9b**). All the spectra show a high-frequency contribution, associated with the ionic conduction in YSZ electrolyte, a middle arc related to the electrochemical contribution of Ag paste, and a very resistive low-frequency contribution, associated with the incorporation/evolution of oxygen on LSF electrode. One can notice that, due to the low range of temperature investigated in this work, the resistive contribution associated with the oxygen incorporation in LSF layer is very high, shifting the characteristic time of the process below the measurable frequency. This highlights the limitations of the chemical capacitance method for deriving the defect chemistry of oxides at low temperature, where the capacitance associated with the electrode cannot be fully resolved.[25]

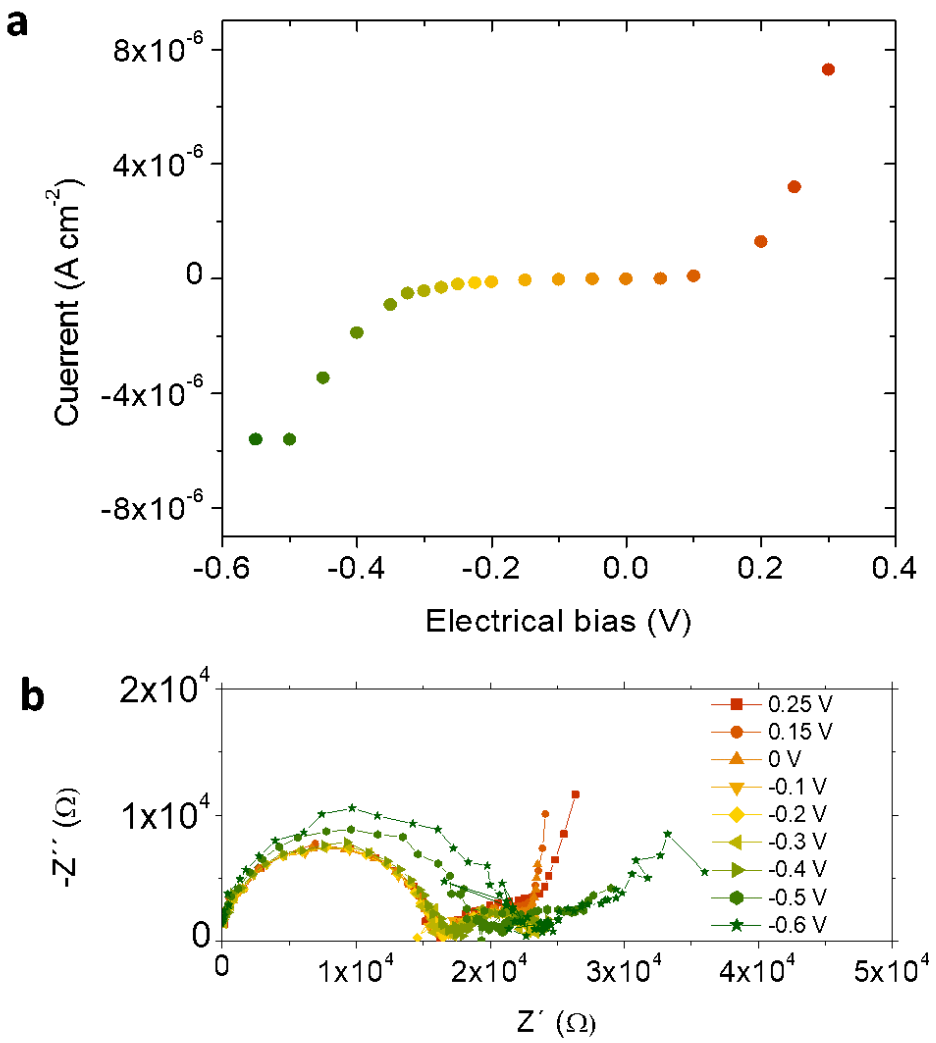


**Figure 3.9** Results of the electrochemical measurements of the LSF50 sample at 400 ºC. **a.** Electrical current induced by the applied Nernstian potential. **b.** Nyquist plot of the representative electrochemical impedance spectra recorded at different applied electrochemical potentials

### 3.4.1.2 Limitation of the electrochemical method

As we stated in the previous section, an electrochemical bias can be used to vary the oxygen equilibrium of an oxide thin film and to measure the evolution of the optical properties in different equivalent oxygen partial pressure (see **Figure 3.8**). Still, as pointed out in literature,[23–25] three conditions must be fulfilled in order to assure a homogenous oxygen chemical potential in the LSF layers: (i.) Oxygen transport must not be limiting across the LSF/electrolyte interface; (ii.) The oxygen incorporation on the LSF surface is limiting the overall electrode reaction (facile oxygen diffusion); (iii.) The sheet electronic resistance of

the LSF layer is low and the electric potential drop along the film's sides are negligible. The use of a CGO barrier avoids the formation of secondary phases at the LSF/YSZ interface, therefore assuring negligible potential drops across this boundary. Condition (ii.) is generally assumed to be true for LSF thin films, where the surface exchange reaction is dominating over the oxygen diffusion across the layer.[25–27] The high electronic conductivity of LSF in oxidizing conditions ensures the fulfilment of condition (iii.) in anodic and small cathodic electrochemical potentials.[23–25] However, high cathodic potentials may give rise to an inhomogeneous electrochemical potential in the thin films, since the decrease of the hole concentration is expected to progressively decrease the electronic conductivity of LSF layers.

To understand the effect of electronic inhomogeneity in the electrochemical measurements, the distribution of electrochemical potentials along the sample was modelled by Finite Element Method (FEM) using COMSOL Multiphysics Modelling software, the modelling details are described in **Chapter 2** (see **Section 2.8**). The model is based on the work of Lynch *et al.*,[28] who simulated the electrochemical distribution in thin film electrodes. One must note that these simulations are mainly intended to depict the effect of inhomogeneous electrochemical potential on the ionic conduction of the YSZ substrates and not to describe the real electrochemical conditions of the thin films under study.

Under electrochemical bias, the reaction of oxygen incorporation competes with the in-plane electronic conduction. Electrons flow from the metallic current collector parallel to the film, reaching the oxygen species on the surface of the electrode where the oxygen reactions take place. **Figure 3.10** shows the ionic potential in the YSZ electrolyte simulated varying the sheet resistivity of the electrode ($10^{-1}$ to $10^{2}$ ohm*cm) and the polarization resistance of the surface ($10^{2}$-$10^{5}$ ohm*cm$^{2}$). This range was chosen to cover realistic values under the experimental conditions studied. The results show that low values of sheet resistivity and high values of surface polarization resistances ensure equipotential electrodes thin film. Nevertheless, it is also interesting to note that equipotential layers can be obtained even with relatively large values of electronic resistivity, provided that the surface polarization resistance is high enough. This condition is easily observed at low temperature, due to the higher activation energy of oxygen incorporation (1 to 2 eV) compared to electronic transport (0.2 eV).[3,29–31]

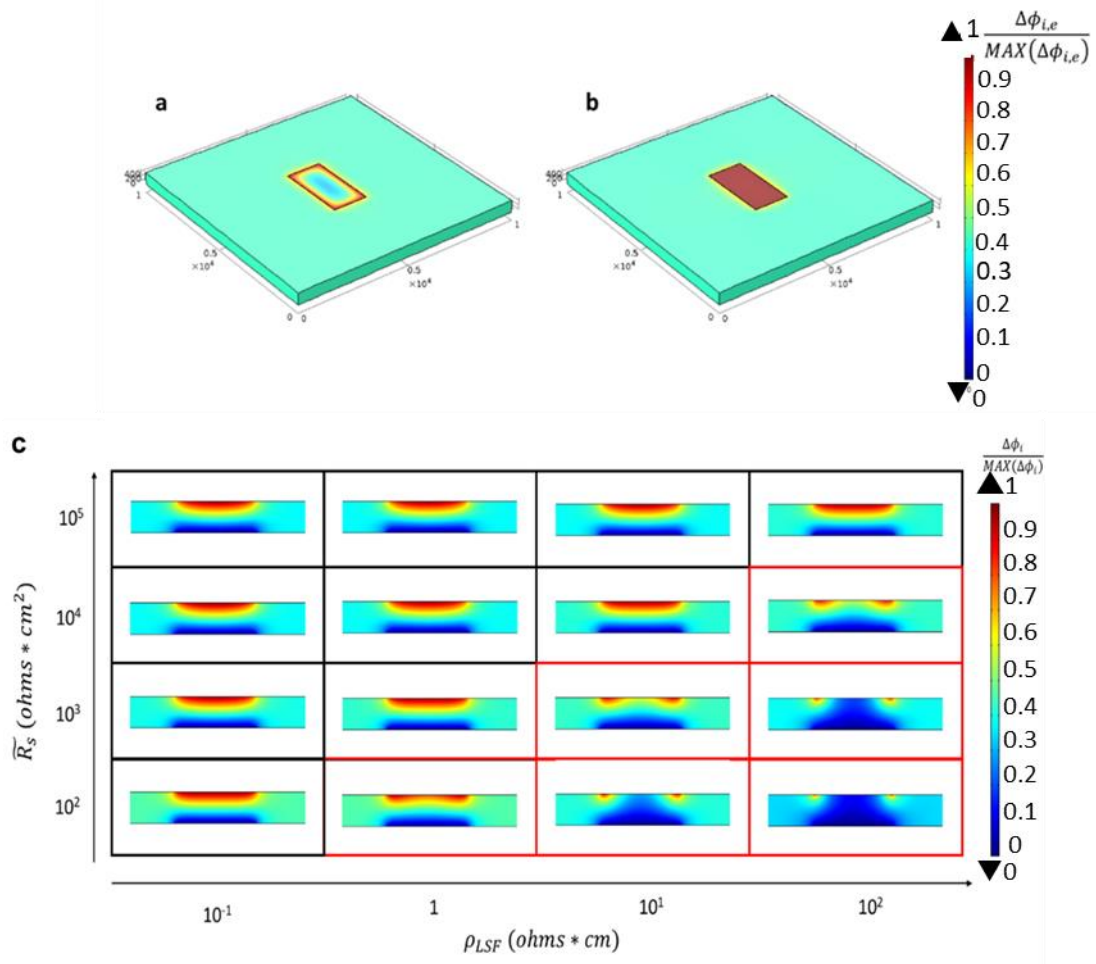


**Figure 3.10** Schematic representation of **a.** heterogeneity and **b.** homogeneity of electronic distribution in LSF thin films. **c.** FEM Modelling of the electronic distribution in the sample as a function of sheet resistivity of LSF film ($\rho_{LSF}$) and polarization resistivity of the surface ($\tilde{R}_s$).

Nevertheless, as commented before, describing the real behaviour of LSF electrodes is challenging, since both surface polarization and electronic conductivity of the layer vary under electrochemical bias. For this reason, we considered a different approach based on the observation of the YSZ resistance in impedance spectroscopy under different chemical potentials. **Figure 3.11a** shows a representative example of the LSF50 sample measured at 400 ºC. The high frequency electrochemical element, associated with the ionic conduction in the YSZ electrolyte, is constant for any value of bias down to -0.4 V. Below this value, the resistance associated with this element starts to increase. The origin of this variation is related to the decrease of active area when passing from homogenous to inhomogeneous chemical potential conditions, as depicted in **Figure 3.11b** and **c**. In other words, for low cathodic potential (V > -0.4 V), the low electronic resistivity of LSF thin films and the high polarization resistance ensure an equipotential chemical potential along the LSF thin film.

Increasing the cathodic potential (V < -0.4 V), the reduction of the hole concentration gives rise to an increase of electronic resistivity that, linked also to a reduction of polarization resistance, gives rise to a non-homogenous distribution of the ionic potential in the LSF layer. This change of regime is observed in the ionic contribution of the YSZ in EIS, where an increase of resistance is measured.

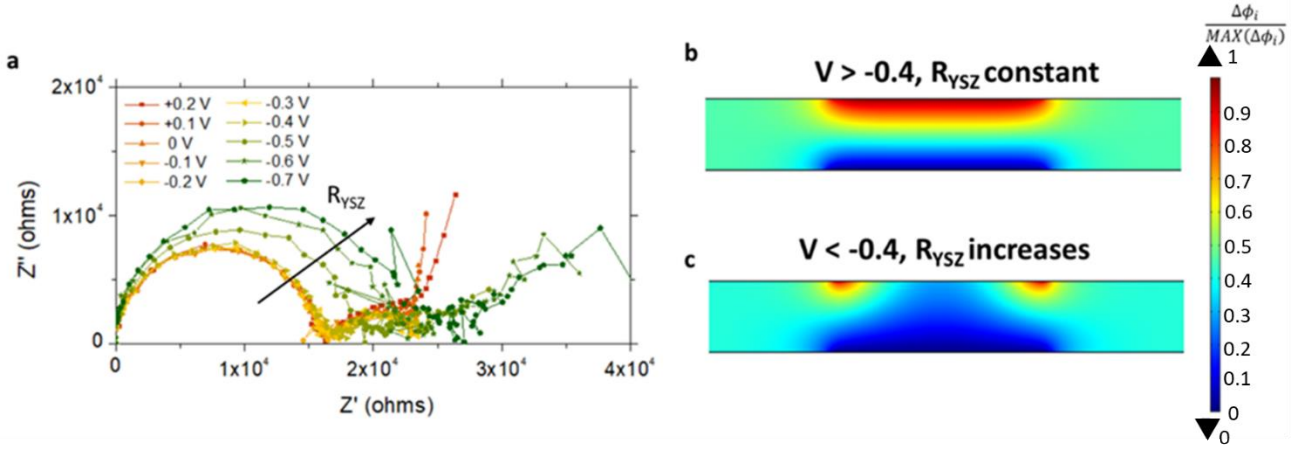


**Figure 3.11** Electronic homogeneity in the representative LSF50 thin film at 400 ºC as a function of Nernstian voltage bias **a.** Electrochemical impedance spectra of the LSF50/CGO/YSZ sample recorded at 400 ºC. The arrow indicates the increase of the ionic resistance of YSZ. **b.** Equipotential LSF thin film at low cathodic voltage. **c.** Non-equipotential LSF thin film at high cathodic voltage.

The method described here was then used to understand the maximum negative bias applicable while maintaining the equipotential conditions. All the results presented in the next sections are within this limit.

### 3.4.1.3 Optical conductivity as a function of oxygen partial pressure in LSF

Based on the previous considerations, in-situ spectroscopic ellipsometry measurements of LSF thin films were carried out under different electrochemical bias, i.e. equivalent oxygen partial pressures, as a function of temperature (T = 350 - 540 ºC) using the set-up described in **Chapter 2**. As an example, **Figure 3.12a** shows the evolution of the ellipsometry parameters $\Delta$ and $\Psi$ measured for the LSF50 sample at 400 ºC. A monotonic modification of the complex reflectance of the sample is observed varying the bias, especially in the low energy region, where interference oscillation typical of semi-transparent layers appears at large cathodic potentials. The raw experimental ellipsometry data were fitted with the model

described in **Chapter 2** to obtain the optical conductivity as a function of equivalent oxygen partial pressure (see **Figure 3.12b)**. One can note that, decreasing the oxygen partial pressure, a gradual decrease of spectral weight of transitions "A" and "B" takes place, along with an increase of transition "C", giving rise to a radical change of optical properties of the LSF thin film, which also changes colour from black to almost transparent, see **Figure 3.12b**. The variation of optical conductivity lowering the $pO_2$ is similar to the behaviour observed in the fully oxidized samples when decreasing the Sr content (see **Figure 3.5**), indicating that the electronic holes progressively deplete in the LSF thin film. This hypothesis is also supported by the evolution of the low energy transition "A" (see **Figure 3.12c**), gradually reducing the spectral weight of the hole-induced empty states above the Fermi level.[10]

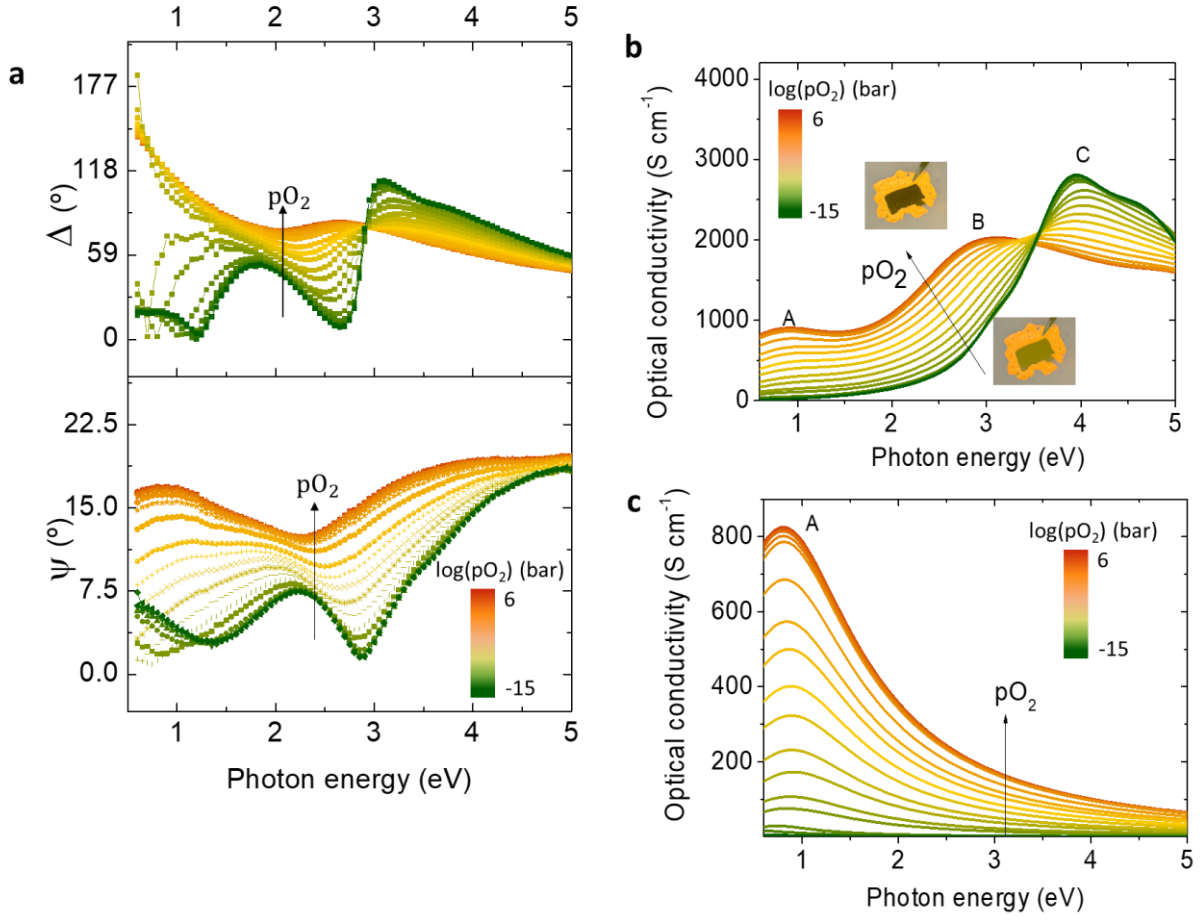


**Figure 3.12 a.** Ellipsometry complex reflectance measured at 400 ºC for the LSF50 sample as a function of $pO_2$ (see the colour scale bar). **b.** The extracted optical conductivity spectra of the LSF50 thin film. The variation of the film colour with $pO_2$ is shown in the inset. **c.** Evolution of the low-energy transition "A" with $pO_2$. The arrows indicate the increment of the equivalent oxygen partial pressure.

For evaluating the reversibility of this approach, we measured the optical properties of the LSF40 sample under identical electrochemical conditions after the complete electrochemical oxidation and reduction. Obtained ellipsometry spectra are shown in **Figure 3.13**. It must be noted here that all the measurements were perfectly reversible and reproducible. This means that the changes observed in the in-situ measurements are entirely originated by the variation of hole concentration and not by structural features (*i.e.* micro voids, cracks) that would lead to a strong non-reversible behavior.

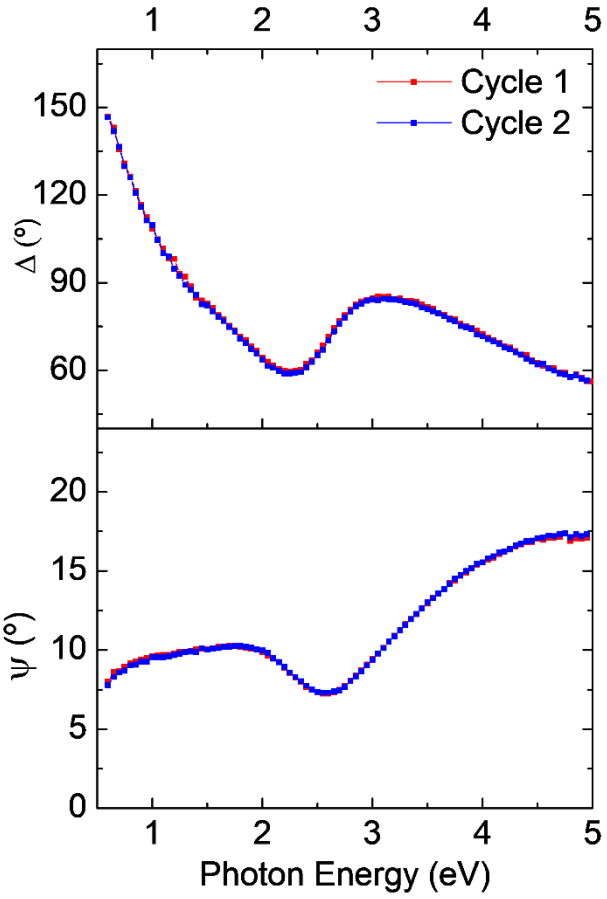


**Figure 3.13** Ellipsometry complex reflectance measured at 400 ºC and equivalent oxygen pressure of 0.0087 bar after the full oxidation (cycle 1) and reduction (cycle 2) for the LSF40 sample.

## 3.4.2 Defect chemistry model for LSF

### 3.4.2.1 Defect chemistry of LSF50

Motivated by the linear relation found in **Section 3.3** between transition "A" and the hole concentration in the LSF system, the maximum of the optical conductivity of "A" was plotted as a function of the oxygen partial pressure in a Brouwer diagram, see **Figure 3.14**. The behaviour found is in agreement with the diluted defect model developed by Mizusaki *et al.*[32], in which the holes progressively decrease their concentration following the oxygen incorporation reaction:

$$V_O^{\bullet\bullet} + \frac{1}{2}O_2 + 2Fe_{Fe}^{\times} \leftrightarrow 2Fe_{Fe}^{\bullet} + O_O^{\times} \qquad \text{(Equation 3.4)}$$

With diluted equilibrium constant ($K_{ox}^{di}$):

$$K_{ox}^{di} = \frac{[Fe_{Fe}^{\bullet}]^2 \cdot [O_O^{\times}]}{(pO_2)^{\frac{1}{2}} \cdot [V_O^{\bullet\bullet}] \cdot [Fe_{Fe}^{\times}]^2} \qquad \text{(Equation 3.5)}$$

Here $[Fe_{Fe}^{\times}]$, $[V_O^{\bullet\bullet}]$, $[Fe_{Fe}^{\bullet}]$ and $[O_O^{\times}]$ refer to the concentration of $Fe^{3+}$, oxygen vacancies, $Fe^{4+}$ holes and oxygen ions written according to the Kröger-Vink notation, respectively. Note that considering both the range of oxygen pressure and the temperature conditions in this study, the concentration of $Fe^{2+}$ electrons is expected to be negligible,[25,32] so that the electronic equilibrium in the LSF system can be simplified to:

$$[Sr_{La}{}'] = 2[V_O^{\bullet\bullet}] + [Fe_{Fe}^{\bullet}] \qquad \text{(Equation 3.6)}$$

**Equations 3.5** and **3.6** can be used to fit the evolution of hole concentration with the $pO_2$ found by spectroscopic ellipsometry, see **Figure 3.14.** The diluted model well describes the experimental data for the LSF50 sample, endorsing the possibility of optically measuring in situ the concentration of holes in the system under real operation conditions.

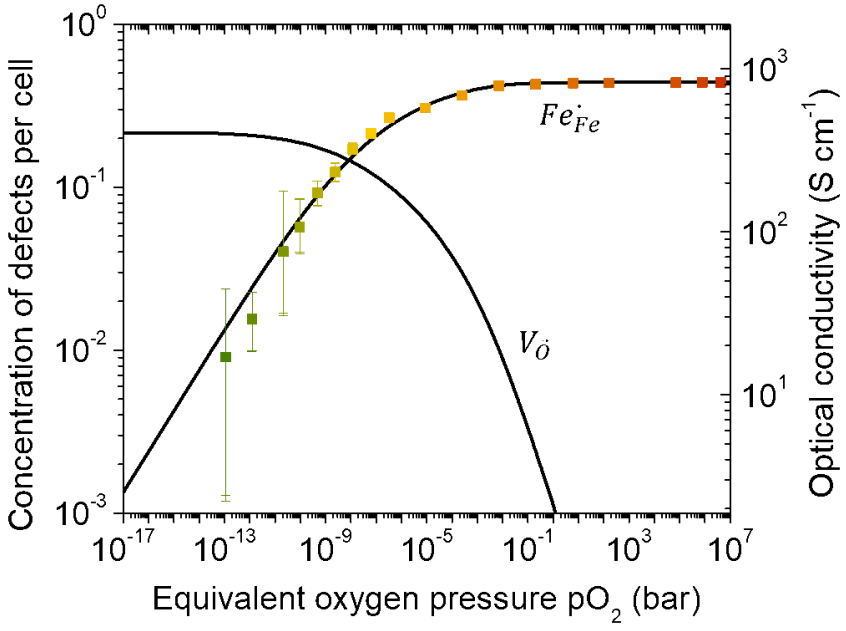


**Figure 3.14** Variation of the maximum of the optical conductivity of transition "A" and the concentration of $Fe^{4+}$ holes per unit cell with the equivalent oxygen pressure measured for the LSF50 thin film at 400 ºC (dots), the solid lines represent the fitting of the concentration of $Fe^{4+}$ holes and oxygen vacancies considering a $K_{ox}^{di}$=7500.

It is interesting to note here that the ellipsometry technique is sensitive not only to the optical constants of LSF films but also to the fluctuation of the thickness of thin films as a function of equivalent $pO_2$. The thickness of the LSF50 was given by the ellipsometry data fitting and is shown as a function of the equivalent $pO_2$ in **Figure 3.15**. In order to compare the results with literature, a second-order polynomial expression developed by Chen *et al.* was considered,[7] where the out-of-plane lattice expansion was measured as a function of the oxygen vacancies concentration in the system. In **Figure 3.15**, the lattice expansion predicted by this model is reported. Please note here that we consider the concentration of oxygen vacancies calculated by the fitting of optical conductivity (**Figure 3.14**), meaning that the measured thickness evolution and the model are independent. Within the error, experimental results are in reasonable agreement with literature.

It must be noted that the large fluctuation of optical constants at high anodic and cathodic voltages decreases the sensitivity of the thickness measurements, lowering the confidence of the fitting in the same way for the other materials LSF40 and LSF20 studied in this chapter. For this reason, the variation of optical conductivity is preferred to quantify the point defect

concentration in the LSF system, in this chapter. Nevertheless, it is important to remark that this approach might be used to study the defect concentration of oxides in systems where the optical properties (electronic structure) are not modified upon oxygen reduction, simply by tracking their chemical expansion/contraction.[33]

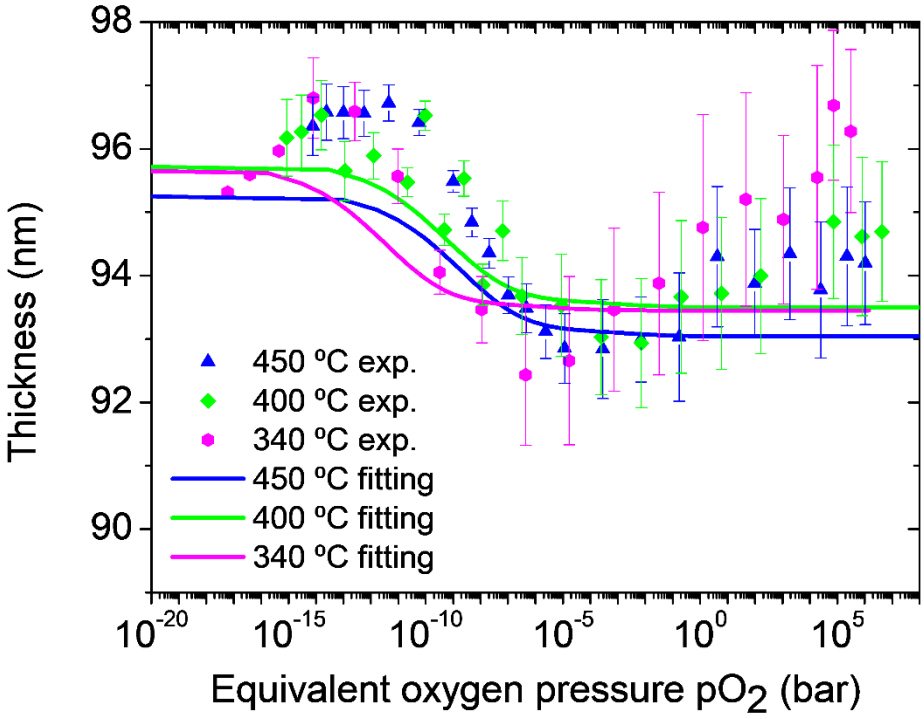


**Figure 3.15** Thickness of the LSF50 thin film as a function of equivalent $pO_2$ at different temperatures obtained from the fitting of the experimental data (symbols) and the expected thickness variation obtained by using a second-order polynomial model developed in literature (Solid lines).[7]

### 3.4.2.2 Role of the Sr content in the defect chemistry of LSF

The point defect concentration as a function of equivalent $pO_2$ was then measured with the same procedure for LSF thin films with different Sr content. **Figure 3.16** shows the evolution of electronic holes in the layers obtained by fitting the maximum of optical conductivity at 400 ºC. One can note that, decreasing the Sr concentration, the dilute model starts to fail in describing the hole concentration, especially at intermediate $pO_2$, where the films are constantly more reduced than expected. In other words, increasing the hole concentration the oxygen incorporation becomes progressively more difficult, giving rise to a less steep growth of $[Fe_{Fe}^{\bullet}]$.

Similar non-ideal behaviours were reported in literature for other oxides, such as $La_{1-x}Sr_xCrO_{3-\delta}$,[34] $La_{1-x}Sr_xCoO_{3-\delta}$,[35,36] $SrFeO_{3-\delta}$,[37] $Ba_{1-x}La_xFeO_{3-\delta}$,[38] and are commonly described considering the Gibbs free energy of incorporation reactions (**Equation 3.4**). Indeed, a non-dilute behaviour can be described by considering a non-diluted chemical potential of defect species:

$$\mu_i = \mu_i^0 + RTln([i] \cdot \gamma_i) \qquad \text{(Equation 3.7)}$$

Where $\mu_i^0$ denotes the standard chemical potential, $[i]$ denotes the concentration of the *i* specie and $\gamma_i$ denotes the activity coefficients, which may deviate from the regular unity. The oxygen incorporation equilibrium constant (**Equation 3.5**) can be rewritten as:

$$K_{ox} = \frac{[Fe_{Fe}^{\bullet}]^2 \cdot [O_O^{\times}]}{(pO_2)^{\frac{1}{2}} \cdot [V_O^{\bullet\bullet}] \cdot [Fe_{Fe}^{\times}]^2} \cdot \frac{\gamma_{Fe_{Fe}^{\bullet}}^2 \gamma_{O_O^{\times}}}{\gamma_{Fe_{Fe}^{\times}}^2 \gamma_{V_O^{\bullet\bullet}}} = K_{ox}^{id} \cdot \frac{\gamma_{Fe_{Fe}^{\bullet}}^2 \gamma_{O_O^{\times}}}{\gamma_{Fe_{Fe}^{\times}}^2 \gamma_{V_O^{\bullet\bullet}}} \qquad \text{(Equation 3.8)}$$

One can note that the equilibrium constant is now composed by the product of the dilute $K_{ox}^{id}$ and the activity coefficients, not necessarily constant in the whole $pO_2$ range. In order to better define the problem, it is useful to consider the Gibbs free energy of the oxygen incorporation reaction defined by a standard term ($\Delta G_{ox}^{id}$ constant for any $pO_2$) and an activity term ($\Delta G_{ox}^{ex}$), as:

$$\Delta G_{ox} = -RTln(K_{ox}) = \Delta G_{ox}^{id} + \Delta G_{ox}^{ex} \qquad \text{(Equation 3.9)}$$

The activity term $\Delta G_{ox}^{ex}$ represents the deviation from the standard free energy of the ideal solution, which is the driving energy for the modification of the oxygen incorporation equilibrium. A commonly employed model for describing non-dilute behaviour in oxides was proposed by Mizusaki *et al.*, who considered $\Delta G_{ox}^{ex}$ to be linearly proportional to the point defect concentration, as:[34]

$$\Delta G_{ox}^{ex} = a[Fe^{\cdot}] \qquad \text{(Equation 3.10)}$$

Alternatively, in this study also a quadratic approximation is considered, probably originated by a non-negligible interaction between the point defect concentration:

$$\Delta G_{ox}^{ex} = b[Fe^{\cdot}]^2 \qquad \text{(Equation 3.11)}$$

**Figure 3.16** demonstrates a comparison of the dilute, linear and quadratic models for the experimental results. All of the three models fit well the hole concentration at high $pO_2$ and

the three models fall into the same value at low pressure. The major difference between them is observed at the intermediate $pO_2$, where the experimental hole concentration is lower than that expected by the dilute model, and a deviation of the experimental results from the fitting curve is clearly observed. The non-dilute model in which the Gibbs free energy of the oxygen incorporation reaction is considered to be linearly proportional to the holes concentration[34] enhances the fitting, although the experimental results are still more reduced than that expected by this model. In this sense, we employed a quadratic model in which the Gibbs free energy of the oxygen incorporation reaction is a second-order polynomial function of the hole concentration. One can note that this quadratic model leads to a satisfactory description of the experimental data. Therefore, the quadratic model is used for fitting the hole concentration as a function of $pO_2$ in this study.

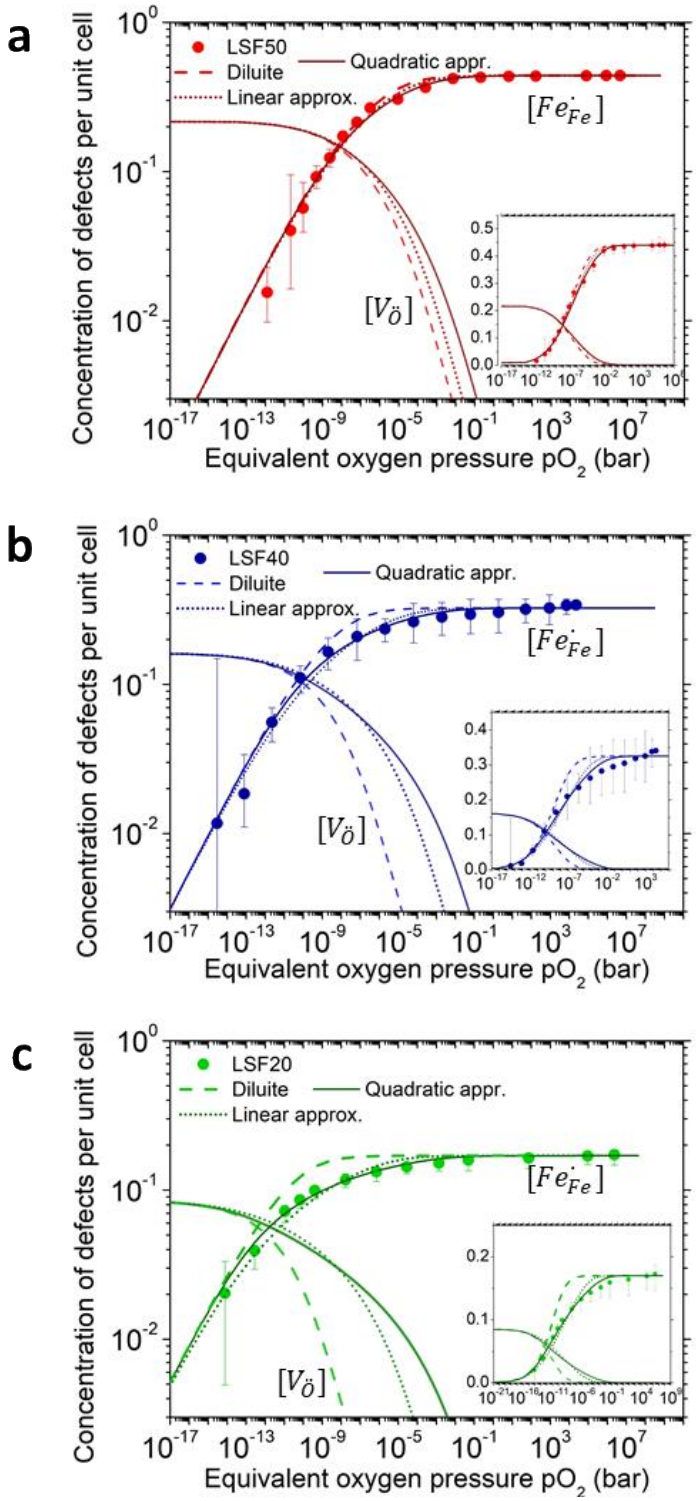


**Figure 3.16** Dilute defect chemistry model (dash lines), linear (dot lines) and quadratic (solid lines) approximations of the concentration of holes (symbols) for **a.** LSF50, **b.** LSF40 and **c.** LSF20 thin films measured at 400ºC as a function of equivalent oxygen pressure.

The ideal equilibrium constant $K_{ox}^{id}$ and quadratic non-ideal parameter *b* obtained at 400 ºC for the different thin films is shown in **Figure 3.17a**. In agreement with the literature, the

oxidation constant progressively lowers increasing the Sr content, shifting the chemical equilibrium of **Equation 3.4** towards a more reduced state. However, also the quadratic parameter *b* is observed to present roughly the same behaviour, rapidly decreasing with the Sr content, similarly to what was observed in $La_{1-x}Sr_xCrO_{3-\delta}$.[34]

Based on the parameter $K_{ox}^{exp}$ obtained from the experimental concentration of point defects, the Gibbs free energy of the LSF thin films for oxygen incorporation can be expressed as a function of holes concentration as:

$$\Delta G_{red} = -\Delta G_{ox} = RTln(K_{ox}^{exp}(T, [Fe^{\cdot}]) \qquad \text{(Equation 3.12)}$$

The Gibbs free energy is plotted in **Figure 3.17b**. One can note that the Gibbs free energy gradually decreases as the hole concentration increases, which is consistent with the fact that the chemical equilibrium of the oxygen incorporation reaction (**Equation 3.4**) is shifted to the reduced state for the LSF films with high concentration of holes. It is noteworthy that in the dilute model, the Gibbs free energy maintains constant over the range of hole concentrations and deviates from the experimental data. However, combining **Equations 3.9** and **3.11**, the quadratic model can be written in Gibbs free energy as:

$$\Delta G_{red} = RTln\left(K_{ox}^{id}\right) - b^2[Fe^{\cdot}] \qquad \text{Equation (3.13)}$$

As depicted in **Figure 3.17**, this second-order non-dilute model effectively matches the experimental data, reinforcing again that this model is suitable for describing the defect chemistry of the LSF thin films.

A comprehensive model for describing the physical origin of $\Delta G_{ox}^{ex}$ and its relation with the other point defects is still uncertain. Lankhorst *et al.* used a rigid band model formalism to interpret the variation of $\Delta G_{ox}$ measured in $La_{1-x}Sr_xCoO_{3-\delta}$.[35,36] In their model, the non-ideal behaviour was explained by a rigid shift of Fermi level when increasing/decreasing the electron concentration, giving rise to a modification of the enthalpy of oxygen incorporation. For metallic and semi-metallic oxides, an alternative explanation based on hole degeneracy was also proposed, where the oxygen incorporation leads to the formation of delocalized and highly degenerated holes that modify their activity.[39,40] Although a modification of the electron hole activity may be at the origin of the behaviour observed in the $La_{1-x}Sr_xFeO_{3-\delta}$ thin films, the presence of a finite bandgap, especially for low Sr content, and of localized electronic defects makes these two models not applicable.[17] Nevertheless, the large variation

of the optical conductivity observed reducing the hole concentration, along with the strong modification of band structure and energy levels measured in previous works,[11,15] suggests a strong non-ideal behaviour of the hole chemical potentials, which is expected to affect both the enthalpy and the entropy of $\Delta G_{ox}$. Moreover, the trend observed for the non-ideal parameter as a function of Sr content (see **Figure 3.17a**), suggests that the non-dilute behaviour is related to the larger bandgap of these films, while increasing the dopant concentration the bandgap tends to reduce and more semi-metallic behaviour is observed, decreasing the influence of the band structure changes on $\Delta G_{ox}$. The most interesting direct consequence of this behaviour is that the concentration of oxygen vacancies is consistently higher than the one predicted by the ideal behaviour, especially for the LSF20 thin film. Although the derivation of the exact mechanism behind the non-ideal behaviour observed is out of the scope of this work, the results show the unique capabilities of spectroscopy ellipsometry to sense the hole concentration in LSF thin films and to disclose non-dilute phenomena in the defect chemistry of MIEC oxides at intermediate-to-low temperatures.

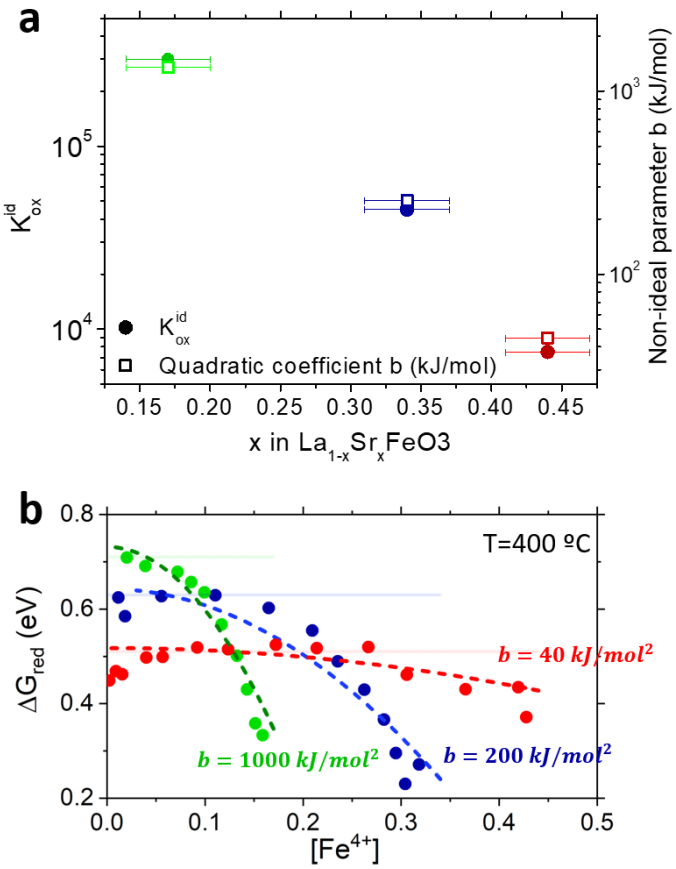


**Figure 3.17 a.** Equilibrium constant $K_{ox}^{id}$ and quadratic non-ideal parameter *b* for the LSF thin films obtained at 400 ºC as a function of the Sr content in the thin films. **b.** Dilute model (lines) and quadratic non-dilute model (dash lines) approximations of the Gibbs free energy for the experimental data (symbols) of LSF thin films measured at 400 ºC.

### 3.4.3 Equilibrium constants as a function of temperature

In-situ ellipsometry measurements were carried out at different temperatures. **Figure 3.18** shows a similar variation of hole concentration as a function of equivalent $pO_2$ at different temperatures, a shift of the curves of hole concentration is clearly observed due to the temperature effects on the electronic structure. Finally, the evolution of the equilibrium constant $K_{ox}^{id}$ with temperature was obtained and is plotted in an Arrhenius-like representation in **Figure 3.19**. Here, equilibrium constants derived from previous high temperature measurements are also reported and extrapolated to the low temperature range investigated in this work. [2532] A good agreement is observed between this set of data and our measurements, despite the difference of temperature window and of the nature of samples, suggesting that difference commonly found in thin films may not be due to the energetics of

the oxygen incorporation equilibrium but to deviation from ideal dilute systems, more predominant at low temperature.

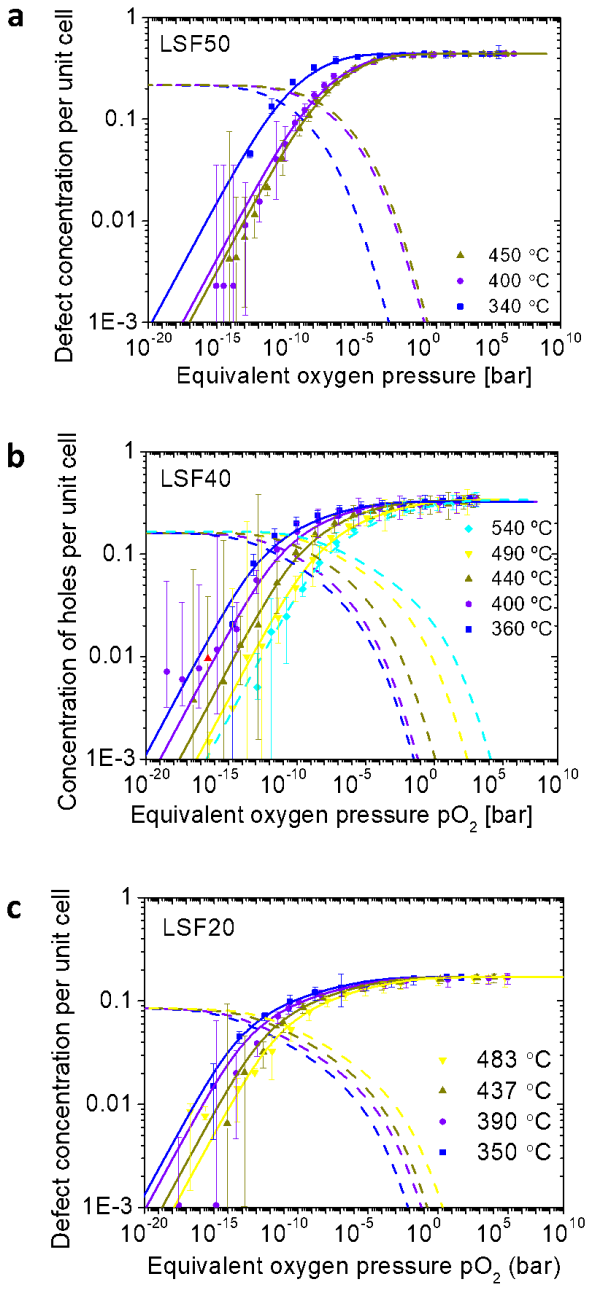


**Figure 3.18** Experimental concentration of holes (symbols) as a function of equivalent $pO_2$ with the quadratic approximation of $Fe^{4+}$ holes (solid lines) and oxygen vacancies (dash lines) for **a.** LSF50, **b.** LSF40 and **c.** LSF20 thin films at different temperatures.

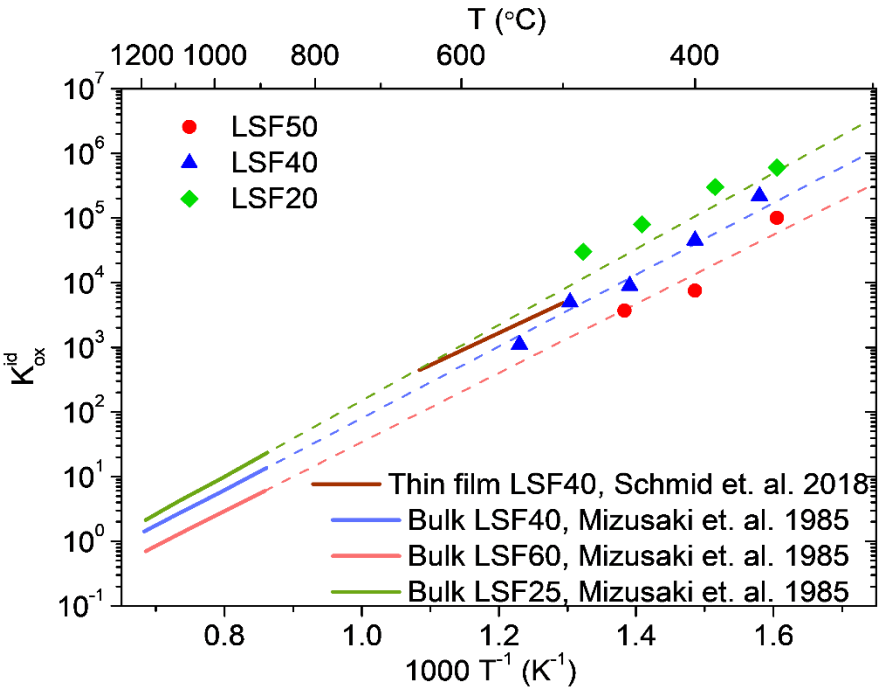


**Figure 3.19** Equilibrium constant $K_{ox}^{id}$ for the oxygen incorporation reaction of the LSF50, LSF40 and LSF20 thin films as a function of temperature (symbols) in comparison with the literature data (solid lines).[25,32] The dashed lines represent the low temperature extrapolation from the literature data.

## 3.5 Conclusions

The defect chemistry of LSF thin films with different Sr content was studied by spectroscopic ellipsometry, for the first time, concluding that low energy transitions (≈1eV) observed in the optical conductivity can be used for tracking and quantifying the concentration of holes in the material. Moreover, LSF was used as an electrode in an electrochemical cell coupled to an ellipsometer, this approach can be extended to calculate the concentration of holes as a function of temperature and oxygen partial pressure in a wide range from $10^{10}$ to $10^{-17}$ bar and 350ºC to 540ºC, respectively. In this way, the defect chemistry of LSF20, LSF40 and LSF50 thin films was unveiled for the intermediate-to-low temperature range, which is not accessible with other techniques. The equilibrium constants extracted from the analysis of the optical constants variation shows a good agreement with the extrapolation from high temperature bulk measurements. Nevertheless, deviations from the dilute defect model are observed in the LSF layers, especially for low Sr-content, consisting in a less abrupt increase of hole concentration while oxidizing the sample. Overall, in this work, it was possible to push the current limits for the direct measurement of defect chemistry in LSF20, LSF40 and LSF50 thin films to lower values of temperature, which is crucial for a systematic description of transition metal oxides nowadays in the core of several emerging energy and information technologies.

# References


1. Tuller, H. L. & Bishop, S. R. Point Defects in Oxides: Tailoring Materials Through Defect Engineering. *Annu. Rev. Mater. Res.* **41**, 369–398 (2011).

2. Gunkel, F., Christensen, D. V., Chen, Y. Z. & Pryds, N. Oxygen vacancies: The (in)visible friend of oxide electronics. *Appl. Phys. Lett.* **116**, 120505 (2020).

3. Xie, Y. *et al.* Control of functional responses via reversible oxygen loss in $La_{1-x}Sr_xFeO_{3-\delta}$ films. *Adv. Mater.* **26**, 1434–1438 (2014).

4. Seh, H., Fritze, H. & Tuller, H. L. Defect chemistry of langasite III: Predictions of electrical and gravimetric properties and application to operation of high temperature crystal microbalance. *J. Electroceramics* **18**, 139–147 (2007).

5. Simner, S. P., Shelton, J. P., Anderson, M. D. & Stevenson, J. W. Interaction between $La(Sr)FeO_3$ SOFC cathode and YSZ electrolyte. *Solid State Ionics* **161**, 11–18 (2003).

6. Tian, D. *et al.* Enhanced performance of symmetrical solid oxide fuel cells using a doped ceria buffer layer. *Electrochim. Acta* **208**, 318–324 (2016).

7. Chen, X. & Grande, T. Anisotropic and nonlinear thermal and chemical expansion of $La_{1-x}Sr_xFeO_{3-\delta}$ (x = 0.3, 0.4, 0.5) perovskite materials. *Chem. Mater.* **25**, 3296–3306 (2013).

8. Scafetta, M. D., Xie, Y. J., Torres, M., Spanier, J. E. & May, S. J. Optical absorption in epitaxial $La_{1-x}Sr_xFeO_3$ thin films. *Appl. Phys. Lett.* **102**, 081904 (2013).

9. Clemens, O., Kuhn, M. & Haberkorn, R. Synthesis and characterization of the $La_{1-x}Sr_xFeO_{3-\delta}$ system and the fluorinated phases $La_{1-x}Sr_xFeO_{3-x}F_x$. *J. Solid State Chem.* **184**, 2870–2876 (2011).

10. Smolin, S. Y. *et al.* Static and Dynamic Optical Properties of $La_{1-x}Sr_xFeO_{3-\delta}$: The Effects of A-Site and Oxygen Stoichiometry. *Chem. Mater.* **28**, 97–105 (2016).

11. Wang, L. *et al.* Hole-induced electronic and optical transitions in $La_{1-x}Sr_xFeO_3$ epitaxial thin films. *Phys. Rev. Mater.* **3**, 025401 (2019).

12. Mueller, D. N., MacHala, M. L., Bluhm, H. & Chueh, W. C. Redox activity of surface oxygen anions in oxygen-deficient perovskite oxides during electrochemical reactions.

*Nat. Commun.* **6**, 6097 (2015).

13. Sanna, S. *et al.* Fabrication and electrochemical properties of epitaxial samarium-doped ceria films on $SrTiO_3$-buffered MgO substrates. *Adv. Funct. Mater.* **19**, 1713–1719 (2009).

14. Chiabrera, F. *et al.* Engineering Transport in Manganites by Tuning Local Nonstoichiometry in Grain Boundaries. *Adv. Mater.* **31**, 1805360 (2019).

15. Wadati, H. *et al.* Hole-doping-induced changes in the electronic structure of $La_{1-x}Sr_xFeO_3$: Soft x-ray photoemission and absorption study of epitaxial thin films. *Phys. Rev. B - Condens. Matter Mater. Phys.* **71**, 035108 (2005).

16. Shen, Z. *et al.* Increased activity in the oxygen evolution reaction by $Fe^{4+}$-induced hole states in perovskite $La_{1-x}Sr_xFeO_3$. *J. Mater. Chem. A* **8**, 4407–4415 (2020).

17. Wadati, H. *et al.* Strong localization of doped holes in $La_{1-x}Sr_xFeO_3$ from angle-resolved photoemission spectra. *Phys. Rev. B* **74**, 115114 (2006).

18. Scafetta, M. D., Cordi, A. M., Rondinelli, J. M. & May, S. J. Band structure and optical transitions in $LaFeO_3$: Theory and experiment. *J. Phys. Condens. Matter* **26**, 505502 (2014).

19. Tokura, Y. *et al.* Thermally induced insulator-metal transition in $LaCoO_3$: A view based on the Mott transition. *Phys. Rev. B - Condens. Matter Mater. Phys.* **58**, R1699–R1702 (1998).

20. Scafetta, M. D. & May, S. J. Effect of cation off-stoichiometry on optical absorption in epitaxial $LaFeO_3$ films. *Phys. Chem. Chem. Phys.* **19**, 10371–10376 (2017).

21. Chiabrera, F., Morata, A., Pacios, M. & Tarancón, A. Insights into the enhancement of oxygen mass transport properties of strontium-doped lanthanum manganite interface-dominated thin films. *Solid State Ionics* **299**, 70–77 (2017).

22. Chiabrera, F., Garbayo, I. & Tarancón, A. Nanoionics and interfaces for energy and information technologies. in *Metal Oxide-Based Thin Film Structures* 409–439 (Elsevier, 2018). doi:10.1016/B978-0-12-811166-6.00017-0.

23. Schmid, A. & Fleig, J. The Current-Voltage Characteristics and Partial Pressure Dependence of Defect Controlled Electrochemical Reactions on Mixed Conducting

Oxides. *J. Electrochem. Soc.* **166**, F831–F846 (2019).

24. Sediva, E., Defferriere, T., Perry, N. H., Tuller, H. L. & Rupp, J. L. M. In Situ Method Correlating Raman Vibrational Characteristics to Chemical Expansion via Oxygen Nonstoichiometry of Perovskite Thin Films. *Adv. Mater.* **31**, 1902493 (2019).

25. Schmid, A., Rupp, G. M. & Fleig, J. Voltage and partial pressure dependent defect chemistry in (La,Sr)$FeO_{3-\delta}$ thin films investigated by chemical capacitance measurements. *Phys. Chem. Chem. Phys.* **20**, 12016–12026 (2018).

26. Baumann, F. S., Fleig, J., Habermeier, H. U. & Maier, J. Impedance spectroscopic study on well-defined (La,Sr)(Co,Fe)$O_{3-\delta}$ model electrodes. *Solid State Ionics* **177**, 1071–1081 (2006).

27. Preis, W., Bucher, E. & Sitte, W. Oxygen exchange kinetics of $La_{0.4}Sr_{0.6}FeO_{3-\delta}$ by simultaneous application of conductivity relaxation and carrier gas coulometry. *Solid State Ionics* **175**, 393–397 (2004).

28. Lynch, M. E. & Liu, M. Investigation of sheet resistance in thin-film mixed-conducting solid oxide fuel cell cathode test cells. *J. Power Sources* **195**, 5155–5166 (2010).

29. Yang, Q., Burye, T. E., Lunt, R. R. & Nicholas, J. D. In situ oxygen surface exchange coefficient measurements on lanthanum strontium ferrite thin films via the curvature relaxation method. *Solid State Ionics* **249**–**250**, 123–128 (2013).

30. Yang, Q. & Nicholas, J. D. Porous Thick Film Lanthanum Strontium Ferrite Stress and Oxygen Surface Exchange Bilayer Curvature Relaxation Measurements. *J. Electrochem. Soc.* **161**, F3025–F3031 (2014).

31. Søgaard, M., Bieberle-Hütter, A., Hendriksen, P. V., Mogensen, M. & Tuller, H. L. Oxygen incorporation in porous thin films of strontium doped lanthanum ferrite. *J. Electroceramics* **27**, 134–142 (2011).

32. Mizusaki, J., Yoshihiro, M., Yamauchi, S. & Fueki, K. Nonstoichiometry and defect structure of the perovskite-type oxides $La_{1-x}Sr_xFeO_{3-\delta}$. *J. Solid State Chem.* **58**, 257–266 (1985).

33. Marrocchelli, D., Bishop, S. R., Tuller, H. L. & Yildiz, B. Understanding chemical

expansion in non-stoichiometric oxides: Ceria and zirconia case studies. *Adv. Funct. Mater.* **22**, 1958–1965 (2012).

34. Mizusaki, J., Yamauchi, S., Fueki, K. & Ishikawa, A. Nonstoichiometry of the perovskite-type oxide $La_{1-x}Sr_xCrO_{3-\delta}$. *Solid State Ionics* **12**, 119–124 (1984).

35. Lankhorst, M. H. R., Bouwmeester, H. J. M. & Verweij, H. Importance of electronic band structure to nonstoichiometric behaviour of $La_{0.8}Sr_{0.2}CoO_{3-\delta}$. *Solid State Ionics* **96**, 21–27 (1997).

36. Lankhorst, M. H. R., Bouwmeester, H. J. M. & Verweij, H. Use of the rigid band formalism to interpret the relationship between o chemical potential and electron concentration in $La_{1-x}Sr_xCoO_{3-\delta}$. *Phys. Rev. Lett.* **77**, 2989–2992 (1996).

37. Bakken, E., Stølen, S., Norby, T., Glenne, R. & Budd, M. Redox energetics of $SrFeO_{3-\delta}$ - A coulometric titration study. *Solid State Ionics* **167**, 367–377 (2004).

38. Zohourian, R., Merkle, R. & Maier, J. Bulk Defect Chemistry of PCFC Cathode Materials: Discussion of Defect Interactions. *ECS Trans.* **77**, 133–138 (2017).

39. Bae, H., Kim, I. H., Singh, B., Bhardwaj, A. & Song, S. J. Defect chemistry of highly defective $La_{0.1}Sr_{0.9}Co_{0.8}Fe_{0.2}O_{3-\delta}$ by considering oxygen interstitials: Effect of hole degeneracy. *Solid State Ionics* **347**, 115251 (2020).

40. Kim, H. S. & Yoo, H. I. On the origin of positive deviation of the defect structure of complex oxides. *Solid State Ionics* **229**, 59–73 (2012).

# 4. Defect chemistry of $La_{0.5}Sr_{0.5}FeO_{3-\delta}$ thin films tailored by ion intercalation in alkaline electrolytes

## 4.1 Introduction

Transition metal oxides are promising electrode materials for room temperature energy conversion and storage applications based on ion intercalation, such as ion batteries,[1–3] supercapacitors,[4,5] and pseudocapacitors.[6,7] In particular, perovskite oxide such as $La_{1-x}Sr_xMnO_{3-\delta}$ (LSM), $La_{1-x}Sr_xCoO_{3-\delta}$ (LSC), $La_{1-x}Sr_xFeO_{3-\delta}$ (LSF) and $La_{1-x}Ca_xFeO_{3-\delta}$ etc. were observed to intercalate oxygen at room temperature in different liquid electrolytes, which raised the attention for their application as battery electrode,[8–10] supercapacitor,[11,12] rapid and efficient electrochromic windows and synaptic memories.[13–15] In these materials, ionic intercalation is a complex phenomenon that involves redox reactions, ionic and electronic transfer through a liquid-solid interphase and ionic transport.[15] Ionic intercalation in perovskites oxides usually comprises a change of oxidation state of the B-site metal, bringing strong modifications of the electronic band structure of the oxide and affecting its electronic, thermal and optical conductivity among others.[5,14,16–19]

Despite this significant interest in low temperature ionic intercalation in perovskite oxides, the exact mechanism and dynamics of ionic insertion are still unclear. For instance, different works show that the main specie diffusing in and out LSF electrodes during intercalation in alkaline electrolytes is oxygen,[5,7,16,20] while other proposed that protons are the main responsible for its pseudo-capacitive behavior.[21] Moreover, ionic intercalation in these materials is usually interpreted on the basis of pseudocapacitive Nernst behavior, where the effect of the different point defects is not taken into account.[22] In this regard, a comprehensive defect chemistry model considering both the intercalating species and the point defect in the perovskite oxide is still lacking. One must also note that the knowledge of the point defect concentration in the oxides is very desirable, due to its impact on many different functional properties.[5,7,16,2012]

This chapter is devoted to study the defect chemistry of $La_{0.5}Sr_{0.5}FeO_{3-\delta}$ (LSF50) thin film along the ion intercalation in alkaline media. LSF50 is a representative example in which the electrochemical properties strongly depend on the concentration of point defects.[23,24] Comparing with bulk materials, the intimate contact between a thin film and the electrical substrate minimizes the potential losses at the interface and favors the polarization of the thin film. In this chapter, an in-situ ellipsometry technique was proposed to study the defect chemistry of LSF50 thin film in 0.1 M KOH electrolyte as a function of the intercalation

potential. **Section 4.2** is devoted to determine the electrochemical reactions occurred upon the ionic intercalation in LSF50 thin films in alkaline electrolyte. **Section 4.3** is dedicated to the investigation of the ion intercalation mechanism using several ex-situ characterization techniques; **Section 4.4** entails the in-situ ellipsometry study of the defect chemistry of LSF50 thin film (including a defect chemistry model).

## 4.2 Ionic intercalation in $La_{0.5}Sr_{0.5}FeO_{3-\delta}$ thin films in alkaline electrolytes

180-nm-thick LSF50 epitaxial films were deposited on 10 mm × 10 mm (100)-oriented Nb doped STO (Nb:STO) substrates (Crystec GmbH) employing PLD. An interlayer of $La_{0.8}Sr_{0.2}MnO_{3-\delta}$ (LSM20) was deposited between LSF50 films and the substrate for improving the electrical conductivity of the sample, ensuring no in-plane drop of the electrical potential.[25,26] The LSF50 layer was deposited using a microfabricated Si mask that allowed the selective growth of a layer of 5 mm×5 mm layer in the central area on top of LSM20. The deposition conditions are detailed in **Chapter 2**. Deposited LSF50/LSM20/Nb:STO samples were encapsulated for the experiments in liquid electrolyte following the method described in **Section 2.4.2.2** in **Chapter 2**, leaving a LSF50 active surface of 11.7 $mm^2$ to the liquid electrolyte (0.1 M KOH solution). Activated carbon was used as the counter electrode and a silver wire as the reference electrode, which was pre-stabilized and measured against an Ag/AgCl reference. Cyclic voltammetry (CV) measurements were conducted on the encapsulated sample in 0.1 M KOH aqueous electrolyte sweeping potential from 0.5 V to -0.5 V at a scan rate of 0.5 mV/s. The resulting CV curve is shown in **Figure 4.1**. The redox reaction peaks centered at $E_{1/2}$ = -0.15 V are observed in the CV curve for the LSF50 thin film, which is consistent with the results reported in literature for similar compounds in powder form.[16] Moreover, the insignificant change in the CV curves with the cycling number demonstrates the electrochemical stability of the film. The asymmetric peaks observed in the CV scans are likely originated by kinetic limitations, different in cathodic and anodic polarization and linked to the sluggish ionic diffusivity in the LSF50 bulk film at room temperature.

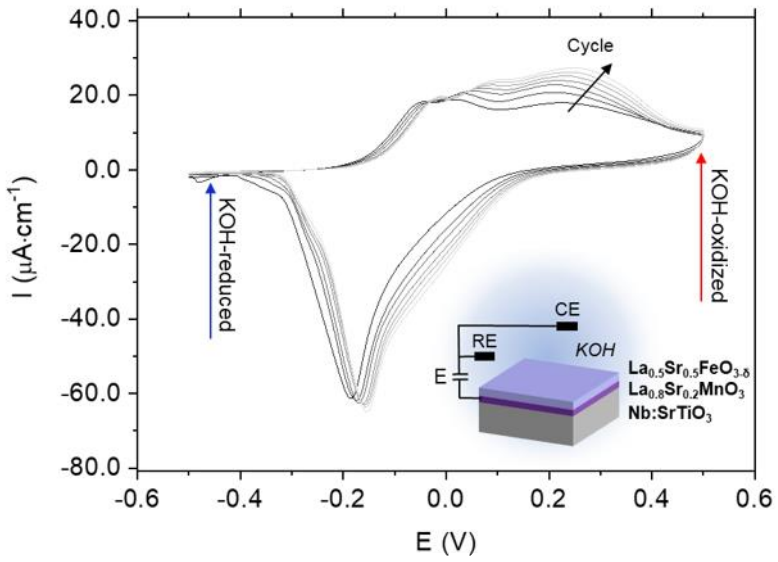


**Figure 4.1** CV curves of the LSF50 thin film measured in 0.1 MKOH electrolyte at a scan rate of 0.5 mV/s. The inset shows scheme of the electrical configuration employed during the experiments.

In order to explore the origin of the electrochemical behavior observed in the electrochemical measurements, LSF50 films were fully oxidized and reduced in the 0.1 M KOH electrolyte by applying a DC voltage of 0.5 V and -0.4 V, respectively (samples are labelled as "KOH-oxidized" and "KOH-reduced", respectively). Furthermore, two LSF50 thin films were annealed in dry $N_2$ and $O_2$ at 575 ºC (named as "$N_2$-annealed" and "$O_2$-annealed", respectively). The post-treated LSF50 thin films were ex-situ analyzed by SEM, XRD and ellipsometry.

In order to explore the chemical stability and morphological characteristics of the LSF50 thin films, the morphology of the $N_2$-annealed and $O_2$-annealed, KOH-reduced and KOH-oxidized LSF50 thin films was evaluated by SEM. As illustrated in **Figure 4.2**, despite an increase in the roughness and grain size of the KOH-reduced and KOH-oxidized LSF50 films (particularly the KOH-reduced film), which is due to the slight chemical etching caused by the 0.1 M KOH solution,[27] the LSF50 films retain a dense granular microstructure after the various treatments, revealing the stability of the LSF50 films. Therefore, no cracks or extended defects are visible on the thin films surface.

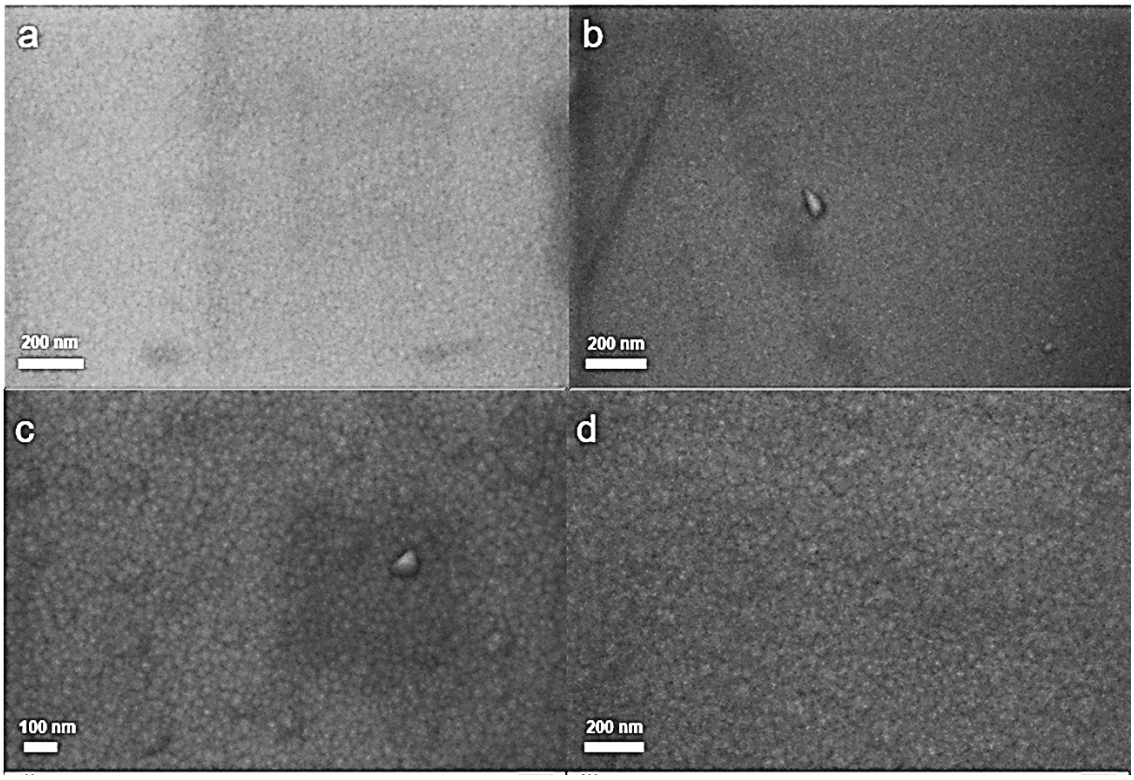


**Figure 4.2** SEM morphology characterization for **a.** the $N_2$-annealed LSF50 film, **b.** the $O_2$-annealed LSF50 film, **c.** the KOH-reduced LSF50 film and **d.** the KOH-oxidized LSF50 film.

HR-XRD was employed to retrieve the film structural parameters, and to characterize the chemical stability and volume expansion of the $O_2$-annealed, $N_2$-annealed, KOH-reduced and KOH-oxidized samples. Resulting XRD patterns are shown in **Figure 4.3a**. Films present a single (h00)-oriented perovskite phase for the entire set of samples, demonstrating the purity and epitaxy of the LSF50 films without secondary phase formation. Details of the (200) diffraction peak shown in **Figure 4.3b** reveal that the diffraction peaks situated at 2θ of 46.44 º and 46.9 º, which are associated to the substrate and the LSM20 layer, remain invariable throughout the samples highlighting the stability of the Nb:STO substrate and LSM20 film. Conversely, a displacement of the diffraction peak position of the $N_2$-annealed LSF50 film from 2θ of 46.75 º to 46.16 º with respect to the $O_2$-annealed LSF50 film indicates a slight chemical expansion in the out-of-plane lattice parameter of the LSF 50 film from 3.883 Å to 3.928 Å (≈2%), upon change of the oxygen content. Interestingly, such a lattice expansion is consistent with the ellipsometry measurement, as the film thickness resulting from the fitting of the LSF50 response increases from 178 nm ($O_2$-annealed) to 180 nm ($N_2$-annealed). This expansion is due to the reduction of $Fe^{4+}$ ions to $Fe^{3+}$ ions which have larger ionic radius as a result of oxygen release from the perovskite structure.[28–31] The

same peak position shift is also observed for the KOH-reduced film, confirming the change of the oxidation state of iron ($Fe^{4+}/Fe^{3+}$) caused by reversible ionic intercalation at room temperature in liquid. One can note that although the KOH-oxidized thin film shows a higher diffraction intensity at 2θ of 46.72 º compared to the KOH-reduced LSF50 film, the diffraction peak (200) is not evident at that diffraction position for the KOH-oxidized LSF50 film, which could be interpreted by its broadening and convolution with the LSM20 diffraction peak. For the KOH-reduced and KOH-oxidized films, the LSF50 diffraction peaks become broader and asymmetric, probably due to the creation of structural defects during the ionic intercalation in liquid electrolytes, in agreement with the SEM results and literature.[32]

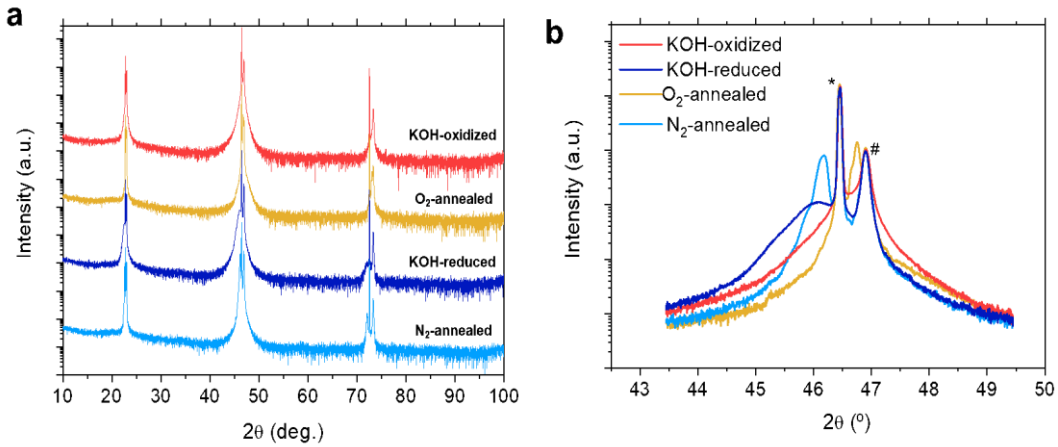


**Figure 4.3 a.** HR-XRD diagrams of the $O_2$-annealed, $N_2$-annealed, KOH-reduced and KOH-oxidized samples **b.** Magnification of the (200) diffraction peak. The diffraction peaks of the Nb:STO substrate and the LSM20 interlayer are marked as * and #, respectively.

The ellipsometry data were processed and analyzed employing four Lorentzian oscillators and the analysis method described in **Section 2.4.3** in **Chapter 2**. The extracted optical conductivity for the KOH-reduced and KOH-oxidized LSF50 films is shown in **Figure 4.4** together with the results measured for the $O_2$-annealed and $N_2$-annealed LSF50 thin films. It is considered that the oxygen vacancies in the $O_2$-annealed LSF50 film were completely removed and the film was fully oxidized, $Fe^{4+}$ holes were dominant in order to compensate the electronic charges ($[Sr'_{La}]\sim[Fe^{\cdot}_{Fe}]$).[30,33,34] In turn, $N_2$-annealed LSF50 thin film presents a fully reduced state, dominated by oxygen vacancies ($[Sr'_{La}]\sim2[V^{\cdot\cdot}_{O}]$).[33] Therefore, the variation of optical conductivity observed for the post-annealed samples, which is consistent with the evolution of optical conductivity of the LSF films as a function of oxygen pressure

described in **Chapter 3**, is totally attributed to the change in $Fe^{4+}$ concentration in the film.[31,34,35] Analogously, the KOH-reduced and KOH-oxidized samples present a similar trend in the variation of optical conductivity, consisting in weakening the low-energy optical transitions at photon energies around 1 eV and 3 eV (features "A" and "B") and intensifying the optical transition at higher photon energy around 4.2 eV (feature "C") upon KOH reduction. This behavior demonstrates that electrochemical redox peaks observed in **Figure 4.1** are related to the intercalation of an ionic species in the LSF50 layers, which gives rise to a change of the $Fe^{4+}$ holes concentration (as charge compensation mechanism).

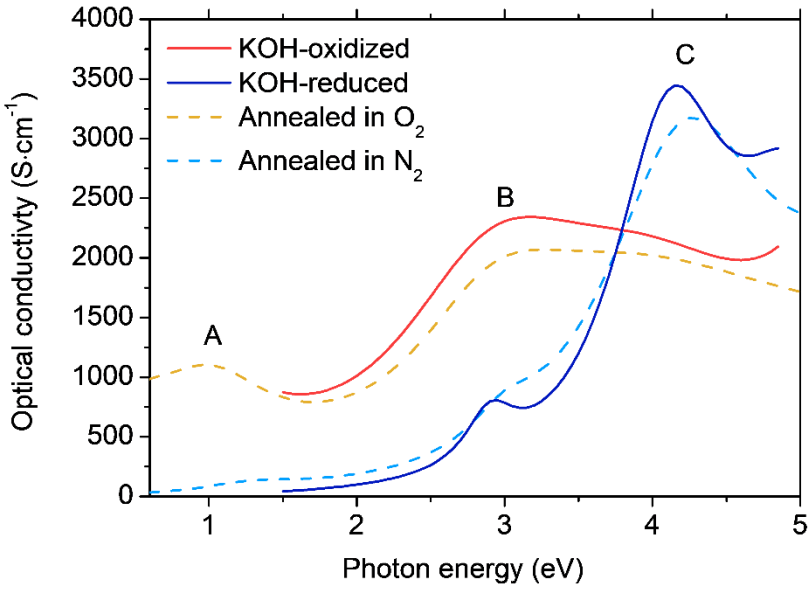


**Figure 4.4** Ellipsometry response of the LSF50 film to the ion intercalation and annealing.

To exclude an electrochemical and optical response of the underlining LSM20/Nb:STO layers in the electrochemical window studied, in-situ ellipsometry measurements were performed for the LSM20/Nb:STO sample at various intercalation potentials under the same experimental conditions. As the CV curve shown in **Figure 4.5a**, no current peak is observed in the potential range of 0.5 V to -0.4 V despite a drop of current intensity associated with the oxygen reduction reaction (ORR) at the onset energy of 0 V.[36,37] The negligible variation of the LSM20 film's optical conductivity with the intercalation potential (**Figure 4.5b**) reveals that the variation of optical conductivity of the LSF50/LSM20/Nb:STO sample shown in **Figure 4.4** is totally associated with the change in the LSF50 thin film. Moreover,

a similar redox behavior was also observed for a LSF50 thin film deposited on FTO-covered glass substrate, confirming that the redox peaks arise entirely from the LSF50 thin film.

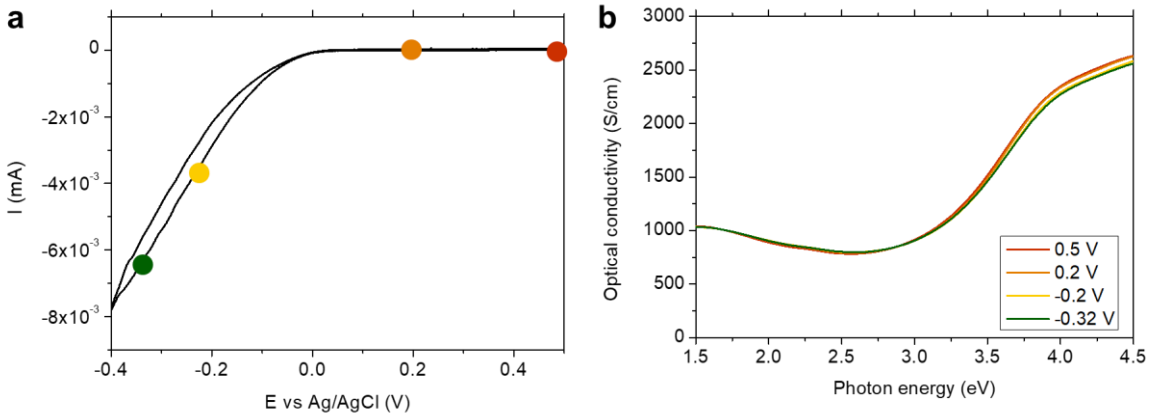


**Figure 4.5** In-situ ellipsometry measurements for the LSM20 thin film **a.** CV curve for the LSM20/Nb:STO sample, the colorful balls represent the intercalation potentials where the ellipsometry spectra were measured. **b.** Ellipsometry response of the LSM20 thin film to the intercalation potentials.

In brief, the redox peaks present in the CV curves in **Figure 4.1** are associated with a reversible ionic intercalation from the KOH electrolyte, resulting in a $Fe^{4+}/Fe^{3+}$ transition as charge compensation mechanism.

## 4.3 Determination of the ion intercalation mechanism

The common intercalation mechanism used in literature for explaining the electrochemical redox peaks observed for perovskite oxide in alkaline electrolytes involves the incorporation of oxygen species through the annihilation of an oxygen vacancy ($V_O^{\cdot\cdot}$) and the formation of two localized electronic holes ($Fe_{Fe}^{\cdot}$), as described in **Figure 4.6a** and **Equation 4.1**:[10,16,22]

$$2OH'\ (l) + V_O^{\cdot\cdot} + 2Fe_{Fe}^{x} \leftrightarrow O_O^{x} + 2Fe_{Fe}^{\cdot} + H_2O(l) + 2e' \qquad \text{(Equation 4.1)}$$

According to the Kröger-Vink notation, $OH'$ , $Fe_{Fe}^{x}$, $O_O^{x}$, and $e'$ represent the $OH^-$ ions in the liquid electrolyte, $Fe^{3+}$ and $O^{2-}$ ions in the lattice of the perovskite structure and the electrons generated as a result of oxygen intercalation, respectively. The variation of iron oxidation state observed in the previous section appears to endorse this mechanism, assuming oxygen is the only species diffusing in and out the LSF50 thin films. Nevertheless, an alternative pathway based on the incorporation of protons ($OH_O^{\cdot}$) may also explain the variation of optical conductivity observed, as described in **Figure 4.6b** and **Equation 4.2**:[14,38–40]

$$OH'\ (l) + OH_O^{\cdot} + Fe_{Fe}^{x} \leftrightarrow O_O^{x} + Fe_{Fe}^{\cdot} + H_2O(l) + e' \qquad \text{(Equation 4.2)}$$

In this case, protons are incorporated in the material through the dissociation of water, reducing the oxidation state of iron as compensation mechanism (please note that protons in the perovskite structure are associated with oxygen atoms with a formal positive charge). This reaction was alternatively proposed for explaining ionic intercalation in perovskite oxides.[21] It is important to note that also both pathways may be active together, each responsible for a part of variation of $Fe_{Fe}^{\cdot}$ holes concentration during the electrochemical intercalation. In order to discriminate the two possible mechanisms, we investigated the active incorporation pathway ToF-SIMS, PALS and ex-situ ellipsometry.

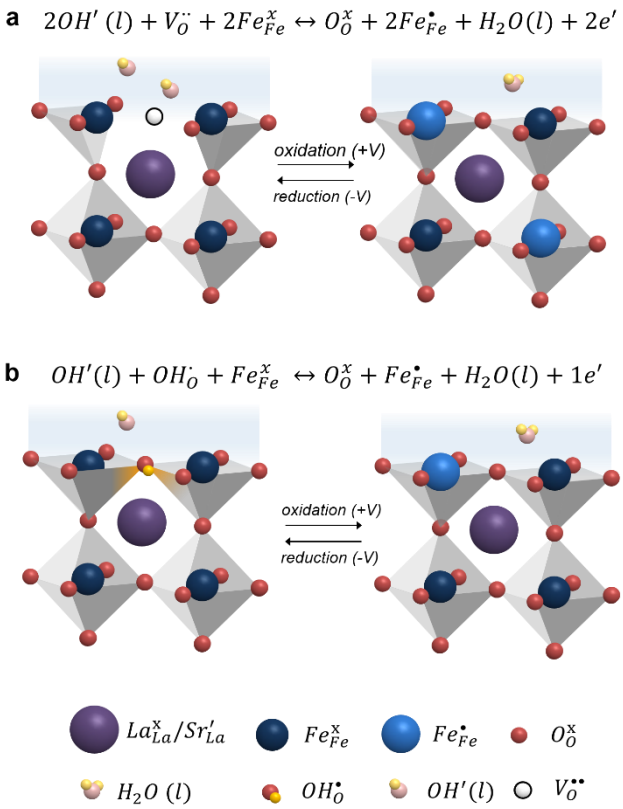


**Figure 4.6** Schematic representation of the oxygen **a.** and protonic **b.** intercalation mechanisms in alkaline electrolytes.

### 4.3.1 The proton and oxygen pathways

In order to determine the feasibility of the protonic pathway shown in **Equation 4.2**, ToF-SIMS experiments have been conducted on the sample reduced in KOH (see **Section 2.6** in **Chapter 2** for details on SIMS technique). The possible proton incorporation was studied by ToF-SIMS in the KOH reduced sample. **Figure 4.7** shows the depth profiles of the $H^-$, $OH^-$, $LaO_2^-$, FeO-, $TiO^-$ and $MnO^-$ ions measured for the KOH-reduced sample. An increased signal of the $H^+$ and $OH^-$ is visible in the LSF50 layer with respect to the background signal (STO layer). The signal for these species strongly decreases together with the $FeO^-$ intensity, indicating the reaching of the LSM layer underneath. This experiment clearly shows that an enhanced proton concentration is present in LSF50 as a consequence of incorporation during the electrochemical reduction in KOH electrolyte, proving that the protonic pathway is active. The sharp decrease of hydrogen species at the LSF/LSM interface suggests that, within the electrochemical window studied, protons are not intercalated in the LSM layer, which remains inactive as shown in **Figure 4.5**.

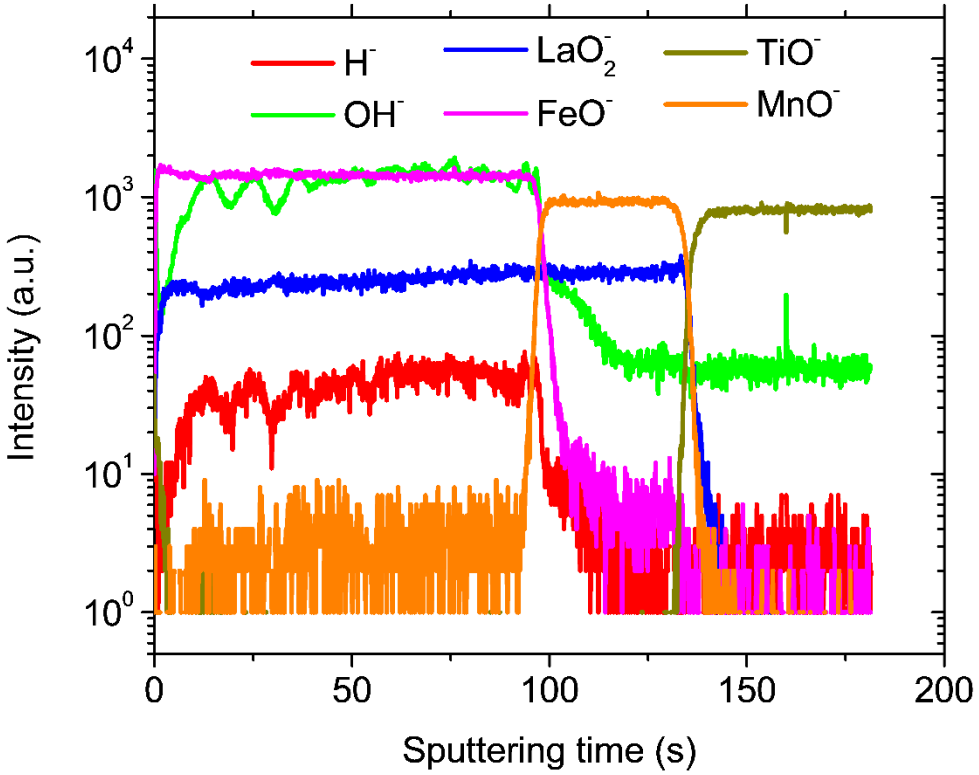


**Figure 4.7** ToF-SIMS depth profiles of $H^-$, $OH^-$, $LaO_2^-$, $FeO^-$, $TiO^-$ and $MnO^-$ ions for the KOH-reduced sample.

The presence of protonic species measured by ToF-SIMS shows that the protonic pathway is active in LSF50 thin films during electrochemical intercalation in alkaline electrolytes. Nevertheless, also the oxygen pathway may be active together with the protonic one, being responsible at least in part of the variation of oxidation state observed. Since oxygen vacancies are not easy to measure in thin film oxides, we performed an indirect experiment to verify the presence of oxygen intercalation in the LSF50 thin film.

First, a LSF50 sample was annealed in dry $N_2$ at T=575 ºC. As shown in the optical conductivity of **Figure 4.8a**, the $N_2$-annealed LSF50 film was fully reduced. Since a dry atmosphere was used, no protons are expected in this state and the dopant is entirely compensated by oxygen vacancies ($[Sr'_{La}] \sim 2[V_O^{\cdot\cdot}]$). The sample was then oxidized in 0.1 M KOH electrolyte by applying potentials of 0.5 V. The optical conductivity presented in **Figure 4.8a** shows that an almost complete oxidation is obtained in the sample, highlighted by the large increase of optical conductivity in the low energy region. According to the

protonic pathway, positive bias should decrease the concentration of protons in the layers. Since no protons were originally present in the sample, the only possible explanation for the oxidation of the layer is an active oxygen pathway allowing the oxygen entering into the reduced sample filling the oxygen vacancies and increasing the oxidation state of Fe (see **Equation 4.1**).

An analogous experiment was also performed with a sample completely oxidized in dry $O_2$ atmosphere, see **Figure 4.8b**. Also in this case, a complete reduction was observed in the sample after electrochemical bias in KOH. It is also interesting to notice that the CV curves of the two different annealed samples (**Figure 4.8c**) are very comparable and present the redox peaks at the same voltage, despite starting from a very different oxygen vacancy (and electron holes) concentration. This also suggests that a new equilibrium is achieved in liquid electrolytes, in which both oxygen and protonic species are intercalating in the layer.

In summary, according to the ex-situ measurements with the different techniques involved, a mixed oxygen and proton mechanism can be concluded for the ion intercalation reaction. Cathodic intercalation potentials cause oxygen anions to be pumped out from the LSF50 structure and protons to be incorporated from the liquid electrolyte into the LSF50 structure, while the opposite reactions take place at anodic potentials.

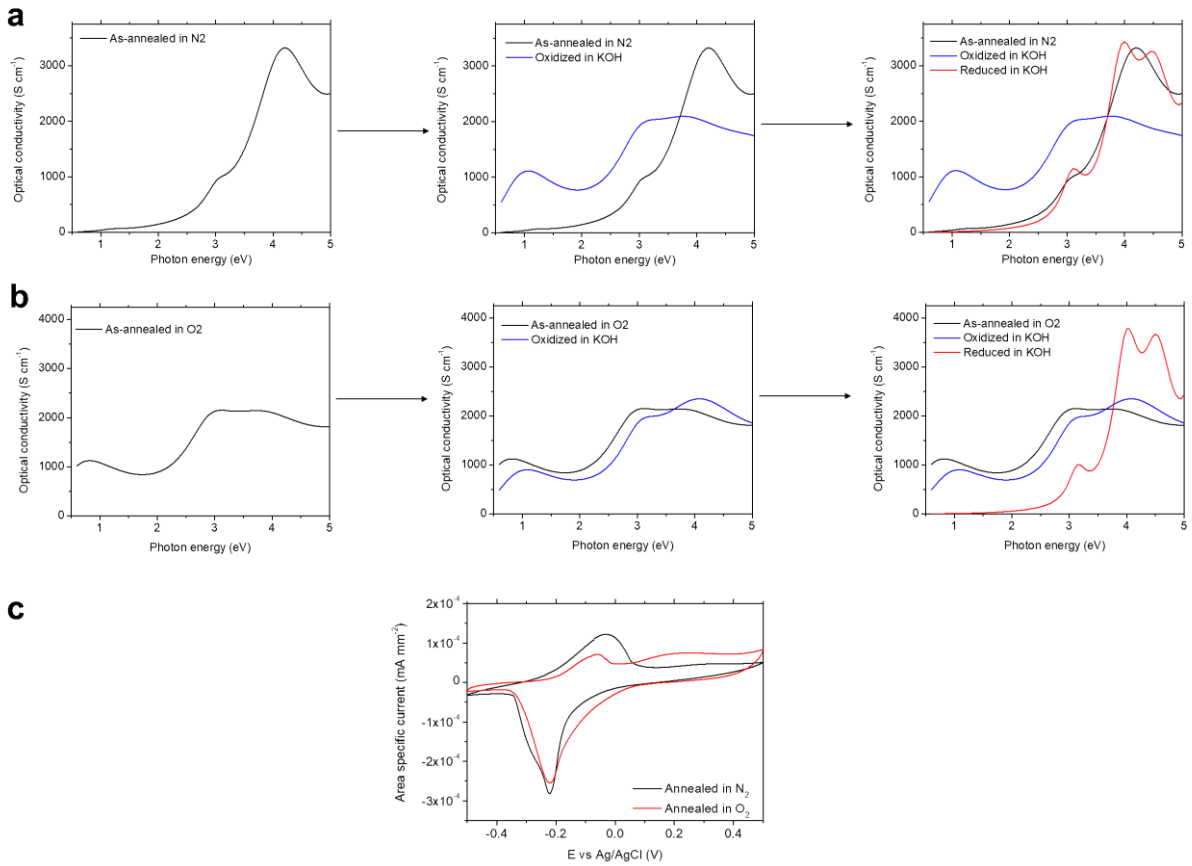


**Figure 4.8 a.** Optical conductivity spectra of the $N_2$-annealed sample followed by the fully oxidation and reduction in 0.1 M KOH solution. **b.** Optical conductivity spectra of the $O_2$-annealed sample followed by the fully oxidation and reduction in 0.1 M KOH. **c.** CV curves of the $O_2$-annealed and $N_2$-annealed LSF50/LSM20/Nb:STO samples.

## 4.3.2 Characterization of lattice open-volume defects by PALS

In order to characterize the nature of the defects in the LSF50 thin films, VEPALS was employed (see **Section 2.7** in **Chapter 2** for details on PALS). PALS is particularly sensitive to localized vacancy-like defects (or close porosities) of neutral or negative charge, which act as annihilation sites for positrons.[41] VEPALS cannot directly measure positive defects such as oxygen vacancies or protons but it is sensitive to their association with negative defects (e.g. cationic vacancies), resulting in the formation of an associate. A higher oxygen vacancy content is expected to lead to an increase of defect lifetime owing to the formation of larger open clusters.[42,43] **Figure 4.9a** shows the average positron lifetime ($\tau_{av}$) obtained as a function of $E_p$ for the KOH-oxidized and reduced samples as well as the $O_2$-oxidized and the $N_2$-reduced LSF50 thin films. Here, $\tau_{av} = \Sigma_i \tau_i \cdot I_i$, as obtained from deconvolution of the measured lifetime in two-lifetime components (cf. also experimental). The average defect

size for all the LSF50 film that corresponds to a lifetime of 200 ps falls into the range of B-site vacancy.[41,44,45] The $N_2$-annealed and KOH-reduced samples are characterized by a larger average positron lifetime $\tau_{av}$ with respect to the oxidized counterpart ($O_2$-annealed and KOH-oxidized, respectively), showing that the reduction in dry $N_2$ increases the defect size, which can be explained by the increased clusters of oxygen vacancies and cationic vacancies.[42,43] Interestingly, for the KOH-oxidized and reduced layers, $\tau_{av}$ is larger than that for the $O_2$-annealed and $N_2$-annealed samples, respectively, suggesting that a more defective structure is induced upon treatment in liquid. All the layers present similar average lifetimes for implantation energy corresponding to the LSM interlayer, confirming that the different treatments do not affect this material.

An analysis of the single lifetime components ($\tau_{d1}$ and $\tau_{d2}$) and the relative intensities allows obtaining further insights, see **Figure 4.9b**. Comparing with literature values of STO,[44] the dominant defect component $\tau_{d1}$ in the LSF50 film is found to be in the range of Ti vacancy ($V_{Ti}''''$) and a complex between Ti and oxygen vacancies. Reducing the sample (both in KOH and in $N_2$) is observed to increase the average time of $\tau_{d1}$, in accordance with an increase of oxygen vacancy concentration and the creation of cation-oxygen vacancy associates. A considerable increment in the intensity $I_{d2}$ is observed for the KOH-reduced sample compared to the other films. This lifetime is comparable with the formation of Schottky type defects in STO or similar type of defects clusters. One can note that the KOH-reduced LSF50 thin film shows larger positron lifetime and higher intensity than the $N_2$-annealed sample. A possible explanation is that the hydration reaction brings an increase of structural disorder, in which the incorporated protons bond with oxygen gives rise to the displacement of oxygen from the equilibrium sites, resulting in lattice distortion and increased defect volume.[1732] This hypothesis appears to be supported by the decrease of crystalline quality observed in the XRD experiments (**Figure 4.3**).

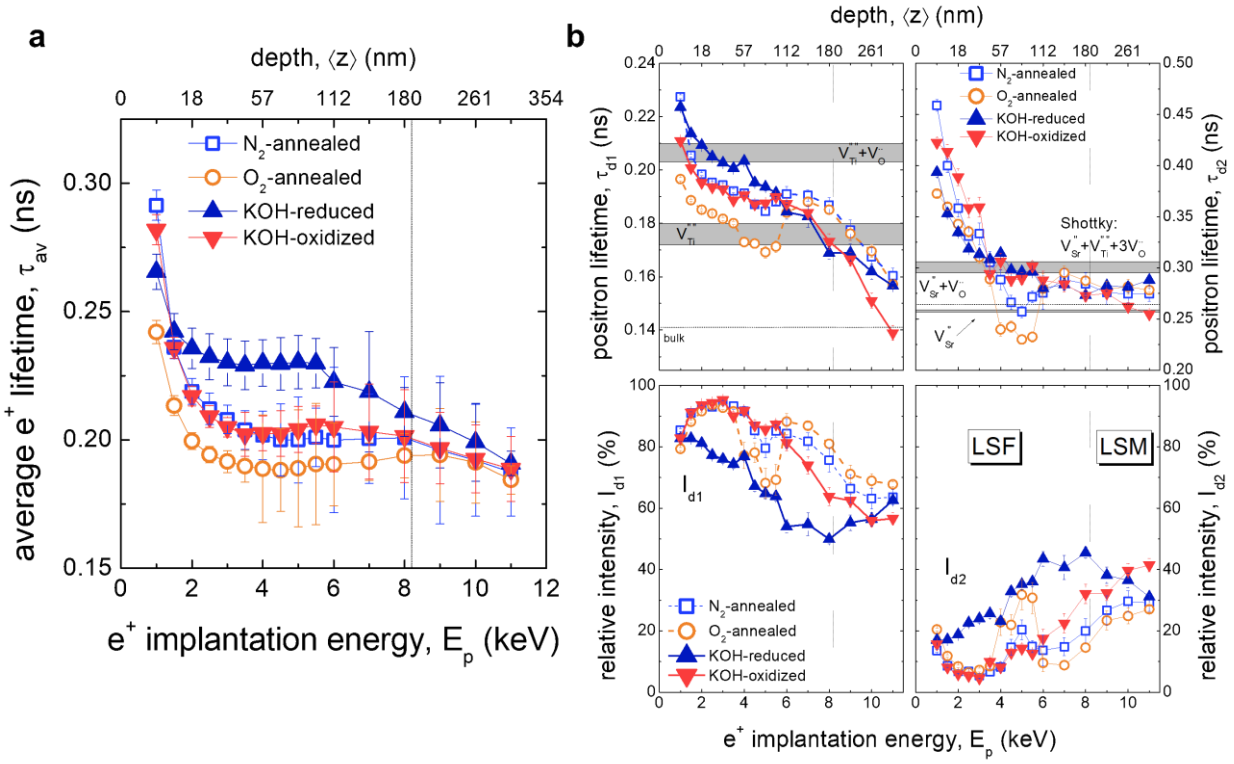


**Figure 4.9** Analyses of PALS parameters for the LSF50/LSM20/Nb:STO samples. **a.** Average positron lifetime $\tau_{av}$. **b.** The first $\tau_{d1}$ (upper left) and the second $\tau_{d2}$ (upper right) components of the positron lifetime and their relative intensities $I_{d1}$ (bottom left) and $I_{d2}$ (bottom right). The vertical line at $E_p$=8 keV represents the position of the interface between LSF50 and LSM20 films. The horizontal lines and grey areas represent the ab-initio calculated positron lifetimes of different defect states in STO based on the published values.[44]

## 4.4 In-situ ellipsometry study of the defect chemistry of $La_{0.5}Sr_{0.5}FeO_{3-\delta}$ thin films

In the previous sections it was shown that protons and oxygen both contribute to the ionic intercalation of LSF50 thin films in alkaline electrolytes. The variation of oxidation state of Fe in the LSF50 layers was directly observed by ellipsometry, as a large variation of optical conductivity, in agreement with the one measured in **Chapter 3.** Here, in-situ ellipsometry measurements are performed during the electrochemical reduction for getting more insights into the mechanisms of ion intercalation.

### 4.4.1 Electrochemical measurements

The variation of optical conductivity in LSF50 thin films was studied by employing the in-situ ellipsometry method and the experimental setup as detailed in **Section 2.4.2.2** in **Chapter 2**. In order to measure the real equilibrium conditions, this study was focused on the reduction reaction at room temperature applying DC voltage steps to the sample, from 0.5 V to -0.4 V. The equilibrium was considered achieved when the electrochemical current, measured after each polarization step, reached a constant value close to zero, see **Figure 4.10a**. In this way, the real equilibrium state at each electrochemical potential could be obtained without kinetic limitations. As exemplified by the current response shown in **Figure 4.10b**, the evolution of electrochemical current can be divided into two stages: in the first stage, the current decreases abruptly in a few seconds, probably due to the extraction of oxygen anions and adsorption of protons on the film's surface (surface limitation);[46] in the second stage, in which the current tends to stabilize slowly, is controlled by the chemical diffusion coefficient.[46]

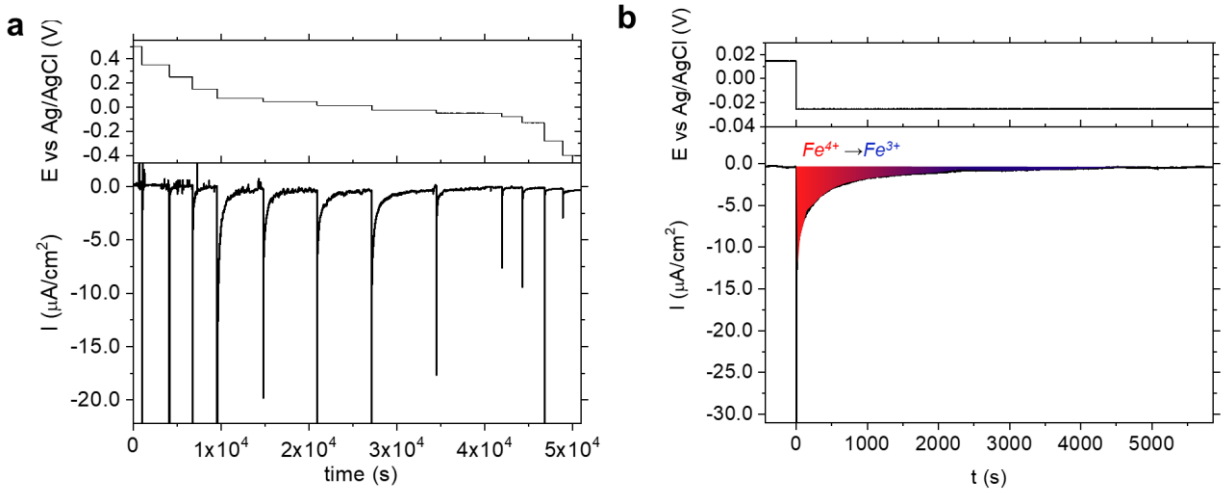


**Figure 4.10** Evolution of the electrochemical current over time at different applied voltages, the inset shows the exemplified evolution of the current when the voltage was switched from 0.045 V to 0.015 V.

### 4.4.2 In-situ ellipsometry measurements

The ellipsometry spectra of the LSF50 sample at each equilibrium potential were in-situ recorded once the electrochemical current was stabilized. The resulting evolution of the ellipsometry signal ($\Delta$ and $\psi$) is illustrated in **Figure 4.11a**. The ellipsometry signals demonstrate a monotonic variation with the intercalation potential revealing the sensitivity of ellipsometry to the ion intercalation. Therefore, in-situ ellipsometry can be applied to study the defect chemistry in the LSF50 thin film as a result of ion intercalation. These raw data were analyzed using four Lorentzian oscillators[47,48] and following the methods described in **Section 2.4.3** in **Chapter 2**. The thickness and roughness of the LSF50 film were kept free for the data fitting, the impact of the thickness and roughness in the data fitting will be discussed later.

To extract the optical properties of LSF50 from the raw ellipsometry data, the previously fitted optical spectra of the LSF50, LSM20 layers and 0.1 M KOH solution were employed. The extracted optical conductivity spectra of the LSF50 thin film, measured by in-situ ellipsometry at various intercalation potentials, are shown in **Figure 4.11b**. The optical conductivity spectra of the LSF50 film show a monotonic variation in the intensity of the optical transitions "A", "B" and "C", consisting in that the features "A" and "B" become weaker and weaker but the feature "C" become stronger and stronger upon cathodic potential

(*i.e.* reduction reaction). This tendency implies a decrease of the hole concentration in the LSF layer, similar to the evolution of the LSF50 film's optical conductivity as a function of $pO_2$ reported in **Chapter 3** and holes concentration as described in literature.[31,35,47,49]

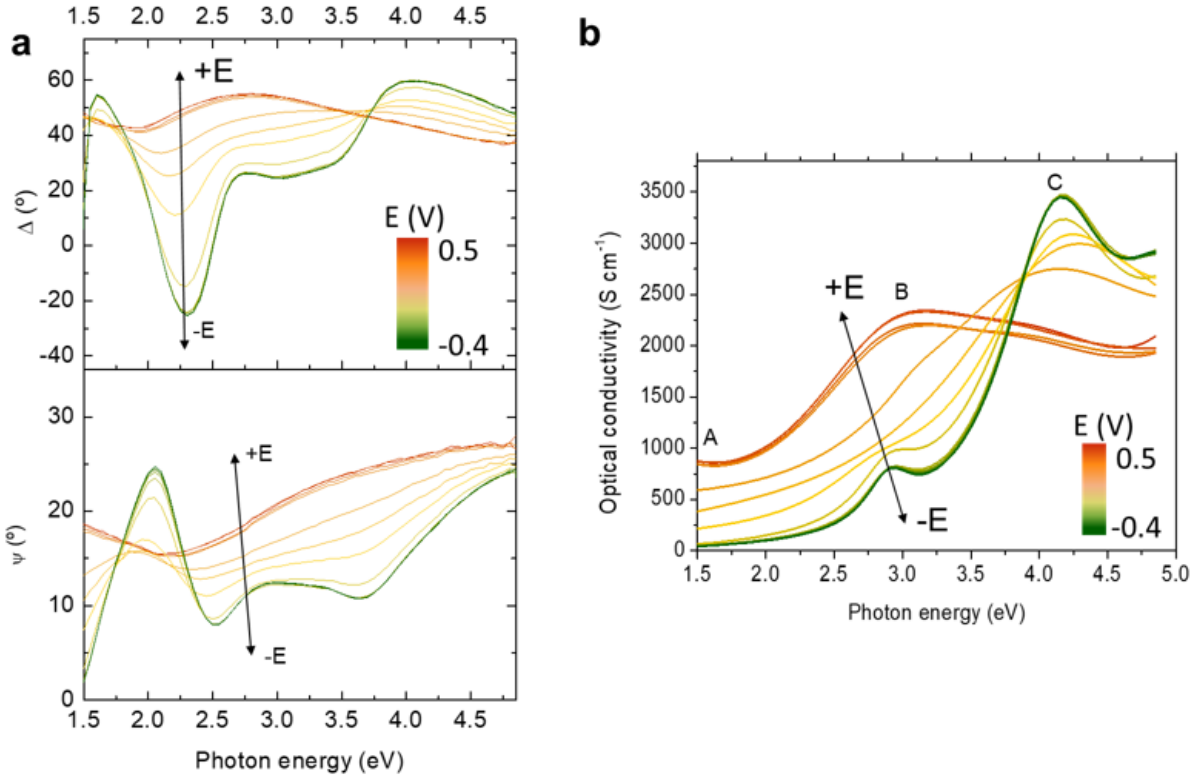


**Figure 4.11 a.** In-situ ellipsometry signals (Δ and $\psi$) of the LSF/LSM20/Nb:STO sample as a function of applied voltage (see the colour scale bar). **b.** Optical conductivity spectra of the LSF50 thin film recorded at various intercalation potentials (applied voltages). The arrows indicate the variation of intercalation potential, "A", "B" and "C" label the optical transitions.

### 4.4.3 Concentration of electronic holes during ionic intercalation

In **Chapter 3**, the concentration of electronic holes in LSF has been directly related to the intensity of the low energy transition "A". However, the high optical absorption of the liquid electrolyte in the infrared region hinders the application of the same procedure in this study. In order to overcome such a limitation, we focus here on the variation of the LSF films' optical conductivity at the photon energy of 2 eV. In **Figure 4.12a**, the presence of a linear relation with the $Fe^{4+}$ holes concentration is demonstrated. Considering the fact that the concentration of holes in the KOH-reduced LSF50 thin film is negligible and the

concentration of holes in the KOH-oxidized LSF50 film is defined by the Sr dopant (≈0.44 per unit cell),[33,50] a linear relation at 2 eV is also considered here to extract the hole concentration at each potential. The slight deviation observed in the KOH-oxidized LSF50 thin film and the one deposited on CGO/YSZ may be attributed to the nature of the LSF50 thin film and the substrate. Therefore, the concentration of electron holes in the LSF50 film can be indirectly determined from the optical conductivity at the photon energy of 2 eV using the linear relation defined by the data of KOH-reduced and KOH-oxidized thin films.

As a result, the $Fe^{4+}$ holes concentration at different intercalation potentials was quantified, see **Figure 4.12b**. The curve strongly suggests a single electrochemical exchange process (proton intercalation or oxygen extraction) during the reduction, as shown by the gradual decrease of the iron valence. Moreover, it is also interesting to compare the charge transferred after each voltage step (*i.e.* incremental capacity[51]) calculated by ellipsometry and by electrochemical method. Since the $Fe^{4+}/Fe^{3+}$ transition is accompanied by charge transfer as:

$$Fe_{Fe}^{\cdot} + 1e' \rightarrow Fe_{Fe}^{x} \qquad \text{(Equation 4.3)}$$

The number of charge transferred in the reduction reaction can be calculated via the ellipsometry approach as:

$$Q_{elliposmetry} = n \cdot [Fe^{4+}] \cdot F \qquad \text{(Equation 4.4)}$$

Where *n* is the number of LSF50 cell (in mol) in the thin film and *F* is the Faraday constant. On the other hand, the charge transferred at each stepwise voltage can be obtained calculating the area under the *I-t* curve of **Figure 4.10b**, as:[52]

$$Q_{electrochemical} = \int_{t1}^{t2} I(t)dt \qquad \text{(Equation 4.5)}$$

**Figure 4.12c** shows the incremental capacity obtained from the electrochemical and ellipsometry measurements employing the **Equations 4.4** and **4.5**, respectively. A good agreement in the trend of the incremental capacity obtained by the two approaches is observed, although the electrochemical method systematically shows a slightly larger value of charge transferred at each voltage step. This behavior can be ascribed to the electrochemical reactions (charge transfer) on the film surface caused, for instance, by oxygen reduction reaction (ORR),[24,53] which would not change the Fe oxidation state. Since in-situ ellipsometry is bulk-sensitive, it is able to differentiate the battery-like behavior

linked to the ionic insertion from the electrochemical reactions taking place on the sample surface.[54]

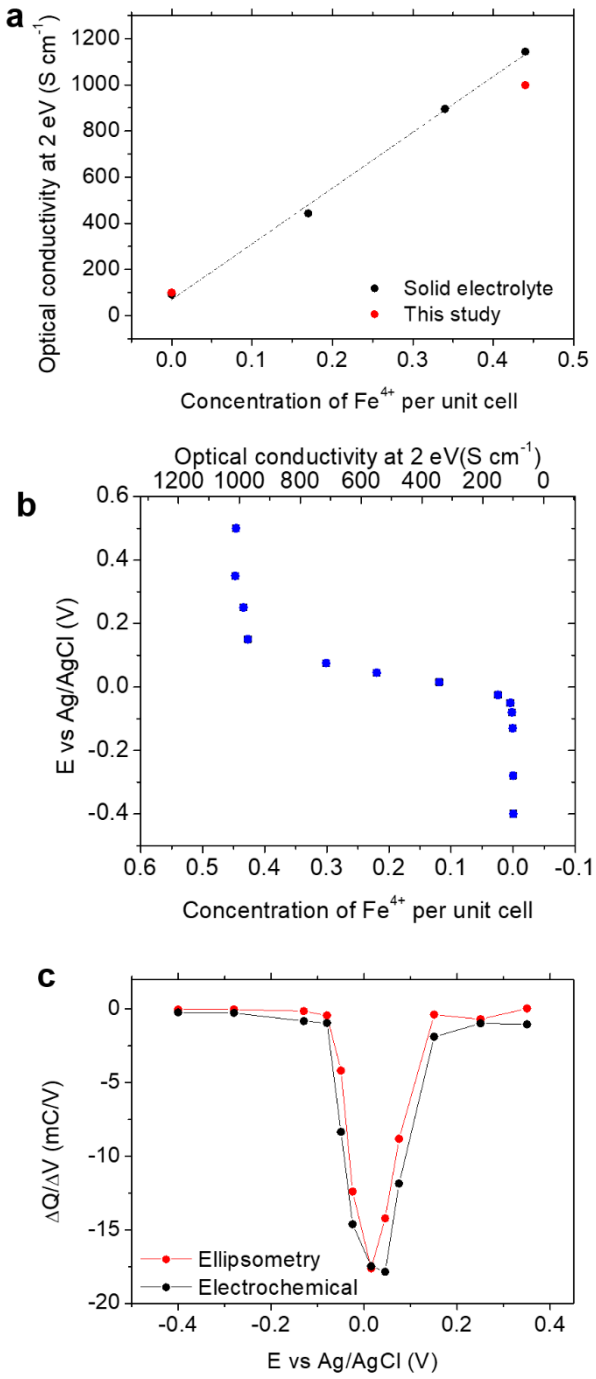


**Figure 4.12 a.** Linear relation between the optical conductivity of LSF at the photon energy of 2 eV and $Fe^{4+}$ concentration, which is extracted from the study reported in **Chapter 3** for the LSF/CGO/YSZ samples. **b.** Potential profiles of the LSF50 layer as a function of $Fe^{4+}$ concentration and optical conductivity. **c.** Comparison of the incremental capacity of the LSF50 thin film obtained from the electrochemical and ellipsometry results.

It is important to discuss here the effect that the different fitting models may have on the equilibrium hole concentration extracted by ellipsometry. For investigating the effects of the LSF50 film's thickness and roughness on the ellipsometry data analysis, three different models are considered, as shown in **Figure 4.13.** In the first model, the thickness and the roughness of the LSF50 film are kept free for data modelling (**Figure 4.13a**). In the second, the thickness of the LSF50 film is kept fixed while the roughness is kept variable (**Figure 4.13b**). In turn, in the third model, the thickness and the roughness of the LSF50 layer are kept constant (**Figure 4.13c**). The sum of the thickness and roughness of the LSF50 film given by the ellipsometry data fitting using the model a (**Figure 4.13a**) is depicted in **Figure 4.13d**. Here, a significant variation about 13% in the film thickness is observed, this conflicts with the slight expansion about 2% detected by HR-XRD and ex-situ ellipsometry as previously stated. The origin of this significant expansion is still unclear, however, it could be due to the surface electrochemical reactions which interfere with the sensitivity of the ellipsometry to the LSF50 film's thickness and roughness.

Nevertheless, one must note that the $Fe^{4+}$ concentration given by the optical conductivity extracted by the three models is coincident (**Figure 4.13e**), revealing that the concentration of electron holes derived from the optical conductivity is unaffected by the sensitivity of the ellipsometry to the film thickness and roughness in the data analysis. Therefore, the model is not expected to influence the equilibrium concentration of $Fe^{4+}$ obtained by in-situ ellipsometry measurements.

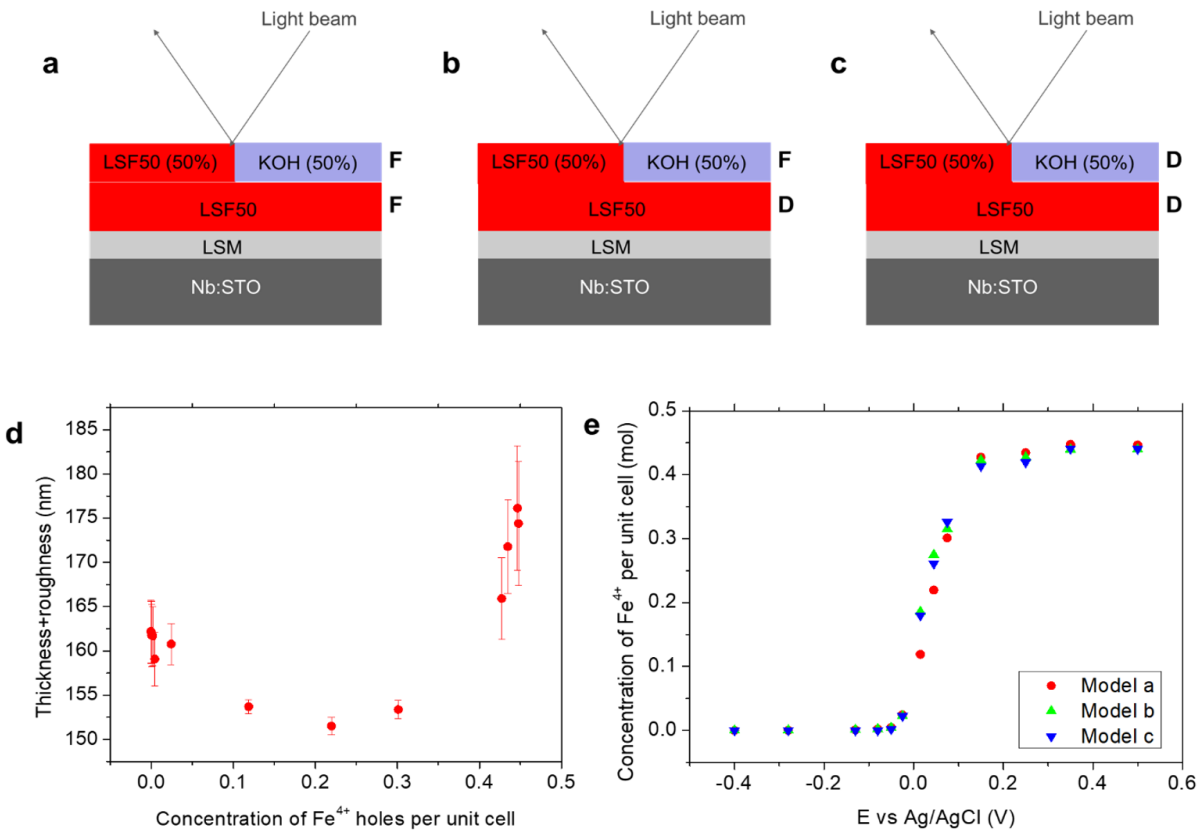


**Figure 4.13 a-c.** Models proposed for simulating and fitting the ellipsometry data. **a.** Model in which both the film thickness and roughness of the LSF50 are kept free, **b.** Model in which the film thickness of LSF50 is kept fixed while the roughness is kept free and **c.** Model in which both the film thickness and roughness are kept fixed for LSF50. **d.** Sum of thickness and roughness given by the model a. **e.** Holes concentration as a function of intercalation potential derived from the optical conductivity which is fitted by employing the three proposed models.

### 4.4.4 Defect chemistry modelling

The results obtained in the previous sections suggest that: (i) Protons enter in the LSF50 thin films upon electrochemical reduction. (ii) Oxygen is also exchanged during ionic intercalation with the electrolyte and the same equilibrium can be reached regardless on the initial defect concentration in the layer. (iii) A single electrochemical process is observed upon reduction, i.e. protons and oxygen are exchanged together. Therefore, ion intercalation can be described as a combination of oxygenation and hydrogenation reaction involving oxygen anions and protons. The global reaction can be written as a sum of the oxygenation reaction (**Equation 4.1**) and the hydration reaction (**Equation 4.2**) as:

$$3OH_i' + V_O^{\cdot\cdot} + OH^{\cdot} + 3Fe_{Fe}^{x} \leftrightarrow 2O_O^{x} + 3Fe_{Fe}^{\cdot} + 2H_2O(l) + 3e_l' \qquad \text{(Equation 4.6)}$$

Applying Nernst equation, the potential for the ion intercalation can be expressed as:

$$E = E_0 + \frac{RT}{3F}\ln\left(\frac{[O_O^x]^2[Fe_{Fe}^{\cdot}]^3}{[V_O^{\cdot\cdot}][OH^{\cdot}][Fe_{Fe}^x]^3}\right) + \frac{RT}{3F}\ln\left(\frac{[H_2O]^2}{[OH']^3}\right) \qquad \text{(Equation 4.7)}$$

Where $E_0$ is the standard potential of the ionic intercalation, $R$ is the gas constant (8.314 $Jmol^{-1}K^{-1}$). The first logarithmic component on the right-hand-side of the equation is linked to the concentration of the point defects in the LSF thin film, and the second logarithmic term is associated with the concentration of the ions in the liquid electrolyte with the activity coefficient assumed to be 1.[55,56] Thus, **Equation 4.7** can be rewritten as:

$$E = E_0 + \frac{RT}{3F}\ln\left(\frac{[O_O^x]^2[Fe_{Fe}^{\cdot}]^3}{[V_O^{\cdot\cdot}][OH^{\cdot}][Fe_{Fe}^x]^3}\right) + 0.16\,V \qquad \text{(Equation 4.8)}$$

Because the electronic transition $Fe^{3+}/Fe^{2+}$ was not detected in the studied potential window,[16] the $Fe^{2+}$ electrons in the LSF50 are negligible. Thus, the electronic equilibrium in the LSF50 film is:[57,58]

$$2[V_O^{\cdot\cdot}] + [OH^{\cdot}] + [Fe_{Fe}^{\cdot}] = [Sr_{La}'] = 0.44 \qquad \text{(Equation 4.9)}$$

$$[Fe_{Fe}^{\cdot}] + [Fe_{Fe}^x] = 1 \qquad \text{(Equation 4.10)}$$

The ratio between the concentration of oxygen vacancies $V_{\ddot{O}}$ and $OH^{\cdot}$ ions can be determined by the hydration reaction:[56,59,60]

$$H_2O(l) + V_O^{\cdot\cdot} + O_O^x \leftrightarrow 2OH^{\cdot} \qquad \text{(Equation 4.11)}$$

With the equilibrium constant $K_w$:

$$K_w = \frac{[OH^{\cdot}]^2}{[H_2O_l][V_O^{\cdot\cdot}][O_O^x]} \qquad \text{(Equation 4.12)}$$

The hydration equilibrium constant depends on the material´s properties and defines the total amount of protons that can be incorporated in the layer. The protonation mechanism of ferrites perovskites in high temperature humid environment was studied in detail by Prof. Maier and co-workers.[39,58,61–63] Interestingly, they found that in the intermediate temperature range 250 °C - 500 °C LSF presents quite a low protonic concentration, especially when compared with Ba-doped ferrites. Nevertheless, the protonation mechanism (**Equation 4.11**) is regulated by an endothermic reaction, meaning that the concentration of protons will be higher at lower temperatures. Considering the enthalpy and entropy of the hydration reaction measured for LSF,[39,58,61–63] a value of $K_w$ around 0.1 can be extrapolated at room temperature,

which is comparable with the protonation constant measured for a good protonic conductor such as $Ba_{0.5}Sr_{0.5}Fe_{0.8}Zn_{0.2}O_{3-\delta}$ at 400 °C. Since no quantitative information on the concentration of protons in the reduced LSF50 thin films can be deduced from SIMS measurements, a value of $K_w$=0.1 has been fixed in this study.

The set of **Equations 4.7-4.12** can be combined for obtaining an expression where the electrochemical potential of intercalation can be described as a function of $Fe^{4+}$ hole concentration, as:

$$E = E_0 + \frac{RT}{3F}\ln\left(\frac{(2.56+[V_O^{\cdot\cdot}]+[Fe_{Fe}^{\cdot}])^2\,[Fe_{Fe}^{\cdot}]^3}{[V_O^{\cdot\cdot}](0.44-2[V_O^{\cdot\cdot}]-[Fe_{Fe}^{\cdot}])(1-[Fe_{Fe}^{\cdot}])^3}\right) + 0.16\,V \qquad \text{(Equation 4.13)}$$

Where $[V_{\ddot{o}}]$ is the solution of the second-order equation:

$$2.56 + [V_O^{\cdot\cdot}] + [Fe_{Fe}^{\cdot}] = \frac{(0.44-2[V_O^{\cdot\cdot}]-[Fe_{Fe}^{\cdot}])^2}{K_w[V_O^{\cdot\cdot}]} \qquad \text{(Equation 4.14)}$$

With these equations, it is possible to fit the equilibrium $Fe^{4+}$ concentration obtained at each electrochemical potential considering only $E_0$ as a free parameter. **Figure 4.14** shows the results of the model obtained for a $E_0$ = 0.83 V (vs RHE) or -0.083 V (vs Hg/HgO). An excellent fit of the experimental data is obtained, suggesting that the proposed model is able to describe the mechanism of ionic intercalation in LSF50 thin films. The model shows that the concentration of protons and oxygen vacancies increases while reducing the samples until the majority of holes is consumed.

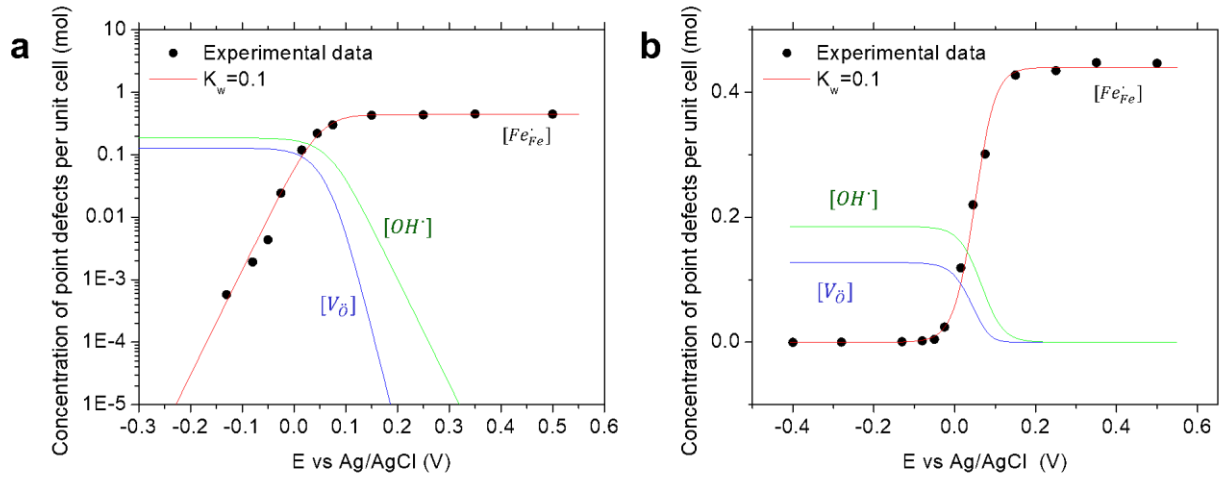


**Figure 4.14 a.** Logarithmic plots and **b.** Linear plots of defect chemistry modelling for the experimentally obtained $Fe^{4+}$ holes concentration with the equilibrium constant $K_w$=0.1.

Finally, it is worth to discuss the effect of the hydration equilibrium constant on the defect chemistry in liquid. Three possible cases are considered: i) the ion intercalation is dominated by the oxygenation reaction (**Equation 4.1**) assuming that the constant $K_w$ equals to $10^{-3}$ (**Figure 4.15a** and **b**); ii) the oxygenation and hydrogenation reactions are supposed to have the similar importance in the ion intercalation assuming that the constant $K_w$ equal to 0.1 (**Figure 4.15c** and **d**); iii) the hydrogenation reaction is assumed to be dominant with the constant $K_w = 100$ (**Figure 4.15e** and **f**). One must note that all three models are able to reproduce the concentration of electron holes in the LSF50 film, however, the concentration of $V_O^{\cdot\cdot}$ and $OH^{\cdot}$distinguishes them. For the mixed reactions in the hydration regime (**Figure 4.15b** and **c**), the concentration of $OH^{\cdot}$ ions is found to be higher than that of $V_O^{\cdot\cdot}$ vacancies, being consistent with what suggested by Zohourian *et al.*.[39] The hydration reaction becomes more favorable with a larger equilibrium constant $K_w$ as the temperature decreases, giving rise to the formation of concentrated $OH^{\cdot}$ ions. Overall, the obtained concentration of $Fe^{4+}$ can be satisfactorily described by the defect chemistry model in a wide range of the equilibrium constant $K_w$, although with different $\frac{[V_O^{\cdot\cdot}]}{[OH^{\cdot}]}$ ratios.

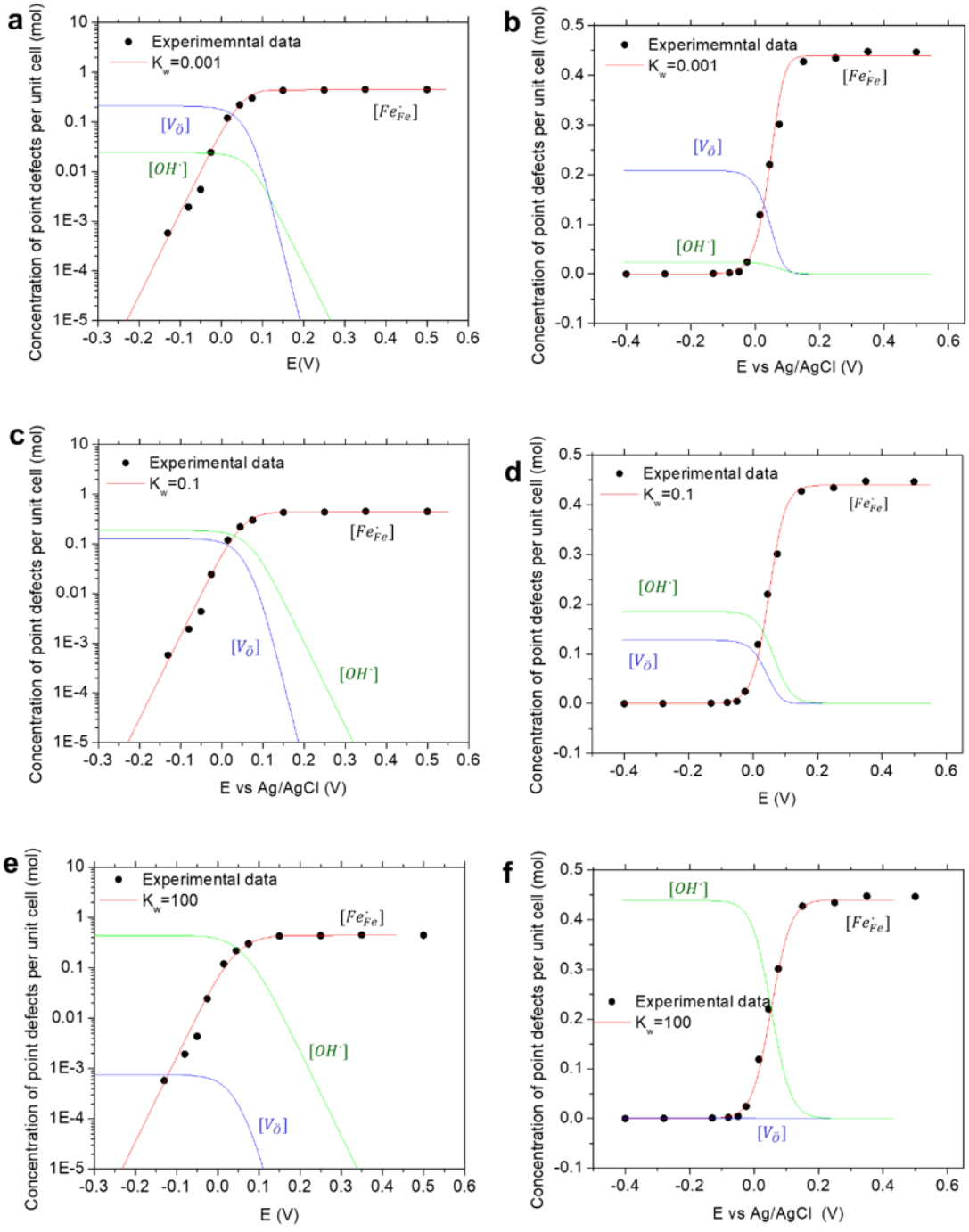


**Figure 4.15** Experimentally obtained $Fe^{4+}$ concentration as a function of intercalation potential (symbols) and defect chemistry modelling of the point defects concentration in the LSF50 thin film for **a-b.** Oxygenation dominated reaction. **c-d.** Mixed oxygenation and hydrogenation reaction and **e-f.** Hydrogenation dominated reaction. (Solid lines). **a.**, **c.** and **e.** show the plots of the point defects concentration in logarithmic scale. **b.**, **d.** and **f.** show the plots of the point defects concentration in linear scale.

## 4.5 Conclusions

In summary, an electrochemical field (induced by an applied voltage) forces the intercalation of ions from the alkaline electrolyte to the LSF50 bulk resulting in the $Fe^{4+}/Fe^{3+}$electronic transition. In this work, the ion intercalation was characterized by CV. The intercalation mechanism consists in the mixed oxygenation and hydration reactions and was unambiguously determined by ex-situ HR-XRD, ex-situ ellipsometry and SIMS techniques. PALS technique was employed to determine the ion intercalation-induced open-volume defects in the thin film while in-situ ellipsometry showed a high sensitivity to the depletion of $Fe^{4+}$ electron holes along the reduction reaction. The concentration of $Fe^{4+}$ holes in the LSF50 film was derived from the optical conductivity via the linear proportionality of the optical conductivity at the photon energy of 2 eV with the concentration of holes. The evolution of $Fe^{4+}$ concentration with intercalation potential was satisfactorily described by the dilute defect chemistry models, highlighting that the intercalation mechanism is defined by oxygenation and hydration reactions. Overall, in-situ ellipsometry approach is successful for studying the defect chemistry of LSF50 oxide thin films upon ion intercalation in alkaline media, opening a new way to the rational engineering of the LSF50 thin film's functional properties for energy and information applications.

# References


1. Nowroozi, M. A., Ivlev, S., Rohrer, J. & Clemens, O. $La_2CoO_4$: A new intercalation based cathode material for fluoride ion batteries with improved cycling stability. *J. Mater. Chem. A* **6**, 4658–4669 (2018).

2. Poizot, P., Laruelle, S., Grugeon, S., Dupont, L. & Tarascon, J. M. Nano-sized transition-metal oxides as negative-electrode materials for lithium-ion batteries. *Nature* **407**, 496–499 (2000).

3. Alcántara, R., Lavela, P., Tirado, J. L., Zhecheva, E. & Stoyanova, R. Recent advances in the study of layered lithium transition metal oxides and their application as intercalation electrodes. *J. Solid State Electrochem.* **3**, 121–134 (1999).

4. Zhao, N. *et al.* Beyond intercalation-based supercapacitors: The electrochemical oxidation from $Mn_3O_4$ to $Li_4Mn_5O_{12}$ in $Li_2SO_4$ electrolyte. *Nano Energy* **71**, 104626 (2020).

5. Nan, H. shan, Hu, X. ying & Tian, H. wei. Recent advances in perovskite oxides for anion-intercalation supercapacitor: A review. *Mater. Sci. Semicond. Process.* **94**, 35–50 (2019).

6. Brezesinski, T., Wang, J., Tolbert, S. H. & Dunn, B. Next generation pseudocapacitor materials from sol-gel derived transition metal oxides. *J. Sol-Gel Sci. Technol.* **57**, 330–335 (2011).

7. Mefford, J. T., Hardin, W. G., Dai, S., Johnston, K. P. & Stevenson, K. J. Anion charge storage through oxygen intercalation in $LaMnO_3$ perovskite pseudocapacitor electrodes. *Nat. Mater.* **13**, 726–732 (2014).

8. Deng, G. *et al.* Electrochemical properties of $La_{1-x}Sr_xFeO_3$ (x = 0.2, 0.4) as negative electrode of Ni-MH batteries. *Electrochim. Acta* **54**, 3910–3914 (2009).

9. Henao, J. & Martinez-Gomez, L. Review: on rare-earth perovskite-type negative electrodes in nickel–hydride (Ni/H) secondary batteries. *Mater. Renew. Sustain. Energy* **6**, 7 (2017).

10. Hibino, M., Kimura, T., Suga, Y., Kudo, T. & Mizuno, N. Oxygen rocking aqueous

batteries utilizing reversible topotactic oxygen insertion/extraction in iron-based perovskite oxides $Ca_{1-x}La_xFeO_{3-\delta}$. *Sci. Rep.* **2**, 601 (2012).

11. Lang, X., Mo, H., Hu, X. & Tian, H. Supercapacitor performance of perovskite $La_{1-x}Sr_xMnO_3$. *Dalt. Trans.* **46**, 13720–13730 (2017).

12. Tomar, A. K., Joshi, A., Singh, G. & Sharma, R. K. Perovskite oxides as supercapacitive electrode : Properties , design and recent advances. *Coord. Chem. Rev.* **431**, 213680 (2020).

13. Nguyen, H. T. D., Zhang, D., Nguyen, T. M., Zhang, H. & Seidel, J. Topotactic Electrochromism for Efficient Coloration Applications. *Adv. Opt. Mater.* **n/a**, 2100955 (2021).

14. Sun, Y. *et al.* Electrochromic Properties of Perovskite $NdNiO_3$ Thin Films for Smart Windows. **3**, 1719–1731 (2021).

15. Sood, A. *et al.* Electrochemical ion insertion from the atomic to the device scale. *Nat. Rev. Mater.* **6**, 847–867 (2021).

16. Alexander, C. T. *et al.* Anion-Based Pseudocapacitance of the Perovskite Library $La_{1-x}Sr_xBO_{3-\delta}$ (B=Fe,Mn,Co). *ACS Appl. Mater. Interfaces* **11**, 5084–5094 (2019).

17. Lu, Q. *et al.* Bi-directional tuning of thermal transport in $SrCoO_x$ with electrochemically induced phase transitions. *Nat. Mater.* **19**, 655–662 (2020).

18. Hu, S. *et al.* Voltage-Controlled Oxygen Non-Stoichiometry in $SrCoO_{3-\delta}$ Thin Films. *Chem. Mater.* **31**, 6117–6123 (2019).

19. Ling, T. *et al.* Atomic-level structure engineering of metal oxides for high-rate oxygen intercalation pseudocapacitance. *Sci. Adv.* **4**, eaau6261 (2018).

20. Xu, Z., Liu, Y., Zhou, W., Tade, M. O. & Shao, Z. B-Site Cation-Ordered Double-Perovskite Oxide as an Outstanding Electrode Material for Supercapacitive Energy Storage Based on the Anion Intercalation Mechanism. *ACS Appl. Mater. Interfaces* **10**, 9415–9423 (2018).

21. Wang, W. *et al.* Synthesis, morphology and electrochemical performances of perovskite-type oxide $La_xSr_{1-x}FeO_3$ nanofibers prepared by electrospinning. *J. Phys. Chem. Solids* **124**, 144–150 (2019).

22. Mefford, J. T. *et al.* Water electrolysis on $La_{1-x}Sr_xCoO_{3-\delta}$ perovskite electrocatalysts. *Nat. Commun.* **7**, 11053 (2016).

23. Grimaud, A. *et al.* Activating lattice oxygen redox reactions in metal oxides to catalyse oxygen evolution. *Nat. Chem.* **9**, 457–465 (2017).

24. Shen, Z. *et al.* Increased activity in the oxygen evolution reaction by $Fe^{4+}$-induced hole states in perovskite $La_{1-x}Sr_xFeO_3$. *J. Mater. Chem. A* **8**, 4407–4415 (2020).

25. Saleem, M. S. *et al.* Electric Field Control of Phase Transition and Tunable Resistive Switching in $SrFeO_{2.5}$. *ACS Appl. Mater. Interfaces* **11**, 6581–6588 (2019).

26. Wu, S. M. *et al.* Reversible electric control of exchange bias in a multiferroic field-effect device. *Nat. Mater.* **9**, 756–761 (2010).

27. Lankauf, K. *et al.* The effect of Fe on chemical stability and oxygen evolution performance of high surface area $SrTi_{x-1}Fe_xO_{3-\delta}$ mixed ionic-electronic conductors in alkaline media. *Int. J. Hydrogen Energy* **46**, 28575–28590 (2021).

28. Wang, L., Yang, Z., Bowden, M. E. & Du, Y. Brownmillerite phase formation and evolution in epitaxial strontium ferrite heterostructures. *Appl. Phys. Lett.* **114**, 231602 (2019).

29. Yang, F. *et al.* Microstructure and magnetic studies of $La_{1-x}Sr_xFeO_3$ nano particles fabricated by the citrate sol-gel method. *Medziagotyra* **25**, 231–237 (2019).

30. Chen, X. & Grande, T. Anisotropic and Nonlinear Thermal and Chemical Expansion of $La_{1-x}Sr_xFeO_{3-\delta}$ (x = 0.3, 0.4, 0.5) Perovskite Materials. *Chem. Mater.* **25**, 3296–3306 (2013).

31. Xie, Y. *et al.* Control of functional responses via reversible oxygen loss in $La_{1-x}Sr_xFeO_{3-\delta}$ films. *Adv. Mater.* **26**, 1434–1438 (2014).

32. Cao, X., Yan, X., Ke, L., Zhao, K. & Yan, N. Proton-Assisted Reconstruction of Perovskite Oxides: Toward Improved Electrocatalytic Activity. *ACS Appl. Mater. Interfaces* **13**, 22009–22016 (2021).

33. MIZUSAKI, J., SASAMOTO, T., CANNON, W. R. & BOWEN, H. K. Electronic Conductivity, Seebeck Coefficient, and Defect Structure of $LaFeO_3$. *J. Am. Ceram. Soc.* **65**, 363–368 (1982).

34. Tang, Y. *et al.* Pushing the Study of Point Defects in Thin Film Ferrites to Low Temperatures Using In Situ Ellipsometry. *Adv. Mater. Interfaces* **8**, 2001881 (2021).

35. Smolin, S. Y. *et al.* Static and Dynamic Optical Properties of $La_{1-x}Sr_xFeO_{3-\delta}$: The Effects of A-Site and Oxygen Stoichiometry. *Chem. Mater.* **28**, 97–105 (2016).

36. Yan, L. *et al.* $La_{0.8}Sr_{0.2}MnO_3$-Based Perovskite Nanoparticles with the A-Site Deficiency as High Performance Bifunctional Oxygen Catalyst in Alkaline Solution. *ACS Appl. Mater. Interfaces* **9**, 23820–23827 (2017).

37. Xu, W. *et al.* Polymer-assisted chemical solution synthesis of $La_{0.8}Sr_{0.2}MnO_3$-based perovskite with A-site deficiency and cobalt-doping for bifunctional oxygen catalyst in alkaline media. *Electrochim. Acta* **273**, 80–87 (2018).

38. Li, H. B. *et al.* Electric Field–Controlled Multistep Proton Evolution in $H_xSrCoO_{2.5}$ with Formation of H–H Dimer. *Adv. Sci.* **6**, 1901432 (2019).

39. Zohourian, R., Merkle, R., Raimondi, G. & Maier, J. Mixed-Conducting Perovskites as Cathode Materials for Protonic Ceramic Fuel Cells: Understanding the Trends in Proton Uptake. *Adv. Funct. Mater.* **28**, 1801241 (2018).

40. Wilde, P. M., Guther, T. J., Oesten, R. & Garche, J. Strontium ruthenate perovskite as the active material for supercapacitors. *J. Electroanal. Chem.* **461**, 154–160 (1999).

41. Keeble, D. J. *et al.* Identification of A- and B-site cation vacancy defects in perovskite oxide thin films. *Phys. Rev. Lett.* **105**, 226102 (2010).

42. Nieminen, R. M. & Laakkonen, J. Positron trapping rate into vacancy clusters. *Appl. Phys.* **20**, 181–184 (1979).

43. Bharathi, A. *et al.* Positron Annihilation Study of Oxygen Vacancies in $Y_1Ba_2Cu_3O_{7-x}$. *Europhys. Lett.* **6**, 369–374 (1988).

44. Qin, M. *et al.* Point defect structure of La-doped $SrTiO_3$ ceramics with colossal permittivity. *Acta Mater.* **164**, 76–89 (2019).

45. Siebenhofer, M. *et al.* Exploring point defects and trap states in undoped $SrTiO_3$ single crystals. *J. Eur. Ceram. Soc.* (2021).

46. Henao, J., Sotelo, O., Casales-Diaz, M. & Martinez-Gomez, L. Hydrogen storage in

a rare-earth perovskite-type oxide $La_{0.6}Sr_{0.4}Co_{0.2}Fe_{0.8}O_3$ for battery applications. *Rare Met.* **37**, 1003–1013 (2018).

47. Scafetta, M. D., Xie, Y. J., Torres, M., Spanier, J. E. & May, S. J. Optical absorption in epitaxial $La_{1-x}Sr_xFeO_3$ thin films. *Appl. Phys. Lett.* **102**, 081904 (2013).

48. Khare, A. *et al.* Topotactic Metal–Insulator Transition in Epitaxial $SrFeO_x$ Thin Films. *Adv. Mater.* **29**, 1606566 (2017).

49. Wang, L. *et al.* Hole-induced electronic and optical transitions in $La_{1-x}Sr_xFeO_3$ epitaxial thin films. *Phys. Rev. Mater.* **3**, 025401 (2019).

50. Mizusaki, J., Yoshihiro, M., Yamauchi, S. & Fueki, K. Nonstoichiometry and defect structure of the perovskite-type oxides $La_{1-x}Sr_xFeO_{3-\delta}$. *J. Solid State Chem.* **58**, 257–266 (1985).

51. Jang, Y. Il, Neudecker, B. J. & Dudney, N. J. Lithium diffusion in $Li_xCoO_2$ ($0.45 < x < 0.7$) intercalation cathodes. *Electrochem. Solid-State Lett.* **4**, A74 (2001).

52. Gogotsi, Y. & Penner, R. M. Energy Storage in Nanomaterials - Capacitive, Pseudocapacitive, or Battery-like? *ACS Nano* **12**, 2081–2083 (2018).

53. Yan, W. Y. *et al.* The influence of KOH concentration, oxygen partial pressure and temperature on the oxygen reduction reaction at Pt electrodes. *J. Electroanal. Chem.* **741**, 100–108 (2015).

54. Morata, A. *et al.* Operando probing of Li-insertion into $LiMn_2O_4$ cathodes by spectroscopic ellipsometry. *Journal of Materials Chemistry A* vol. **8** 11538–11544 (2020).

55. Perry, N. H., Pergolesi, D., Bishop, S. R. & Tuller, H. L. Defect chemistry and surface oxygen exchange kinetics of La-doped $Sr(Ti,Fe)O_{3-\alpha}$ in oxygen-rich atmospheres. *Solid State Ionics* **273**, 18–24 (2015).

56. Poetzsch, D., Merkle, R. & Maier, J. Proton conductivity in mixed-conducting BSFZ perovskite from thermogravimetric relaxation. *Phys. Chem. Chem. Phys.* **16**, 16446–16453 (2014).

57. Kuhn, M., Hashimoto, S., Sato, K., Yashiro, K. & Mizusaki, J. Oxygen nonstoichiometry, thermo-chemical stability and lattice expansion of $La_{0.6}Sr_{0.4}FeO_{3-}$

$_{\delta}$. *Solid State Ionics* **195**, 7–15 (2011).

58. Poetzsch, D., Merkle, R. & Maier, J. Proton uptake in the $H^+$-SOFC cathode material $Ba_{0.5}Sr_{0.5}Fe_{0.8}Zn_{0.2}O_{3-\delta}$: transition from hydration to hydrogenation with increasing oxygen partial pressure. *Faraday Discuss.* **182**, 129–143 (2015).

59. Kreuer, K. D. Proton-Conducting Oxides. *Annu. Rev. Mater. Res.* **33**, 333–359 (2003).

60. Papac, M., Stevanović, V., Zakutayev, A. & O'Hayre, R. Triple ionic–electronic conducting oxides for next-generation electrochemical devices. *Nat. Mater.* **20**, 301–313 (2021).

61. Gryaznov, D., Merkle, R., Kotomin, E. A. & Maier, J. Ab initio modelling of oxygen vacancies and protonic defects in $La_{1-x}Sr_xFeO_{3-\delta}$ perovskite solid solutions. *J. Mater. Chem. A* **4**, 13093–13104 (2016).

62. Hoedl, M. F., Gryaznov, D., Merkle, R., Kotomin, E. A. & Maier, J. Interdependence of Oxygenation and Hydration in Mixed-Conducting $(Ba,Sr)FeO_{3-\delta}$ Perovskites Studied by Density Functional Theory. *J. Phys. Chem. C* **124**, 11780–11789 (2020).

63. Poetzsch, D., Merkle, R. & Maier, J. Stoichiometry variation in materials with three mobile carriers-Thermodynamics and transport kinetics exemplifi ed for protons, oxygen vacancies, and holes. *Adv. Funct. Mater.* **25**, 1542–1557 (2015).

# 5. Synaptic transistor with solid-state electrolyte

# 5.1 Introduction

## 5.1.1 Electrolyte-gated transistors

The rapid development of artificial intelligence results in an increased demand for miniaturized hardware for neuromorphic computing with high efficiency and low energy consumption. Conventional silicon-based transistors based on Complementary Metal-Oxide Semiconductor (CMOS) technology can also be employed for neuromorphic computing but involve large areas and tremendous energy budget.[1–4] Therefore, alternative technologies emulating neuron-like behavior are being explored. Among others, memristors proved their suitability as potential alternative.[5,6] However, their device-to-device (even cycle-to-cycle) variability represents a major drawback for the real implementation of the technology.[5]

Alternative to memristors, three-terminal transistors emerged as a promising option for neuromorphic circuit devices. Three-terminal Electrolyte-Gated Transistors (EGTs) are similar to conventional transistors but with an adjustable channel able to analogically modify its electrical properties by ion-gating. In EGTs, an electrolyte substitutes the dielectric in conventional transistors in such a way that the charge carrier concentration in the channel is controlled by the ions accumulated at the electrolyte-channel interface.[7] Since the accumulation is in the vicinity of the interface (nanometric gap), the formed capacitor presents a very high capacitance inducing a large variation in the channel carrier density.[7] More interestingly, if the channel consists on a MIEC, it can accept intercalation and transport of ions in and out , which permanently modifies its state of charge giving rise to a long-term plasticity effect.[8,9] This plasticity in the channel opens the way to fabricate EGTs for neuromorphic applications.[8,10] The insulating characteristics of the electrolyte prevent the current leakage resulting in less energy loss.[11,12]

Different ion conductors have been employed as electrolytes for developing EGTs. In the case of protons, the mechanism of insertion of $H^+$ into the channel of the transistor is found to be reversible and non-volatile, however, the poor retention properties of the $H^+$ intercalation-based transistors and a notable moisture sensitivity limit their use in long-term applications.[6,13] Similar limitations are found when using Li as intercalating ion. While high Li mobility at room temperature has made this ion a preferred choice for transistor applications.[14] Its intrinsic volatility problems represent a hindrance for its implementation. In several studies, synaptic transistors based on the topotactic transformation of $SrMO_{3-\delta}$ (M = Fe or Co etc.), which was carried out by controlling the intercalation of $O^{2-}$ anions, were

developed and good synaptic properties were reported.[8,13,15–17] Nevertheless, the liquid electrolyte used in these experiments complicates a practical device fabrication (especially regarding miniaturization). Therefore, the requirements of non-volatility, high switching speed, stability, scalability and reliability etc. should be considered in the device design in order to optimize the functionality of microelectronic devices.[3,4,18,19]

Solid-state electrolyte not only enables the coherent interface contact, which facilitates modulation of the transistor channel's electrical properties, but it also helps with circuit integration.[20,21] Considering the highly humidity-dependent performance of the transistors based on protons gating in the $SiO_2$ electrolyte and the narrow operation potential window,[21–23] Tsuchiya *et al.* developed a series of electric-double-layer transistors based on oxide ion conduction employing various solid oxide electrolytes,[21,24–26] in which the oxide ions diffuse along the oxygen vacancies without relying on the atmosphere, and the stability of thin films expands the operation potential window.[21,24–26] Moreover, Krick and Mayre ported a three-terminal $La_{1/3}Sr_{2/3}FeO_{3-\delta}$/Gd-doped $CeO_2$ transistor based on the reversible and non-volatile manipulation of oxygen vacancies in $La_{1/3}Sr_{2/3}FeO_{3-\delta}$ channels.[27]

### 5.1.2 Design concept of an ionic solid-state transistor

Inspired by the previous studies, as the schematic representation shown in **Figure 5.1a**, a solid-state electrolyte transistor, which consists of three terminals (source, drain and gate), is proposed in this chapter. Epitaxial $Bi_4V_{1.8}Cu_{0.2}O_{10.7}$ (BICUVOX) thin film deposited on (100)-oriented $(LaAlO_3)_{0.3}$-$(Sr_2AlTaO_6)_{0.7}$ (LSAT) substrates presented in **Chapter 2** and described elsewhere[28] performs the role of the electrolyte. According to the ionic conductivity of BICUVOX films reported by Garbayo *et al.*,[28] ionic conductivity of BICUVOX thin films is anisotropic, with in-plane conductivity being more than two orders of magnitude higher than out-of-plane conductivity due to the higher oxygen mobility in the in-plane direction. Furthermore, the in-plane ionic conductivity of BICUVOX thin film is significantly higher than that of YSZ and CGO, especially at low temperatures (see **Section 5.3**).[28] In this study, the in-plane configuration for the oxide ions conduction in the BICUVOX electrolyte is chosen in order to achieve the best performance of the device. Two layers are deposited on top of the BICUBOX thin film electrolyte: LSF50 thin film with dimensions of 3 mm *2.5 mm acts as the gate, and a second LSF50 film with dimensions of 0.26 mm *2.5 mm acts as the channel. Au paste was painted and cured at 600 ºC above the

gate and the two ends of the channel acting as the gate electrode, source and drain. To minimize the transit distance of oxygen ions, the Au top electrode covers the entire gate surface, as well as the separation distance between the channel and the gate was scaled down to micrometers.

The electrical properties of the LSF50 channel are modulated by the gate voltage $V_G$, as sketched in the electrical configuration shown in **Figure 5.1b**. Taking into account the electronic structure of doped LSF described in **Chapter 1**, the Sr doping gives rise to the growth of the density of the hole-induced electronic state and the shift of the majority Fe 3d/O2p orbitals towards the conduction band, enclosing the bandgap and enhancing the electrical conductivity. In **Chapter 3**, it is detailed that oxygen content has similar effects on the electronic structure of LSF: in agreement with **Equation 5.1**, under oxidizing conditions, the oxygen vacancies in LSF are filled and the concentration of iron holes increases, resulting in an enhanced electrical conductivity of LSF;[29–32] under reducing conditions, the oxygen anions in LSF are expelled and the oxidation state of Fe atoms is +3, resulting in the decreased electrical conductivity.[29–32]

$$V_O^{\bullet\bullet} + \frac{1}{2}O_2 + 2Fe_{Fe}^{\times} \leftrightarrow 2Fe_{Fe}^{\bullet} + O_O^{\times} \qquad \text{(Equation 5.1)}$$

Considering the extremely low surface exchange coefficient of LSF oxides at low temperatures,[33] the oxygen adsorption or desorption reaction on the films' surface is absent. As a result, the migration of oxide ions primarily lies on the oxygen vacancies in the bulk films. When an anodic (cathodic) voltage is applied between the gate and the source, the electric field created between the gate and the channel leads to the migration of $O^{2-}$ ions accumulated in the gate (channel) to the channel (gate) passing through the BICUVOX electrolyte. Referring to the studies of defect chemistry of LSF thin films reported in **Chapter 3** and **Chapter 4**, the concentration of point defects (oxygen vacancies and electron holes) in LSF films is highly sensitive to the Nernstian potential, even at room temperature in ionic liquid, see **Chapter 4**. It is well known that the point defects (oxygen vacancies and electron holes) strongly impact the electrical properties of LSF50 film,[34–36] the variation of the electrical properties of the channel as a response to the gate voltage was measured by applying a voltage $V_{DS}$ as low as 0.01 V between the source and the drain.

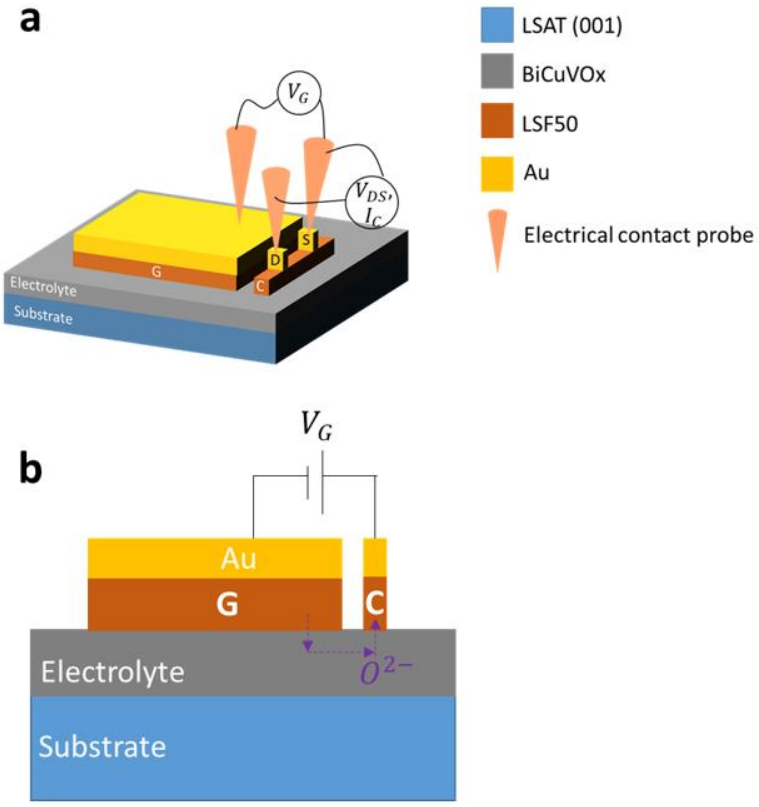


**Figure 5.1 a.** Schematic of the three-terminal solid-state electrolyte transistor. The letters "G", "C", "D" and "S" represent the Gate, Channel, Drain and Source, respectively. **b.** Schematic of the cross section of the transistor with the oxygen pathway represented by arrows.

This chapter deals with the development of a solid-state electrolyte transistor with three terminals based on the modulation of carrier density in the channel by oxide-ion intercalation. LSF50 oxide thin films with mixed ionic and electronic conductivity are employed as the gate and the channel, while BICUVOX oxide thin film is employed as the low-temperature oxygen conductor electrolyte. In this chapter, **Section 5.2** is devoted to the PLD deposition and the microstructural characterization of the oxide thin films. **Section 5.3** deals with the ionic conductivity of epitaxial BICUVOX films deposited by PLD; **Section 5.4** details the performance of the solid-state electrolyte transistor and **Section 5.5** outlines the work that would be required in the future to improve the transistor's functionality.

## 5.2 Fabrication of the synaptic transistor

BICUVOX thin films were deposited on (001)-oriented LSAT substrates with dimensions of 5 mm * 5 mm using LA-PLD. The BICUVOX film was grown with a laser frequency of 10 Hz in an oxygen partial pressure of 0.267 mbar, the substrate temperature was kept at 600 ºC and the substrate-to-target distance was set to 110 mm.[28] The LSF50 thin films were then deposited on top of the BICUVOX-covered LSAT substrates using a hard mask that allows the two LSF50 films to be separated in two independent sections. The LSF50 films were grown at the substrate temperature of 600 ºC in an oxygen partial pressure of $6.7*10^{-3}$ mbar with a laser frequency of 10 Hz. **Figure 5.2** shows the SEM image of the as-prepared sample. The LSF thin films show a different contrast in the image due to the higher electronic conductivity compared to BICUVOX. A separation distance of 0.22 mm was measured between the gate and channel.

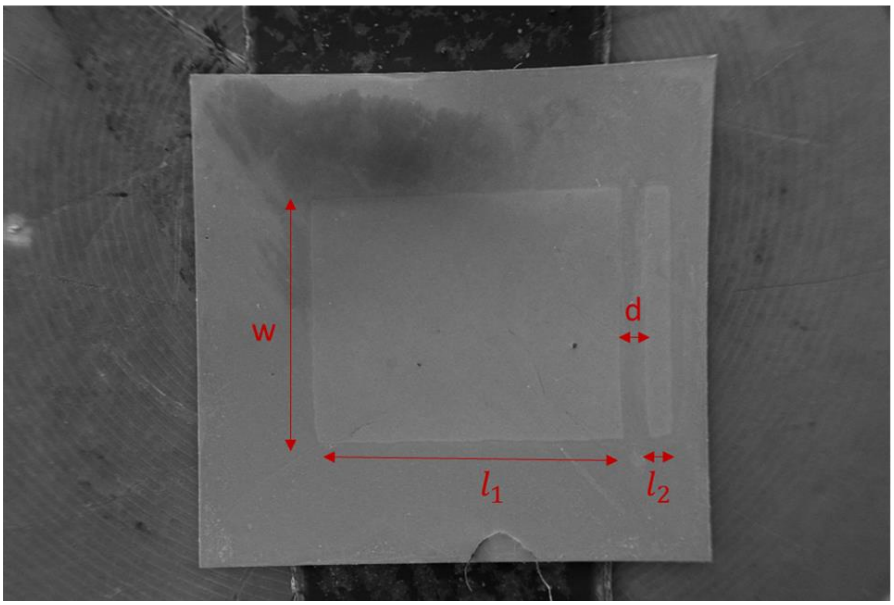


**Figure 5.2** SEM image of the LSF50/BICUVOX/LSAT sample prepared by PLD. The separation distance *d* between the two LSF50 films is 0.22 mm. The lengths $l_1$and $l_2$ are 3 mm and 0.26 mm, respectively. The width *w* is 2.5 mm.

The spectroscopic ellipsometry measurements for the LSF50/BICUVOX/LSAT sample provide the thickness of the different layers: 47±1 nm and 37±1 nm for the BICUVOX and LSF50 layers, respectively. The microstructural characteristics of the as-deposited films were measured by XRD. The XRD diagram shown in **Figure 5.3a** reveals that the unique (00$l$)-oriented BICUVOX and LSF50 phases are present in the BICUVOX and LSF50 layers without the formation of visible secondary phases, confirming the purity and epitaxy of both

films. The thickness fringes present on the both sides of the (002) diffraction peak of the BICUVOX phase (**Figure 5.3b**) indicate the coherent interference between the deposited film and the substrate.[37–39] Therefore, the BICUVOX and LSF50 films fabricated by LA-PLD present very high quality and are suitable for developing the three-terminal EGT.

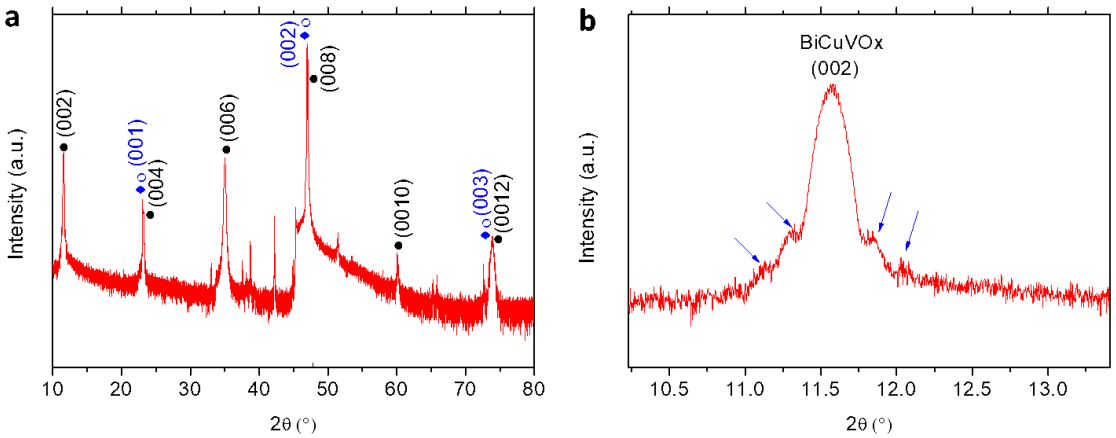


**Figure 5.3 a.** XRD diagram of the as-deposited BICUVOX and LSF50 thin films. The diffraction planes are labelled. The symbols o and ♦ represent the LSAT substrate and the LSF50 phase and the symbol ● represents the BICUVOX phase. **b.** Magnification of the (002) diffraction peak of the BICUVOX film. The arrows indicate the thickness fringes.

## 5.3 Ionic conductivity of BICUVOX electrolyte

The in-plane ionic conductivity of the epitaxial BICUVOX thin film was measured by EIS in air at different temperatures (300 ºC, 200 ºC, 150 ºC and 100 ºC). The Au electrodes on top of the gate and the channel were used as the current collectors. **Figure 5.4a** shows the Nyquist plot of the EIS spectra measured for the LSF50/BCV/LSAT sample. As the inset in **Figure 5.4a** shows, three resistive contributions to the EIS are observed at 300 ºC. The semicircle at high frequency is interpreted as the one linked to the ionic contribution of the BICUVOX bulk electrolyte, the arc at intermediate frequency is attributed to the Au metal and the arc at low frequency is associated with the surface oxygen exchange reaction on the LSF50 film. This interpretation is corroborated by the similar EIS spectra for the electrochemical cells of LSF films with YSZ electrolytes.[40] Furthermore, the ionic conductivity of BICUVOX thin film derived from the resistance of the high-frequency resistive contribution in the EIS spectra is in good accordance with the values reported in literature,[28,41] which will be discussed in details later. It is noted that the low-frequency contribution is not discernible at low temperatures, this can be explained by the high polarization resistance of the oxygen exchange reaction on the LSF50 film's surface, which shifts the impedance to very low frequency outside the measurement range.

The equivalent circuit used to simulate the EIS spectra is included in **Figure 5.4a**, the resistance $R_s$ represents the resistance of the BICUVOX electrolyte, $R_p$ indicates the polarization resistance of the oxygen exchange on the LSF50 thin film's surface and the constant phase element CPE represents the capacitance. The in-plane ionic conductivity ($\sigma_{in}$) of the epitaxial BICUVOX thin film is calculated as the inverse of the resistivity ($\rho$):

$$\sigma_{in} = \frac{1}{\rho} = \frac{d}{R_s A} \qquad \text{(Equation 5.2)}$$

Where $d$ is the ions transport distance defined as the separation distance between the gate and channel and $A$ is the area of the transversal section, which is defined as $w$ multiplied by the thickness of the BICUVOX film.

The resulting in-plane ionic conductivity of the BICUVOX film is plotted in an Arrhenius plot and compared with that of CGO and YSZ, as shown in **Figure 5.4b**. It is noted that the in-plane ionic conductivity of the epitaxial BICUVOX thin film is linearly proportional to the increment of temperature. Taking into account the margins of error owing to the uncertainty of temperature, the obtained ionic conductivity is in good agreement with that

measured for the BICUVOX film grown on $SrTiO_3$ substrate in literature.[28] Comparing with the ionic conductivity of YSZ and CGO,[42–45] the in-plane ionic conductivity of the BICUVOX film is three orders of magnitude higher, particularly at low temperatures,[28] it can be concluded that the epitaxial BICUVOX film is a pivotal electrolyte material for low-temperature solid-state electrolyte transistors.

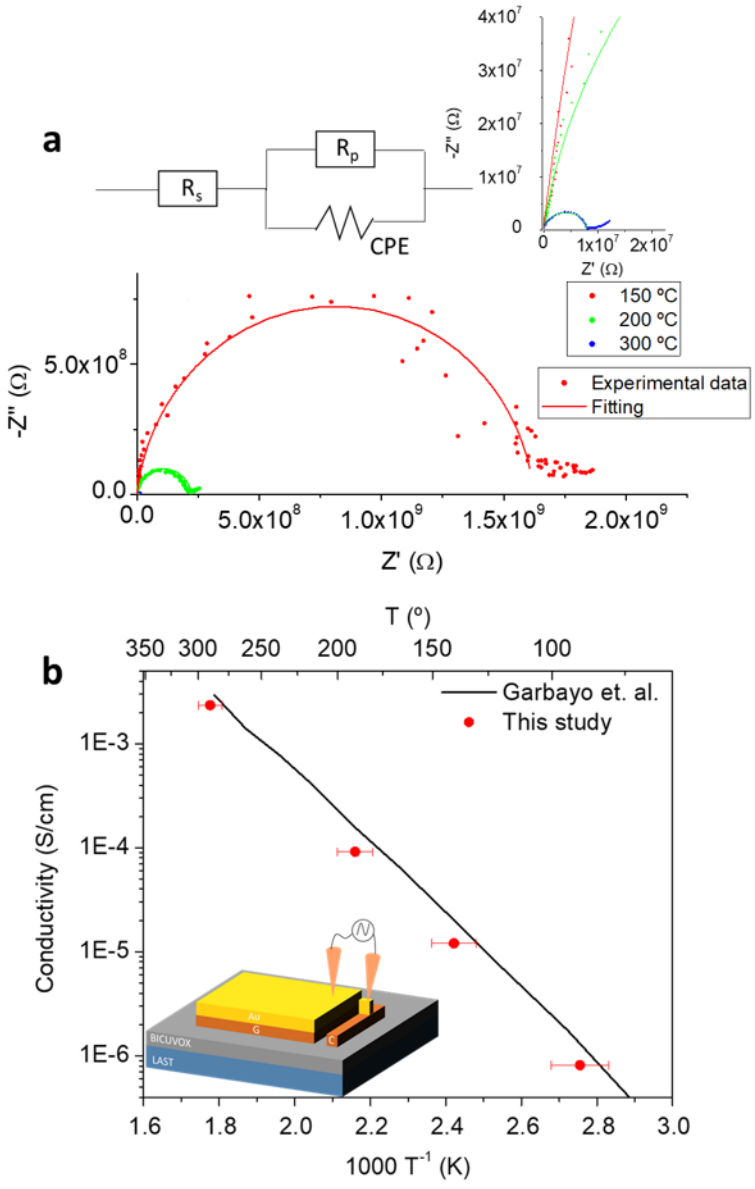


**Figure 5.4 a.** Nyquist plots of the EIS spectra measured for the LSF50/BICUVOX/LSAT sample at different temperatures. The inset presents the equivalent circuit. **b.** Arrhenius plot of the ionic conductivity of BICUVOX film measured by EIS (symbols) as a function of temperature. The inset shows the sketch of the experimental setup for the experimental EIS measurements. The in-plane ionic conductivity of the epitaxial BICUVOX thin film grown on $SrTiO_3$ (100) substrate and the ionic conductivity of YSZ and CGO are extracted from the references.[28,42–45]

## 5.4 Electrical characterization of the transistor

### 5.4.1 Channel conductance modulation and potentiation/depression

The developed device is operated by applying a voltage to the gate while the channel conductivity is measured. The channel current in response to the gating voltage is shown in **Figure 5.5a** (measured with a fixed $V_{DS}$ voltage of 0.01V), demonstrating the viability of controlling the electrical properties of the channel by applying a DC voltage at the gate.

The anodic DC voltages ($+V_G$) force the LSF50 gate material to be reduced and drive the oxide ions to the LSF50 channel passing through the BICUVOX electrolyte, while the cathodic DC gate voltages ($-V_G$) force the channel material to be reduced and drive the oxide ions to the gate. The incorporation of oxide ions into the LSF50 channel at anodic gate voltages decreases oxygen vacancies and increases electron holes for charge compensation, enhancing the electrical properties.[8] The variation of the electrical current in the LSF50 channel ($I_C$) shown in **Figure 5.5b** is quite similar to the evolution of the concentration of $Fe^{4+}$ holes described in **Chapter 3**, identifying that the voltages applied at the gate modify the point defect concentration in the channel, although with a deviation in the slope of the $I_C$ vs $V_G$ dependency, which is attributed to the uncertainty of the electrical potential loss in the in-plane setup.

One can note that at 0.4 V the LSF50 channel becomes fully oxidized and the channel current therefore becomes saturated. Although at the gate voltage of -0.2 V the electrical current flowing in the channel ($I_C$) is similar to that between the gate and the source ($I_G$) due to the large concentration of oxygen vacancies in the LSF50 film at the reduced state (see **Chapter 3**), the electrical current $I_G$ is two orders of magnitude smaller than the electrical current $I_C$, indicating that the BICUVOX thin film poses a high electrical resistance which leads to a negligible current leakage in the transistor.

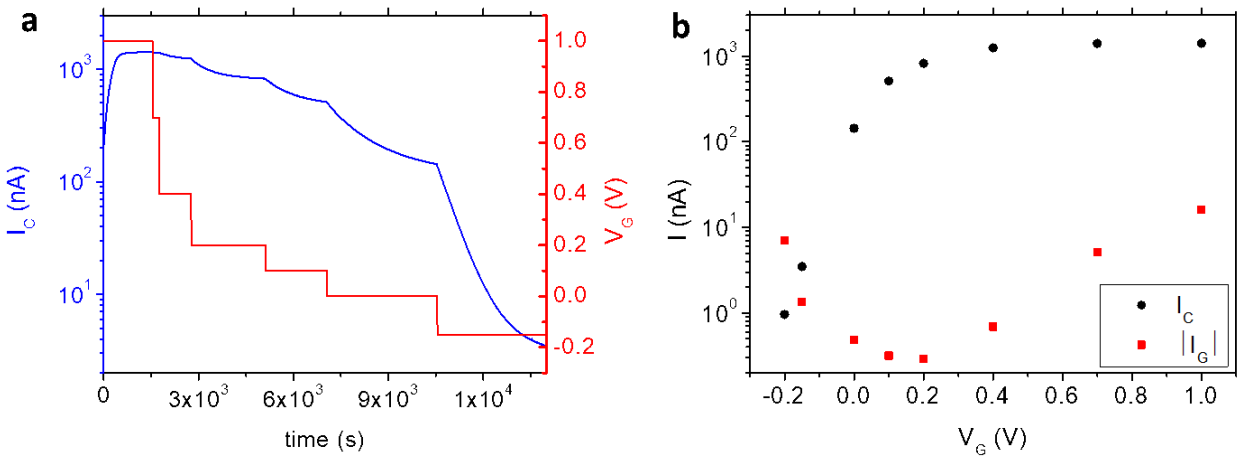


**Figure 5.5 a.** Current response between the drain and source ($I_C$) to different gate voltages at 300 ºC (applying a measurement voltage $V_{DS}$=10 mV). **b.** *I-V* characteristics of the transistor.

After these results, we can conclude that the gate voltage is able to modulate the channel conductance state at 300 ºC by controlling the amount of oxide ions incorporated into the channel. The potentiation and depression of the channel conductance were achieved by applying gate voltages between +20 V and -20 V. The positive gate voltages cause $O^{2-}$ ions to be incorporated into the channel, causing the potentiation effect in the channel conductance. In contrary, the negative gate voltages cause the $O^{2-}$ anions to migrate away from the channel, leading to the depression effect in the channel conductance. Before the investigation of the potentiation/depression behaviour at low temperatures, the LSF50 channel was fully oxidized at 300 ºC by applying a gate voltage of 1.5 V, the gate was therefore fully reduced and the $O^{2-}$ ions were attracted and accumulated in the channel. Then, the sample was quenched down to 150 ºC in order to maintain the oxygen content in the films. As demonstrated in **Figure 5.6a**, the depression of the channel conductance was carried out at 150 ºC starting from the stabilization at the gate voltage $V_G$ of 0 V, then from around 175 s a negative voltage of -20 V was implemented to the gate for 180 s, followed by recovering the voltage back to 0 V for the same length of time, this depression period was repeated for 3 cycles and the change in the channel conductance was tracked with $V_{DS}$=0.01 V.

The negative gate voltage -20 V attracts the oxide ions accumulated in the channel to the gate reducing the channel conductance from 90 µS to 88.7 µS in the first period. When the gate voltage was decreased back to 0 V, the channel conductance did not return to its initial

state, revealing the non-volatility feature of the transistor.[6] Moreover, it is noteworthy that the electrical conductance of the channel was decreased around 5.6 % after three cycles of the depression. The voltage-manipulated channel's electrical state and the non-volatile behaviour demonstrate the applicability of the transistor at temperatures as low as 150 ºC. One can note, however, that the electrical conductance was likely not stabilized within the period of 180 s due to a long-term electrical relaxation process caused by the slow chemical diffusion of $O^{2-}$ ions in the BICUVOX electrolyte at low temperatures.[46,47] This issue can be mitigated by minimizing the distance between the gate and the channel. More accurate approaches, such as the ones involving photolithography, would reduce migration path of $O^{2-}$ ions between the gate and the channel from millimeters to micrometers.

The potentiation process was carried out in the same manner by changing the polarity of the applied gate voltages with a length of time of 120 s for each applied voltage. As shown in **Figure 5.6b**, the positive gate voltage reverses the flow of $O^{2-}$ ions from the gate back to the channel, enhancing the channel conductance. As well as the depression behaviour, the potentiation is also non-volatile and reproducible. Therefore, the three-terminal LSF50/BICUVOX transistor presented in this study can be operated at 150 ºC, representing the proof-of-concept of a low-temperature solid-state oxide-based transistor.

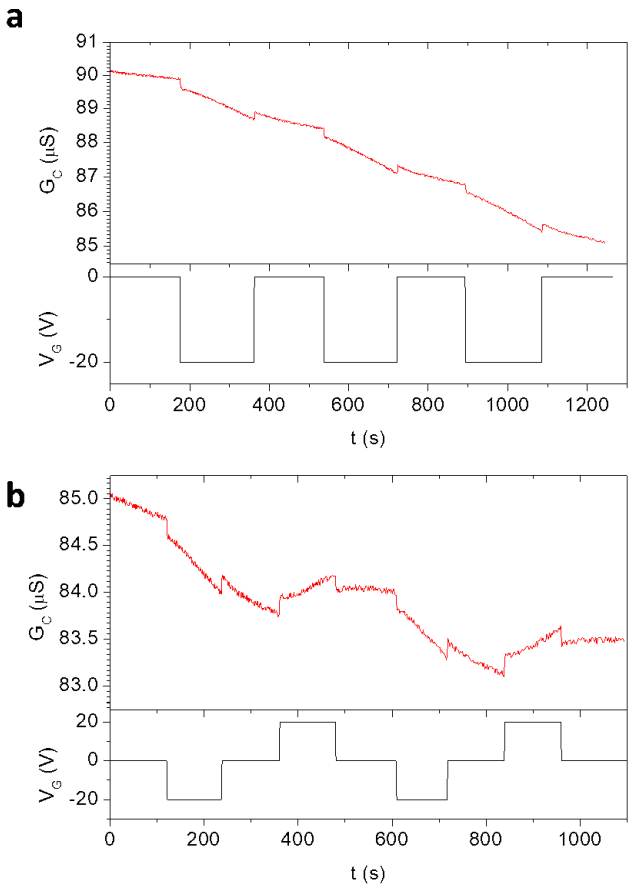


**Figure 5.6** **a.** Response of the channel conductance for pulsed voltages of -20 V and 0 V with pulse width of 180 s measured at 150 ºC with $V_{DS}$=0.01 V. **b.** Response of the channel conductance to the pulsed voltages of 20 V, 0 V and -20 V with pulse width of 120 s measured at 150 ºC with $V_{DS}$=0.01 V.

### 5.4.2 Retention properties

The long-term retention at room temperature of a certain channel state (fixed at elevated temperature) was studied. For that, gate voltages were applied at 300 ºC to ensure a proper ion intercalation (overcoming high resistance of the electrolyte at lower temperatures). Then, after a stabilization time, the device was quenched to room temperature in absence of voltage bias. Once stabilized at room temperature, the device was heated back to 300 ºC at the applied gate voltage. The results shown in **Figure 5.7a** demonstrate that the post-cooling sample restores its conductance state at 300 ºC at the same voltage bias, revealing that this process is reversible. Once stabilized again at 300 ºC, the gate voltage was changed in order to modify the channel's electrical state, and then the sample was quenched to room temperature with the gate voltage removed. The retention measurements were carried out by varying the gate voltage from -0.1 V to 1.1 V at 300 ºC and measuring the channel's electrical

conductance at room temperature with open circuit. As depicted in **Figure 5.7a**, the gate voltages applied at 300 ºC not only vary the electrical conductance at 300 ºC, but also modify the channel's electrical properties at room temperature. It is notable that the electrical conductance of the room-temperature channel increased from $5*10^{-5}$ μS to 26 μS as varying the gate voltages from -0.1 V to 1.1 V at 300 ºC. In agreement with the behaviour of the $La_{1/3}Sr_{2/3}FeO_{3-\delta}$/Gd-doped $CeO_2$ transistor proposed by Krick *et al.*,[27] the increase in the conductance at room temperature is proportional to the magnitude of the voltages applied at 300 ºC.

The stability of the conductance state at room temperature induced by the gate voltages of -0.1 V and 0.5 V applied at 300 ºC is illustrate in **Figure 5.7 b** and **c**, respectively. It is worth noting that after 14 hours, roughly 80% of the conductance state remained. In summary, the gate voltages applied at high temperatures are able to increase the electrical conductance of the channel at room temperature.

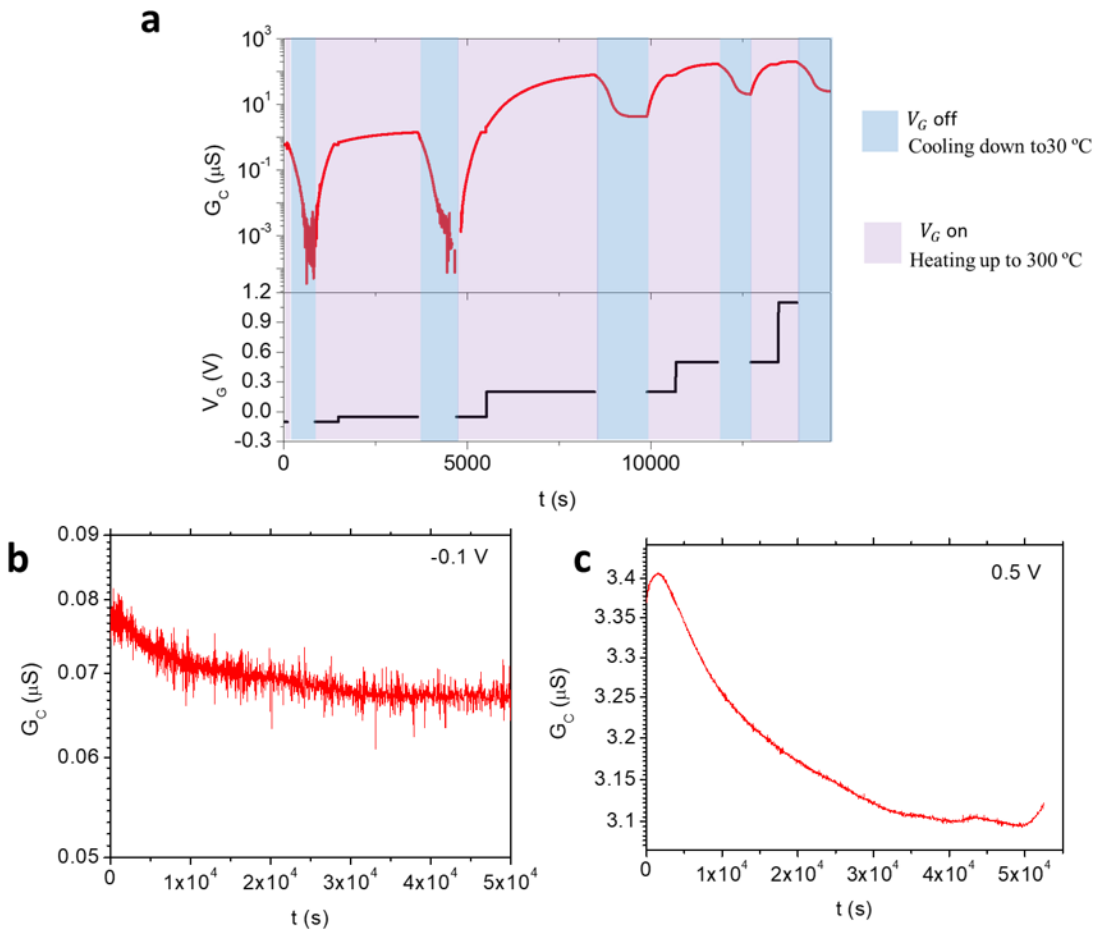


**Figure 5.7 a.** Multilevel channel conductance states modulated at 300 ºC and the retention properties for the different conductance states quenched from 300 ºC to 30 ºC. Evolution of the channel conductance at room temperature over time for the conductance states induced by the gate voltages of **b.** -0.1 V and **c.** 0.5 V applied at 300 ºC.

## 5.5 Further work towards room temperature oxide-ion synaptic transistors

Although the proof-of-concept of the LSF50/BICUVOX transistor has been demonstrated at temperatures as low as 150 ºC, the long-term electrical charge/discharge process caused by the sluggish oxygen diffusion through the BICUVOX and the LSF hinders its practical application.[33,46–48] Further work is ongoing in the following areas in order to improve performance and lower the operation temperature:

i. Increasing the thickness of the BICUVOX electrolyte while keeping its epitaxial nature: As **Equation 5.2** indicates that the resistance of the oxides is inversely proportional to the area of the transversal section for oxide ions conduction, thus, increasing the thickness of the BICUVOX electrolyte will effectively reduce its resistance, facilitating the conduction of oxide ions. However, as the film thickness increases, the strain between the film and the substrate weakens and the difference of lattice parameter between the film and the substrate becomes insignificant,[49–51] causing the film to lose its epitaxial characteristic and having a negative impact on BICUVOX's ionic conductivity. Thus, the balance between the film thickness and the ion transport distance is important for optimizing the transistor's performance.

ii. Minimizing the separation distance between the gate and the channel: As indicated in **Equation 5.2**, minimizing the separation distance between the gate and the channel is to shorten the oxide ions diffusion length, which is beneficial for reducing the oxide ions conduction resistance in BICUVOX and enhancing the response of the transistor. According to the calculations, if the thickness of the BICUVOX thin film is 300 nm, the separation distance should be roughly 0.5~2 μm, which can be achieved by microfabrication or focused ion beam.

iii. Reducing the width of the channel (the parameter $l_2$ in **Figure 5.2**): When a voltage bias is applied between the gate and the source, the oxide ions first oxidize the region of the channel closest to the gate; following that, the oxide ions extend to the places further away from the gate.[25] Thus, reducing the length $l_2$ improves the kinetics of the charge/discharge process of the channel by lowering the mass of the channel to oxidize or reduce and shortening the oxide ions transport length.

These modifications (already ongoing) are expected to end up with a solid oxide synaptic transistor based on oxygen and able to operate at low temperatures, eventually approaching ambient temperature.

## 5.6 Conclusions

In this chapter, a three-terminal transistor with solid electrolyte was developed. $(00l)$-oriented BICUVOX thin films demonstrated to be appropriate for being used as an electrolyte in the transistor thanks to its high in-plane ionic conductivity. Because of the ability to change the electronic structure at low temperatures by regulating the amount of oxide ions, LSF50 thin films were employed as gate and channel. The conduction of oxide ions in the BICUVOX electrolyte under the effects of the gate voltages causes oxide ions to be intercalated and de-intercalated in and out of the LSF50 channel, allowing to precisely control the conductance of the channel. At the current stage of development, the transistor is able to operate only above 150 ºC showing good non-volatile performance and thermal retention properties. In this synaptic transistor the solid-state BICUVOX electrolyte not only effectively solves the difficulties of integration faced by the transistors based on the ion gating in liquid electrolyte, but also lowers working temperature over the transistor based on the YSZ electrolyte, reducing the energy consumption. Nevertheless, additional future work is still needed (ongoing) to bring the operation temperature to room temperature. Furthermore, the BICUVOX and LSF50 thin films scale down the dimensions of the transistors, which ensures future miniaturization of high density devices. Overall, the LSF50/BICUVOX synaptic transistor proposed in this study provides a new alternative for neuromorphic computing applications.

# References


1. Rajendran, B. & Alibart, F. Neuromorphic Computing Based on Emerging Memory Technologies. *IEEE J. Emerg. Sel. Top. Circuits Syst.* **6**, 198–211 (2016).

2. Alamo, A., Onen, M., Emond, N., Li, J. & Yildiz, B. CMOS-Compatible Protonic Programmable Resistor Based on Phosphosilicate Glass Electrolyte for Analog Deep Learning. *Nano Lett.* **21**, 6111–6114 (2021).

3. Wan, Q., Sharbati, M. T., Erickson, J. R., Du, Y. & Xiong, F. Emerging Artificial Synaptic Devices for Neuromorphic Computing. *Adv. Mater. Technol.* **4**, 1900037 (2019).

4. Zhu, J., Zhang, T., Yang, Y. & Huang, R. A comprehensive review on emerging artificial neuromorphic devices. *Appl. Phys. Rev.* **7**, 011312 (2020).

5. Li, Y., Wang, Z., Midya, R., Xia, Q. & Yang, J. J. Review of memristor devices in neuromorphic computing: materials sciences and device challenges. *J. Phys. D. Appl. Phys.* **51**, 503002 (2018).

6. Nikam, R. D., Kwak, M. & Hwang, H. All-Solid-State Oxygen Ion Electrochemical Random-Access Memory for Neuromorphic Computing. *Adv. Electron. Mater.* **7**, 2100142 (2021).

7. Ling, H. *et al.* Electrolyte-gated transistors for synaptic electronics, neuromorphic computing, and adaptable biointerfacing. *Appl. Phys. Rev.* **7**, 011307 (2020).

8. Ge, C. *et al.* A Ferrite Synaptic Transistor with Topotactic Transformation. *Adv. Mater.* **31**, 1900379 (2019).

9. Han, H., Yu, H., Wei, H., Gong, J. & Xu, W. Recent Progress in Three-Terminal Artificial Synapses: From Device to System. *Small* **15**, 1900695 (2019).

10. Shi, J., Ha, S. D., Zhou, Y., Schoofs, F. & Ramanathan, S. A correlated nickelate synaptic transistor. *Nat. Commun.* **4**, 2676 (2013).

11. Yang, C. Sen *et al.* All-Solid-State Synaptic Transistor with Ultralow Conductance for Neuromorphic Computing. *Adv. Funct. Mater.* **28**, 1804170 (2018).

12. Fuller, E. J. *et al.* Redox Transistors for Neuromorphic Computing. *IBM J. Res. Dev.*

**63**, 9:1-9:9 (2019).

13. Huang, H. Y. *et al.* Electrolyte-Gated Synaptic Transistor with Oxygen Ions. *Adv. Funct. Mater.* **29**, 1902702 (2019).

14. Chen, S., Sood, A., Pop, E., Goodson, K. E. & Donadio, D. Strongly tunable anisotropic thermal transport in $MoS_2$ by strain and lithium intercalation: first-principles calculations. *2D Mater.* **6**, 025033 (2019).

15. Zhang, S. & Galli, G. Understanding the metal-to-insulator transition in $La_{1-x}Sr_xCoO_{3-\delta}$ and its applications for neuromorphic computing. *npj Comput. Mater.* **6**, 170 (2020).

16. Rao, J. *et al.* An electroforming-free, analog interface-type memristor based on a $SrFeO_x$ epitaxial heterojunction for neuromorphic computing. *Mater. Today Phys.* **18**, 100392 (2021).

17. Cui, B. *et al.* Direct imaging of structural changes induced by ionic liquid gating leading to engineered three-dimensional meso-structures. *Nat. Commun.* **9**, 3055 (2018).

18. Islam, R. *et al.* Device and materials requirements for neuromorphic computing. *J. Phys. D. Appl. Phys.* **52**, 113001 (2019).

19. Wang, Z. *et al.* Nanoionics-Enabled Memristive Devices: Strategies and Materials for Neuromorphic Applications. *Adv. Electron. Mater.* **3**, 1600510 (2017).

20. Zhou, Y., Li, J., Yang, Y., Chen, Q. & Zhang, J. Artificial Synapse Emulated through Fully Aqueous Solution-Processed Low-Voltage $In_2O_3$ Thin-Film Transistor with $Gd_2O_3$ Solid Electrolyte. *ACS Appl. Mater. Interfaces* **12**, 980–988 (2020).

21. Tsuchiya, T., Terabe, K. & Aono, M. All-solid-state electric-double-layer transistor based on oxide ion migration in Gd-doped $CeO_2$ on $SrTiO_3$ single crystal. *Appl. Phys. Lett.* **103**, 073110 (2013).

22. Guo, L. Q. *et al.* Effects of humidity on performance of electric-double-layer oxide-based thin-film transistors gated by nanogranular $SiO_2$ solid electrolyte. *AIP Adv.* **3**, 072110 (2013).

23. Lu, A., Sun, J., Jiang, J. & Wan, Q. Microporous $SiO_2$ with huge electric-double-layer

capacitance for low-voltage indium tin oxide thin-film transistors. *Appl. Phys. Lett.* **95**, 222905 (2009).

24. Tsuchiya, T., Moriyama, S., Terabe, K. & Aono, M. Modulation of superconducting critical temperature in niobium film by using all-solid-state electric-double-layer transistor. *Appl. Phys. Lett.* **107**, 013104 (2015).

25. Tsuchiya, T., Ochi, M., Higuchi, T., Terabe, K. & Aono, M. Effect of Ionic Conductivity on Response Speed of $SrTiO_3$-Based All-Solid-State Electric-Double-Layer Transistor. *ACS Appl. Mater. Interfaces* **7**, 12254–12260 (2015).

26. Takashi Tsuchiya;, Ochi;, M., Higuchi;, T. & Terabe, K. Comparison of subthreshold swing in $SrTiO_3$ - based all-solid-state electric-double-layer transistors with $Li_4SiO_4$ or Y-stabilized-$ZrO_2$ solid electrolyte. *Jpn. J. Appl. Phys* **55**, 06GJ03 (2016).

27. Krick, A. L. & May, S. J. Evidence for oxygen vacancy manipulation in $La_{1/3}Sr_{2/3}FeO_{3-\delta}$ thin films via voltage controlled solid-state ionic gating. *APL Mater.* **5**, 042504 (2017).

28. Garbayo, I. *et al.* Thin film oxide-ion conducting electrolyte for near room temperature applications. *J. Mater. Chem. A* **7**, 25772–25778 (2019).

29. Saleem, M. S. *et al.* Electric Field Control of Phase Transition and Tunable Resistive Switching in $SrFeO_{2.5}$. *ACS Appl. Mater. Interfaces* **11**, 6581–6588 (2019).

30. Nallagatla, V. R. *et al.* Topotactic Phase Transition Driving Memristive Behavior. *Adv. Mater.* **31**, 1903391 (2019).

31. Kuhn, M., Hashimoto, S., Sato, K., Yashiro, K. & Mizusaki, J. Oxygen nonstoichiometry, thermo-chemical stability and lattice expansion of $La_{0.6}Sr_{0.4}FeO_{3-\delta}$. *Solid State Ionics* **195**, 7–15 (2011).

32. Xie, Y. *et al.* Control of functional responses via reversible oxygen loss in $La_{1-x}Sr_xFeO_{3-\delta}$ films. *Adv. Mater.* **26**, 1434–1438 (2014).

33. Yoo, J., Verma, A., Wang, S. & Jacobson, A. J. Oxygen Transport Kinetics in $SrFeO_{3-\delta}$, $La_{0.5}Sr_{0.5}FeO_{3-\delta}$, and $La_{0.2}Sr_{0.8}Cr_{0.2}Fe_{0.8}O_{3-\delta}$ Measured by Electrical Conductivity Relaxation. *J. Electrochem. Soc.* **152**, A497 (2005).

34. Shin, Y. *et al.* Effect of oxygen vacancies on electrical conductivity of $La_{0.5}Sr_{0.5}FeO_{3-}$

$_{\delta}$ from first-principles calculations. *J. Mater. Chem. A* **8**, 4784–4789 (2020).

35. Søgaard, M., Vang Hendriksen, P. & Mogensen, M. Oxygen nonstoichiometry and transport properties of strontium substituted lanthanum ferrite. *J. Solid State Chem.* **180**, 1489–1503 (2007).

36. Lohne, Ø. F. *et al.* Oxygen Non-Stoichiometry and Electrical Conductivity of $La_{0.2}Sr_{0.8}Fe_{0.8}B_{0.2}O_{3-\delta}$, B = Fe, Ti, Ta. *J. Electrochem. Soc.* **161**, F176–F184 (2014).

37. Vailionis, A. *et al.* Symmetry and lattice mismatch induced strain accommodation near and away from correlated perovskite interfaces. *Appl. Phys. Lett.* **105**, 131906 (2014).

38. Lu, Q. & Yildiz, B. Voltage-Controlled Topotactic Phase Transition in Thin-Film $SrCoO_x$ Monitored by in Situ X-ray Diffraction. *Nano Lett.* **16**, 1186–1193 (2016).

39. Weber, M. L. *et al.* Development of Epitaxial Thin Film Model Electrodes for the Systematic Investigation of Metal Exsolution from MIEC Perovskite Oxides. *ECS Trans.* **91**, 1783–1789 (2019).

40. Kogler, S., Nenning, A., Rupp, G. M., Opitz, A. K. & Fleig, J. Comparison of Electrochemical Properties of $La_{0.6}Sr_{0.4}FeO_{3-\delta}$ Thin Film Electrodes: Oxidizing vs. Reducing Conditions. *J. Electrochem. Soc.* **162**, F317–F326 (2015).

41. Opitz, A. K. *et al.* Thin film cathodes in SOFC research: How to identify oxygen reduction pathways? *J. Mater. Res.* **28**, 2085–2105 (2013).

42. Chiodelli, G., Malavasi, L., Massarotti, V., Mustarelli, P. & Quartarone, E. Synthesis and characterization of $Ce_{0.8}Gd_{0.2}O_{2-y}$ polycrystalline and thin film materials. *Solid State Ionics* **176**, 1505–1512 (2005).

43. Rupp, J. L. M. & Gauckler, L. J. Microstructures and electrical conductivity of nanocrystalline ceria-based thin films. *Solid State Ionics* **177**, 2513–2518 (2006).

44. Joo, J. H. & Choi, G. M. Electrical conductivity of YSZ film grown by pulsed laser deposition. *Solid State Ionics* **177**, 1053–1057 (2006).

45. Garbayo, I. *et al.* Electrical characterization of thermomechanically stable YSZ membranes for micro solid oxide fuel cells applications. *Solid State Ionics* **181**, 322–331 (2010).

46. Vannier, R. N. *et al.* Oxide ion transport in bismuth-based materials. *Mater. Res. Soc. Symp. - Proc.* **756**, 95–103 (2003).

47. Guillodo, M., Bassat, J. M., Fouletier, J., Dessemond, L. & Del Gallo, P. Oxygen diffusion coefficient and oxygen exchange coefficient of BIMEVOX.10 (ME=Cu, Co) ceramic membranes. *Solid State Ionics* **164**, 87–96 (2003).

48. Bae, H. *et al.* Investigations on defect equilibrium, thermodynamic quantities, and transport properties of $La_{0.5}Sr_{0.5}FeO_{3-\delta}$. *J. Electrochem. Soc.* **166**, F180–F189 (2019).

49. Myoung, J. M. *et al.* Effects of thickness variation on properties of ZnO thin films grown by pulsed laser deposition. *Japanese J. Appl. Physics, Part 1 Regul. Pap. Short Notes Rev. Pap.* **41**, 28–31 (2002).

50. Cammarata, R. C. & Sieradzki, K. Surface stress effects on the critical film thickness for epitaxy. *Appl. Phys. Lett.* **55**, 1197–1198 (1989).

51. Ravaliya, K., Ravalia, A., Pandya, D. D., Solanki, P. S. & Shah, N. A. Strain and morphology control over electrical behavior of pulsed laser deposited $BiFeO_3$ films. *Thin Solid Films* **645**, 436–443 (2018).

# 6. Conclusions

# 6. Conclusions

This thesis was devoted to the point defects engineering in oxides thin films for energy and information technologies. The work dealt with three main topics: (i) Indirect quantification of point defects in $La_{1-x}Sr_xFeO_{3-\delta}$ thin films by in-situ ellipsometry in gas atmosphere at intermediate-to-low temperatures; (ii) track of the defect chemistry of $La_{0.5}Sr_{0.5}FeO_{3-\delta}$ thin films during ionic intercalation in alkaline electrolyte at room temperature; and (iii) development of a $La_{0.5}Sr_{0.5}FeO_{3-\delta}$ thin film-based synaptic transistor with solid-state electrolyte. The main outcomes can be summarized as follows:

- **Indirect quantification of point defects in $La_{1-x}Sr_xFeO_{3-\delta}$ thin films by in-situ ellipsometry.** The concentration of electron holes in $La_{1-x}Sr_xFeO_{3-\delta}$ (x=0.2, 0.4 and 0.5) thin films was indirectly quantified by in-situ ellipsometry as a function of oxygen pressure at temperatures ranging from 540 ºC to 350 ºC, overcoming the restrictions of high temperature requirements in conventional techniques for the study of defect chemistry in oxide thin films. The main findings can be listed as follows:
    - The low energy transition observed in optical conductivity has been univocally linked to the concentration of electron holes in the ferrite thin films. The analysis of the optical permittivity as a function of Sr concentration in fully oxidized $La_{1-x}Sr_xFeO_{3-\delta}$ thin films demonstrates that ellipsometry can be used for tracking and quantifying the concentration of holes in $La_{1-x}Sr_xFeO_{3-\delta}$ thin films.
    - The in-situ ellipsometry analysis of an electrochemical cell based on $La_{1-x}Sr_xFeO_{3-\delta}$ electrode allows to calculate the equilibrium $Fe^{4+}$ concentration at intermediate-to-low temperatures as a function of oxygen pressure ranging from $10^{7}$ to $10^{-17}$ bar.
    - A non-dilute defect chemistry model that satisfactorily describes the concentration of electron holes, enabling the study of the defect chemistry of $La_{1-x}Sr_xFeO_{3-\delta}$ thin films, has been developed. The results highlight the importance of considering non-dilute phenomena in the study of oxygen incorporation in oxide thin films at intermediate-to-low temperature.

Overall, the in-situ ellipsometry technique offers a new way to measure the defect chemistry of $La_{1-x}Sr_xFeO_{3-\delta}$ (x=0.2, 0.4 and 0.5) thin films as a function of oxygen pressure at intermediate-to-low temperatures, which is crucial for engineering their functional properties for energy and information applications.

- **Study of the defect chemistry of $La_{0.5}Sr_{0.5}FeO_{3-\delta}$ thin film during ion intercalation in alkaline electrolyte.** The variation of $Fe^{4+}$ concentration in $La_{0.5}Sr_{0.5}FeO_{3-\delta}$ thin film induced by the intercalations of ionic species in alkaline electrolyte (0.1 M KOH solution) at room temperature was quantified by in-situ ellipsometry, and the underlying mechanism was understood by means of ex-situ ellipsometry, ToF-SIMS and PALS etc. The main results are listed as follows:
    - Electrochemical potentials applied between alkaline electrolyte and $La_{0.5}Sr_{0.5}FeO_{3-\delta}$ electrode cause ions to incorporate (or release) into (out of) $La_{0.5}Sr_{0.5}FeO_{3-\delta}$ thin film, resulting in the electronic transition between $Fe^{4+}$ and $Fe^{3+}$ in the film, depending on the polarity of the potentials.
    - Ex-situ measurements coupled with a variety of characterization techniques (ToF-SIMS, PALS, XRD, ellipsometry) proved that both oxygen and protons in aqueous KOH electrolyte are actively involved in the ion intercalation.
    - The concentration of electron holes in $La_{0.5}Sr_{0.5}FeO_{3-\delta}$ thin film tailored by the ion intercalation can be tracked in situ during electrochemical ionic intercalation by ellipsometry. A defect chemistry model involving both oxygen and protons as active species has been developed. The model is observed to correctly describe the hole concentration in the layers during ionic intercalation.

Therefore, the point defects in LSF50 thin films tailored by the ion intercalation in alkaline electrolyte at room temperature were quantified by in-situ ellipsometry. This technique shows the possibility to get insight into the defect chemistry of $La_{0.5}Sr_{0.5}FeO_{3-\delta}$ thin film in alkaline electrolyte, which is pivotal for the understanding and engineering of the functionality of oxide thin films in real devices, such as supercapacitors, transistors, and so on.

- **Development of a synaptic transistor with solid-state electrolyte:** A synaptic transistor based on the variation of electronic conductivity in the $La_{0.5}Sr_{0.5}FeO_{3-\delta}$ channel through solid-state electrolyte electrochemical intercalation was developed.

A $Bi_4V_{1.8}Cu_{0.2}O_{10.7}$ (BICUVOX) oxide thin films was used as fast oxygen ion electrolyte. The main results are:

- BICUVOX thin film presents an excellent in-plane ionic conductivity of $1.21*10^{-5}$ S $cm^{-1}$ at 150 ºC, which makes it suitable for being electrolyte in the synaptic transistor.
- The oxygen content in the non-stoichiometric $La_{0.5}Sr_{0.5}FeO_{3-\delta}$ thin film strongly impacts its electrical properties, due to variation of $Fe^{4+}$ concentration. The large and continuous variation of electronic conductivity during oxygen intercalation qualifies LSF as a promising gate and channel semiconductor in synaptic transistors.
- The voltage applied between the LSF channel and gate is observed to directly control the amount of oxide ions intercalated through the BICUVOX electrolyte, modulating the electrical conductance of the $La_{0.5}Sr_{0.5}FeO_{3-\delta}$ thin film channel.
- The channel conductance can be modulated by the presynaptic gate voltages at low temperatures down to 150 ºC with good non-volatility and retention properties. Besides, a room temperature operation is envisioned by optimizing the dimensions of the device.

In brief, the synaptic transistor based on $La_{0.5}Sr_{0.5}FeO_{3-\delta}$ and BICUVOX thin films breaks the limitations of working temperature of traditional solid-state oxygen electrolyte transistors and enhances the integrity compared to liquid-electrolyte transistors, providing a new promising candidate for synaptic memories.

In summary, this thesis presents systematic studies of the point defects in $La_{1-x}Sr_xFeO_{3-\delta}$ thin films under real electrochemical conditions using a novel in-situ ellipsometry technique. Based on the knowledge of defect chemistry, a new synaptic transistor with solid-state electrolyte that can operate at low temperatures is developed, showing that $La_{1-x}Sr_xFeO_{3-\delta}$ thin films can be promising materials for energy and information applications through engineering the concentration of point defects.

# Appendix

# Optical impedance spectroscopy of ferrite thin films

# A.1 Optical impedance spectroscopy for electrochromic thin films

Electrochromic materials, which are able to change their optical properties under the effects of electrochemical potentials,[1–3] have been investigated for smart windows applications in architecture in order to increase the energy efficiency and modulate the indoor light.[2,4,5] As presented in the previous chapters of this thesis, the $Sr^{2+}$ substitution for $La^{3+}$ in $LaFeO_3$ originates oxygen vacancies and/or the $Fe^{4+}$ electronic holes.[6] Nernstian voltages applied to $La_{1-x}Sr_xFeO_{3-\delta}$ (LSF) thin films allow for the adjustment of the oxygen chemical potential and electronic structure of the materials,[7,8] giving rise to the variation of the $Fe^{4+}$ concentration and changes in optical properties and color in the visible range.[9–11] Thus, controlling the variation of LSF's optical properties with the applied voltages and understanding the parameters that affect the electrochromic properties are critical for optimizing the materials' functionality in the electrochromic applications. Although Park *et al.* qualitatively demonstrate the time-dependent color change of Ca-doped $BiFeO_3$ thin films under the effect of an electrochemical potential by in-situ optical microscopy,[12] there is still a lack of a characterization technique for tracking the dynamic variation of optical properties of the materials with electrical voltages and determining the parameters involved in the dynamic change. Manka *et al.*[13] proposed for the first time the term "optical impedance spectroscopy" in order to characterize the optical behaviour of the electrochromic materials, their research work shows the possibility of obtaining the materials' optical impedance spectra and parameters involved in the variation of optical properties using optical transmittance which is intimately related to the electrical signals. Nevertheless, the measurements of optical transmittance require that the substrates of samples must be transparent. Based on the sensitive response of the ellipsometric parameters of LSF thin films to Nernstian voltages (see **Chapter 3** and **Chapter 4**), this appendix is devoted to the development of an optical impedance spectroscopy for characterizing the voltage-dependent dynamic change in the optical properties of LSF thin films using in-situ ellipsometry. The oscillatory ellipsometric response to the applied AC voltages allows for obtaining the optical impedance spectra for LSF thin films using an appropriate formalism. The optical impedance spectroscopy enables the extraction of the electrochemical parameters involved in the electrochromic process.

## A.2 Optical impedance spectroscopy on electrochemical cells with solid-sate electrolyte

In-situ ellipsometry measurements were conducted at 540 ºC in air on a 98 nm-thick $La_{0.6}Sr_{0.4}FeO_{3-\delta}$ (LSF40) thin film deposited on a CGO-coated YSZ (001) substrate (see **Chapter 3** for the fabrication procedure as well as the microstructural and compositional characterization). In order to enhance the optical response, the sample was stabilized at a bias of -0.1 V which corresponds to an oxygen partial pressure $pO_2$ of $2.24*10^{-4}$ bar. A sinusoidal voltage bias set at -0.1 V with an amplitude of ±0.05 V and frequency ranging from 0.01 Hz to 1 Hz was then applied to the LSF40 thin film using LASV. Evolution of optical properties of the sample was simultaneously characterized by ellipsometry in kinetic mode fixing the photon energy at 1.21 eV. More details about the experimental setup can be found in **Chapter 2**.

Kinetic evolution of the ellipsometry parameter $\Psi$ with electrical voltage is illustrated in **Figure A.1**. The optical parameter $\Psi$ is directly related to the imaginary part of the overall optical constants of the measured sample. It should be mentioned that in the experimental configuration, the switch of electrical voltage from -0.1 V to -0.15 V reduces the LSF40 thin film by decreasing the oxygen partial pressure from $2.24*10^{-4}$ bar to $1.29*10^{-5}$ bar, as a result, the LSF40 thin film takes on a more transparent color tone; the switch of electrical voltage from -0.1 V to -0.05 V oxidizes the LSF40 film by increasing the oxygen partial pressure from $2.24*10^{-4}$ bar to $3.87*10^{-3}$ bar, in this sense, the color tone of the LSF40 thin film becomes darker. The input sinusoidal electrical voltages applied at the LSF40 thin film give rise to frequency-dependent oscillatory optical response with a delay in the optical response that is significant at low frequency. Moreover, the amplitude of the optical response increases with decreasing the frequency, characteristic of a kinetic limited process. Both the electrical and optical signals can be fitted with a sinusoidal equation as:

$$y(t) = A_0 \sin(\omega(t - t_0)) \qquad \text{(Equation A.1)}$$

Where $A_0$ is the amplitude of the sinusoidal-shape wave, which is denoted as $E_0$ for electrical signals and $\Psi_0$ for optical signals; $\omega$ is the angular frequency which is related to the frequency in Hertz as: $\omega = 2\pi f$; $t_0$ is the initial time for the period.

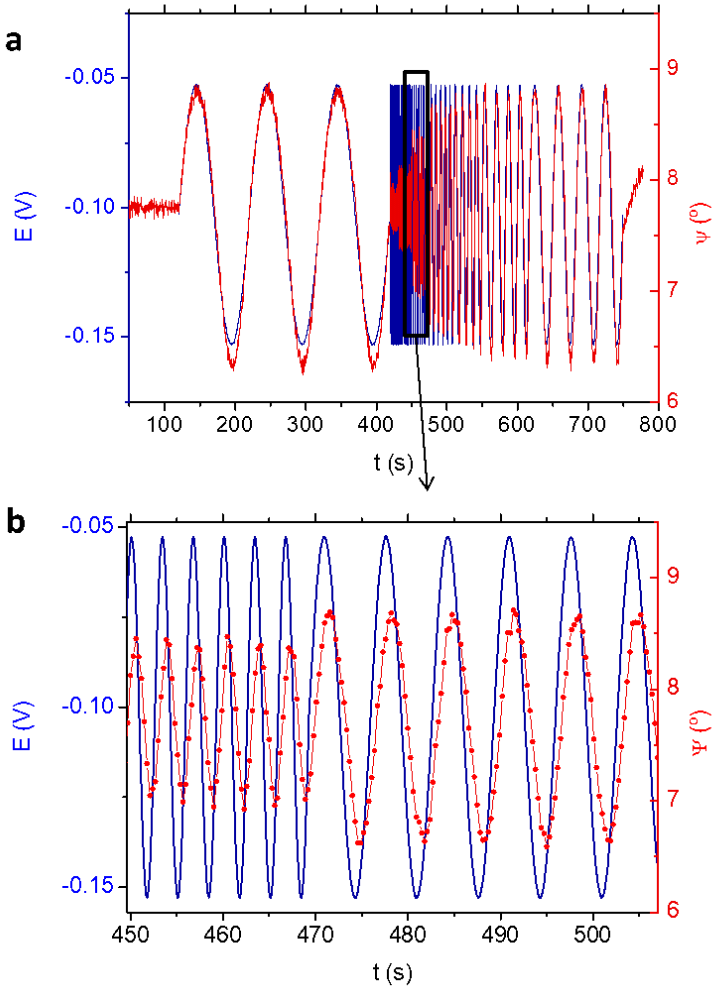


**Figure A.1 a.** Sinusoidal optical signals at the photon energy of 1.21 eV for the LSF40/CGO/YSZ sample measured at 540 ºC as the response to the input sinusoidal electrical voltages. **b.** Details of the signals at high frequency.

Similar to the mechanism of EIS and electrochemomechanical spectroscopy presented by Swallow *et al.* for the material $Pr_xCe_{1-x}O_{2-\delta}$,[14] the optical admittance can be defined as:

$$Y(t) = \frac{\Psi_0(\omega)}{E_0}\frac{\sin(\omega t+\varphi(\omega))}{\sin(\omega t)} \qquad \text{(Equation A.2)}$$

$\varphi(\omega)$ represents the phase lag between the optical signals and the electrical signals, which can be calculated by:

$$\varphi(\omega) = \omega(t_{0,E} - t_{o,\Psi}) \qquad \text{(Equation A.3)}$$

$t_{0,E}$-$t_{0,\Psi}$ represents the delay time in the optical response respect to the input electrical stimulation.

The function of optical admittance can be written in a complex form as:

$$Y(\omega) = \frac{\Psi_0(\omega)}{E_0}(\cos\varphi(\omega) + jsin\varphi(\omega)) \qquad \text{(Equation A.4)}$$

**Figure A.2a** depicts the module $\frac{\Psi_0(\omega)}{E_0}$ and the phase lag $\varphi$ as a function of frequency derived from the parameters of the sinusoidal fitting. It is confirmed that the amplitude $\frac{\Psi_0(\omega)}{E_0}$ increases as decreasing the frequency, because at low frequency the LSF40 thin film has more time to equilibrate with the new conditions. One can note that the phase lag increases with the frequency and the error becomes significant at high frequency, which can be associated with a higher relative delay in the launch of the optical and electrical experiments.[14] **Figure A.2b** shows the Nyquist plot of the optical admittance for the LSF40/CGO/YSZ sample measured at 540 ºC. A semicircle is observed in the figure, closing for lower frequencies.

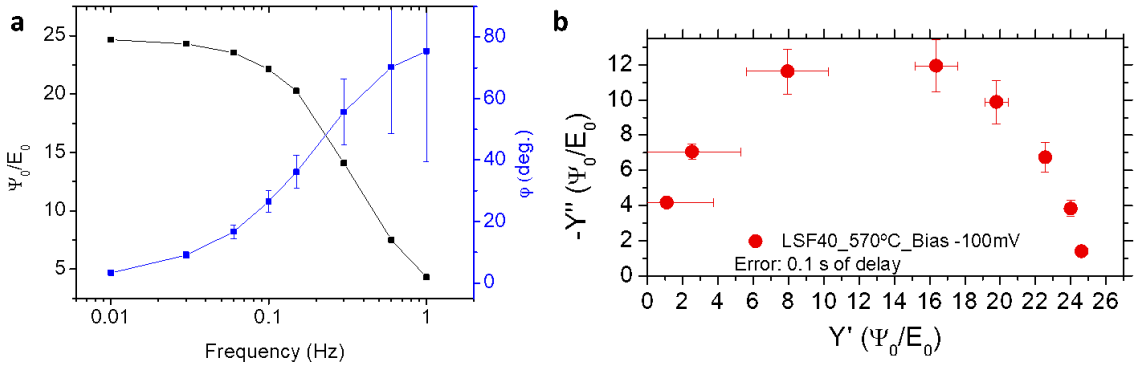


**Figure A.2 a.** Bode plots of the module $\frac{\Psi_0(\omega)}{E_0}$ and the phase lag $\varphi$ as a function of frequency. The error was calculated considering an error of delay time of 0.1 s. **b.** Nyquist plot of the optical admittance for the LSF40/CGO/YSZ sample measured at 540 ºC.

In order to better understand the physical significance of the optical impedance spectra, the optical admittance should be transformed to the well-known parameters which are associated with the electrochemical properties. In this sense, it is useful to consider the equivalent circuit of the electrochemical system in the case of an electrical and optical impedance spectroscopy (see **Figure A.3**). In the case of classical EIS, the observable parameter is the variation of current through the cell in response to an AC voltage signal. The simplified equivalent circuit of the system is composed by: (i) a series resistance $R_{YSZ}$, deriving from the oxygen conduction through the YSZ; (ii) a surface resistance $R_s$ due to oxygen

incorporation on the LSF surface; (iii.) a chemical capacitance $C_{chem}$, representing the accumulation of charges in the LSF layer in response of a Nernstian voltage, see **Figure A.3a**.[15] This is the classical equivalent circuit derived by Maier *et al.* for a surface limited incorporation mechanism.[16] It is important to note that under DC voltage the system will give rise to a DC current, limited by the sum of the overall series contributions.

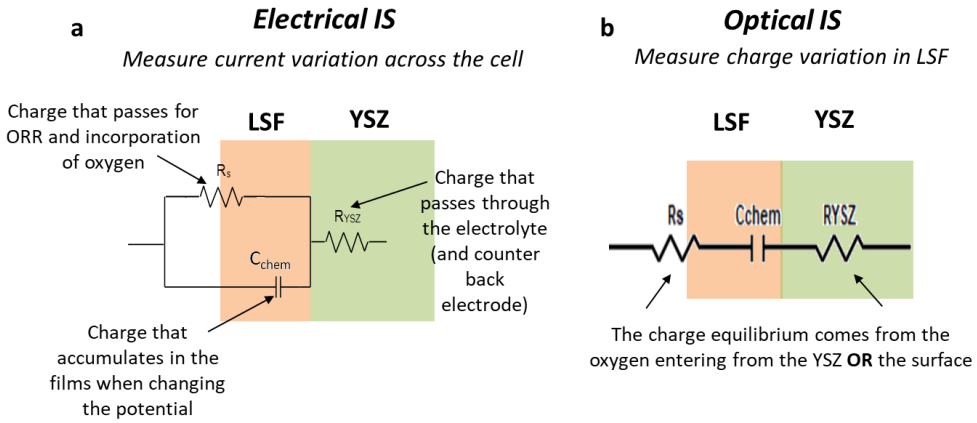


**Figure A.3** Schematic representation of the equivalent circuit in the case of **a.** electrical and **b.** optical IS.

On the other hand, in the case of optical impedance (**Figure A.3b**), the observable parameter is the variation of optical properties in the LSF layer. As discussed in **Chapter 3**, the ellipsometric parameters at low photon energy are sensitive to the variation of the concentration of $Fe^{4+}$ holes under the effects of Nernstian voltage.[17,18] **Figure A.4a** compares the evolution of the ellipsometry data $\Psi$ for the overall LSF40/CGO/YSZ sample with the concentration of electron holes in the LSF40 thin film at different applied voltages extracted from the study discussed in **Chapter 3**, confirming that the change in the optical parameter $\Psi$ mainly comes from the evolution of $Fe^{4+}$ holes. Since the films are surface limited, the oxygen chemical potential is expected to be constant across the thin film, meaning that no diffusion losses are expected. A linear correlation between the hole concentration and $\Psi$ down to 10% hole concentration is shown in **Figure A.4b**, enabling the linear transformation of the measured $\Psi$ data to hole concentration in LSF40 thin film.

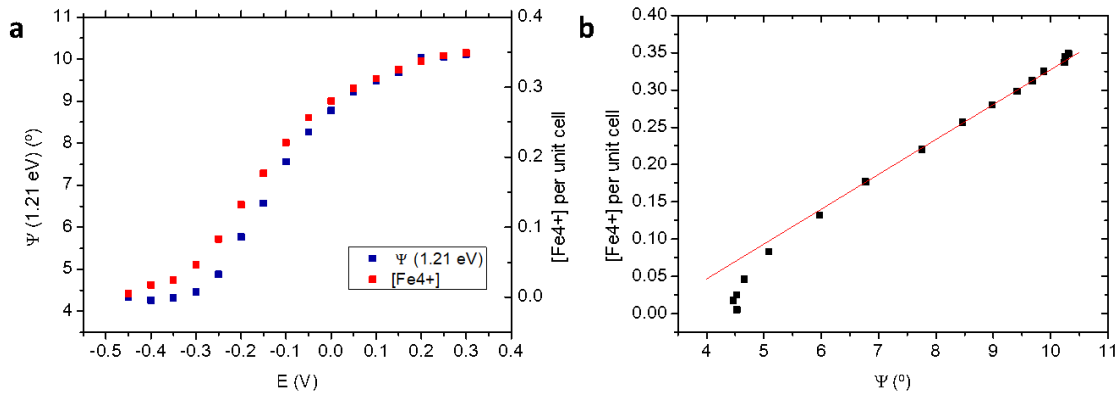


**Figure A.4 a.** Ellipsometry data $\Psi$ of the overall LSF40/CGO/YSZ sample and the $Fe^{4+}$ concentration of the LSF40 thin film extracted from the measurements at 540 °C reported in **Chapter 3**. **b**. Linear correlation between the $Fe^{4+}$ concentration and $\Psi$.

Therefore, optical impedance spectroscopy directly measures the variation of charge in the LSF layer under the application of a Nernstian AC potential. These charges are related to the variation of $Fe^{4+}$ concentration taking place while oxygen flows in and out of the layer. As shown in **Figure A.3b**, oxygen may either come from the surface of the LSF film or from the backside electrode through the YSZ electrolyte, depending on the fastest path (*i.e.* lower resistance). Due to these considerations, **Equation A.4** can be transformed to **Equation A.5** as:

$$I(\omega) = \frac{q_h}{E_0}\left(\cos\varphi(\omega) + jsin\varphi(\omega)\right) = I' + jI'' \qquad \text{(Equation A.5)}$$

$$\text{With } q_h = e[Fe^{4+}]$$

Where $q_h$ represents the charge variation in the LSF40 film, $e$ is the elementary charge which equals to $1.6*10^{-19}$ C. The Nyquist plot of the optical admittance adapted to **Equation A.5** is shown in **Figure A.5a**. We note that in this form, the optical admittance has the unit of a specific capacitance (charge divided by voltage), which can be represented in $F/cm^2$. In this sense, the optical admittance represents the chemical capacitive contribution of the LSF thin films due to the change of Fe oxidation state for different frequencies. According to the chemical capacitance model for LSF with dilute defects reported by Schmid *et al.*:[15]

$$C_{chem} = \frac{e^2}{KT} n_{uc} \left(\frac{1}{4c_V} + \frac{1}{c_h}\right)^{-1} \qquad \text{(Equation A.6)}$$

Where *K* represents the Boltzmann constant; *T* denotes the temperature; $c_v$ and $c_h$ denote the concentration of oxygen vacancies and electron holes in the LSF40 thin film; $n_{uc}$ represents the amount of LSF40 unit cells. Considering the voltage bias of -0.1 V (equivalent oxygen partial pressure of $2.24*10^{-4}$ bar) applied in this study, oxygen vacancies are four times more numerous than electron holes,[157] so that **Equation A.6** can be simplified to **Equation A.7** omitting the component $\frac{1}{4c_V}$:

$$C_{chem} = \frac{e^2}{KT} n_{uc} c_h \qquad \text{(Equation A.7)}$$

Since a direct correlation between the ellipsometry data $\Psi$ and the holes concentration is found in **Figure A.4b**, the capacitance $\frac{q_h}{E_0}$ is thus linked with the chemical capacitance of the LSF40 thin film. At high frequencies, the kinetic limitations impede the equilibrium of the applied voltage, resulting in a low variation of oxidation state and a large time delay. Lowering the frequency, the system has more time to reach the equilibrium, resulting in a larger variation of Fe oxidation state and in a smaller delay.

Due to the significant higher surface polarization resistance of the sample at 540 ºC compared to the YSZ ionic resistance,[15,19] the optical admittance can be fitted with an equivalent circuit which consists of an in-series connection of a capacitor and the YSZ resistor as shown in the inset of **Figure A.5a**. Therefore, it is possible to derive a mathematical expression of the equivalent circuit, which differs the EIS formulation due to the fact that the charge, and not the current, is considered. The variation of charge in the layer can be written with the following differential form:

$$\frac{dq_h}{dt} = C_{chem} \frac{dV}{dt} \qquad \text{(Equation A.8)}$$

Which leads to an admittance equal to:

$$Y_C = C_{chem} \qquad \text{(Equation A.9)}$$

This equation represents the response of the layer in the case of no kinetics limitation. Nevertheless, the presence of a finite ionic diffusion in the YSZ generates a delay in the measured charge, which can be written as:

$$V = R_{YSZ} \frac{dq_h}{dt} \qquad \text{(Equation A.10)}$$

It is interesting to note that this equation is formally equal to an inductive contribution for electrical impedance spectroscopy (where the current and not the charge is observable). The admittance of the resistive component $R_{YSZ}$ can be then written in its complex formulation as:[14]

$$Y_{YSZ} = \frac{1}{j\omega R_{YSZ}} \qquad \text{(Equation A.11)}$$

Therefore, the overall admittance of the equivalent circuit can be written as:

$$Y = \left(\frac{1}{C_{chem}} + j\omega R_{YSZ}\right)^{-1} = \frac{C_{chem}}{1+j\omega R_{YSZ}} = \frac{C_{chem}}{1+(\omega R_{YSZ} C_{chem})^2} - j\frac{C_{chem}\omega R_{YSZ} C_{chem}}{1+(\omega R_{YSZ} C_{chem})^2} \qquad \text{(Equation A.12)}$$

Substituting $R_{YSZ}C_{chem}$ by the characteristic time $\tau$, **Equation A.12** is rewritten as:

$$Y = \frac{C_{chem}}{1+(\omega\tau)^2} - j\frac{C_{chem}\omega\tau}{1+(\omega\tau)^2} = Y' - jY'' \qquad \text{(Equation A.13)}$$

**Figure A.5** shows the fitting of the optical impedance spectra obtained according to this equation. It is worth noting that the reliability of the fitting is revealed not only in the Nyquist plot but also in the Bode plots of the real and imaginary parts of the optical admittance of the LSF40/CGO/YSZ sample, as shown in **Figure A.5b**. A chemical capacitance of 3270 F/cm$^3$ for the LSF40 thin film is obtained from the fitting, which is in good agreement with the value reported in the literature.[15]

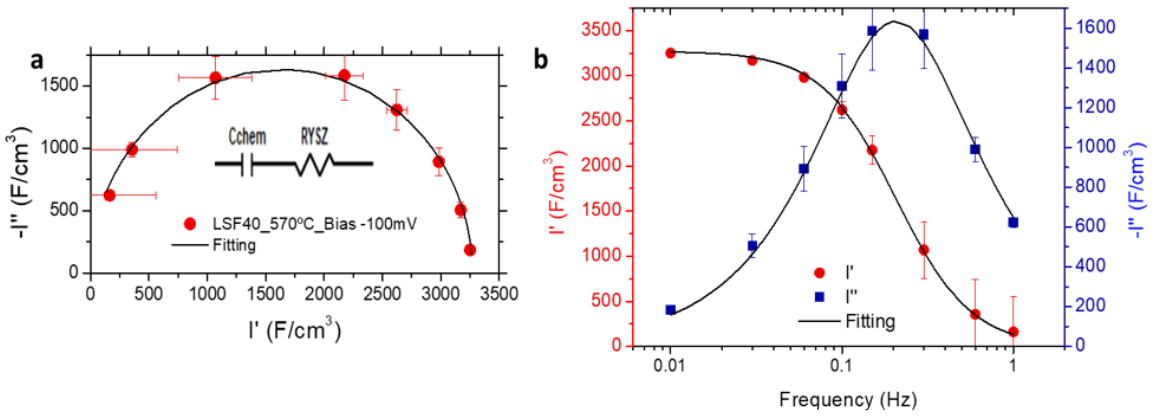


**Figure A.5 a.** Nyquist plot of the real and imaginary parts I′ and I″ of the optical admittance with the fitting using the equivalent circuit presented in the inset. **b.** Bode plots of the real and imaginary parts I′ and I″ of the optical admittance vs frequency with the fitting.

In addition, the resistance of YSZ can be calculated according to:

$$R_{YSZ} = \frac{\tau}{C_{chem} v} \qquad \text{(Equation A.14)}$$

Where $v$ is the volume of the LSF40 film, $\tau$ is obtained from the fitting as 0.76 s. The resulting resistance of YSZ is 436 Ω, being consistent with the value measured by EIS as shown in **Figure A.6**.

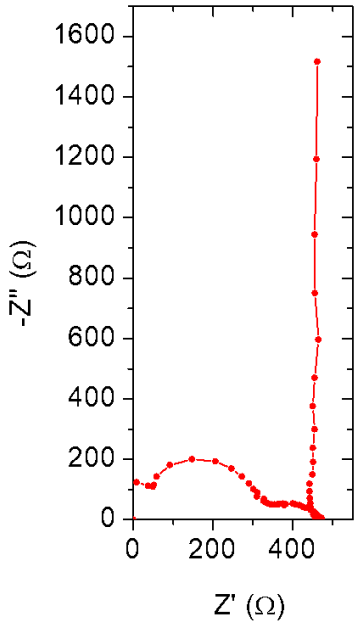


**Figure A.6** Nyquist plot of electrochemical impedance of the LSF40/CGO/YSZ sample measured at 540 ºC with a Nernstian voltage of -0.1 V.

Overall, an optical impedance spectroscopy based on the real-time optical response with the AC voltages is successfully developed for the LSF40/CGO/YSZ electrochemical cell at 540 ºC.

## A.3 Optical impedance spectroscopy of a thin film LSF50 cathode in alkaline electrolyte

As discussed in **Chapter 4**, the electrical potentials applied to LSF50 films are able to induce ion intercalation in alkaline electrolyte, giving rise to the variation of the $Fe^{4+}$ concentration in LSF50 thin films that can be observed by ellipsometry. Therefore, a study of the applicability of optical impedance spectroscopy at room temperature for LSF50 thin films in alkaline electrolyte is explored.

The experimental setup illustrated in **Chapter 2** was employed to carry out the in-situ kinetic ellipsometry measurements at room temperature (RT) and 40 ºC for LSF50 films deposited on FTO-covered glass substrates. Firstly, electrochemical behavior of the LSF50/FTO sample was characterized by CV at RT and 40 ºC at a scan rate of 0.5 mV $s^{-1}$. As depicted in **Figure A.7**, the cathodic peaks centered at -0.05 V and 0.03 V (vs Ag/AgCl) indicate the $Fe^{4+}/Fe^{3+}$ electronic transition in the LSF50 thin film in 0.1 M KOH electrolyte at RT and 40 ºC, it is clearly observed that the higher temperature improves electrochemical capacitance.

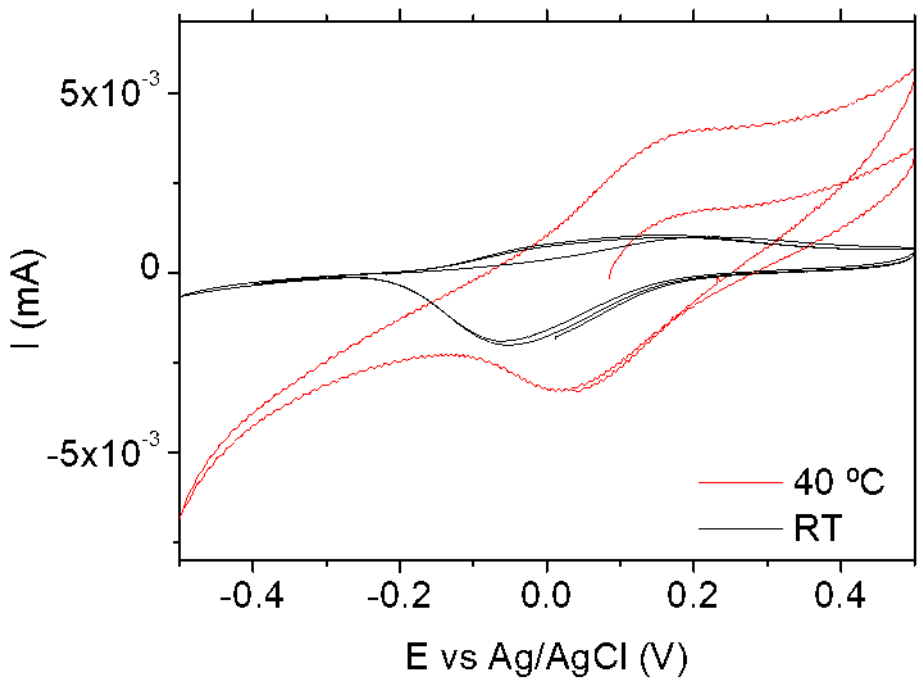


**Figure A.7** CV curves of the LSF50/FTO sample in alkaline electrolyte measured at RT and 40 ºC.

A DC bias was applied between the LSF50 film and the KOH electrolyte to enhance the variation of the optical signals (-0.02 V and 0.02 V for the measurements at RT and 40 ºC, respectively). The amplitude of the sinusoidal voltage was set to 0.05 V and the frequency was varied from 0.1 Hz to 1 mHz. The ellipsometry data were collected concurrently with the application of electrical voltage using multiwavelength ellipsometry. The resulting in-situ kinetic ellipsometry data are shown in **Figure A.8**. Differing from the data presented in the previous section, in this study the elliposmetry parameter $\Delta$, which is directly related to the real part of optical properties of the sample, is chosen for the analyses due to the better oscillatory signal evolution measured. Similar to the results for the solid-electrolyte sample at high temperature stated above, the applied AC voltages give rise to an oscillatory variation of the optical parameter $\Delta$. The amplitude and phase lag of the signals are related to the change in the $Fe^{4+}$ concentration as a result of equilibrium with the electrochemical conditions, as investigated in **Chapter 4**.

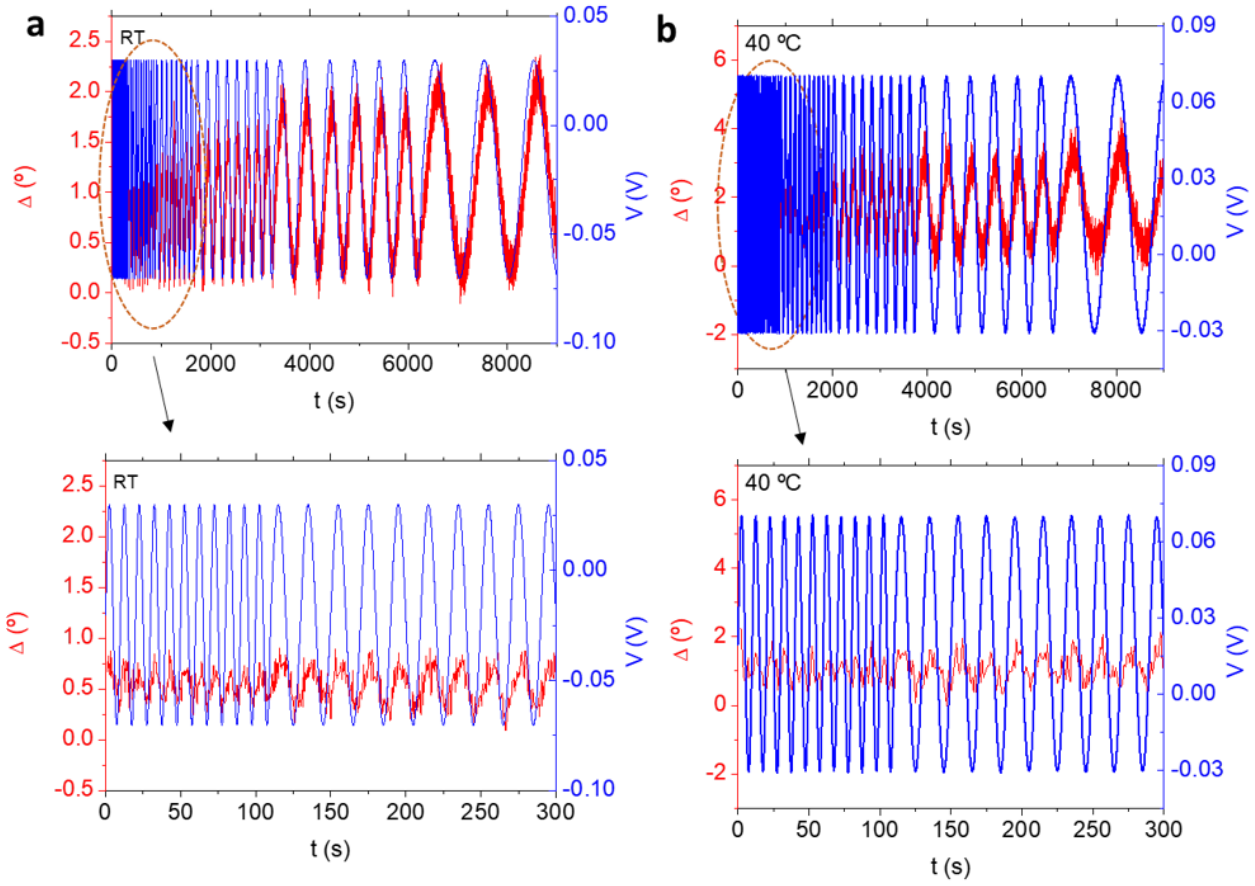


**Figure A.8** Oscillatory voltage-induced optical response $\Delta$ at the photon energy of 2.06 eV of the LSF50/FTO sample measured at **a.** RT and **b**. 40 ºC.

The input AC voltage and the output oscillatory optical response $\Delta$ can be fitted using a sinusoidal function, as indicated in **Equation A.1**. The resulting values of the $\frac{\Delta_0}{V_0}$ ratio and phase lag $\varphi$ are shown in **Figure A.9a**. Similar to what observed in the previous section of this chapter, the optical signal ($\frac{\Delta_0}{V_0}$) increases with decreasing the frequency, because low frequencies promote the electrochemical equilibrium of the LSF50 film. Furthermore, at RT the phase lag $\varphi$ increases with frequency until 0.02 Hz, after which the $\varphi$ starts to decrease. This divergence may originate from the fitting error due to the considerable noise in the optical signals at high frequencies. A large phase lag of roughly 26° for the sample measured at RT exists even at the extremely low frequency (1 mHz), indicating a considerable delay in the optical response. This suggests very slow kinetics, probably due to the slow ion diffusion rate in the LSF50 thin film at low temperatures.[20–23] The phase lag is decreased by increasing temperature from RT to 40 ºC, although a significant phase lag of 23 º is still evident at 1 mHz. The significant phase lag between the input electrical voltages and the output optical response leads to an incomplete semicircle in the optical admittance as shown in **Figure A.9b**, increasing the error associated with the fitting and hindering the development of a precise model for the optical admittance. Indeed, we note that the physical model in the case of diffusion limited process may be far more challenging than the one under surface limited kinetics, due to a gradient in the oxygen chemical potential across the thin films that reflects into a gradient of optical properties. Therefore, the ellipsometry signal observed is probably a convolution of many different optical states, varying across the films with the characteristic diffusive profile.

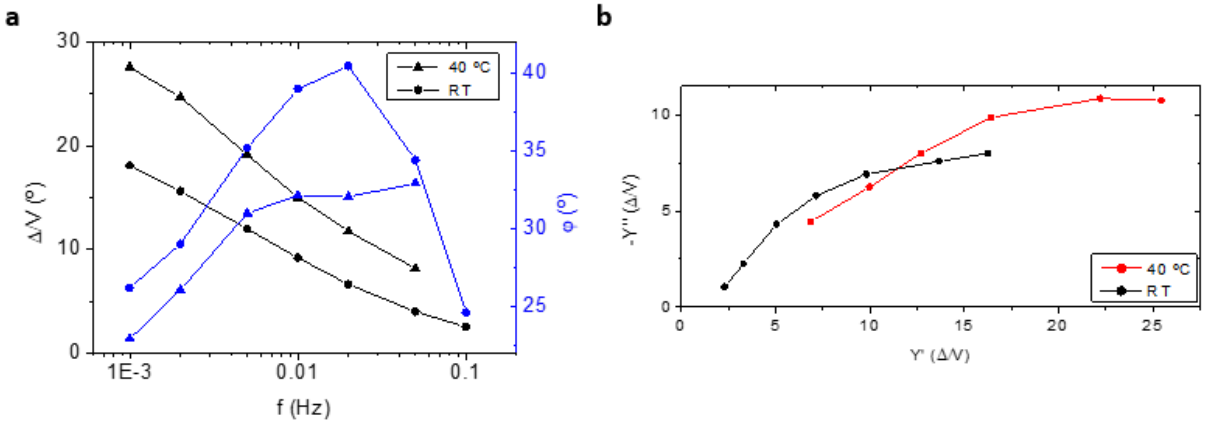


**Figure A.9 a.** Bode plots of the $\frac{\Delta_0}{V_0}$ ratio and phase lag $\varphi$ for the LSF50/FTO sample measured at RT and 40 ºC. **b.** Nyquist plots of the optical admittance for the sample measured at RT and 40 ºC.

Therefore, further research into the applicability of optical impedance spectroscopy to LSF50/FTO samples in alkaline electrolyte is required in the future. The experiments can be improved in the following aspects:

i. Reducing the oxygen diffusion length by decreasing the thickness of the LSF50 layer.
ii. Improving the experimental setup in order to increase the measurement temperature since the oxygen diffusion coefficient of LSF is linearly proportional to temperature.[22,24]
iii. Enabling the experiments at frequencies below 1 mHz, although it will be time-consuming.
iv. Developing a theoretical model able to correctly describe the optical impedance spectra of diffusion-limited ionic incorporation.

## A.4 Conclusions

In this Appendix, an in-situ kinetic ellipsometry technique was developed to monitor and quantify the change in the optical properties of LSF films with sinusoidal electrical potentials. The method was tested for both the solid-electrolyte LSF sample at high temperature and the liquid-electrolyte LSF sample at room temperature. The parameters derived from the coupling electrical and optical signals allow the measurement of optical impedance spectroscopy. The obtained optical impedance spectra can be fitted using a proper model. The electrochemical parameters extracted from the measured optical impedance spectra were in good agreement with the EIS measurements. Overall, the developed optical impedance spectroscopy is applicable and reliable for solid-electrolyte LSF50/CGO/YSZ samples at high temperatures, although more efforts are needed for liquid-electrolyte LSF samples.

# References


1. Rowley, N. M. & Mortimer, R. J. New Electrochromic Materials. *Sci. Prog.* **85**, 243–262 (2002).

2. Granqvist, C. G. Electrochromics for smart windows: Oxide-based thin films and devices. *Thin Solid Films* **564**, 1–38 (2014).

3. Wang, F. *et al.* Latest advances in supercapacitors: From new electrode materials to novel device designs. *Chem. Soc. Rev.* **46**, 6816–6854 (2017).

4. Azens, A. & Granqvist, C. G. Electrochromic smart windows: Energy efficiency and device aspects. *J. Solid State Electrochem.* **7**, 64–68 (2003).

5. Granqvist, C. G. *et al.* Recent advances in electrochromics for smart windows applications. *Sol. Energy* **63**, 199–216 (1998).

6. Cheng, J., Navrotsky, A., Zhou, X. D. & Anderson, H. U. Thermochemistry of $La_{1-x}Sr_xFeO_{3-\delta}$ solid solutions ($0.0 \leq x \leq 1.0$, $0.0 \leq \delta \leq 0.5$). *Chem. Mater.* **17**, 2197–2207 (2005).

7. Schmid, A. & Fleig, J. The Current-Voltage Characteristics and Partial Pressure Dependence of Defect Controlled Electrochemical Reactions on Mixed Conducting Oxides. *J. Electrochem. Soc.* **166**, F831–F846 (2019).

8. Alexander, C. T. *et al.* Anion-Based Pseudocapacitance of the Perovskite Library $La_{1-x}Sr_xBO_{3-\delta}$ (B = Fe, Mn, Co). *ACS Appl. Mater. Interfaces* **11**, 5084–5094 (2019).

9. Xie, Y. *et al.* Control of functional responses via reversible oxygen loss in $La_{1-x}Sr_xFeO_{3-\delta}$ films. *Adv. Mater.* **26**, 1434–1438 (2014).

10. Scafetta, M. D., Xie, Y. J., Torres, M., Spanier, J. E. & May, S. J. Optical absorption in epitaxial $La_{1-x}Sr_xFeO_3$ thin films. *Appl. Phys. Lett.* **102**, 081904 (2013).

11. Smolin, S. Y. *et al.* Static and Dynamic Optical Properties of $La_{1-x}Sr_xFeO_{3-\delta}$: The Effects of A-Site and Oxygen Stoichiometry. *Chem. Mater.* **28**, 97–105 (2016).

12. Park, H. S., Lim, J. S., Suh, J. & Yang, C. H. Real-time observation of filamentary conduction pathways in Ca-doped BiFeO3. *Appl. Phys. Lett.* **115**, 183901 (2019).

13. Manka, D., Schiller, C. A., Weber, A. & Ivers-Tiffée, E. Optical Impedance

Spectroscopy as a New Characterization Method for Electrochromic Windows. in *ECS Meeting Abstracts* (2012).

14. Swallow, J. G. *et al.* Dynamic chemical expansion of thin-film non-stoichiometric oxides at extreme temperatures. *Nat. Mater.* **16**, 749–754 (2017).

15. Schmid, A., Rupp, G. M. & Fleig, J. Voltage and partial pressure dependent defect chemistry in (La,Sr)$FeO_{3-\delta}$ thin films investigated by chemical capacitance measurements. *Phys. Chem. Chem. Phys.* **20**, 12016–12026 (2018).

16. Jamnik, J. & Maier, J. Generalised equivalent circuits for mass and charge transport: Chemical capacitance and its implications. *Phys. Chem. Chem. Phys.* **3**, 1668–1678 (2001).

17. Tang, Y. *et al.* Pushing the Study of Point Defects in Thin Film Ferrites to Low Temperatures Using In Situ Ellipsometry. *Adv. Mater. Interfaces* **8**, 2001881 (2021).

18. Wang, L. *et al.* Hole-induced electronic and optical transitions in $La_{1-x}Sr_xFeO_3$ epitaxial thin films. *Phys. Rev. Mater.* **3**, 025401 (2019).

19. Kogler, S., Nenning, A., Rupp, G. M., Opitz, A. K. & Fleig, J. Comparison of Electrochemical Properties of $La_{0.6}Sr_{0.4}FeO_{3-\delta}$ Thin Film Electrodes: Oxidizing vs. Reducing Conditions. *J. Electrochem. Soc.* **162**, F317–F326 (2015).

20. Opitz, A. K. *et al.* Thin film cathodes in SOFC research: How to identify oxygen reduction pathways? *J. Mater. Res.* **28**, 2085–2105 (2013).

21. Rekas, M., Bak, T., Nowotny, J., Sorrell, C. C. & Zhao, Y. Chemical diffusion of (La,Sr)$CoO_3$ and (La,Sr)$FeO_3$. *J. Mater. Sci. Electron.* **11**, 691–696 (2000).

22. Bae, H. *et al.* Investigations on defect equilibrium, thermodynamic quantities, and transport properties of $La_{0.5}Sr_{0.5}FeO_{3-\delta}$. *J. Electrochem. Soc.* **166**, F180–F189 (2019).

23. Wang, W. *et al.* Synthesis, morphology and electrochemical performances of perovskite-type oxide $La_xSr_{1-x}FeO_3$ nanofibers prepared by electrospinning. *J. Phys. Chem. Solids* **124**, 144–150 (2019).

24. Yoo, J., Verma, A., Wang, S. & Jacobson, A. J. Oxygen Transport Kinetics in $SrFeO_{3-\delta}$, $La_{0.5}Sr_{0.5}FeO_{3-\delta}$, and $La_{0.2}Sr_{0.8}Cr_{0.2}Fe_{0.8}O_{3-\delta}$ Measured by Electrical Conductivity Relaxation. *J. Electrochem. Soc.* **152**, A497 (2005).

# Scientific Contributions

## Peer reviewed articles:[ii]

Tang, Y., Chiabrera, F., Morata, A., Garbayo, I., Alayo, N., Tarancón A. Pushing the study of point defects in thin film ferrites to low temperatures using in situ ellipsometry. *Advanced Materials Interfaces.* 8, (2021) 2001881.

Tang, Y., Chiabrera, F., Morata, A., Cavallaro, A., Liedke, M. O., Avireddy, H., Maller, M., Butterling, M., Wagner, A., Stchakovsky, M., Baiutti, F., Aguadero, A., Tarancón, A. Defect Chemistry of Lanthanum Ferrite Thin Films during Ion Intercalation in alkaline electrolytes. Submitted.

## Patent:

Albert Tarancón, Francesco Chiabrera, Iñigo Garbayo, Nerea Alayo, Alex Morata, Yunqing Tang. *Electronic transistor*. Ref: EP21382543 (Submitted).

## Contributions in conferences:[iii]

1. Tang, Y., Chiabrera, F., Morata, A., Garbayo, I., Alayo, N., Tarancón A. Quantification of point defects in $La_{1-x}Sr_xFeO_{3-\delta}$ thin films by in-situ ellipsometry. Electronic Materials and Applications (EMA) (2021). Oral presentation.

2. Tang, Y., Chiabrera, F., Morata, A., Garbayo, I., Alayo, N., Tarancón A. Ellipsometry study of defect chemistry in $La_{1-x}Sr_xFeO_{3-\delta}$ (x=0.2, 0.4 and 0.5) thin films at intermediate-to-low temperatures. E-MRS Spring meeting (2021). Oral presentation.

[ii] Part of this thesis is adapted from the paper "Pushing the study of point defects in thin film ferrites to low temperatures using in situ ellipsometry" Tang, Y., Chiabrera, F., Morata, A., Garbayo, I., Alayo, N., Tarancón A. published in the journal *Advanced Materials Interfaces.* 8, (2021) 2001881. With the permission of Wiley-VCH GmbH.

[iii] The underlying indicates the presenting author.